ITAP: Clinical outcomes and implant design optimisation using numerical modelling

Kirstin Ahmed

UCL

Submitted for the degree of Doctor of Philosophy

2021

I, Kirstin Ahmed confirm that the work presented in this thesis is my own. Where information has been derived from other sources, I confirm that this has been indicated in the thesis.

Acknowledgements

The work presented in this thesis would not have been possible without the help of many brilliant people. I owe my deepest gratitude and would like to dedicate this thesis to Dr Angus Ramsay of Ramsay Maunder Associates Ltd., whom I was fortunate enough to meet at the start of this journey. He has been an invaluable academic mentor, scientific advisor and now lifelong friend, I cannot imagine how this would have been possible without his guidance. Angus I thank you from the bottom of my heart, I feel very lucky to have you in my life and I promise never to become a button pushing finite element analyst.

I would also like to thank Professor Gordon Blunn, my academic supervisor, for making all this possible and believing that I could achieve it. Thank you for everything that you invested into me, the time you made for me, the doors you opened for me, for never saying no to me and the wisdom of your experience. It has been invaluable, and I will forever be grateful that you said yes the first day I nervously turned up in your office.

I would next like to thank the rest of my UCL supervisory team; Dr Catherine Pendegrass, Dr Mehran Moazen and Dr Steve Taylor for giving me their time, patience and wisdom. Steve, I have no idea how I would have collected the patient data without you, thank you for spending so much of your time on my project. Mehran thank you for our long supervisory calls, often out of hours. Catherine thank you for navigating us and keeping me grounded.

Beyond UCL there are many people who I would like to thank; Professor Noel Fitzpatrick and Dr Cameron Black for their support with canine data collection, I am sorry I ran out of time on our project. Morven McAlinden, thank you for all your time, expertise, friendship and unwavering support; most of what I learned about these patients has come from you. Iva Hauptmannova, thank you for taking the pain of NHS ethical approvals away from me. You have been a wise, calm and an immeasurably supportive influence on me throughout this journey. Dr Richard Greene of Strain Solutions, thank you for your belief in me and for sharing your wealth of knowledge and scientific rigour in such a good-hearted manner.

Most importantly I would like to thank my family for their unconditional love and support along this very rocky road. I feel your love every day, thankyou Mum and Dad.

Finally, I would like to thank all my friends and colleagues in the postgraduate office in the Biomedical Centre; whom I knew for too short a time and hope that our paths will cross again..

Abstract

Redistribution of the flow of forces through the body, such as that after amputation and/or implantation of a skeletally anchored amputation prostheses, leads to bone remodelling. Periprosthetic bone resorption can destabilise skeletally anchored amputation prostheses. Therefore, implants that minimise bone resorption will achieve a more successful long term bone fixation. Bone remodelling outcome measures rely on implant design using mechanoregulatory bone remodelling theory. Mechanoregulation is implemented by functions that link a local mechanical stimulus to a local change in the structure or properties of bone material. This thesis uses the strain adaptive remodelling theory at the time of implantation with periprosthetic strain energy density as the outcome parameter.

Clinical trial data was collected from a patient with a skeletally anchored amputation prostheses; The Intraosseous Transcutaneous Amputation Prosthesis (ITAP). The clinical trial ran from 2008 – 2019, the data was investigated for patterns between implant design and fixation success. This thesis reports trends in fixation success and bone change using a developed fixation success score. There was an ideal implant length to bone length ratio range and a straight, tapered stem with a flared bone collar growth shape were beneficial to fixation success. Conversely, one or more parameters associated with pressfit fixation were detrimental to fixation success.

Results between the clinical and numerical data compared favourably; clinically, regions of periprosthetic bone growth were also observed by regions of high strain energy density in the finite element analysis and vice versa at the implant tip and osteotomy face. This thesis provides skeletally anchored amputation prostheses design guidelines that will minimise bone resorption when measured with strain energy density. Moreover, that future skeletally anchored amputation prostheses parameterised design can and should be used as a tool to assess bone fixation outcome in pre-clinical assessments.

Impact statement

There are more than one million annual limb amputations globally (Amputee, 2012). Approximately 210,000 are transfemoral (without vascular complications, thus suitable for skeletally anchored amputation prosthesis (SAAP) surgery) of whom 22,500 are in the UK and 2,500 are performed annually in the UK (Berke et al., 2008). Presently, the ambulatory prescription is the fitting of a prosthetic socket to the patient's residual limb. Achieving stable mechanical attachment to the limb is a challenge since the socket must be tight fitting. This generates unnaturally high pressure and friction on the residual soft tissues. Additionally, temperature and humidity fluctuations can change the shape and volume of the amputated limb (Paternò et al., 2018). As a result prosthetic sockets frequently cause discomfort, skin problems and restricted blood circulation and can relegate patients to wheelchairs (Pascale and Potter, 2014). SAAPs offer an alternative; an artificial limb is attached to a percutaneously implanted metal extension of the residual bone. This results in channelling load through the skeleton bypassing the soft tissues and has shown to increase wearing time and function (Hagberg et al., 2008).

There are five well known SAAP designs varying marginally in surgical method used for implantation, fixation type, material and geometry. All have published data demonstrating that at least some minor infection and/or aseptic loosening occurs. Aseptic loosening can be the result of the bone stress shielding effect by the implant, bone infection or implant wear debris. This thesis demonstrates how implant design and fixation method can minimise or omit aseptic loosening due to stress shielding. This is one of two steps towards developing SAAP implants that can be globally adopted with confidence in a successful long term fixation to the bone. In parallel ongoing research is being carried out to minimise and manage infection rates.

SAAP economics are favourable in the long term compared with socket prostheses (Frossard et al., 2018) and societal cost benefits from a more independent and mobile workforce (Burger and Marincek, 2007). This, together with a reduction in levels of patient pain and an increase in quality of life (Hagberg et al., 2008), provides a very strong case for widescale adoption of SAAPs to treat lower limb amputees.

Despite skeletal fixation, a SAAP is unconnected from the neuromuscular system and therefore the patient cannot intuitively control it as they would a biological limb. Establishing a direct connection between the limb and the user's skeleton, nerves, and muscles has been achieved (Ortiz-Catalan et al., 2020) and the bidirectional communication between the external prostheses and implanted electrodes will facilitate a more natural prosthetic function with improved outcomes (Zaid et al., 2019b).

Contents

Table of Figures

Table of charts

Table of Tables

Glossary of Terms

% RMSE	% Root Mean Square Error
AFcollar	Bone between zones A and F and the osteotomy face
ANOVA	A One Way Analysis of Variance
AP	Anterior posterior
APDL	ANSYS Parametric Design Language
BC	Boundary Condition
BMD	Bone Mineral Density
BMP	Bone Morphogenetic Protein
BMU	Basic Multicellular Units
BW	Body Weight
CCC	Concordance Correlation Coefficient
CIG	Collar cortical Ingrowth
CoCr	Cobalt-Chromium
CoCrMo	Cobalt-Chrome-Molybdenum
COG	Centre of Gravity
COM	Centre of Mass
cp	Cortical Plate
CPS	Compress Compliant Pre-Stress device
DIC	Digital Image Correlation
DICOM	Digital Imaging and Communications In Medicine
DLC	diamond like carbon
EMG	Electromyography
F ratio	residuum: femur
FDA	US Food and Drug Administration
FE	Finite Element
FEA	Finite Element Analysis
FEM	Finite Element Method
FGF	Fibroblast Growth Factors
FS SCORE	Fixation Success Score
GC	Gait Cycle
GRF	Ground Reaction Force
HA	Hydroxyapatite
IFG	Insulin-Like Growth Factors
ILP	Integral Leg Prosthesis
IM	Intramedullary
IT	Iliotibial
ITAP	Intraosseous Transcutaneous Amputation Prosthesis
LC	Load Case
LCS	Local Coordinate System
LHS	Left Hand Side

MCK	Microprocessor Controlled Knee
MCP	Multi-Point Constraints
MCS	Mental Component Summary
ML	Medial lateral
OGAAP	Osseointegration Group of Australia Accelerated Protocol
OH	Overhang
OLP	Osseointegrated Prosthetic Limb
OPG	Osteoprotegerin
OPRA	Osseointegrated Prosthesis for the Rehabilitation of Amputees
PCS	Physical Component Summary
PDGF	Platelet-Derived Growth Factor
PMMA	Polymethyl Methacrylate
Q-TFA	Questionnaire for Persons with a Transfemoral Amputation
RHS	Right Hand Side
RL	Radiolucent
RNOH	National Royal Orthopaedic Hospital, Stanmore, UK
ROH	Royal Orthopaedic Hospital, Birmingham, UK
ROM	Range of Movement
RSA	Roentgen Stereophotogrammetric Analysis
S ratio	stem: femur
S1	Surgery 1
S2	Surgery 2
SAAP	Skeletally anchored amputation prosthesis
SD	Standard Deviation
SED	Strain Energy Density
Sema3A	Semaphorin3A
Sema4D	Semaphorin4D
SF-36	Short Form Survey
SIGAM	Special Interest Group in Amputee Medicine
TF	Transfemoral
TFL	Tensor Fascia Lata
TGF- β	Transforming Growth Factor β
THR	Total Hip Replacement
Ti	Titanium
Ti6Al4V	Ti alloy 6 % aluminium and 4 % vanadium
TKR	Total Knee Replacement
UC	Undercut
UHMWPE	Ultra-High Molecular Weight Polyethylene
V & V	Verification and Validation
V3D	Visual 3D biomechanics software

CHAPTER 1

A literature review on the structure, mechanics and simulation of skeletally anchored amputation prostheses in transfemoral amputees.

1.1. Introduction and aims

This review chapter intends to report the current understanding of bone mechanobiology and skeletally anchored amputation prostheses (SAAPs). A review of the Finite Element Method (FEM) is also included. In summarising the literature, it has been possible to formulate aims and goals for subsequent Chapters.

Attaching an artificial limb to an amputee has, until recently, been restricted to the fitting of a prosthetic socket to the patient's residual limb. There are more than one million annual limb amputations globally (Amputee, 2012), approximately 210,000 of these are transfemoral (TF) amputations, of these 22,645 were performed between 2003 and 2013 in adults aged 50 – 84 in the UK (Ahmad et al., 2016). Although methods of soft tissue stabilisation in TF amputation surgery have improved (Gottschalk, 2016b), the soft tissues still experience significant pressure using a prosthetic socket. The pressure restricts blood and air circulation and leads to sores and skin ulcers on the residual limb which can become necrotic (Salawu et al., 2006, Meulenbelt et al., 2007, Gailey et al., 2008). A patient's range of movement is restricted by the socket edge and slip, and their biomechanics are altered (Nolan et al., 2003, Rabuffetti et al., 2005, Mengelkoch et al., 2017). This can lead to osteopenic bone (through disuse), abandonment of the artificial limb, and in some cases relegation to a wheelchair (Pascale and Potter, 2014). Often TF amputees experience secondary symptoms such as back pain, contralateral leg knee and hip osteoarthritis, reduced independence, wellbeing and societal economic value (Burger and Marincek, 2007, Gailey et al., 2008).

An alternative is a SAAP; where an artificial limb is attached to an implanted metal extension of the residual bone, thus directly loading the skeleton (Li and Branemark, 2017, Sullivan et al., 2003). In this procedure a metal pylon is inserted into the intramedullary (IM) canal of the host bone in a one or two step surgical operation. An exoprosthetic percutaneous part is used as an attachment for the artificial limb via a failsafe device (see A.1.3) . A SAAP does not restrict the patient's range of motion, improves sitting comfort and minimises discomfort associated with ambulation (Hagberg et al., 2005b). Patients cite an improved quality of life (Van de Meent et al., 2013) with increased limb use (Hagberg et al., 2008, Hagberg et al., 2004). Furthermore, the lifetime cost of the SAAP is less than the socket prosthesis when the patient quality of life is factored into the assessment (Frossard et al., 2018, E. Hansson et al., 2018). Currently there are 100 - 150 TF SAAP patients in the UK, 300 - 350 in Europe and over 1000 globally using one of five SAAP designs; Intraosseous Transcutaneous Amputation Prosthesis (ITAP),

Osseointegrated Prostheses for the Rehabilitation of Amputees (OPRA), Integrated Leg Prosthesis (ILP), Osseointegrated prosthetic Leg (OPL) or the Compress Prosthetic Device (CPS). TF SAAP research encompasses two *clinical* trials; the OPRA in Sweden and the ITAP in the UK.

Current research on SAAP patient biomechanics is limited to one SAAP, the OPRA (Frossard, 2019, Lee et al., 2007). Whether these biomechanics reflect those of amputees fitted with different SAAP designs is unknown. Furthermore, the way in which the biomechanics of SAAP users differs between prosthetic socket users and non-amputated individuals is unclear. One of the overriding aims of this thesis will be to answer these questions by firstly augmenting the current OPRA biomechanical data with that from an ITAP patient. And secondly by investigating how both sets compare to prosthetic socket users and non-amputated individuals. Chapter Three describes the protocol used to obtain this data as well as the development of the bespoke load cell used. The kinetic and kinematic data gathered walking on level and sloped ground from an ITAP patient is of great scientific value since it can be used to inform the development of prosthetic devices for TF amputees. Specifically, whether settings for micro processor controlled or fully active prosthetic devices or rehabilitation protocols should be adapted according to user population and SAAP type.

Redistribution of the flow of forces through the body, such as that after amputation and/or SAAP surgery, leads to bone remodelling. Bone remodelling ensures that the minimal amount of bone material capable of providing the strength required of it is present at any time. Periprosthetic bone resorption can destabilise SAAPs, therefore, implants that minimise bone resorption will achieve a more successful long term bone fixation. This thesis uses the strain adaptive remodelling theory (Lanyon et al., 1982, O'connor et al., 1982, Huiskes et al., 1987, Lanyon, 1987, Huiskes et al., 2000) to investigate the most favourable SAAP design features for successful fixation. Chapter Five describes how this is achieved using Finite Element Analysis (FEA). At the time of writing there is no published parametric FEA on any SAAP design for TF amputees. This gap in the literature is of significant value since it offers information on how a SAAP design can directly influence clinical outcome.

1.2. Bone biology and mechanics

1.2.1. Structure/function

1.2.1.1. Overview

In the body, the primary building blocks of load bearing tissues are collagen (a protein) and hydroxyapatite, HA (a mineral; $Ca_{10}(PO_4)_6(OH)_2$) in differing amounts and structural organisation Figure 1.1 shows these are inversely proportional along a percentage by weight (wt%) contiuum.

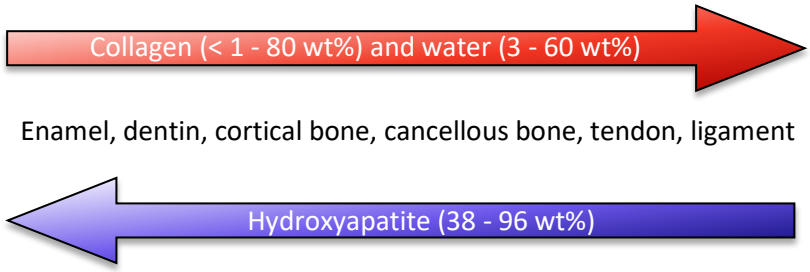

Fig. 1.1: Load bearing tissues constituent continuum

There are more than 20 types of collagen, type I is found in bone, dentin, ligaments and tendons. Three polypeptide chains combine into tropocollagen molecules (300 nm long and 1.5 nm thick molecules) which assemble into collagen fibrils (~ 100 nm in diameter) that bundle together in collagen fibres (Fratzl et al., 2004). Fibres form cross linkages with neighbouring tropocollagen molecules providing tensile strength and viscoelasticity. Viscoelastic materials display time dependant material properties (Furmanski et al., 2011b), which is an important behaviour of load bearing tissues to consider when quantifying the effect of forces on them. Further strength and HA binding regulation results from crosslinks with other non-collagenous proteins such as osteocalcin, osteonectin, bone sialoprotein II, and osteopontin (General, 2004, Florencio-Silva et al., 2015). Collagen fibres are flexible but tougher than HA, the degree of hydration determines its elasticity but aging (increased cross linkage) and dehydration lead to an embrittlement process (Furmanski et al., 2011a).

In bone, the stiff and brittle HA mineral is made up of 2 - 4 nm thick plate like crystals. The mineralisation of collagen by HA forms sheets of mineralised tissue (lamellae) aligned in a dominant direction. (Fratzl et al., 1992). The longitudinal axis of HA is parallel to that of the fibril and determines the reinforcement orientation. Lamella orientation changes from layer to layer by ~ 30 ° (Wagermaier et al., 2006) enabling bone to withstand shearing forces through a multidirectional stress range and giving rise to bone's high resistance to fracture (Fig. 1.2 bottom right). A second function of HA is that of a mineral reservoir (calcium and phosphorous) for the body in times of need, accessed via a system of regulatory hormones and ensuring the maintenance of mineral levels in cells and blood. Trace elements including carbonate, sodium and citrate can be found in the HA and these increase the mineral's solubility (Boskey, 2001). Bone is a hierarchical material; at the cellular level, activities of bone enable it to perform as a structural and protective tissue, mineral reservoir and bone marrow harbour whilst undergoing a cyclical process of resorption and formation (Robling et al., 2006, Datta et al., 2008). At the tissue level bone is in two forms; cortical and cancellous, the major distinction between these bone types is porosity. Cortical bone is a tightly packed structure where layers of lamellae form a cylinder around a central conduit (haversian canal) carrying blood and lymphatic vessels, this unit is an osteon.

Pores or lacunae, between the layers of lamellae are connected via canaliculi (channels), osteocytes (see 221.2.1.2.) reside in lacunae. Cancellous bone is highly porous where the lamellae do not form cylinders around blood vessels, instead they form a network of rods and plate like trabeculae through which red bone marrow (in which red blood cells are produced) is interspersed (Fig. 1.2).

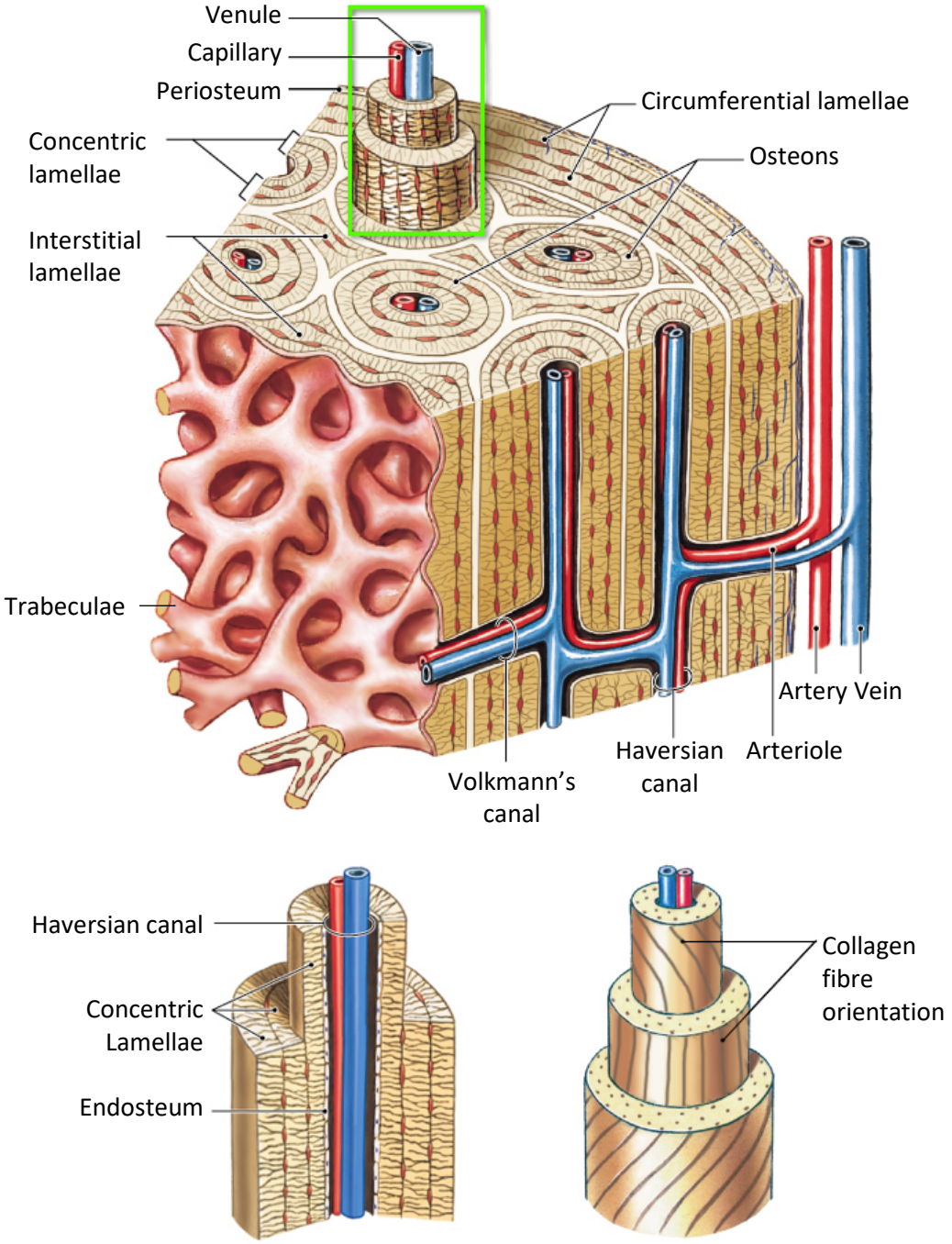

Fig. 1.2: Compact bone organisation
Top = The organisation of osteons and lamellae in compact bone.
Green magnification box = Collagen fibres and lamellae in an osteon.
Adapted from Pearson education Inc. 2012

1.2.1.2. Bone cells

There are four types of bone cell:

Osteocytes: The most numerous of the bone cells arises from the differentiation of osteoblasts after a bone formation cycle. The fully mature osteocyte, encased in a lacunae, has up to 50 cytoplasmic processes that tunnel through the canaliculi and join other osteocytic processes forming the osteocyte lacunocanalicular system. This cell to cell communication is responsible for intracellular transport of signalling molecules (Bilezikian, 2002) and enables mechanosensing (Rochefort et al., 2010). The mechanism that converts mechanical stimuli to biomechanical signals is not well understood (see 1.2.2).

Osteoblasts: Derived from mesenchymal stem cells and having a bone forming function, osteoblasts are responsible for depositing tropocollagen molecules, non-collagenous proteins and proteoglycan to form an organic matrix into the extra cellular space for subsequent mineralisation (Florencio-Silva et al., 2015). Mineralisation occurs in two phases: the vesicular and fibrillar phases (Anderson, 2003) which results in HA crystals being released into the surrounding matrix.

Osteoclasts: These cells originate from hematopoietic stem cells and are controlled by the interactions between receptor activator of NFkB (RANK) and receptor activator of NFkB ligand (RANKL) and osteoprotegerin (OPG) (Phan et al., 2004, Tyrovola et al., 2008). They are responsible for the degradation of bone: a microvillus membrane develops during bone remodelling wherein a vacuolar-type protein pump (V-ATPase) is located, this enables dissolution of HA. From this membrane, enzymes and proteins responsible for bone degradation are transported to the Howship lacuna and by-products endocytosed across the membrane (Graves et al., 2008).

Bone lining cells: Although their function is not fully understood, they appear to lift and form a canopy under which bone remodelling (see 1.2.2) events occur (Hauge et al., 2001). Furthermore, evidence indicates an intrinsic control of the differentiation of hematopoietic stem cells to osteoclasts (Kollet et al., 2006), removing non-mineralised collagen fibrils and depositing collagen on bone surface after remodelling (Everts et al., 2002).

1.2.2. Bone modelling/remodelling

In contemporary biomechanics the term “remodelling” is often used to mean “adaptation” however there are two types of bone adaptation processes; modelling and remodelling. These are separate events; bone modelling is a morphological adaptation describing bone resorption and formation occurring on separate unlinked surfaces. It most often takes place during birth to adulthood sculpting bones so that they gain skeletal mass, change in form and/or shift in space. Bone remodelling occurs throughout life and ensures bone remains mechanically sound, preventing microdamage, and is related to renewal. It is a coupled process where new bone tissue replaces old bone tissue at the same site, continuously changing the internal architecture. Most of the human skeleton is replaced via bone

remodelling every ten years. Bone remodelling takes place on bone surfaces; in cancellous bone this is the marrow/bone surface and in cortical bone these are the surfaces of Haversian and Volksmann's canals as well as the periosteum and endosteum, although much less on the periosteum (Orwoll, 2003).

1.2.2.1. The bone remodelling cycle

The bone remodelling cycle is initiated by bone cell communication and drives the formation of basic multicellular units (BMUs). A BMU is made up of osteoclasts in front resorbing bone in longitudinally orientated channels (cutting cone) followed by osteoblasts, depositing layers of lamella bone (closing cone). It is thought a canopy of bone lining cells forms on the bone surface, under which these events take place (Hauge et al., 2001), the cycle takes approximately four months. The remodelling process in cortical and cancellous bone is the same but the organisation of BMUs differs: in cortical bone the cutting cone forms a cylindrical canal and normally occurs on the endosteal surface (next to the bone marrow) whereas in cancellous bone, osteoclast activity results in a trench on the bone surface. Cortical bone remodelling produces a secondary osteon of new bone (Parfitt, 1994), which unlike primary osteons, is bound by a cement line derived from the cessation of osteoclast activity and the start of osteoblast bone formation. Cancellous bone remodelling produces an equivalent structure called a cancellous osteon or hemiosteon (Frost, 1986) at up to a ten times faster rate (Marcus et al., 2001).

1.2.2.2. Bone cell communication

A coupling mechanism orchestrates bone cell communications; soluble coupling factors such as insulin-like growth factors (IFGs), transforming growth factor β (TGF-β), bone morphogenetic proteins (BMPs), fibroblast growth factors (FGF), and platelet-derived growth factor (PDGF) from the bone matrix are released in resorption (Linkhart et al., 1996). Semaphorin glycoproteins are thought to play a role in this communication too; osteoclasts release semaphorin4D (Sema4D) which stops bone formation by osteoblasts during bone resorption (Negishi-Koga et al., 2011). Conversely Sema3A, in osteoblasts, inhibits bone resorption (Hayashi et al., 2012) and is released prior to bone formation (Delorme et al., 2005). Other factors involved are thought to include the ephrinB2/ephrinB4 pathway signalling the end of bone resorption and inducing osteoblast differentiation before the bone formation phase (Zhao et al., 2006). Osteoblast differentiation is also stimulated by signalling molecules Wnt10b, BMP6, and the signalling sphingolipid, sphingosine1-phosphate (Pederson et al., 2008).

One theory by which osteocytes may detect stimulus is via their cytoplasmic processes; bending moments from bone loading are thought to drive interstitial fluids through the lacunocanalicular network and these changes are registered. Registry is achieved through fluid flow detecting primary cilia (Malone et al., 2007), tethering elements responding to resultant forces from fluid flow (such as hoop

strain on the process membrane and underlying central actin filament bundle) and/or integrins associated with stretch-activated ion channels to convey fluid shear stress to the cytoskeleton (Reilly et al., 2003). Another way osteocytes may sense a stimulus is through actin to extracellular matrix attachments. These employ integrins and CD44 receptors on the cell membrane (Aarden et al., 1996). Once detected, the osteocyte appears to amplify the signal, and then transduce it via one or more pathways including kinase signalling, calcium signalling, g-protein-mediated signalling, prostaglandins and nitric oxide which initiates the effector cell (osteoblast/osteoclast) response (resorption/apposition).

1.2.2.3. Bone cell mechanobiological route

The mechanobiological route by which mechanical forces are expressed by the bone cells is still unresolved, but has evolved to some generally accepted theories today: Wilhelm Roux in the 19th century (Roux, 1881) was aware that biological processes were regulated by signals to cells generated by mechanical loading, followed shortly after by Julius Wolff (Wolff, 1892) with his *Das gesetz der transformation der knochen* (law of transforming bones) wherein he proposed bones will adapt to the loads under which they are placed, and in 1917 by Thompson D'Arcy (Thompson d'Arcy, 1917) in his treatise On Growth and Form: *". . . the very important physiological truth (is) that a condition of strain, the result of a stress, is a direct stimulus to growth itself."* Towards the end of the century, mathematical models were developed to describe the functional adaptation of bone loading. Huiskes et al. (1987) outlined a strain adaptive remodelling theory to incorporate a homeostatic zone (lazy zone) proposed by Carter (1984). At a similar time, Frost (1987) coined the phrase 'mechanostat' with respect to the remodelling response behaving like a thermostat, i.e. occurs within strain magnitude or rate threshold.

1.2.2.4. Stimulus for bone remodelling

From animal studies (Rubin et al., 1996) it has been shown that strain magnitude alone is not the stimulus for bone remodelling. It is more likely that the components of the strain tensor (i.e. the full strain state of the bone tissue) perform different roles in bone homeostasis (i.e. the metabolism of the osteoclast, osteoblast or osteocyte). Strain rate (dynamic but not static strains), strain frequency (high frequency low magnitude strains) and cycle number (triggered after a limited number of cycles) have osteogenic potential. Strain gradients (spatial distribution of strains), which are proportional to lacunocanalicular fluid flow in bone also play a role in the osteogenic response (Orwoll and Bliziotes, 2002).

1.2.2.5. Strain adaptive remodelling theory

A solid's strain energy density (SED) is "…the work done per unit volume to deform a material from a stress free reference state to a loaded state" (Bower, 2009), units are Jm^{-3} or Pa (see Appendix A.1.2). In the 'strain adaptive remodelling theory', Huiskes et al. (1987) used SED as the remodelling signal described mathematically as an iterative feedback loop (Equation 1.1).

$$\frac{dE}{dt} = \begin{cases} C_a (U - (1 + s) U_h) & U > (1 + s) U_h \Rightarrow \text{Bone apposition} \\ 0 \quad \text{when} & (1 - s) U_h \leq U \leq (1 + s) U_h \Rightarrow \text{Lazy zone} \\ C_r (U - (1 - s) U_h) & U < (1 - s) U_h \Rightarrow \text{Bone resorption} \end{cases}$$

C_a or C_r = Remodelling rate constants

U_h = Homeostatic SED threshold

U = Local SED

S = Half width of the lazy zone

Eqn.1.1

A local SED (U) was referenced against a homeostatic threshold level (U_h), above which bone apposition occurred and below which resorption occurred. The 'lazy zone' was proposed as a fraction of U_h (*s*) either side of U_h, a zone (of width 2*s*) in which there was no net bone mass change. A linear remodelling rate is observed plotting SED against rate (Chart 1.1). Values for U_h vary depending on bone site and density, however Weinans et al. (1992) suggest 0.004 MPa. Modelling the lazy zone (2*s*), values for *s* from 5 – 30 % were used experimentally by Huiskes et al. (1987) but 10 % is the most commonly reported value (Mellal et al., 2004, Schmitz et al., 2004). There are several groups who have suggested there is no 'lazy zone' (Sugiyama et al., 2012, Schulte et al., 2013, Christen et al., 2014) but still report the homeostatic critical SED (U_h) and a linear relationship between U and remodelling rate. Furthermore, Christen et al. (2014) suggest load driven bone remodelling does not explain fully their observations and that remodelling may also be driven by the need to balance calcium levels and renew bone tissue. The Stanford theory (Beaupré et al., 1990) is a strain error adaptive remodelling theory, defining the strain error stimulus as the difference between the daily strain and the attractor strain. A daily strain (or stress) is defined by an empirical constant that weights the relative contribution of strain magnitude and the number of loading cycles. Experimental data suggests the magnitude of the cyclic strain is more important than the number of loading cycles (Worthen et al., 2005).

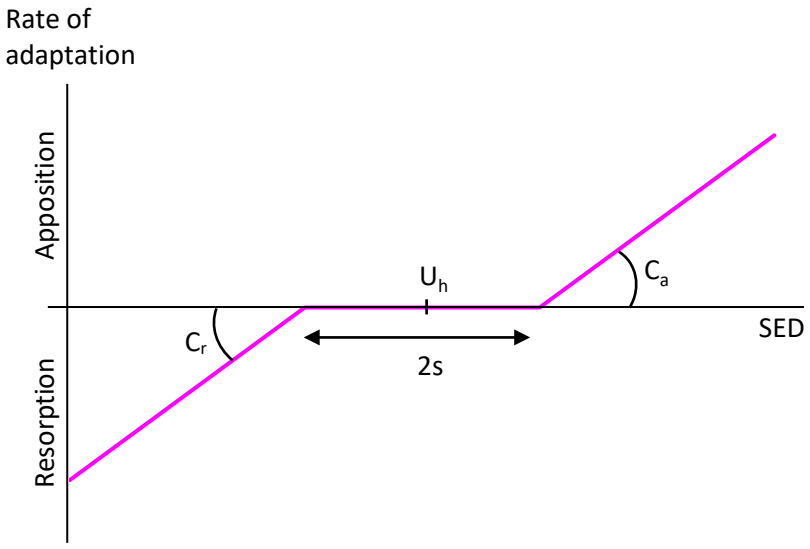

Chart 1.1: Local bone adaptation as a function of SED
Lazy zone width = 2s. Homeostatic SED (U_h) at centre. Constants of remodelling (C_a and C_r) dictate the remodelling rate.

1.2.2.6. Damage repair remodelling theory

The damage repair theory suggests that when damage from fatigue or impact occur, bone is able to detect, remove and replace it (Parfitt, 2002). This reparative remodelling may be triggered as microcracks cut through the processes of osteocytes (Dooley et al., 2012) and/or osteocyte apoptosis, wherein the neighbouring, non-apoptotic osteocytes have been shown to produce osteoclastogenic factors such as RANKL (Kennedy et al., 2012). Woven bone is deposited under a variety of loading conditions including in reparative remodelling and is produced at a much faster rate than lamellar bone (50 µm/day compared with 0.5 µm/day for circumferential lamellar bone (Carter and Beaupre, 2000).) It is not clear if this is as a result of bone damage or at one end of the strain-adaptive continuum.

1.2.2.7. Bone remodelling current understanding

Further mechanisms have been proposed controlling the remodelling of bone that become important when iteratively applying load cases to a model (Mullender et al., 1994, Mullender and Huiskes, 1995, Huiskes et al., 2000, Ruimerman et al., 2001). It is likely that bone remodelling is multifactorial and may encompass an adaptive strain remodelling component as well as a response to damage (overload) along with mineral balance and tissue renewal control factors. Our current understanding is that the remodelling effect on bone influenced by a mechanical signal tends to some general rules (Turner, 1998):

1. Dynamic loads elicit a bone response, static loading does not.
2. There is a minimum strain magnitude or rate threshold, only over which bone responds (new bone formation amount correlates with strain magnitude and rate).
3. Bone adapts in response to short loading periods. Longer duration loading has diminished returns. Routine loading results in bone apposition plateauing after a low number of cycles.

The signal is thought to be strain, acting on mechanosensors which are most likely osteoblasts (Iqbal and Zaidi, 2005) along a signal transdution pathway that convert the mechanical stimuli into a biochemical reaction. Incorporating the rules of Turner (1998) within a mathematical relationship would allow the prediction of bone remodelling. The adaptive strain remodelling theory or the strain error driven bone remodelling theories hypothesise that a higher stimulus leads to increased bone mass and vice versa. This thesis therefore uses SED as the outcome measure.

1.2.3. Bone mechanical properties

Cortical bone is stronger in compression than tension (Park and Lakes, 2007) and stronger along its long axis than radially or circumferentially (transversely) (Bartel et al., 2006) it is relatively weak in shear. Cortical bone behaves in a linear elastic manner at moderate loads, until plastically deforming at a yield point. Although structurally heterogenous, transverse strength and elastic moduli are similar in both axes, whereas longitudinal modulus is approximately double the transverse elastic moduli. For this reason, bone is often modeled as transversely isotropic or orthotropic (Ashman et al., 1984, Taylor, 2002, San Antonio et al., 2012, Newcombe et al., 2013, Geraldes and Phillips, 2014).

Cancellous bone, despite most often being modelled as linearly elastic, is nonlinearly elastic (Morgan et al., 2000). In compression, yield is achieved at strains of ~ 1 %, thereafter it can sustain up to ~ 50 % strain. This behaviour is due to its foam like material behaviour; under compression the cellular structure crushes until pore space is eliminated (Ashby and Gibson, 1997). Conversely, in post-yield tension the cell walls align and then rupture abruptly and catastrophically. The anisotropy of cancellous bone is due to its porosity and alignment of trabeculae; bone will migrate to the axis of force until the stresses on the compression side equal those on the tensile side, in doing so it will resorb under the tensile forces and align along the axis of compression.

1.2.3.1. Theoretical mechanics of long bone

At the whole tissue level, Huiskes (1983) suggests that beam theory can sufficiently model long bone diaphyses. Beam theory assumes that:

- The cross section is symmetrical about the loading axis
- Cross sectional shape is maintained along the length of the beam

- There is no shear deformation

Equations 1.1 – 1.3 demonstrate how rigidity and strength of bone is determined by the cross sectional area and the arrangement of bone around the neutral axis (shape). Furthermore, that the area or polar moment of inertia (Eqns. 1.4 + 1.5) describes a stronger and more rigid material under bending and torsion respectively as its mass moves further from its neutral axis. It follows that the most efficient cross sectional shape for long bones is a hollow one. Whilst beam theory simplifies a bone stress analysis, it does provides a valuable tool for comparing strength and rigidity *in vivo* in many cases (Lieberman et al., 2004, Ruff et al., 2006). Bones rarely experience these forces in isolation; bending and torsion are usually experienced in combination in a daily cycle.

$\sigma_{ax} = \frac{F}{\pi(R^2 - r^2)}$	σ_{ax} = Axial stress. F = Force. R = Outer radius of bone. r = Inner radius of bone	*Eqn. 1.1*
$\sigma_b = \frac{My}{I}$	σ_b = Bending stress. M = Bending moment. y = Distance from neutral axis. I = Moment of inertia around neutral axis	*Eqn. 1.2*
$\tau = \frac{TR}{J}$	τ = Shear stress. T = Torque. R = Outer radius of bone. J = Polar moment of inertia	*Eqn. 1.3*
For a hollow cylinder: $I = \frac{\pi}{4}(R^4 - r^4)$ $J = \frac{\pi}{2}(R^4 - r^4)$	R = Outer radius of bone. r = Inner radius of bone	*Eqn. 1.4* *Eqn. 1.5*

1.2.3.2. Theoretical mechanics of SAAP implanted bones

Once a femur is amputated and an implant is inserted into the bone the mechanics change. Since bone dynamics seek to keep strain within a homeostatic range, then it is reasonable to assume the following:

- Resecting the femoral bone will alter the internal strain distribution of the remaining femur as a result of the change in length and bone curvature and may activate mechanosensory modelling/remodelling.
- TF amputees display altered biomechanics, which will affect the bone internal forces, thus bone strain, and may activate mechanosensory modelling/remodelling.
- Implanting a TF SAAP will reroute internal forces with the predominate portion going through the stiffer material (SAAP) and unloading the bone. This may activate mechanosensory modelling/remodelling.

Using beam theory to investigate how sectional changes affects the flow of forces, a few approximations are made (see A.1.1):

- Only the central part of the bone (diaphysis) is considered.
- Bone, (cement) and SAAP stem lengths are equal.
- There is a rigid bond between materials.
- The implant entirely fills the IM canal.

The outcome of a theoretical analysis is that a thinner bone cortex generates a lower $\frac{\text{bone}}{\text{implant}}$ stress *ratio* (i.e. more stress in the implant, less in the bone) under bending and torsional forces while remaining constant under an axial force in cemented and uncemented patients.

In a similar analysis, Engh and Bobyn (1988) illustrated a critical ratio between the stem and femoral bone diameter in pressfit hip stems in relation to stress shielding exists. They showed that as the ratio of bone/implant diameter decreased (towards a thinner bone cortex), that bone stress shielding increased in a theoretical model. This conclusion (assuming bone stress shielding to be the primary cause of bone resorption) was also observed in their clinical results; bone density in radiographs decreased as the ratio bone/implant diameter decreased.

Most mammalian long bones are curved along their length (Bertram and Biewener, 1988), when considered as a slender cylinder, this introduces a bending moment in axial loading. Since evolution strives to provide maximum strength with minimal material this curve is a paradox since a greater axial load could be supported in a straight bone. It was thought that bone curves countered the bending produced by eccentric loading (e.g. due to the offset of the femoral head) however, it was shown that in fact this augments rather than counters the magnitude of the bending moment (Biewener and Taylor, 1986). It is more likely that the theory developed by Bertram and Biewener (1988) holds some truth; they showed that due to the complex loading in terrestrial locomotion a straight bone when bending under load will do so in an unpredictable orientation. Placing the same bone with a bend in it under the same load introduces a more predictable bending orientation. Knowing the likely direction of bend would mean that the likely stress distribution would be known. This means the cross sectional geometry of the bone could be designed to resist the stresses without wasting too much material whilst providing the necessary strength. The result is that the loss of the peak strength that could have resulted from a straight bone is compensated for by the predictability of bending.

Beam theory can be corrected to accommodate for bone curvature and asymmetry (Brassey et al., 2013). And in an intact human femur, it may be reasonable to negate the torsional stress contribution to total bone stress (Turner and Burr, 1993) since aspect ratios (length/diameter) are approximately 16 (Eftekhar et al., 2015). However, in a stouter and/or shorter than average bone (such as the bone remaining after amputation), negating the torsional stress component will underestimate the total stress. The other deviations from beam theory governance are more challenging to account for in an analytical analysis, such as the non-linear behaviour of materials and contact interactions.

A beam analysis is unlikely to reliably describe the mechanics of the force flow through a SAAP in a bone because beam theory governing principles are not always met:

- The contact between cement and implant is not a rigid connection, there is some slip (friction).
- Bone sections (even if only looking at the diaphysis) are not faithfully symmetrical about the loading axis and the centreline of the femur is curvilinear.
- Sectional shape of bone and tapered implant stems change along the length of the beam.
- Bone material is inhomogeneous.
- The load cases as a result of daily living do have a rotational component around the longitudinal axes, plus those generated by muscles attempting to oppose bending forces, thus there is some shear deformation.

This thesis will compare an analytical results of an implant/bone model with a numerical analysis to investigate how deviations from beam theory governance affect the stress distribution under load cases experienced by SAAP patients.

1.3. Finite element analysis (FEA)

The question of how to calculate *in vivo* stress and strain (or SED) of a bone arises when investigating cortical bone remodelling and associated implant stability. One method of experimentally obtaining bone strain is with strain gauges, however this is not possible *in vivo* due to gauge placement impracticalities such as the moisture of the environment and there being no way to access the implant/bone interface. FEA is a method of simulating the *in vivo* environment; models of the bone/implant assembly can offer insight into bone reactions to applied conditions.

1.3.1. The Finite Element Method (FEM)

The FEM calculates a field quantity (in a stress analysis this is the displacement field) from which quantities of interest can be calculated such as stress and strain components and rates, contact pressures and failure criteria (Cook, 1995, Bower, 2009). The method discretises a continuous, complex model into a finite number of blocks (elements) and the field quantity is interpolated from individual

values at the nodes (points at which elements meet). Piece wise interpolation of the element field values results in a set of simultaneous algebraic equations which provides the solution for the whole structure. In stress analyses these are the equations of motion (or equilibrium) for the nodes; the cumulative force on each node should be zero apart from the externally loaded ones. Along with boundary conditions it is then possible to calculate the displacements, stresses and strains. The matrix symbolism for this set of simultaneous algebraic equations (for a force/displacement analysis) takes the form:

$\{F\}=[k]\{d\}$	F = Force vector of known loads k = Stiffness matrix (nodal stiffness terms are the summation of the stiffness terms from the elements joined at that node) d = Unknown vector of nodal displacements	*Eqn. 4.1*

In 1943 a prominent mathematician, Courant (1943), presented a solution using a piece wise polynomial approach to a torsion problem. This publication was overlooked by engineers and physicists and it took ten more years for mainstream adoption of the FEM. The FEM was introduced to practising engineers by the aerospace industry in the 1950's; Turner et al. (1956) showed that in a box beam model, the FEM was able to more accurately model deflection than beam theory.

Brekelmans et al. (1972) was amongst the first to publish the FEM in orthopaedic biomechanics using a 2D femoral model to illustrate "suitability par excellence for analysis of complex constructions such as the femur". Others included Belytschko et al. (1974) who modelled loading of an intervertebral disc and Farah et al. (1973) who presented a full field (photo elastic technique) validation of a 2D FE axisymmetric model of a tooth. Commonly, today research centres have access to vast computational power and the FEM is used in applications beyond structural and mechanical engineering design. We have the technology to build patient specific 3D models of inhomogeneous, skeletal material under complex loading conditions and model biological phenomena and processes such as cell wall/particle interactions and drug delivery behaviours. With advancements in imaging techniques and model reconstruction, simulation-based medicine is becoming a standard in biomedical engineering (Erdemir et al., 2012). However, to deploy these technologies commercially, implant testing regulations (ASTM F2996) need to evolve to use FEA in manufacturing rather than just to inform the amount of physical testing to be conducted (ASTM, 2020).

Above all it must be remembered that the FEM is an approximate solution; even a well-constructed finite element model approximates the field equations, which are in turn based on an idealised clinical state using finite arithmetic precision. In a biological system there are multiscale interactions (cellular, tissue, organ and whole body) it is a challenge for the FEM to calculate interactions at multiple scales,

and so it is important to acknowledge what question the method answers. In the SAAP/femur model presented in this thesis, multi scale interactions have been simplified so that muscular interactions are accounted for in the application of real life load cases (Chapter Five). Remaining multiscale interactions (or lack thereof) are consistent throughout all models to be compared. The FEM has been selected to assess the effects of SAAP design changes on the periprosthetic bone. It is an ideal tool, since a comparative analysis over many iterations with multiple parameters and complex loading conditions are performed.

1.3.2. FEA in SAAP bone remodelling simulations

1.3.2.1. SED as the bone remodelling performance indicator

To quantify implant fixation when comparing implant designs a performance indicator that can measure periprosthetic bone remodelling is required. Based on the theory of strain adaptive remodelling if $U < (1 - s)\ U_h$ or $U > (1 + s)\ U_h$ at time = 0 then it follows that as time unfolds, remodelling will ensue (due to C_r or C_a, Chart 1.1, Equation 1.1). In making this assumption the requirement for a dynamic analysis is removed and the simulation becomes quasi-static in nature (under the changing load cases at different gait stages). Local SED values can provide an indication to the bone's likely initial and ongoing remodelling response to implantation where U_h is assumed at 0.004 MPa and 0.0036 MPa ≤ 'lazy zone' ≤ 0.0044 MPa (Mellal et al., 2004). It is not possible to validate a bone remodelling algorithm experimentally due to the inability to replicate a bone tissue *in vivo* environment (Hambli, 2014) (although predicted bone density distributions obtained from bone remodelling algorithms can be compared with histological bone sections from the literature to establish concordance).

1.3.2.2. Inertial forces

The forces experienced by the femur are the combination of muscular forces, inertial forces, gravitational forces and ground reaction forces. At any instant in time a segment (a member in a physical system) will be in equilibrium with applied forces at each end and inertial forces at the centre of gravity. To accurately represent the mechanics of the femur the effect of all forces must be accounted for. There are limited studies in the literature on biomechanical models that include inertial properties for lower limb amputees (Sagawa Jr et al., 2011); Hale (1990) showed that hip muscular effort and knee resultant joint moments are significantly increased when varying prosthetic shank mass in above knee amputees. Similarly, Selles et al. (2004) demonstrate that the stump socket interface forces in transtibial amputees increased after increasing the weight of distal components (e.g. foot, ankle, shoe). Conversely Diffo Kaze et al. (2017) conclude that the inertial forces observed in their simulations were so small compared with hip joint reaction forces that they were considered negligible. Chapter Four will capture

the inertial properties of the femur and in Chapter Five they will be applied to the SAAP/femur FE model to fully represent femoral force flow at each stage of gait.

1.3.2.3. SAAP design parameters of interest

When selecting SAAP design parameters for the FEA, results from the ITAP clinical trial were considered along with the mechanics of the assembly. Stem taper, radius and length all had influence on the fixation outcome in the ITAP clinical trial (Chapter Two) and so were included in the numerical analysis. Furthermore, the addition of a cortical plate in all SAAP model designs was investigated; equivalent canine ITAP patients (PerFiTS) often incorporate at least one cortical plate (Fitzpatrick, 2008, Golachowski et al., 2019) and the question of whether this is a superior design was addressed.

In summary, the parameters investigated with the FEM in Chapter Five are:

- Stem length
- Stem radius
- Stem taper
- Fixation method (cemented or pressfit)
- Cortical plate (addition of and length)

1.4. TF amputation

The most common reason for patients to undergo lower limb amputation in developed countries is atherosclerosis; of these, 82 % will have diabetes mellitus (in the United States) (Molina and Faulk, 2019). In developing countries the leading cause is trauma relating to industrial, traffic and wartime injury (Dillingham et al., 1998, Marks and Michael, 2001). In amputation there are two priorities; first, residual limb length preservation and second, to balance the agonist and antagonistic muscles. Limb length is largely dictated by the location of the damage/disease, sometimes distraction osteogenesis is used to achieve optimal residual limb length (Kuiken et al., 2017). Muscle balance is important; without performing this adequately the residual limb will flex and abduct, and the patient will not be able to load the limb (Kobayashi et al., 2013, Gottschalk, 2016a). Abduction occurs because the adductor magnus, which provides 70 % of the adductor moment when transected, leaves the hip abductors relatively unopposed. Flexion occurs similarly when the residual extensors are overpowered by the residual flexors which are attached to the trochanter of the proximal femur and so above the level of amputation.

Myodesis surgically sutures muscle to bone through drilled holes or to the periosteum whereas myoplasty sutures muscle to muscle. The challenge is in muscle fibres not holding sutures well, (Study,

2008) (conversely tendons and skin do) and so myodesis may not always be successful. Myodesis and myoplasty perform an additional important function, that of padding the end of the femur bone so that the patient can more comfortably load it (Fig. 1.3). The tension with which the resected muscle are reattached have a direct effect on the amount of force the muscle can generate thereafter (Ranz et al., 2017).

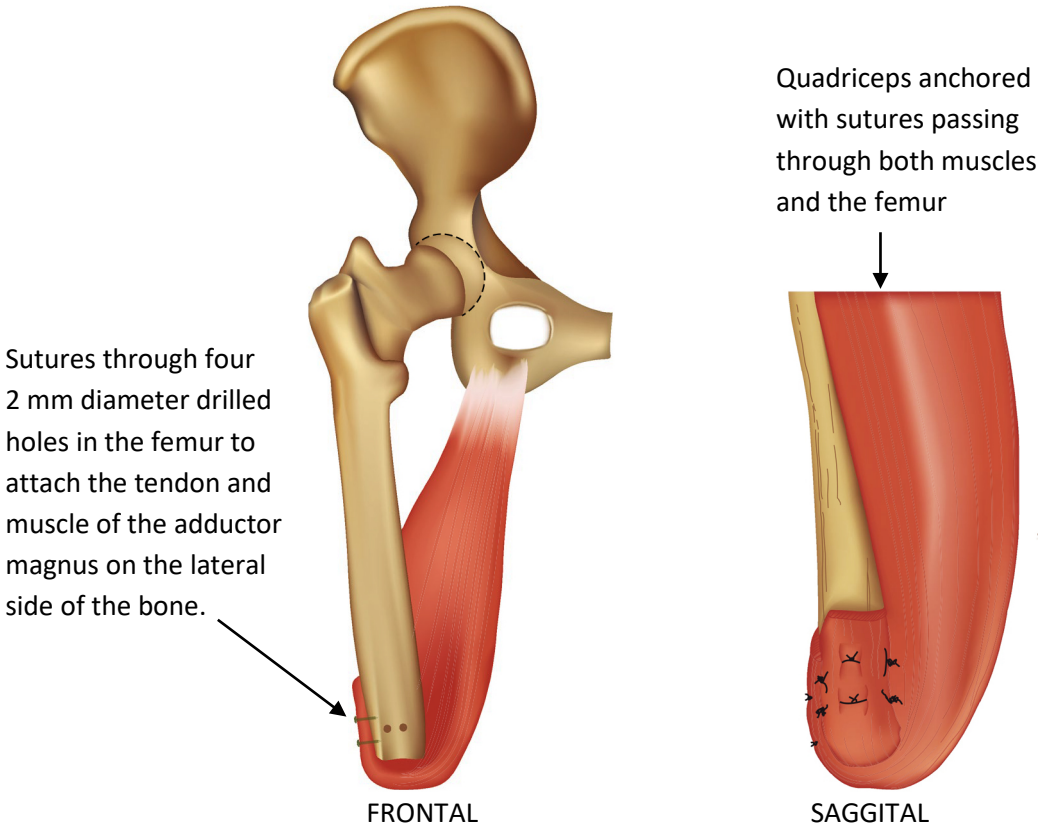

Fig. 1.3: Myoplasty and myodesis in TF amputation surgery
Left = myodesis of the adductor magnus to the femur. Right = myoplasty and myodesis of the quadriceps over the adductor magnus. Images adapted from Gottschalk (2016b).

1.5. SAAP surgery

There have been only two SAAP human clinical trials; the ITAP and the OPRA (the CPS device is currently in an FDA trial). Surgical technique is broadly divided into two types; a one stage or a two stage operation. A single stage SAAP surgery, such as that used with the ITAP implant, implants in one operation with an exoprosthetic part (the spigot) that can be incrementally loaded in a rehabilitation program immediately after the surgery. Conversely the two stage operation, favoured by the OPRA device, implants the endoprosthetic part for six months in a first operation (S1), Fig. 1.4 and then in a second operation (S2) attaches the exoprosthetic part (the abutment) through a small soft tissue incision, to begin incremental loading in a rehabilitation program.

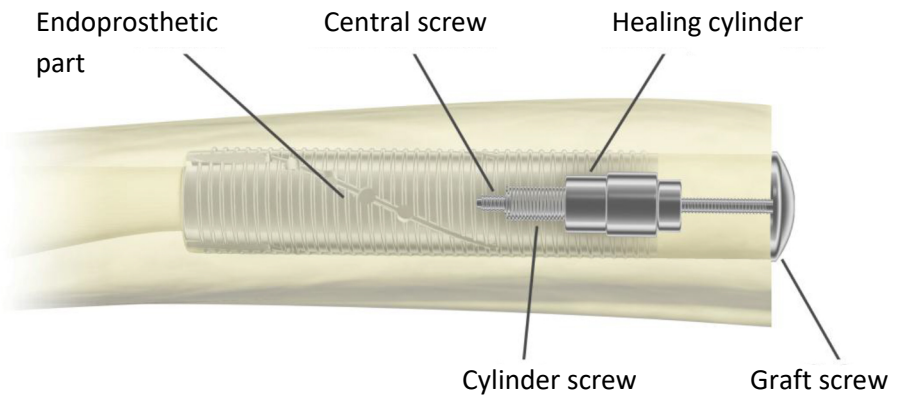

Fig. 1.4: Schematic OPRA implant after S1 surgery
In S2 the screws and healing cylinder are replaced with a transcutaneous abutment.
Image from Integrum A.B

1.5.1. Osseointegration in pressfit fixations

Biological fusion of bone and titanium (osseointegration) is the principle of implant stability in all pressfit SAAP surgeries. SAAP fixation is referred to as primary (relying on a snug mechanical fit) or secondary (referring to osseointegration). Immediately (minutes) after surgery a blood clot is formed as fibroblasts (cells synthesising the extracellular matrix and collagen) divide and fibrin monomers spontaneously cross link and adhere to the implant surface (Kuzyk and Schemitsch, 2011). Fibroblasts are the most common cells of connective tissue in animals. After an inflammatory phase (hours after surgery) the body enters a proliferative phase (three to four days post-surgery) where fibroblasts synthesis collagen, elastin and proteoglycans in the extracellular matrix that are subsequently employed for protection and stability. Mesenchymal stem cells (perivascular cells) form new blood vessels and osteoclasts resorb the edges of bone that were damaged in surgery, thought to provide space for bone healing (Mavrogenis et al., 2009). This reduces the primary stability of the implant and care must be taken during this phase (approximately one week after surgery). Perivascular cells also migrate to the bone and implant surface where they differentiate to osteoblasts which form an organic matrix that becomes mineralised by calcium phosphate. Eight days post-surgically interlocking woven bone is formed at the implant surface which provides increasing secondary stability. After a few weeks the remodelling phase of osseointegration begins; load adaptation dictates the architecture and organisation of the bone and communication between the bone cells resorbs the woven bone and lays down highly organised lamellar bone (see 1.2.1.1.) (Zaid et al., 2019a).

1.5.2. Infection in SAAP surgeries

The most usual complication with the surgery is superficial infection around the transcutaneous interface of the implant. If dermal fibroblasts can migrate to the implant/bone surface before the bacteria, then it is likely a cellular layer will form inhibiting the attachment of bacteria. Conversely if bacteria attach to the surface, infection and biofilm formation is likely and could lead to implant removal if it cannot be managed (Chimutengwende-Gordon et al., 2014). Usually cases are managed with oral or parenteral antibiotics (Branemark et al., 2014, Al Muderis et al., 2016, Tillander et al., 2017). Research with titanium oxide nanotubes and seeded with dermal fibroblasts (Shevtsov et al., 2015, Giusto et al., 2019) show promising results in stabilising contact between metal pylons and soft tissues. Surface modifications such as silane and keratin derivatives have been shown to support skin cell adhesion (Trent and Van Dyke, 2019) and cobalt-chrome-molybdenum (CoCrMo) implants with a zirconium nitride top coat have demonstrated a relative reduction in staphylococcus epidermidis (Pilz et al., 2019).

1.5.3. OPRA surgical technique

After reaming and cleaning the IM canal in bone preparation, the S1 OPRA surgery ensures the device is in close contact with the femoral inner cortex by using a thread cutting self-tapping device. More recently fixtures have been countersunk 20 mm proximal to the osteotomy face, rather than flush, to address the problem of distal bone resorption (Thesleff et al., 2018a). Residual muscles are shaped and a myodesis sutures them to the periosteum 5 – 10 mm proximal to the bone end. Often a bone graft is harvested from the iliac crest and transplanted to the bone end maintained by compression in healing. The skin is closed with sutures and drained for 24 hours and antibiotic prophylaxis is administered. Between S1 and S2 patients may use their socket prosthesis. S2 surgery is performed through the terminal scar; S2 surgery removes subcutaneous fat under the skin at the point where the abutment would pass through using the edge of a glass microscope slide. A circular entry point is cut with a cylindrical skin biopsy cutter. Finally, the abutment screw is inserted into the endoprosthetic part of the device and compression with the screw is applied, skin is sutured and drained for 24 hours. (Li and Brånemark, 2017, Matthews et al., 2018)

1.5.4. ITAP surgical technique

The ITAP surgery implants a pressfit or a cemented device; after reaming and lavaging, bone preparation techniques differ depending on fixation method. For the pressfit implant a tooth cutting tool is used to slice longitudinal grooves into the inner cortex wall which marry with the position of the longitudinal cutting teeth on the implant stem (the cutting teeth provide resistance to rotation displacement, Fig. 1.5 left). If cement is used, pressurised gentamicin impregnated cement is delivered to the IM in a

retrograde manner. Impaction is used for the pressfit devices until the collar is flush with the distal end of the bone (osteotomy face), a stem interference fit of 150 – 200 µm is generated. Prior to final seating of the collar in the cemented fixations, cement is cleaned from the osteotomy face. A vacuum drain is inserted in the void behind the flange, the skin is denuded in an area corresponding to the size of the flange (Fig. 1.5 middle), muscles sutured to the flange (Fig. 1.5 right), hole punched through the skin for the spigot to pass though and the skin flaps are close. The vacuum drain is engaged for ~ 48 hours to establish a tight flange/tissue interface (this is also performed in OPRA surgery).

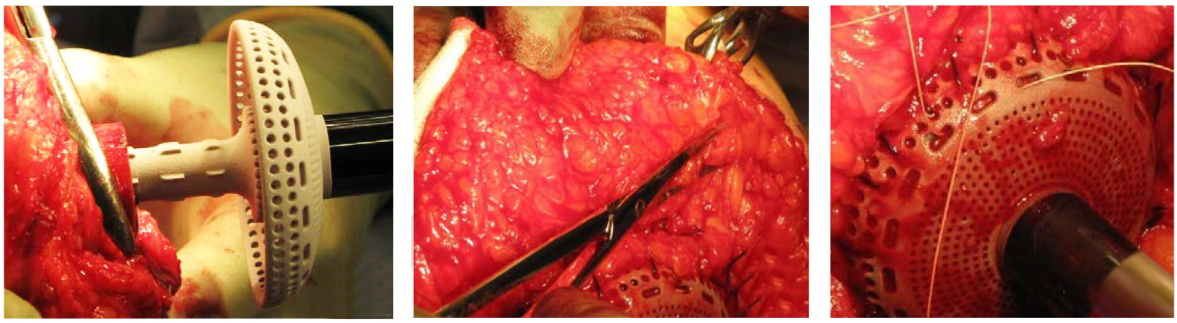

Fig. 1.5: Photos of ITAP surgery stages
Left: A pressfit ITAP showing cutting teeth.
Middle: Denuding the skin flap. Right: Suturing the muscle to the flange.

1.5.5. Comparison of one stage and two stage surgical techniques

The ITAP procedure using a single stage operation has the advantages of one less surgical procedure, the option to fit a cemented device in patients with poor bone stock without the need for grafting and the speed post operatively after which the patient can fully weight bear (three months). If the process of osseointegration is disturbed, a thin fibrous sheath may develop at the interface (Lang et al., 1997). It prevents the bone integrating onto the implant surface resulting in a weaker connection. Over time this may mean implant loosening and revision or removal surgery; the fibrous sheath can be seen on patient radiographs as a very fine white line at the interface (radiolucent line/gap). This thesis, and others such as Engh et al. (1990) uses this as an indication of unsuccessful implant fixation for reasons discussed in Chapter Two.

Full weight bearing on devices employing the two stage surgical approach takes ~ 15 months (nine months after the S2) (Matthews et al., 2018), however there is little risk of disturbing osseointegration. Another significant difference in surgical choices is that of dermal attachment, both methods suffer from a similar rate of infection (SIW, 2017). OPRA surgery sutures the skin to the distal end of the bone through which the abutment passes (Integrum A.B.). ITAP surgery aims to generate a tight infection-resistant seal between the skin and the spigot.

1.6. SAAP material, manufacture + structure

1.6.1. SAAP biocompatibility

Biocompatibility is "the ability of a biomaterial to perform its desired function with respect to a medical therapy, without eliciting any undesirable local or systemic effects in the recipient or beneficiary of that therapy, but generating the most appropriate beneficial cellular or tissue response in that specific situation, and optimising the clinically relevant performance of that therapy" (Williams, 2008). SAAP implants must be anti-corroding and strong enough to resist large, cyclical, and often complex load cases. Achieving anti-corrosive protection in metal implants means that they have to be near the noble metals on the galvanic scale (corrodibility) and/or use a protective mechanism such as passivation (Kruger, 1988). The formation of a metal oxide passive film on the surface of a metal prevents the exchange of metal ions and electrons (oxidative corrosion) across the metal/aqueous interface. Most orthopaedic alloys rely on passivation.

1.6.2. Medical grade titanium material structure

Metals used in orthopaedic implants include titanium (Ti) and its alloys, cobalt-chromium (CoCr), stainless steels and zirconium alloys. Ti and its alloys uniquely integrate with bone (by a process of osseointegration, described in section 1.5.1) making it a good choice for SAAPs. Furthermore, the Ti alloys are approximately half the material stiffness (115 GPa compared with 250 GPa) of the other alloys which means that although it still shields stress from the bone, it does so to a lesser degree. Numerical studies have shown that controlling SAAP stem stiffness can minimise the rerouting of stress (Ahmed et al., 2020). The standard medical grade Ti alloy has 6 % aluminium and 4 % vanadium added producing 'grade V' Ti or Ti6Al4V which has excellent fatigue and yield strength (as well as corrosion resistance). Long term implantation research shows that vanadium and aluminium ion exchanges occurring with the tissue fluids can cause sterile abscess and an increase in the potential for the development of Alzheimer's disease respectively (Ikeda et al., 2002, Abdel-Hady Gepreel and Niinomi, 2013) so alternative Ti alloys have been developed.

Pure Ti atoms align in a hexagonal close-packed crystalline structure (α phase) or a body centred cubic structure (β phase). Transition from α to β phase occurs above 883 °C but alloying elements will stabilise a phase: aluminium (Al) is an example of an α stabilising element, vanadium (V) and niobium (Nb) are β stabilising elements. *β*-type Ti alloys with zirconium (Zr), niobium (Nb) and tantalum (Ta) have a lower modulus compared with the grade V alloy e.g. Ti 35Nb 5Ta 7Zr, Ti 29Nb 13Ta 4.6Zr and Ti 13Nb 13Zr which range between 55 - 79 GPa (Davidson et al., 1994, Kuroda et al., 1998). These materials have the potential to dramatically reduce the stress shielding effect on bone. Uptake of Ti and its alloys in joint arthroplasty is blighted by their poor tribological properties (Jiang et al., 2000) which is an essential

consideration in these implants. However, the advantages in modulus and its osseointegrating properties drive research to develop Ti alloys with improved wear resistance, for example by reinforcing β-Ti alloys with hard TiB (boron) particles (Geng et al., 2003, Feng et al., 2004). A SAAP is not restricted in the same way if made from one piece (or multiple pieces that do not articulate with one another) and so the commercially available *β*-type Ti alloys should be the material of choice.

It may be feasible in the future to manufacture porous SAAP stems akin to cancellous bone (Li et al., 2012) with additive manufacturing (AM) technology. Porous stems could reduce the material stiffness further still and close the material difference gap between implant and host bone. Most SAAP patients present with osteopenia (Benichou and Wirotius, 1982, Kulkarni et al., 1998), this can decrease bone density and bone stiffness (by 30 % and 1.2 %, respectively) compared with non-amputated individuals (Burstein et al., 1976, Rush et al., 1994, Sherk et al., 2008). Although, if a revision or removal were required, full invagination of the host bone could make this challenging.

1.7. TF SAAP current market designs and outcomes

Development of SAAP has revolutionised the lives of many TF amputees (Hagberg et al., 2008), however the procedure is not perfect with superficial infection at the stoma site being the most commonly reported issue (Hagberg et al., 2008, Aschoff et al., 2010, Branemark et al., 2014, Juhnke et al., 2015, Tillander et al., 2017). There have also been cases of deep infections sometimes associated with implant removal (Branemark et al., 2014, Juhnke et al., 2015). As implant design and surgical techniques develop, these rates are being reduced (Al Muderis et al., 2016) but it remains an unsolved concern for the procedure. Consequently, SAAP procedures are usually not performed on TF amputees unless they are experiencing difficulties using their socket prosthesis. Sections 1.7.1 – 1.7.5 describe the global market (with and without clinical trials) in TF amputee SAAP designs and published outcomes.

1.7.1. The OPRA device

1.7.1.1. Design

The endoprosthetic part (the fixture, Fig. 1.6) is a Ti6Al4V tube with a laser-induced nanoporous surface (BioHelix™) (Thesleff et al., 2018b). The outer diameter is 9 – 20 mm and the length is 110 – 150 mm; selected based on pre-operative CT scans (Matthews et al., 2018). This is the only screw type (uncemented) SAAP; the entire fixture is a thread cutting type of self-tapping screw with flutes machined across the threads to create the cutting edges. The inner surface of the fixture is also threaded. The abutment (the transcutaneous part) sits inside the fixature and is secured with an abutment retaining bolt (of titanium alloy) that passes through it and screws onto the inner fixture thread. The abutment retaining bolt is tightened to 12 Nm. It is worth noting that the OPRA system was

developed such that the abutment and the abutment bolt would fail before the fixture under excessive loading, thereby preventing a more complicated revision surgery.

1.7.1.2. Outcome

Nebergall et al. (2012) used Roentgen Stereophotogrammetric Analysis (RSA) of the OPRA (n = 47) and noted no substantial motion was observed up to seven years after S2. They also showed bone initially resorbs in at least one zone in over half of the patients but then stabilises, moreover, the periprosthetic bone that resorbs does not cause loosening or failure. Superficial infection in this study was observed in one patient every two years. In a similarly sized study (n = 51), Branemark et al. (2014) followed patients for two years between 1999 and 2007. Superficial infections were reported in 55 % of patients and treated effectively with oral antibiotics. 8 % had a deep infection which in one patient led to removal. 4 % of remaining patients had implant removals due to pain on loading.
8 % reported fracture or bending of the abutment and/or the abutment screw. Despite which scores from the Questionnaire for Persons with a Transfemoral Amputation, Q-TFA (Table 2.13) improved significantly when compared with before S1. Additionally, the Short Form Survey (SF – 36) physical function scores (Table 2.12) showed that general quality of life improved. By 2010, 96 patients had received a femoral OPRA implant and a retrospective analysis on the risks osteomyelitis was published (Tillander et al., 2017). Implant-associated osteomyelitis was diagnosed in 20 % of patients and 9 % of implants had been removed owing to osteomyelitis during a ten year implant period. Matthews et al. (2018) analysed the UK cohort of patients who have received an OPRA (n = 18) and reported that 94 % of patients have had infection related problems, five of whom had implants removed as a result. Two of the remaining 13 patients have peri-implant infections with osteomyelitis which is suppressed with oral antibiotics. Prior to any removals 61 % of patients cited reoccurring abutment site penetration infections (treatment is with oral antibiotics). 12 patients had fractured or

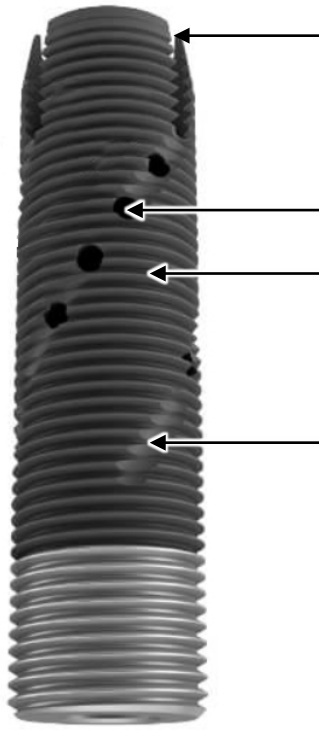

Fig. 1.6: Endoprosthetic part (fixture) of the OPRA device

bent the abutment or abutment retaining bolt (surgery was required). SF - 36 scores were compared before S1 and up to five years post-operatively; physical scores, physical functioning and physical component scores improved significantly. Q - TFA scores were also compared with significant improvements in all the main scores. In 2019, the American OPRA clinical trial with nine patients published its one year results: superficial infection was 44 %, and deep infection rate with explantation was 11 % (Zaid et al., 2019c).

1.7.2. Integral Leg Prosthesis (ILP) / Osseointegrated Prosthetic Limb (OPL)

1.7.2.1. Design and surgery

Another uncemented device, the ILP (ESKA Orthopaedic) is a pressfit, slightly curved, microporous surface ('spongiosa metal', 1.5 mm thick), CoCrMo implant 140 – 180 mm long (Fig. 1.7, left) developed by the German group led by Horst Aschoff (formally known as the Endo-Exo Femur Prosthesis) (Aschoff et al., 2010). Surgery is a two stage procedure; the femur is resected 200 mm proximal to the contralateral knee joint and reamed for ILP insertion (Haket et al., 2016). The second stage is performed after six to eight weeks and inserts a dual cone adapter which joins the endoprosthetic part to the exoprosthesis. Until 2012 the subcutaneous fat around the stoma was not removed, thereafter it has been removed in surgeries.

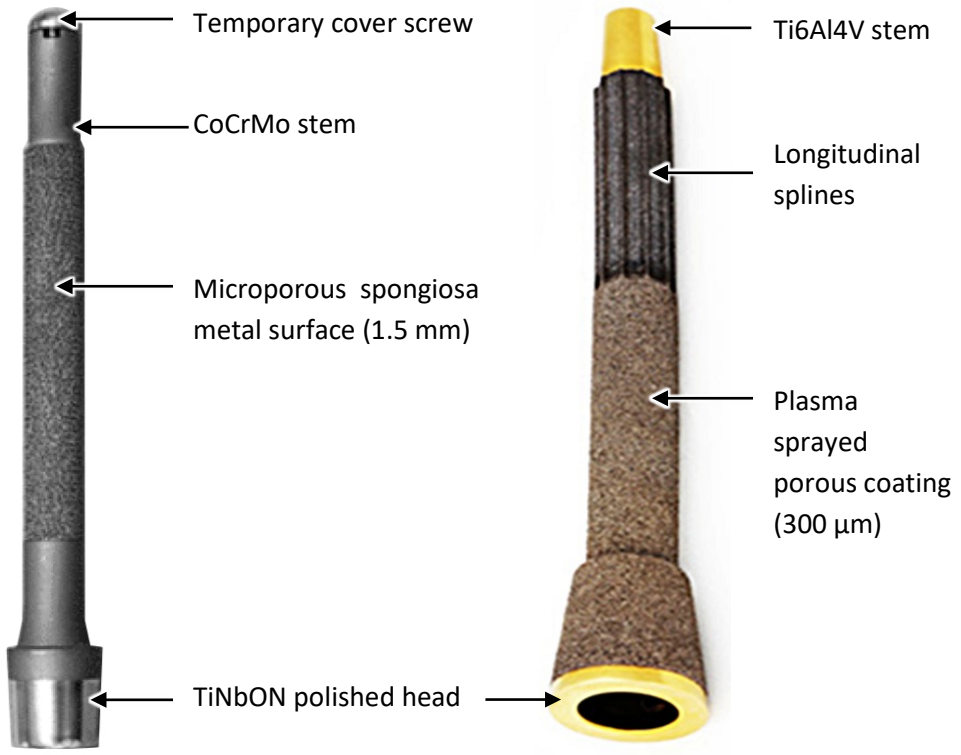

Fig. 1.7: ILP and type B OPL implants
Left = The ILP endoprosthetic part (implant curvature into the page (adapted from Juhnke et al. (2015)). Right = Type B OPL endoprosthetic part (from Al Muderis et al. (2017b))

It has been intimated (Frolke et al., 2017) that the ILP spongiosa metal surface indirectly (by virtue of reducing the stem diameter by 3 mm) contributed to the mechanical failure of the ILP in the three countries it has been used in (Germany and Netherlands from 2009 and Australia from 2010). As result the ILP design was altered once more to produce the Osseointegrated Prosthetic Limb (OPL) (Permedica s.p.a, Milan, Italy), Fig. 1.7, right and introduced in Australia in 2013 and the Netherlands in 2015. The OPL is a Ti6Al4V implant with a thin plasma-sprayed (300 µm) Ti coating, 1 mm high longitudinal splines proximally and a standard length of 140 or 160 mm but custom lengths can be fabricated. For patients with a residuum < 160 mm a locking screw is used. The OPL has a distally situated enlarged titanium niobium oxynitride (TiNbON) polished end that sits either intra (type A) or extramedullary (type B) (Frolke et al., 2017). The OPL surgical procedure in Australia is offered as a single stage surgery (Osseointegration Group of Australia Accelerated Protocol-2 (OGAAP-2)) with full weight bearing expected three to six weeks after surgery (ongoing daily weight bearing training up to three months thereafter is recommended).

1.7.2.2. Outcome

Of the 37 TF amputees implanted with the ILP device between 1999 and 2009, 11 % of the implants were removed (half of which were replaced). 54 % underwent one or more revision surgery. 70 % of the revisions were attributed to soft tissue irritation at the stoma due to a porous surface on the connector which has been replaced with a smoothly polished (nonporous) surface in recent designs. A bone stabilising bracket attachment has also been removed in the final version of the ILP and between 2009 and 2013 Juhnke et al. (2015) reports all patients remained infection free (without antibiotics and following a wound-hygiene protocol) and none were removed. In a larger separate study across two centres (Netherlands and Australia) results with the newer ILP implant from 86 patients were reported by Al Muderis et al. (2016): 29 % suffered a low grade soft tissue infection and most were managed with oral antibiotics, 1 % required parenteral antibiotics and 1 % required surgical intervention and 5 % suffered high grade soft tissue infections that all required surgical intervention. OPL outcomes of 22 patients between 2013 and 2014 have been published (Al Muderis et al., 2017a) indicating low grade infections in 55 % of patients. Patients Q-TFA global scores and SF - 36 physical component summary scores were significantly higher than pre-operatively. There were no cases of revision surgery, bone fracture or implant failure during the short follow-up period.

1.7.3. Compress Compliant Pre-Stress device (CPS) Device

1.7.3.1. Design and surgery

The CPS implant was initially developed as an endoprosthesis for oncologic limb salvage reconstruction (Thesleff et al., 2018a) receiving US Food and Drug Administration (FDA) approval in 2003. Latterly, a

transcutaneous version was developed and implanted in ten TF amputees in an FDA trial. Five were performed in a one stage and the other five in a two stage procedure similar to the aforementioned surgical procedures but with a gap of 12 – 18 weeks between surgeries (McGough et al., 2017). CPS surgical IM canal preparation is similar to the other SAAPs. This is an uncemented fixation where primary/mechanical fixation is achieved via two sets of pins. Proximal transverse pins pass through cortical holes drilled during surgery orthogonal to the IM longitudinal axis. Once seated on the spindle collar, a second set of pins are screwed into the cortex of the osteotomy face to minimise rotation. Axial compression of the cortical bone is induced via a traction bar which passes longitudinally through the spindle to the anchor plug. The traction bar end distal to the spindle passes through a series of bevel washers and has a tightening nut at the end. Using a torque wrench the nut can be tightened to achieve the desired compression of the spindle against the bone (either 1780 N, 2669 N or 3559 N (Calvert et al., 2014, Goldman et al., 2016)). Two of the patients were implanted with the 'short' compress spindle which can place the bone anchor in bone < 45 mm long. Anchorage in very short and/or divergent residuum's is a unique advantage to this system, the standard CPS requires only 80 mm of medullary placement (Biomet, 2018).

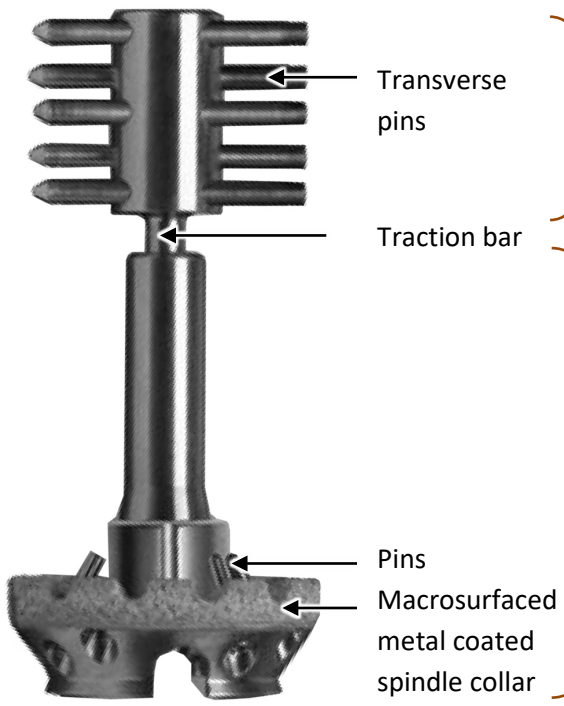

Fig. 1.8: The endoprosthetic parts of the Compress® device (Biomet Orthopaedics)

1.7.3.2. Outcome

Results from McGough et al. (2017) report no infections, 18 % periprosthetic fractures, no medical complications and no component loosening. At the time of publication one patient was awaiting fracture revision surgery and the other had been performed; it was noted the bone stock at the revision had increased in quantity and quality as a result of the bone hypertrophy.

1.7.4. Keep Walking device

1.7.4.1. Design and surgery

The original Keep walking device is an endoprosthesis only (Fig. 1.9); the spacer at the distal end of the implant spreads the load and resolves the sharp edges of the resected femur so that patients can walk more comfortably with a socket prosthesis whilst loading the femur. The primary advantage of this prosthesis is that patients with amputations of vascular origins can be included, thus benefit from the skeletal loading method of SAAPs. In a second stage operation the Keep Walking Advanced Connector inserts into the distal face of the spacer and joins transcutaneously to the prosthesis in the manner of an exoprosthetic part. The Keep Walking stem is 120 – 180 mm long and 11 – 17 mm in diameter, the spacer is an ultra-high molecular weight polyethylene (UHMWPE) of diameter 54 – 62 mm connected to the stem by a titanium screw and a polyethylene plug (Guirao et al., 2017). The device is uncemented. 29 patients were implanted with the Keep Walking device and one TF amputee patient in 2013 was implanted with the Keep Walking Advanced device.

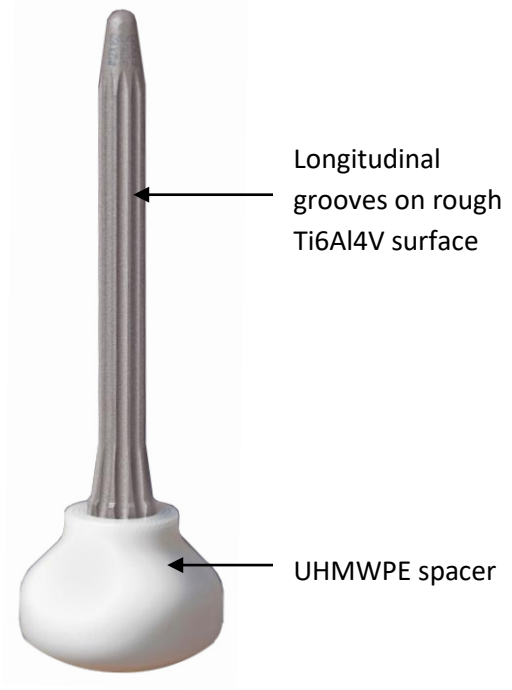

Fig. 1.9: Keep walking advanced endoprosthesis (Tequir S.L., Spain)

1.7.4.2. Outcome

No outcome information has been published at the time of writing

1.7.5. Intraosseous Transcutaneous Amputation Prosthesis (ITAP)

1.7.5.1. Design and surgery

A UK clinical trial implanted 20 TF amputees in 2008 (cohort I, n = 10) or 2013 (cohort II, n = 10). The trial was an interventional (single group assignment) clinical trial with the primary purpose of 'treatment' for transfemoral amputation. All measures were recorded but not published, although a preliminary report was produced internally (SIW, 2017). This thesis presents a summary of the recorded data in Chapter Two, so that a comparison between numerical (FEA), analytical (composite beam theory) and clinical results can be compared in Chapter Five. The primary outcome measures were: adhesion of skin surrounding the ITAP, assessment of skin colour surrounding the ITAP, measuring temperature of the skin surrounding the ITAP, condition of skin surrounding the ITAP, pain at the end of residual limb,

swelling of the skin around the ITAP. The secondary outcome measures were: radiographic assessment to measure osseointegration, radiographic assessment to measure fixation of the ITAP, microbiological assessment of the stump by standard microbiological screen, calculate score for the 'Questionnaire for persons with a Transfemoral Amputation' to measure quality of life, calculate a score for the 'Special Interest Group in Amputee Medicine' to measure mobility.

Patients were *included* from the trial according to the following criteria:

- TF amputee
- Six months or more attempted prosthetic rehabilitation (use of walking aids not relevant)
- Between the ages of 18 to 60 inclusive
- Length of stump: Sufficient bony stock for bony integration (at the investigator's discretion) and sufficient clearance (at the investigator's discretion) from medial joint line to accommodate failsafe device/ adaptor and knee mechanism
- Suitable soft tissues to perform the operative procedure
- Flexion Deformity (FFD) at hip no more than 15°
- Normal range of flexion and adduction other than FFD
- Oxford Grade 4 muscle power in all groups around hip
- Normal contralateral leg function
- Psychologically suitable (as deemed by screening process)
- Sufficient standard of English to understand the Patient Information Sheet and general study requirements
- Ability to understand and comply with study requirements - notably study timelines and additional clinic visits
- Patients willing to take part in the study and sign the Informed Consent form

Patients were *excluded* from the trial according to the following criteria:

- Radiotherapy to target limb at any time
- Chemotherapy within the preceding 12 months
- Cognitive impairment likely to affect participation
- Pre-existing ipsilateral hip pathology
- Limited cardiorespiratory reserve / inability to walk at normal pace
- Any significant co-morbidity that, in the investigator's opinion, is likely to affect outcome (e.g. osteoporosis, heart disease, peripheral vascular disease, obesity or unrelated cancer)
- Any co-morbidity in the contra-lateral leg that precludes walking
- Any significant previous infection within the previous 12 months, such as apical stump sepsis or dental sepsis

- MRSA
- Using another silver-dosed medical device/treatment
- Patients with hypersensitivity to silver
- Concurrent medico-legal proceedings taking place
- Patients currently included in other clinical trials

Patients had suffered amputations as a result of traumatic injury or osteosarcoma. The ITAP surgery is one stage; patients were encouraged to remain in bed lie still for up to one week after surgery and then were rehabilitated in house by a physiotherapist. The ITAP, made of Ti6Al4V, is the only SAAP that allows for a cemented as well as an uncemented fixation. Stems diameters were 9 - 15 mm and a 100 – 145 mm long stem was either straight or slightly curved based on the geometry of the patient IM canal. The ITAP has a porous flange type structure distal to the implant stem and collar. The flange enhanced soft tissue (dermal) attachment, prevent epidermal invagination and reduce infection. A grooved hydroxyapatite (HA) coated collar acts as a buttress on the bone osteotomy face which allows for bone ingrowth and is thought to reduce aseptic loosening (Coathup et al., 2015). The collar was either circular or oval in cross-section, to match the profile of the patient's osteotomy face, diameters were 24 - 35 mm. The transcutaneous part (spigot) was coated with a layer of diamond like carbon (DLC) a hydrophobic, hard and scratch resistant surface to reduce the risk of infection.

Cemented stems were used in patients whose IM diameter was > 15 mm and/or where the implant was fixed above the isthmus of the diaphysis (i.e. divergent canal). A stem diameter that allowed for a 2 mm cement mantle was used. Where the IM diameter was < 15 mm, parallel, not divergent and where the bone quality was good, then a pressfit stem was used. Pressfit stems were nearly all parallel and had anti rotation teeth (1 mm height) on the distal third of their stems and an HA coating (150 – 200 µm thick) on either the full (cohort I) or only their distal half (cohort II). The polished cemented stems were tapered at an angle of 0.75 ° with longitudinal and radial cement grooves 1.5 mm deep to prevent rotation and pull out. Stems were designed to be line to line (exactly equal to) with the inner cortex; the layer of HA produced the interference fit.

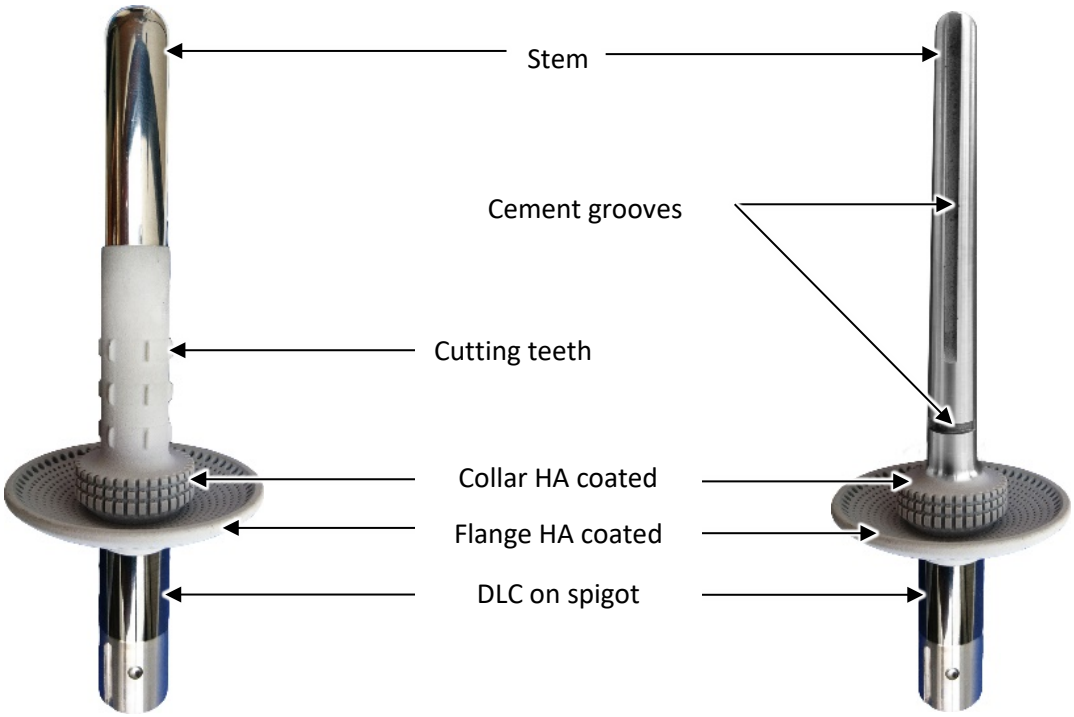

Fig. 1.10: The ITAP device (endo and exo prosthetic parts)
left = uncemented type (cohort II), right = cemented type

1.7.5.2. Outcome

ITAP outpatients were split between two UK hospital sites, there is no published data on ITAP patient outcomes at the time of writing and follow up raw data is only available from one site (n = 12). Overall, four patients (03, 05, 07, 12) equating to 33 % of the RNOH patients, have had their ITAP removed at the time of writing. Three of these patients (03, 05, 07) equating to 25 % of the RNOH patients, experienced a deep infection and had their implant removed between five to nine years of implantation. One of whom (07) had experienced a series of minor infections for which the prescribed antibiotics were not taken, concurrently they experienced severe intermittent pain from a large sciatic nerve neuroma. The other two infection-related removals (eight and nine years post-surgery) had been able to ambulate without discomfort until close to the removal surgery. Patient 12 suffered an ITAP fracture at the neck of the collar and spigot, five years post implantation, the implant has been removed and the patient is currently being assessed for revision surgery. All other patients experienced minor or no adverse effects.

1.7.6. SAAP design fixation and surgical variations

SAAP design, fixation and surgical variations offer different advantages; the ability of the CPS to fix in very proximal residuum's and the ITAP offering patients with poor bone quality a cemented fixation are stand out features. Comparing the reported SAAP outcomes is challenging due to the heterogeneity in SAAP design, fixation, study design, surgical variations and crucially follow up time. For example, two of

the four ITAP removals occurred eight and nine years after implantation yet none of the OPL, CPS or keep walking implants have been implanted for that length of time. There is no standard way of tracking and evaluating SAAP outcomes (Hebert et al., 2017); development of a global fixation success scale that measures implant stability with respect to infection and bone growth is needed (see Chapter Two). Patient selection criteria is already relatively consistent across implant types but ideally there should be a standardised agreement on surgical technique and study format in order to compare outcome differences. In all designs over time there is an issue with bone remodelling and infection driven loosening; this thesis aims to address the issue of periprosthetic bone remodelling.

1.7.7. Thesis aims

- This thesis will attempt to provide information, currently not available in the literature, regarding the long term fixation success of one type of SAAP (the ITAP) from the UK clinical trial.
- Also it aims to measure ITAP patient radiographic changes in periprosthetic bone and qualitatively compare results with those from FEA.
- Furthermore, using data gathered from the biomechanical assessment of one ITAP patient, it aims to compare the biomechanics of different populations / SAAP designs.
- Finally, it aims to provide a validated FEA to generate guidelines based on periprosthetic bone remodelling, for future SAAP designs.

1.8. Concluding remarks

This review has presented a background bone mechanobiology, SAAP and amputation surgeries and outcomes to date. A method of a reliably accurate stress analysis with differing SAAP designs has been discussed and will be presented in Chapter Five. The knowledge gap in SAAP biomechanics and how these compare between TF amputees with different prosthetic solutions and non-amputated individuals has been highlighted and will be addressed in Chapter Three. The data from the ITAP clinical trial has yet to be thoroughly mined, although a preliminary report was produced internally (SIW, 2017). In order to evaluate the relative merits of different SAAP designs, the gap in available data on ITAP patient outcomes will be addressed in Chapter Two. Next follows a breakdown of what the remaining Chapters of this thesis contain.

1.9. Chapter overview

Chapter 2. A radiographic study of bone remodelling in 12 ITAP patients relating implant design features and fixation method to cortical thickness and fixation success over an 11 year period. This Chapter reports on the principle that ITAP fixation success is described by an increase in distal cortical bone growth and little or no radiolucency and goes on to assess whether there are ITAP design features that offer a superior fixation success. These features are assessed using a developed fixation success scale and the second outcome measure of radial cortical thickness.

Chapter 3. A report of kinematic and kinetic data collection from one ITAP patient via gait analysis and a custom made six axis wireless load cell. The aim of this Chapter was to compare the kinematics and kinetics of an ITAP patient to non-amputated individuals, prosthetic socket TF amputees and other SAAP TF amputees.

Chapter 4. A full field and discrete point displacement and strain analysis respectively. FEA, Digital Image Correlation (DIC) and uniaxial strain gauges are used on a cadaveric femur implanted with a SAAP. This Chapter provides an experimental validation for the FE model used in Chapter Five and aims to develop a reliable model that demonstrates equivalence between the experimental displacement and strain results with the FEA results.

Chapter 5. A parametric FEA using the validated SAAP/bone FE model from Chapter Four and ITAP patient load cases from Chapter Three. SAAP features chosen for parameterisation were: ITAP stem length, radius and taper, inclusion or not of a cortical plate and its length and the fixation method (cemented or pressfit). The Chapter tests the hypothesis that the results of an analytical stress analysis will be a good representation of the FEA when conditions of beam theory are met. Furthermore, this chapter will qualitatively investigate whether the results of the FEA will be a good representation of the clinical results. And finally, that there will be some features of a SAAP design that will be more advantageous for successful implant fixation than others.

CHAPTER 2

An 11-year retrospective radiographic analysis of bone remodelling in ITAP patients

2.1. Introduction

Building on what we know of bone mechanobiology (Chapter One) it is possible to see how ITAP geometry and fixation methods may have influenced host bone remodelling. This Chapter aims to investigate the bone changes observed in 12 ITAP patients in an 11 year retrospective longitudinal radiographic analysis. Results of the bone changes will be compared with the implant design features used in each case to build a picture of each feature's effect on the bone. This knowledge can be used to make recommendations for future implant designs and compared with other SAAP design outcomes as well as the FEA results (Chapter Five).

Studies on previous SAAPs lack a global success outcome scoring system; a few groups have measured transverse cortical thickness as an index for bone remodelling success (Haket et al., 2016, Thomson et al., 2019, Örgel et al., 2020). Patient quality of life, mobility and discomfort levels have been quantified in many SAAP studies (Hagberg et al., 2005a, Hagberg et al., 2014, Hebert et al., 2017). Preliminary ITAP results have collated 12 month post-surgical skin reaction data to provide information on the integration of the device, soft tissues and soft tissue viability (SIW, 2017). Yet there still is no universal scale that unites and normalises the scoring systems across SAAP implant types to assess success of long-term implant fixation. This Chapter aims to develop such a score and then uses it to assess clinical ITAP fixation success. As a secondary measure of outcome success and to compare with other SAAPs, radial cortical thickness will be measured.

2.1.1. Measuring ITAP success

2.1.1.1. Developing a fixation success (FS SCORE) score

Quality of life and replacing a limb (or joint) to restore function is a concept that is unique to each patient. Commonly reported Total Hip Replacement (THR) outcome measures include activities of daily living, the hip outcome score, pain and satisfaction scores and the Harris hip score (Lansdown et al., 2018, Kahlenberg et al., 2017). Total Knee Replacement (TKR) outcome measures include the knee society score (Scuderi et al., 2012) and joint measurements such as range of movement (ROM). In the ITAP patients the clinical outcome measures, after 18 months, included the SF-36 (a quality of life measure (Jenkinson et al., 1999)), the Q-TFA (a self-report measure to reflect use, mobility, problems and global health (Hagberg et al., 2004)), the Special Interest Group in Amputee Medicine (SIGAM) mobility grading and an interview at the end of the study to discuss practical and emotional aspects of the ITAP process. There may be inter and intra patient scoring variability due to both patient and

clinician assessment subjectivity despite best efforts to calibrate these grading scales. For example, using the Harris hip score to determine limp; in discerning between 'slight' or 'moderate' a patient may be categorised differently by different clinicians. Similarly, the SF-36 asks 'how much bodily pain have you had during the past four weeks?' one patient may answer 'very mild' to another's 'mild'. Accordingly, when developing a FS SCORE, it would be useful to quantify to what degree the score can be relied upon if it contains an element of subjectivity, or better still, for it not to be at all subjective.

2.1.1.2. Radiographic measures of outcome

A clinical assessment using measurements from radiographs may reduce the subjectivity, but variability can be introduced from differences in image resolution and orientation. Furthermore when looking for the presence of bone abnormalities or osteolysis this may come down to the experience of the clinician (Muir et al., 2011). In TKR radiological outcomes can be assessed using joint angles and alignments as well as abnormalities or osteolysis (Jeon et al., 2019). Radiographic evaluation is used extensively in the follow up of THR surgeries (Teeny et al., 2003, Clohisy et al., 2008), but despite this being a commonly performed procedure there is not a standardised process of evaluation. The Engh grading scale, Table 2.1 (Engh et al., 1990) is the most prominently reported scale

Scale	Score
Fixation	
Radiolucency at porous interface	- 5.0 to + 5.0
Spot welds	- 2.5 to + 5.0
Stability	
Radiolucency at smooth interface	- 3.5 to + 5.0
Pedestal	- 3.5 to + 2.5
Cortical remodelling	- 4.0 to + 3.0
Interface radiolucency	- 2.5 to + 2.5
Migration	- 5.0 to + 3.0
Particle shredding	- 5.0 to + 1.0
Total score	**Fixation + stability**

Table 2.1: The Engh grading scale for pressfit hip implants

used in the follow up of uncemented THR (Muir et al., 2011). It comprises a fixation and stability sub score that are summed for a total score. The sub scores are weighted up to a maximum of + 5.0 and minimum of - 5.0. Engh et al. (1990) achieved this by normalising each feature in the sub score depending on the effect it had on fixation outcome as determined from clinical measures of pain and walking scores in patients in their study.

2.1.2. Inclusions for the ITAP FS SCORE

This section assesses a variety of bone outcome states and observations in order to define the inclusions for an FS SCORE. It will assess whether a: they are universally applicable across all SAAP types and b: that they have a quantifiable and universal effect on the fixation outcome.

2.1.2.1. ITAP collar cortical bone ingrowth (CIG) as a measure of fixation success

The Engh score considers osseointegration a scoring success factor. Since cemented hip implant stems rely solely on a mechanical fixation, this scale was unsuitable unless stems were pressfit. The difference with a score that is to be developed for the ITAP is that the percutaneous part of the ITAP (the spigot) is mechanically unsupported and must sustain a dynamic ground reaction force. Accordingly, the anchoring of the osteotomy face to the ITAP collar and subsequent cortical bone ingrowth (CIG) is vital for long term stability to augment the remaining musculature and offer a stable platform for loading, Fig. 2.1 (Fromme et al., 2017, Coathup et al., 2013). Therefore, osseointegration of the pressfit stem *and* osseointegration of the osteotomy face in both pressfit and cemented stems are vital stability measures. Accordingly, both CIG and cortical thickening around the ITAP stem must be incorporated into the grading system. Cortical bone thickening around an ITAP stem may not necessarily indicate fixation

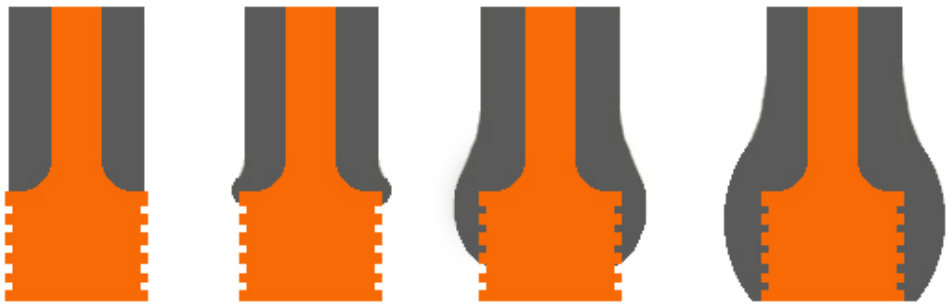

Fig. 2.1: Cortical bone (grey) collar ingrowth illustration over time
(+F growth shape, see 2.2.5) around ITAP grooved collar (orange) over time.

success if unanchored at the osteotomy face (for example, if as the result of osteomyelitis). Conversely, mechanical fixation success can improve under a good amount of CIG, moreover, the risk of

periprosthetic fracture decreases as collar ingrowth increases (Fromme et al., 2017). Since CIG is essential for stability and occurs whether stems are pressfit or cemented this will be a vital indicator of a successful fixation and can be included in the FS SCORE.

2.1.2.2. Radiolucency (RL) as a measure of fixation success

The benefit of CIG stability is voided if there is interface radiolucency (RL) due to the development of a fibrous surrounding sheath (see 1.5.5) in pressfit or cemented stems. Previous work with distal femoral endoprostheses has shown osseointegration at implant collar and stem RL to be inversely related (Coathup et al., 2015). Additionally, it was identified by Moore et al. (2006) as an outcome that would challenge osseointegration in THR patients and also incorporated into the Engh score as a negative outcome with respect to implant success. Finally, work by (Chan et al., 2017) suggests presence of RL indicates complications relating to implantation and positioning. Accordingly, RL presence will be considered a vital indicator of an unsuccessful fixation in the FS SCORE.

2.1.2.3. Weighting the CIG and RL contributions to the FS SCORE

The Engh grading scale proposes three RL measurements (at the porous, smooth and full interface). Two of the three grade ranges were equidistance from zero (- 5.0 to + 5.0 and - 2.5 to + 2.5), RL at the smooth interface was weighted in terms of an absence scoring higher (- 3.5 to + 5.0). It proposes a cortical remodelling score (around the stem) slightly weighted in favour of resorption rather than apposition (- 4.0 to + 3.0) having more of an effect (detrimental) on the fixation success. Although a very useful scale for THR assessment there are crucial differences between the mechanics of a THR and an ITAP that render it different enough to independently address the weighting of the sub scores (CIG and RL). First, cortical thickening is not being included in an ITAP FS SCORE. Second, the addition of a CIG sub score should be considered at least as valuable as the RL score and there should be the same number of measurement sites for each. Importantly the weighting for CIG and RL cannot be evaluated in the same manner as Engh et al. (1990) due to the lack of patients and since multiple features were altered between patients (making a significant comparison challenging). As a result, the approximation that both are equally influential as each other to the FS SCORE in presence and absence was made.

2.1.3. Other bone changes as a measure of fixation outcome

2.1.3.1. Cortical bone thickness

Cortical bone thickness change refers to radial bone growth (changes in the cross section) and is the result of bone remodelling (resorption or apposition). It is the measurand that the majority of SAAP literature cites, although how the measurement was taken varies tremendously. Matthews et al. (2018)

analysed the UK cohort of patients who have received an OPRA (n = 18). 83 % of patients showed distal bone resorption and 33 % showed proximal bone apposition. 66 % have developed proximal pedestals and 33% display radiolucency in different zones next to the fixture. Nebergall et al. (2012) in a larger OPRA study (n = 47) showed bone initially resorbs in at least one zone in over half of the patients but then stabilises. Analyses of radiographic data and FE studies corroborate cortical bone observations in patients using the OPRA: distal bone resorption and proximal bone apposition (Xu and Robinson, 2008, Tomaszewski et al., 2012a). Periprosthetic cortical thickness was measured on 27 ILP implant patients between 2009 and 2012 on patients in the Netherlands (Haket et al., 2016). An average 9 % increase in all zones was observed after 24 months with the largest increase in the medio distal zone (18 %). The largest increase in cortical thickness between 12 and 24 months was observed on the medial side halfway along the stem, indicating that after an initial medio distal thickening at 12 months thickening at this level continues at a faster rate than distally thereafter. Conversely there is a small amount of resorption at the mid stem level between 12 and 24 months (~ 1 %). A retrospective longitudinal study of ILP and OPL (Thomson et al., 2019) with 28 patients up to 24 months wherein none suffered “gross implant loosening” or failure indicates cortical thickening in both designs in all zones except the medio distal zone of the ILP patient (this is inconsistent with the ILP results of Haket et al. (2016)). Results from McGough et al. (2017) on the CPS implant report 18 % periprosthetic fractures, no component failures and in one patient the bone stock at the revision had increased in quantity and quality as a result of the bone hypertrophy.

2.1.3.2. Radiographic abnormalities and osteolysis as a measure of fixation success

In pressfit implants, stability, thus fixation success can be indicated by the development of spot welds (bone sclerosis from stem to endosteal surface) (Engh et al., 1987). Pedestal formation (Fig. 2.5 e) is another visible endosteal sclerosis described as a shelf of bone in the IM canal apparently ‘supporting’ a hip implant stem. If not associated with radiolucency, pedestals can be considered an aid to successful fixation but with radiolucency are associated with unstable stems (Engh et al., 1990, Pluot et al., 2009b). Since both spot welds and pedestals are only visible in radiographs of pressfit fixations they cannot be included in a universal fixation score, however, will be recorded to augment fixation observations.

2.1.3.3. Surgical alignment

In THR and TKR there is significant literature outlining the importance of aligning the implant and/or components correctly to ensure optimal biomechanics. This is supported with studies showing that patients go on to lead an improved quality of life, have a better joint function with less pain and revision surgeries (Choong et al., 2009, Ritter et al., 2011, Schroer et al., 2013, Myers et al., 2018). The ITAP, although likely to be similarly affected by surgical alignment, is different from arthroplasty: First, inter

patient muscle activation varies depending on limb amputation level and how the muscles were (if at all) reattached. Second, as previously discussed, CIG is essential for successful fixation. Measurements to assess surgical alignment should therefore be twofold; first, to check the implant alignment matches the anatomical axis of the bone residuum (Fig. 2.5 c) and second, to check that the bone osteotomy face is in full contact with the proximal face of the collar thus offering maximum contact area for osseointegration and facilitating CIG (Fig. 2.5 a and Fig. 2.5 b).

2.1.3.4. Shape of CIG growth

On initial observation of the radiographs there were notable differences in the way CIG, if present, spread and may be a criteria of fixation success (Fig. 2.5 d)

2.1.4. Non-bone changes as a measure of fixation outcome

A clinical assessment in isolation may not be enough for thoroughly evaluating implant fixation success. Unstable components may not show any deleterious signs, conversely an osseointegrated part may be symptomatic (Engh et al., 1990). For example, an unanchored osteotomy face on the ITAP collar despite stem integration. For this reason, the data obtained from the SF-36, Q-TFA and the SIGAM will be included to comprehensively report the ITAP success.

2.1.5. Measuring ITAP success summary

All patients will receive a FS SCORE from the summation of the RL and CIG scores (outcome one) against which all design and surgical features of interest (inputs) will be compared. Success will be measured quantitatively using periprosthetic bone thickness changes, shape of CIG growth and bone abnormalities such as pedestals (outcome two). Additionally, non-bone outcomes will be reported.

2.1.6. Chapter aims

- To develop fixation success score (FS SCORE) that will reliably indicate implant design features that have a positive or detrimental effect on fixation success.
- To investigate whether regions of higher bone stress will result in cortical thickening.
- To investigate whether distal bone growth will stabilise an implant.

2.2. Method

The ITAP clinical trial patient cohort and implant designs are outlined below, followed by the radiographic processing method and all measurements taken from them and the implants.

2.2.1. The patients

The ITAP clinical trial implanted 20 unilateral transfemoral (TF) amputees (18 male, two female) in a single stage operative procedure in 2008 (cohort I, n = 10) or 2013 (cohort II, n = 10). Patients had suffered amputations as a result of traumatic injury (n = 14) or osteosarcoma (n = 5) (unknown, n = 1) and were experiencing difficulties using their prosthetic socket. There were ten right and ten left femoral amputations/ITAP surgeries. Patients had been TF amputees for between six months and 30 years. None had pre-existing ipsilateral hip pathology nor a co-morbidity that would affect outcome (e.g. osteoporosis, heart disease, peripheral vascular disease, obesity or unrelated cancer). Patients were encouraged to lie in bed as still as possible for up to one week after surgery and then were rehabilitated by a physiotherapist. They were followed up as rehabilitation patients for the first six to 12 months and thereafter became outpatients at the Royal National Orthopaedic Hospital (RNOH), Stanmore, UK (n = 13) or the Royal Orthopaedic Hospital (ROH), Birmingham, UK (n = seven); follow up raw data was only available from the RNOH. One patient was lost in the follow up leaving ten male and two female patients, who were 28 to 53 years old at the time of surgery (median age = 44.5 years). An observational protocol (IRAS number 226799) was approved to access all patient radiographic data.

2.2.2. The ITAP

Fig. 1.10 and Fig. 2.2 illustrate the ITAP; pressfit stems were nearly all parallel and had anti rotation teeth (1 mm proud from the surface) on the distal third of their stems and an HA coating on their distal half. The polished cemented stems were all tapered at an angle of 0.75 ° with longitudinal and radial cement grooves 1.5 mm deep to prevent rotation and axial pull out. There were six pressfit implant patients in cohort I and four cemented, while in cohort II all were cemented. Pressfit stems were designed to be line to line with the inner cortex; the layer of HA coated resulted in a 150 - 200 µm interference fit. Cohort II received a silver coating (Agluna®) on the collar, flange and part of the spigot to combat superficial infection.

2.2.3. The radiographs

Patients had baseline (time = 0) inpatient radiographs taken in the frontal plane (along the anterior posterior (AP) axis, Fig. 2.3 a) and the sagittal plane (along the medial lateral (ML) axis). The first postoperative radiograph was taken one month post-operatively. Thereafter, radiographs were taken at

intervals (of differing lengths) at outpatient clinics, up until the present (an 11 year period for cohort I patients). Radiographs were filtered initially for quality and completeness, resulting in a working set for each patient; each set was subdivided into AP or ML subsets. Within each subset, an image was selected to be the reference image, radiographs in each subset were scale normalised against the reference image as the ITAP spigot was known to consistently be 18 mm in diameter. Adobe Photoshop CS6 (Adobe systems Incorporated, San Jose, California, United States) was used. Each measurement was taken twice by measuring to the outer edge of the last pixel by the same researcher (KA).

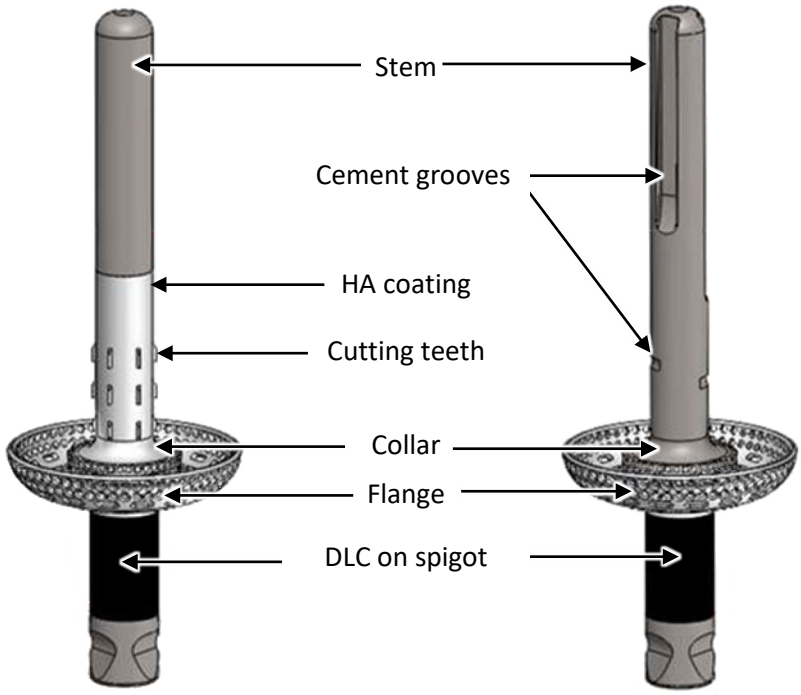

Fig. 2.2: CAD files of both ITAP fixation types
A pressfit (left) and parallel cemented (right) ITAP illustration (adapted from SIW (2017))

2.2.4. The FS SCORE

Since FS SCORE sub score (CIG and RL) measurements were taken from two dimensional radiographs, scoring was calculated around the image perimeter of the collar and implant respectively. A similar zoning method around a SAAP stem was used by Nebergall et al. (2012) and Tomaszewski et al. (2012b). The perimeter of the collar and implant were geometrically different (Fig. 2.3 b and c), however each one was split into the same number (eight) of equidistant zones in each plane (total = 16 zones for CIG or RL scoring). CIG presence scored positively in each zone; absence scored zero, so the range was 0 to + 16. RL presence scored negatively in each zone; absence scored zero, so the range was – 16 to 0. Summation resulted in a possible range of FS SCORES from -16 to +16 where a more successful fixation outcome was a higher FS SCORE and the sub scores were evenly weighted either side of zero (see 2.1.2.3.).

2.2.5. Input and outcome measurands

The ITAP stem designs varied depending on fixation method and bone morphology and quality. Measurements were considered as **input** parameters (ITAP stem geometry and implant fit/alignment) or **outcomes** (cortical bone growth, cortical bone shape change/abnormalities and FS SCORE), listed in Table 2.2 and Table 2.3 respectively. Measurement methods are described in footnotes with measurement zoning shown in Fig. 2.3, alignment in Fig. 2.4 and bone shape changes / abnormalities in Fig. 2.5.

Table 2.2: FS SCORE input measurands

Input	Metric		Description
Stem geometry	Taper		Present (T) or absent (P) (parallel)
	Curve		C (curved), Cs (slight curve) or S (straight)
	Length	S ratio	ITAP stem length : residuum length
		F ratio	Residuum length : contralateral femur length
	$(R^4 – r^4)$		R = bone radius (mm), r = ITAP stem radius (mm) [1]
Implant fit	Alignment [2]	Stem	Colinear with femoral longitudinal axis (Y / N_{ax})
		Face	Gap between osteotomy face and ITAP collar (Y / N_g)
	Implant seating [2]		Bone overhang (OH) or undercut (UC)
	Fixation type		C (cemented) or PF (pressfit)

Table 2.3: FS SCORE outcome measurands

Outcome	Metric		Description
Cortical bone measurement	Growth [3]		Change in absolute cortical thickness (mm)
	Rate		Rate of cortical growth (mm / month)
Cortical bone shape changes	Pedestal [4]		Pedestal growth in up to four quadrants
	AFcollar [5]	Area	In AP and ML (mm ^{2})
		Shape (Fig. 2.5 d)	Abnormal (A)
			Flare wide distally (F+)
			Flare narrow distally (F-)
			No change (O)
Fixation success	FS SCORE [6]	CIG	Cortical ingrowth onto collar (in up to 16 zones)
		RL	Radiolucency (in up to 16 zones)

Key to footnotes:

[1] Implant stem and bone radii are used to calculate moment area of inertia (Eqn. 2.4) and polar moment area of inertia (Eqn. 2.5); I and J respectively, in calculations of bending and torsional stresses of hollow cylinders (beam theory). Since (R^4- r^4) is common to both I and J, this metric was recorded. Before the effect of the implant is considered an increase in this value (towards a thicker cortex) correlates directly with a decrease in bending and torsional stress (Eqn. 2.2 and 2.3 respectively) and a decrease in axial stress under a constant force (Eqn. 2.1). However, in a composite beam model (such as a SAAP implanted bone) changes in cortical thickness will depend on the ratio of implant to bone in the cross section (see A.1.1)		
$\sigma_{ax} = \frac{F}{\pi(R^2 - r^2)}$	σ_{ax} = Axial stress. F = Force. R = Outer radius of bone. r = Radius of implant	*Eqn. 2.1*
$\sigma_b = \frac{My}{I}$	σ_b = Bending stress. M = Bending moment. y = Distance from neutral axis. I = Moment of inertia around neutral axis	*Eqn. 2.2*
$\tau = \frac{TR}{J}$	τ = Shear stress. T = Torque. R = Outer radius of bone. J = Polar moment of inertia	*Eqn. 2.3*
For a hollow cylinder: $I = \frac{\pi}{4}(R^4 - r^4)$ $J = \frac{\pi}{2}(R^4 - r^4)$	R = Outer radius of bone. r = Radius of implant	*Eqn. 2.4* *Eqn. 2.5*

[2] Alignment measurements

Stem alignment and osteotomy face surface area seating (Fig. 2.4) on first post-operative radiograph.

[3] Change in absolute cortical thickness

Once all radiographs within a subset (AP or ML) were scale normalised as described in section 2.2.3, they were placed side by side in chronological order with the oldest one on the left forming a montage. Montages were split horizontally into three equal zones (red lines) from just distal to the stem tip curve to the stem base just proximal to the fillet. Each zone was further divided in half by a (yellow) horizontal line along which cortical bone thickness was measured on each radiograph (all montages in AP and ML from all patients are in A.2.1 of the Appendix). Laterally from distal to proximal the measurement lines (yellow) were A, B, C. Medially from distal to proximal the measurement lines were F, E, D (see Fig. 2.3 d

and Fig. 2.3 e). A consistent measurement system was developed where the measurement was taken from the exterior edge of the cortical bone to the outer edge of the ITAP stem as the absolute 'cortical bone' measurement. This meant in the cemented ITAP patients it also included the cement layer, however since cortical growth will never occur into the cement (as it is a non-penetrable layer), any radial *change* will be the result of cortical growth. See Fig. 2.3 a and Fig. 2.3 d for measurement reference. Cortical growth change over the period for which there were radiographs in each patient was calculated by subtracting the first thickness measurement from the last in each zone.

[4] Pedestal growth

Pedestal growth describes a sclerosis next to the tip of the stem thought to be caused by prosthesis motion which may be an indication of implant stability if not associated with other features such as radiolucency or instability if there are reactive lines around the stem tip as well (Engh et al., 1990, D'ANTONIO et al., 1996, Weaver, 2017), see Fig. 2.5 e.

[5] AFcollar

Bone bound proximally by the line bisecting zones A and F and distally by the osteotomy face was termed AFcollar and is illustrated in Fig. 2.3 e. This cortical region was the site where CIG was scored, and it also offered a consistent area in which to calibrate the spread of CIG growth. CIG spread was categorised depending on the shape of bone growth in AFcollar as either no change (O), abnormal (A), positive flare (+ F) and negative flare (- F) growth shapes (Fig. 2.5 d).

[6] FS SCORE

FS SCORE = RL + CIG. Both measurements were made on the last radiograph of each subset.

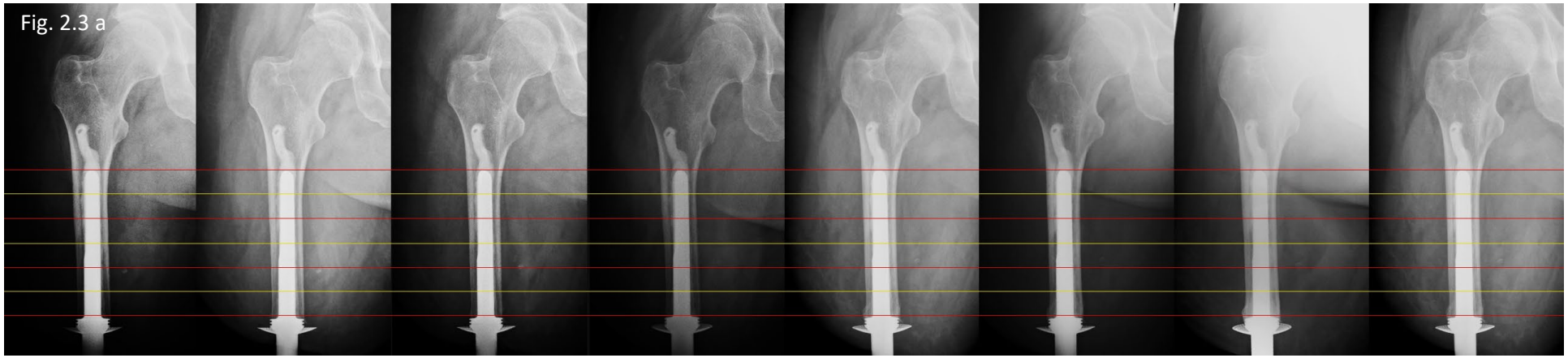

Fig. 2.3: Diaphyseal cortical growth, CIG and RL zoning maps:

a = Montage of AP radiographs from a cemented RHS implanted patient from cohort I over two years (from left/bottom to right/top).

b = A pressfit RHS implanted patient illustrating the six zones (red borders) and measurement lines (yellow).

c, top and bottom = 16 RL zones. Note the numbers refer to the interface between bone/implant in each zone.

d = Eight ITAP CIG zones (the same in AP and ML)

e = A cemented LHS patient with the AFcollar zone magnified.

Fig.2.3 b

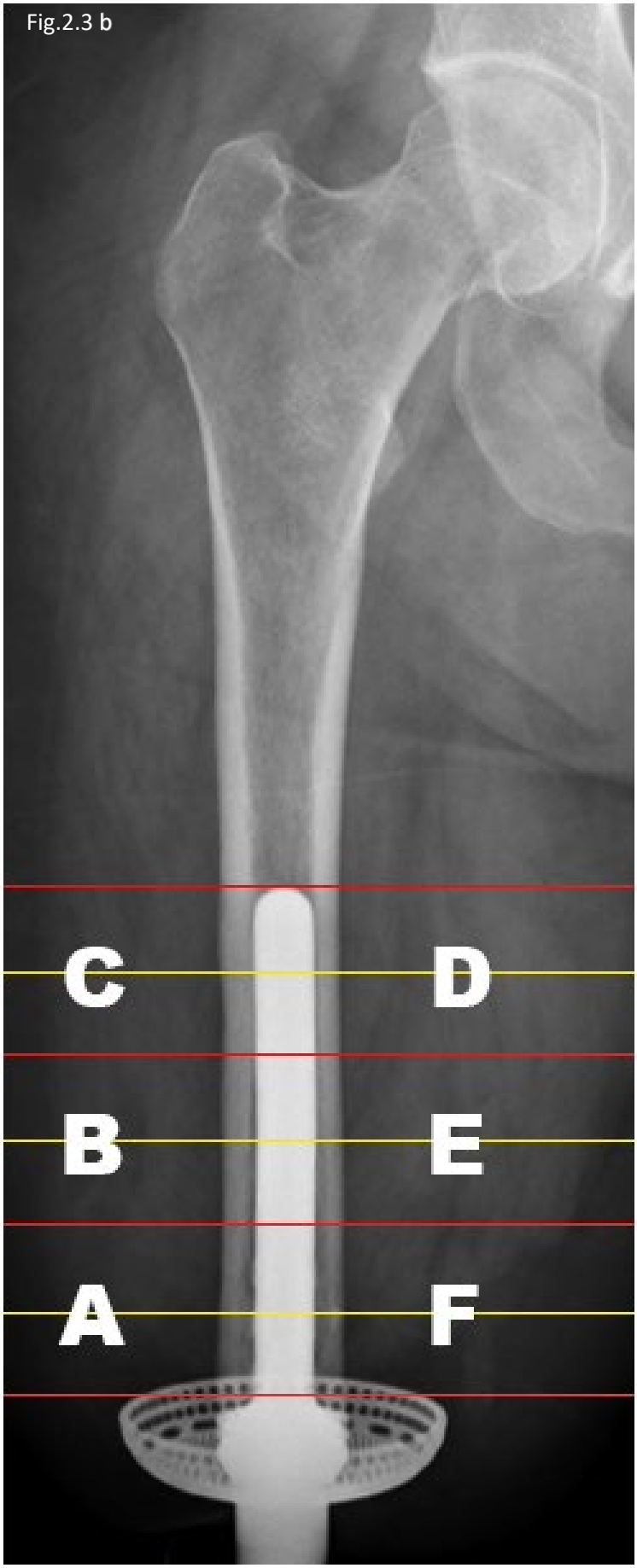

Fig.2.3 c

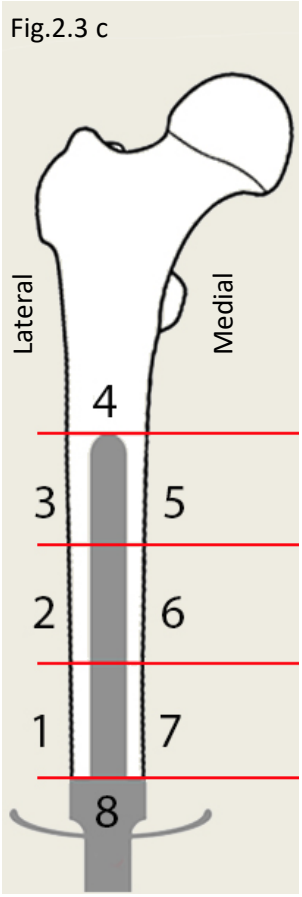

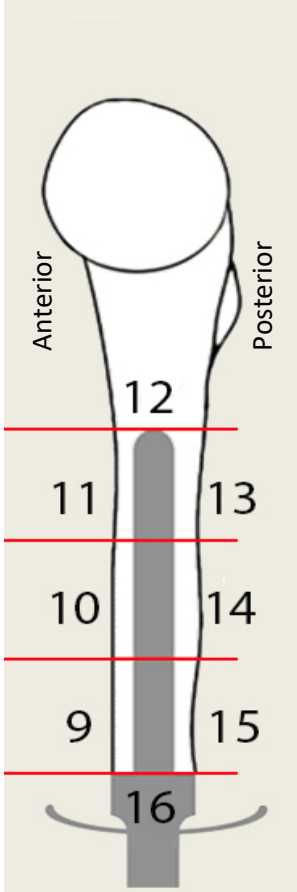

Fig.2.3 d

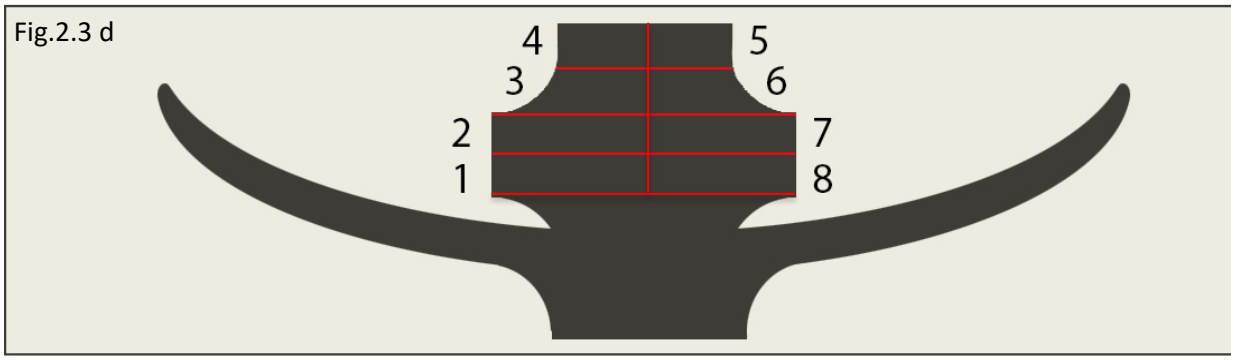

Fig.2.3 e

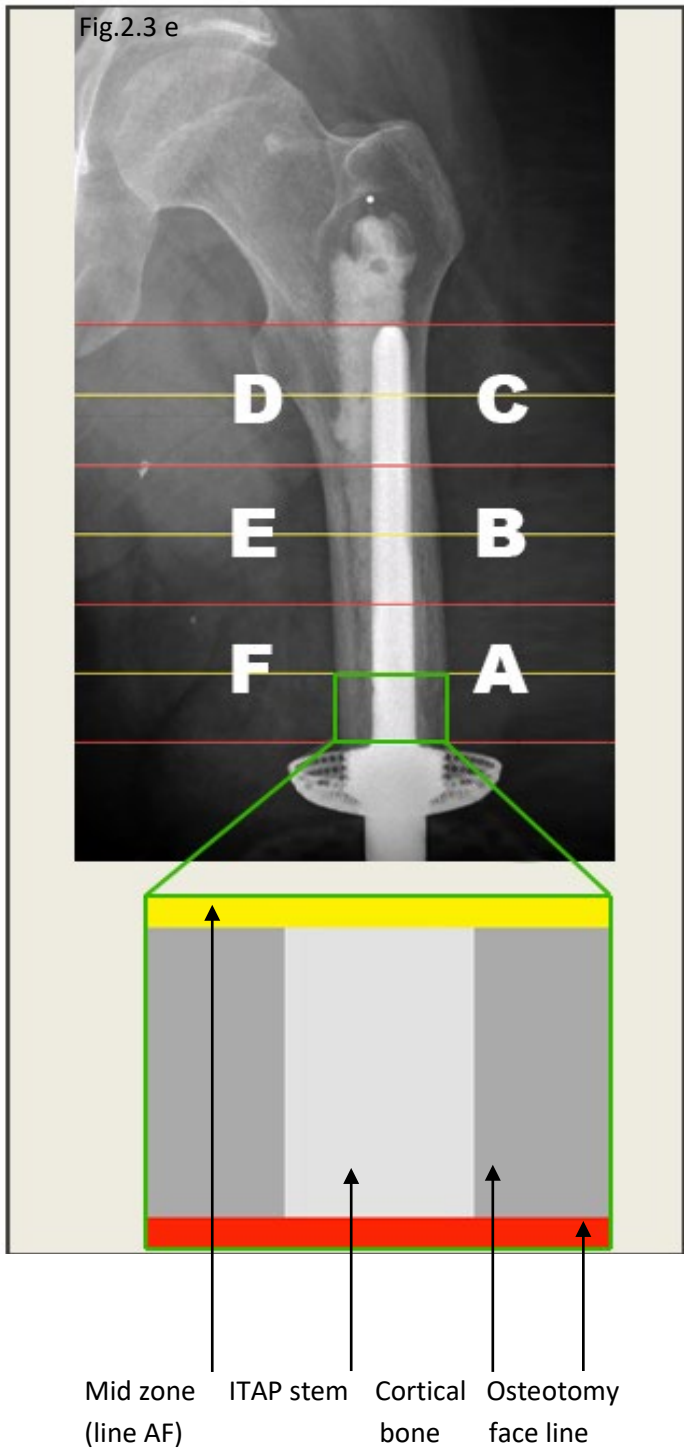

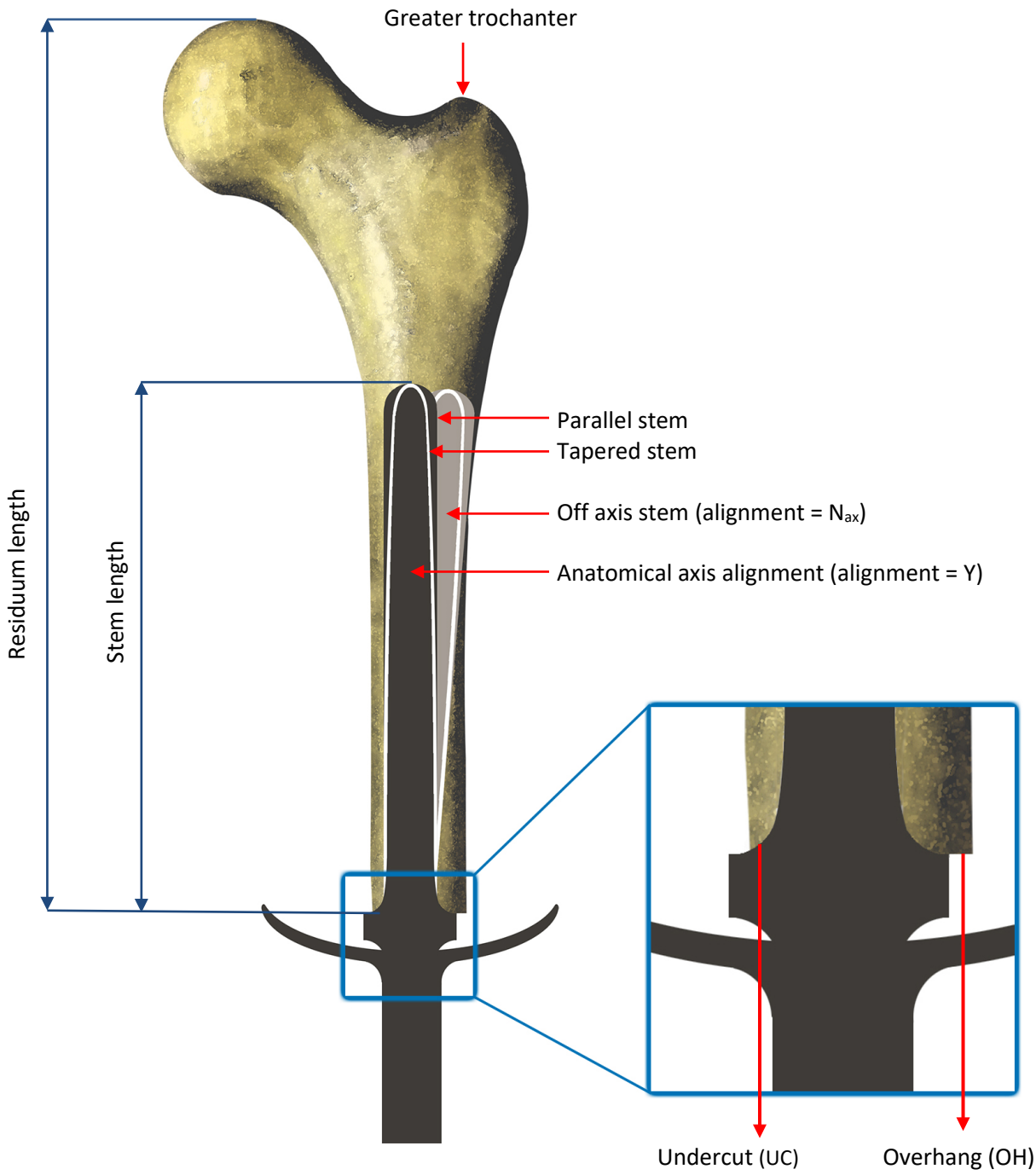

Fig. 2.4: Illustration of FS input measurements
Zoom box = Seating OH/UC measurement

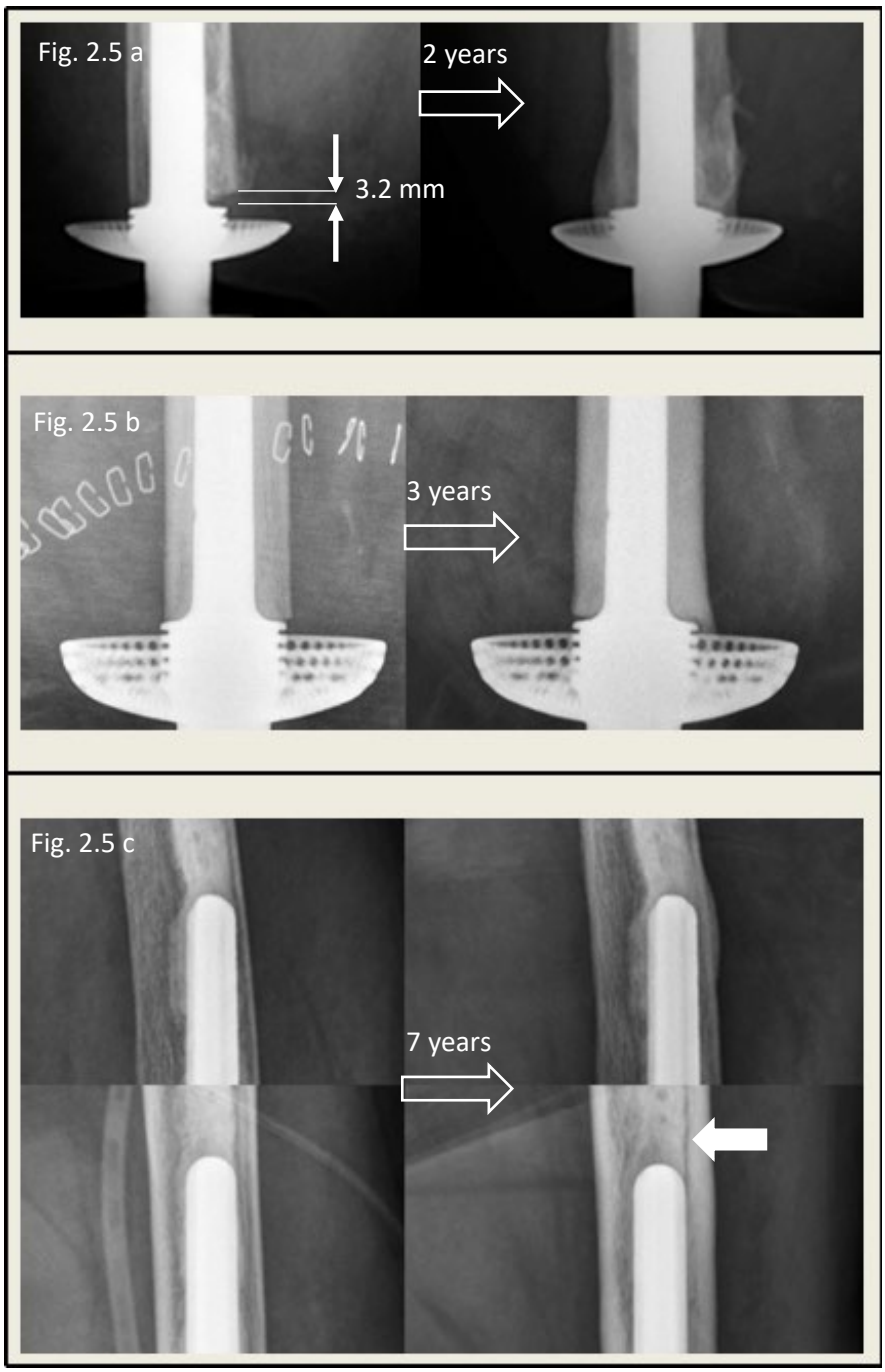

Fig. 2.5: Radiographic bone changes in ITAP patients over time

a = Significant distal cortical thickening overcomes initial large (3.2 mm) cement gap (N_g) at the osteotomy face on the posterior side of these AP radiographs.

b = A pair of ML radiographs show initial OH laterally developing some CIG in proximal collar zones. Some medio distal gaps can be observed on the osteotomy face; possibly due to initial RL or a cement gap.

c = 'Off axis' (N_{ax}) ITAP position developing localised cortical thickening in AP (top) and ML (bottom). Radiolucent line between cement and cortical bone in zones 4, 10, 11 and 13.

d = Growth in AFcollar sections shown over nine years from three different patients illustrating development of A (left), +F (middle) and -F (right) growth shapes.

e = Development of a pedestal in one quadrant (lateral) of this patient, radiographs in AP showing poor integration of the stem distally, potentially the reason for pedestal formation.

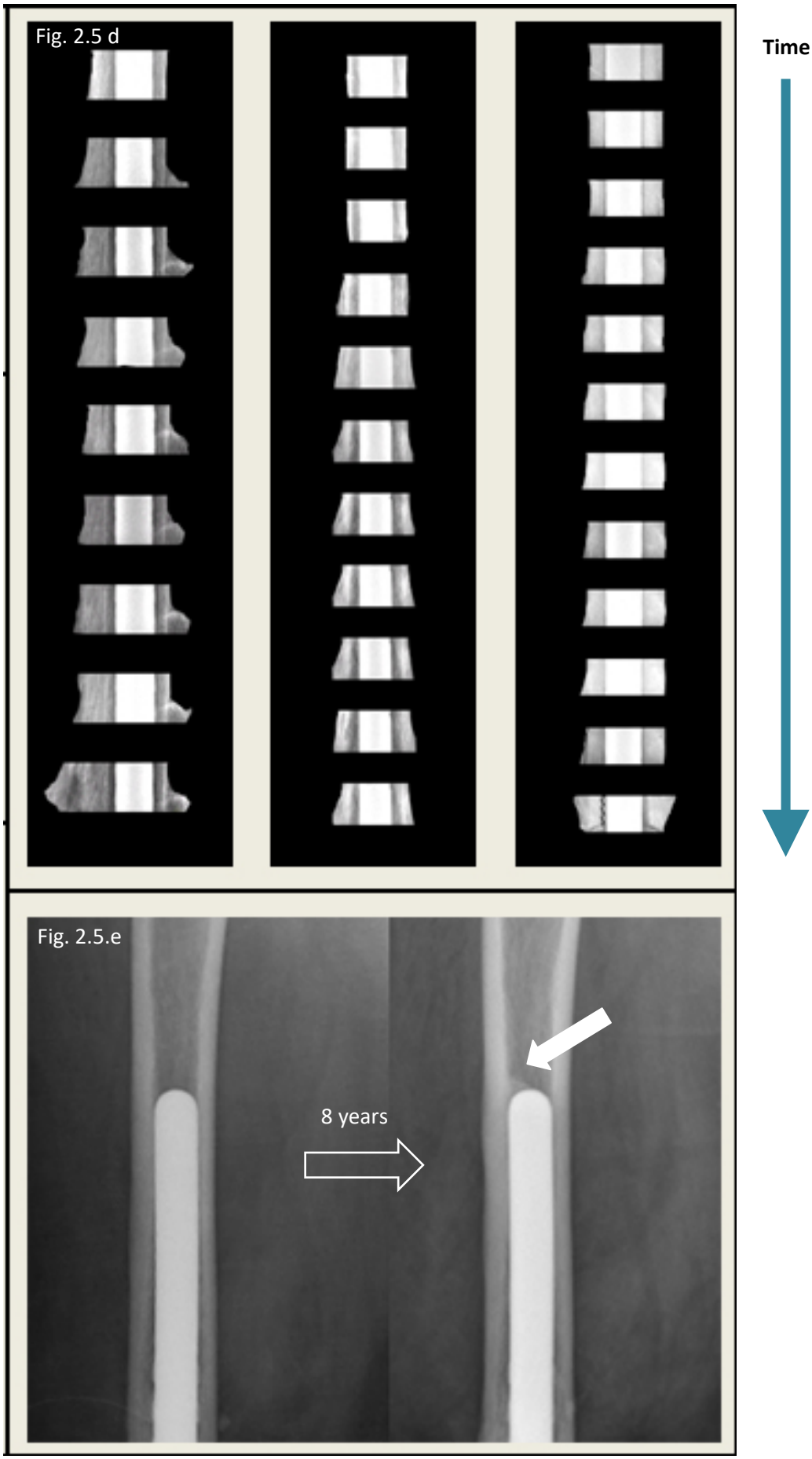
Fig. 2.5 d
Time
Fig. 2.5.e
8 years

2.3. Results:

Results have been split in two, first: patient data, input parameters and associated fixation success outcomes. Second, cortical bone changes and associated fixation success outcomes.

2.3.1. Patients, Input parameters and fixation success outcomes

Table 2.4 contains patient information, input and outcome parameters. There was an average (median) span of 6.19 (+/- 1.40) years of radiographic image data collection in this study, the average ratio of the stem:femur (S ratio) was 0.53 (+/- 0.07) and that of the residuum:femur (F ratio) was 0.49 (+/- 0.05). Every patient had some degree of OH or UC, in an average of 1.0 (+/- 0.56) and 0.5 (+/- 0.38) quadrants respectively. Most patients (58 %) did not display pedestal growth. The average CIG was 8.00 (+/- 4.32), indicating that there was a trend for ingrowth onto an average of 50 % of the collar surface (scale range is 0 to 16) but that there was a +/- 25 % spread either side of this. Whereas RL average was -2.00 (+/- 1.63) suggesting there was average radiolucency at 16 % of the bone/implant interface (scale range is -16 to 0) with a much smaller CI. The average FS SCORE was 6.5 (+/- 4.81) indicating a good outcome overall with clear room for improvement (scale range is -16 to 16).

Key for Table 2.4

Image span	= Length of time between the first and last measured radiograph (yr)	
Age	= Age at date of surgery (yr)	
T / P	= Tapered / Parallel implant stem	
C / Cs / S	= Curve / Slight curve / Straight stem	
S-ratio	= ITAP stem length **:** femur residuum length	
F-ratio	= Residuum length **:** pre-operative femoral length	
r	= Radius of ITAP stem at most distal point (mm)	
R	= Mean distal radius of bone in AP / ML on first Xray (mm)	
Align	= Yes or N_{ax} (stem off axis) or N_g (gap between osteotomy and collar)	
OH / UC	= Overhang / Undercut number of quadrants (up to two in each plane)	(Range = 0 - 4)
Ped	= Pedestal; number of quadrants observed (up to two in each plane)	(Range = 0 - 4)
Fix	= Cemented / Pressfit	
CIG	= Cortical bone ingrowth to collar (sub) score	(Range = 0 to +16)
RL	= Radiolucent lines / gap (sub) score	(Range = -16 to 0)
FS SCORE	= Fixation success score	(Range = -16 to 16)

Table 2.4: Patients, FS SCORE input and outcome parameters

Numerical variable averages with a 95% CI. Patient supplementary radiographic notes are A.2.2 of the Appendix.

Patient information						INPUT parameters									OUTCOME parameters			
						Stem		Geometry			Fit				Abnormal growth	Fixation success		
Patient	Gender	Image Span (yr)	Cohort	Age (yr)	Leg	Taper	Curve	S ratio	F ratio	$R^4 - r^4$ (mm^4)	Fix	Align	Seating		Ped	CIG	RL	FS SCORE
													OH	UC				
01	M	5.88	II	53	L	T	C	0.58	0.58	4.76 e4	C	Y	1	0	0	8	0	8
02	M	10.00	I	45	L	T	S	0.50	0.47	1.93 e4	PF	Y	1	1	1	16	0	16
03	F	8.79	I	28	R	P	C	0.42	0.49	3.20 e4	PF	Y	1	1	2	0	-4	-4
04	M	5.17	II	42	L	T	Cs	0.85	0.36	4.57 e4	C	N_g	4	0	0	0	0	0
05	M	9.22	I	48	R	P	S	0.37	0.61	3.28 e4	PF	N_{ax}	1	1	0	0	-4	-4
06	M	3.96	I	49	R	T	S	0.55	0.43	3.10 e4	C	N_{ax}	1	0	0	16	0	16
07	M	6.50	I	39	R	P	C	0.44	0.50	3.52 e4	PF	Y	2	0	4	0	-6	-6
08	M	5.17	II	51	R	T	C	0.42	0.67	3.71 e4	C	Y	0	1	0	0	-2	-2
09	M	11.09	I	34	R	T	S	0.57	0.49	3.96 e4	C	N_g	1	2	1	16	0	16
10	M	10.01	I	44	L	T	S	0.47	0.49	6.10 e4	C	N_{ax}	1	1	0	16	-9	7
11	F	4.98	II	35	L	T	Cs	0.62	0.47	2.75 e4	C	Y	2	0	0	8	-2	6
12	M	5.10	II	50	L	T	Cs	0.65	0.41	5.87 e4	C	N_{ax}	1	0	2	16	-3	13
Median	-	6.19	-	44.50	-	-	-	0.53	0.49	3.62 e4	-	-	1.00	0.50	0	8.00	-2.00	6.50
C.I (95%)	-	1.40	-	4.40	-	-	-	0.07	0.05	6.99 e3	-	-	0.56	0.38	0.72	4.32	1.63	4.81

2.3.1.1. Chart plots and correlations

A box and whiskers plot are presented for each categorical (nominal and ordinal) measurand against the FS SCORE in Charts 2.1 – 2.11.

Chart 2.1: Gender vs. FS SCORE

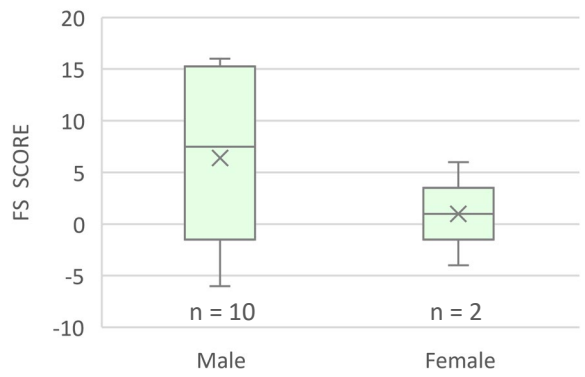

Male ITAP patients achieved a higher median FS SCORE than females (7.5 and 1.0 respectively) although the score inter-quartile range was greater in males than females.

Chart 2.2: Cohort vs. FS SCORE

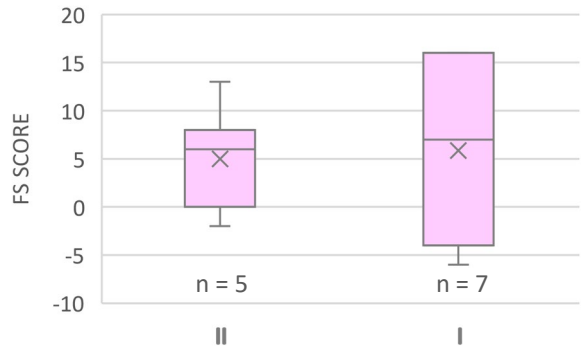

Median FS SCORE in cohort I was slightly higher than cohort II (7.0 and 6.0 respectively) although the score inter-quartile range was greater in cohort I.

Chart 2.3: Leg laterality vs. FS SCORE

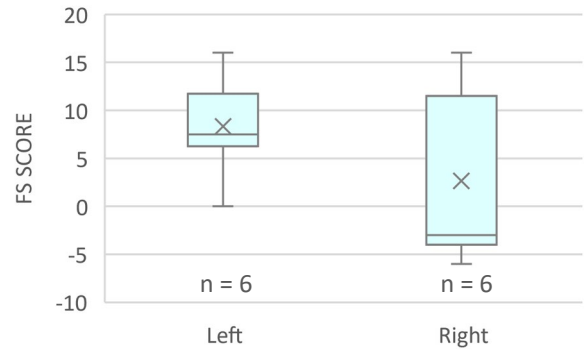

The median FS SCORE in right hand side (RHS) amputees was - 3.0 whereas in left hand side (LHS) amputees was 7.5. The score interquartile range was greater in the RHS amputees compared with the LHS, predominantly due to the large variability in scores in the third quartile of the RHS group.

Chart 2.4: Taper vs. FS SCORE

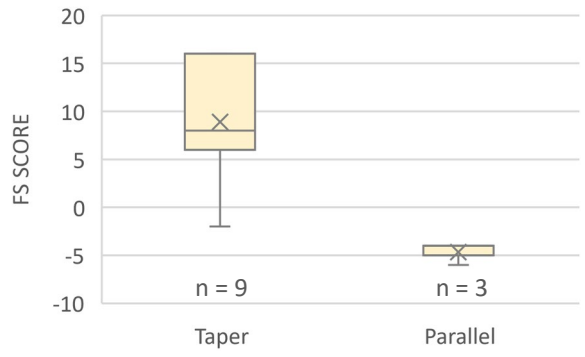

Median FS SCORE of the tapered stems was 8.0 and of the parallel stems was - 4.0. FS SCORE range in the tapered group was highly variable in the first and third quartile. The score interquartile range in the tapered stems was greater than that of the parallel stems.

Chart 2.5: Stem curve vs. FS SCORE

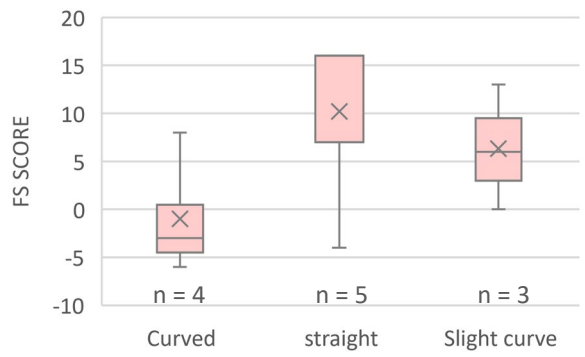

Median FS SCORE was lowest in the curved stems (- 3.0) and highest in the straight stems (16.0) with the slightly curved stems achieving a 6.0. There was no FS SCORE range variability in the third and fourth quartile of the straight stemmed group but there was notable variability in the first quartile.

Chart 2.6: Stem fixation vs. FS SCORE

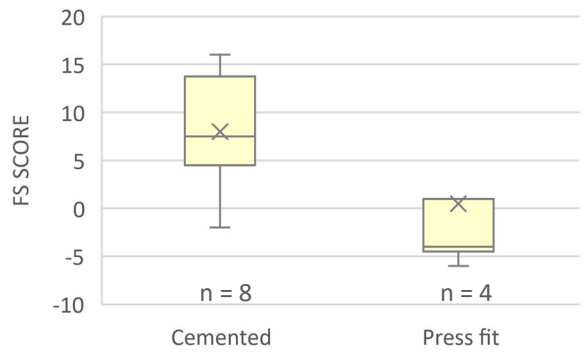

Cemented stems median FS SCORE was higher than the pressfit stems (7.5 and - 4.0 respectively) with a larger interquartile range.

Chart 2.7: Stem alignment vs. FS SCORE

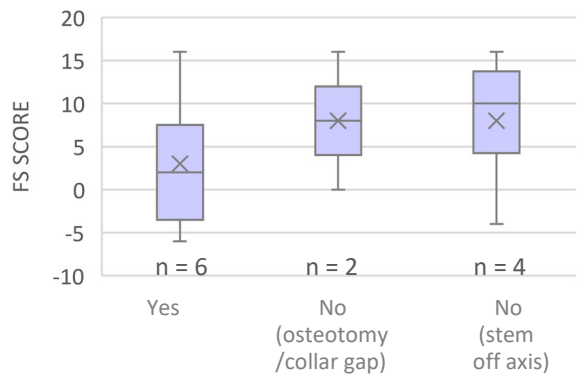

Median FS SCORE was lowest in the aligned group and highest in the 'stem off axis' group (2. 0 and 10.0 respectively). The surgeries with an osteotomy/collar gap resulted in a median FS SCORE of 8.0 (none had osteotomy/collar gap *and* stem off axis).

Chart 2.8: OH vs. FS SCORE

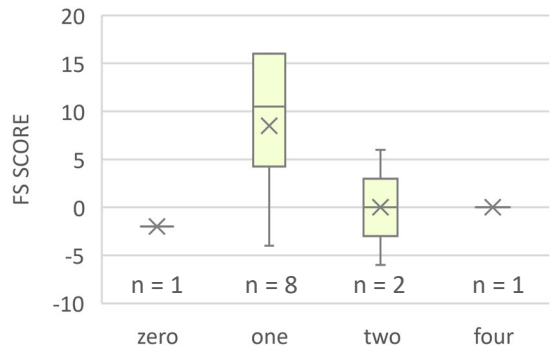

Median overhang (OH) FS SCORE reduced as number of quadrants it was observed in increased except when there was no OH (10. 5, 0, 0 in surgeries with one, two and four quadrant OH). Zero OH was only observed in one surgery and so the median was the FS SCORE (- 2.0). The interquartile score range for the one OH group was notably greater than the rest.

Chart 2.9: UC vs. FS SCORE

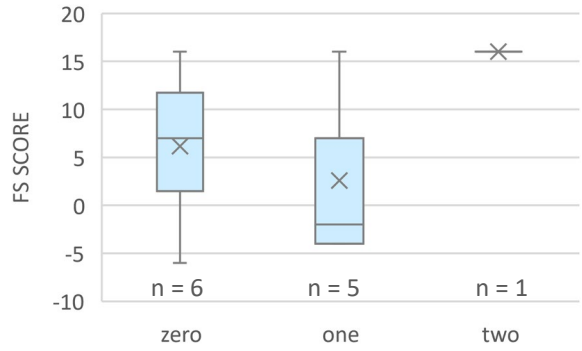

The median FS SCORE for zero quadrant undercuts (UC) was 7.0, for one quadrant UC was - 2.0 and for two quadrants UC was 16.0. There was notable variability in the third and fourth quartile of the surgeries with one quadrant UC.

Chart 2.10: OH + UC vs. FS SCORE

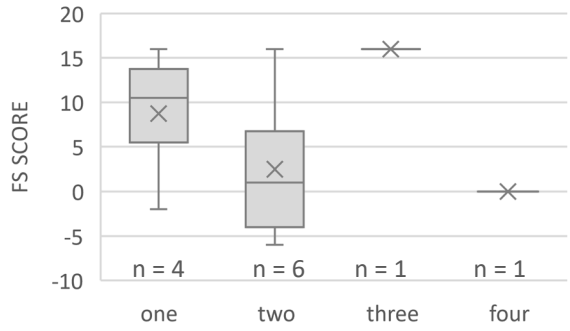

Median OH and UC alignment when observed in one, two, three and four quadrants respectively was 10.5, 1.0, 16.0 and 0. No surgeries were without OH or UC.

Chart 2.11: Pedestal count vs. FS SCORE

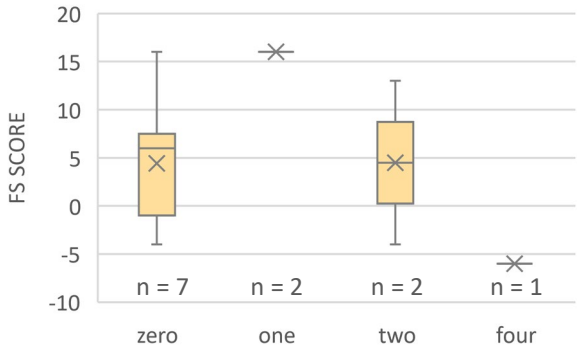

Unless a pedestal was not present, the medial FS SCORE decreased with the more quadrants it was present in (6.0, 16.0, 4.5, - 6.0 in zero, one, two and four quadrants respectively).

A Pearsons correlation was calculated for each quantitative measurand with the FS SCORE:

Measurand	Correlation with FS SCORE	
Image span	0.088	= Negligible correlation
Age	0.208	= Negligible correlation
S ratio	**0.321**	**= Low positive correlation, i.e. as S ratio increased, FS SCORE increased**
F ratio	**-0.386**	**= Low negative correlation, i.e. as F ratio increased, FS SCORE decreased.**
$(R^4 - r^4)$	0.051	= Negligible correlation

The spread of the S ratio and F ratio were plotted for closer investigation in Chart 2.12 and Chart 2.13 and show that S ratio ranges between 0.47 – 0.65 and F ratio ranges between 0.41 – 0.49 produced the highest FS SCORES.

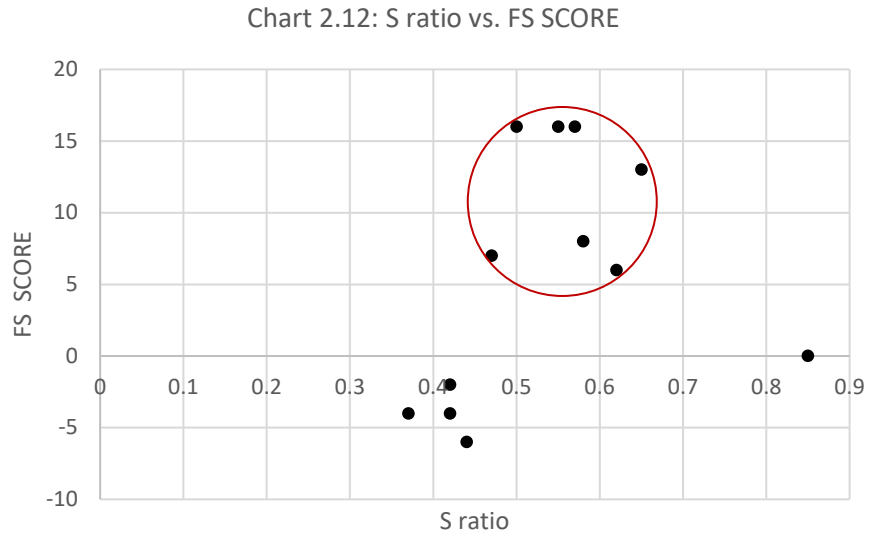

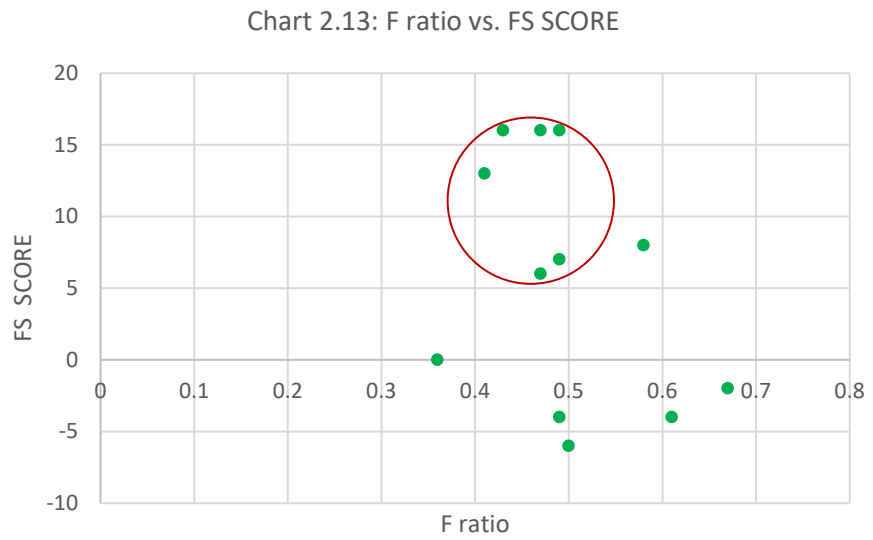

Charts 2.12 and 2.13: plotting S ratio (black markers) and F ratio (green markers) highlighting ratio ranges (red circles) in which FS SCORES are highest.

2.3.2. Cortical bone changes

2.3.2.1. Absolute change in cortical bone thickness

Table 2.5 and Table 2.6 show changes in cortical thickness, the period of time between the first and the last radiograph from each patient ranged from 4.98 - 11.01 years. Median (across all patients) cortical bone thickness change was positive in all zones in AP and four out of six in ML (zones B and C were negative). Cortical thickness change as an average across the zones was positive in 11 patients (patient

12 was negative) in AP and in seven patients in ML (patients 03, 08, 09, 11 and 12 were negative). Of the patients who experienced an average negative thickness change across all zones there was no clear pattern attributing this to a specific zone. Patient 05 (image span = 9.22 years) achieved the largest median positive thickness change across all zones in AP and ML. The largest median positive thickness change was observed in zone A in AP (distal lateral) and zone F in ML (posterior distal). There was almost double the sum of all cortical thickness change in all zones in all patients in AP compared with ML (57.6 mm compared with 33.7 mm).

Table 2.5: AP Change in cortical thickness (mm) between first and last radiographs

Patient	AP Zone						Median	CI
	A	**B**	**C**	**D**	**E**	**F**		
01	0.68	0.27	-0.27	0.00	0.14	0.27	0.21	0.25
02	0.82	0.41	-0.14	0.14	0.00	0.95	0.28	0.36
03	0.82	0.00	0.41	0.27	0.27	0.41	0.34	0.22
04	0.40	0.66	0.93	0.00	0.13	0.00	0.27	0.31
05	4.77	4.09	2.05	5.73	7.64	5.05	4.91	1.48
06	-0.56	0.28	0.00	0.56	0.42	-0.14	0.14	0.33
07	2.23	0.00	2.51	1.25	0.55	0.00	0.9	0.88
08	1.53	1.53	0.28	-0.42	1.26	1.81	1.4	0.7
09	3.02	1.37	0.69	0.96	1.92	1.24	1.31	0.67
10	0.14	0.71	0.99	0.14	0.43	0.43	0.43	0.27
11	0.53	-0.53	0.00	0.00	0.00	0.13	0	0.27
12	-1.52	-0.89	-0.25	-0.38	-1.01	-0.51	-0.7	0.38
Median	0.75	0.35	0.35	0.14	0.35	0.34	Total change = 57.6 mm	
CI	0.94	0.73	0.51	0.94	1.25	0.84		

Table 2.6: ML change in cortical thickness (mm) between first and last radiographs								
Patient	ML Zone						Median	CI
	A	**B**	**C**	**D**	**E**	**F**		
01	-0.55	-0.95	-0.41	1.91	2.18	2.86	0.75	1.33
02	0.00	0.29	-0.29	2.59	2.45	4.18	1.37	1.44
03	-0.71	-0.43	-0.57	0.28	0.85	1.13	-0.08	0.62
04	0.14	0.95	0.95	0.00	0.00	0.00	0.07	0.38
05	4.46	3.91	2.51	0.56	2.37	2.79	2.65	1.09
06	0.28	0.70	0.28	-0.70	0.00	0.00	0.14	0.37
07	0.15	0.00	0.15	0.00	0.88	0.59	0.15	0.29
08	1.15	0.29	-0.29	-0.29	-0.58	-0.72	-0.29	0.55
09	0.47	-0.47	-2.48	-1.09	0.00	2.02	-0.24	1.21
10	0.00	-0.14	0.55	0.14	0.82	0.41	0.28	0.29
11	0.27	-0.27	0.00	-0.55	0.00	-0.41	-0.14	0.24
12	0.47	-0.95	-3.95	1.42	-1.11	0.63	-0.24	1.53
Median	0.21	-0.07	-0.15	0.07	0.41	0.61	Total change = 33.7 mm	
CI	0.75	0.73	0.92	0.62	0.66	0.86		

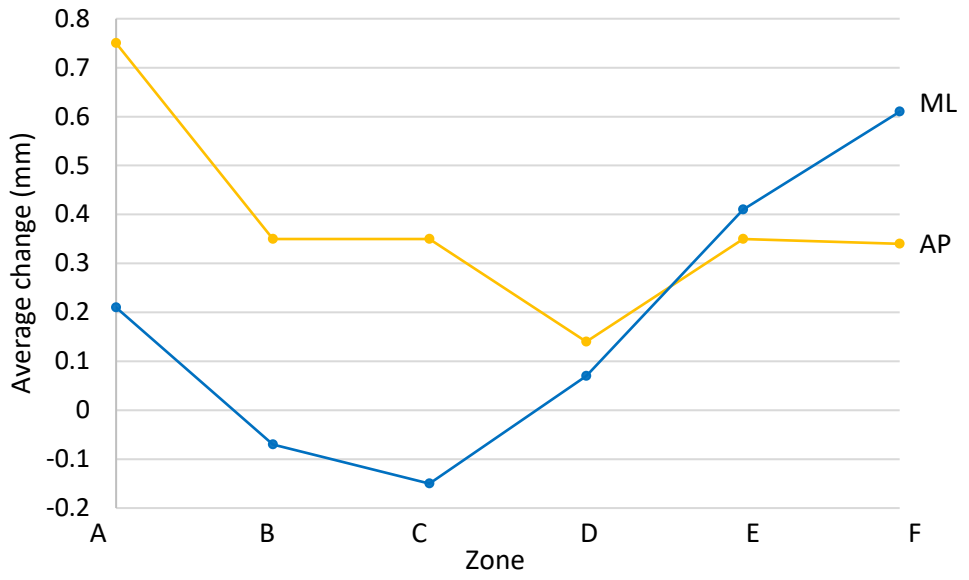

Chart 2.14: Median cortical bone thickness changes in all zones AP (orange) and ML (blue) over 4.98 - 11.01 years.

Chart 2.14 plots the median (across all patients) cortical thickness change from the first to the last radiograph available in all zones. Both aspects show the least change at the proximal end of the implant, increasing distally. In AP, the least median thickness change was observed in zone D (medial proximal),

in ML it is zone C (anterior proximal). The greatest bone thickness changes are observed laterally (zone A) and posteriorly (zone F).

2.3.2.2. Cortical bone growth rate

Cortical thickness *change* measurements were normalised over time to produce growth *rate* data (Table 2.7 and Table 2.8). Average growth rate increased each month (was positive) in all zones in AP and four out of six in ML (zones B and C were negative). Cortical growth rate as an average across the zones was positive in 11 patients each month in AP (patient 12 was negative) and in seven patients each month in ML (patients 03, 07, 09, 11, and 12 were negative). Of the patients who experienced an average negative monthly growth rate across all zones there is no clear pattern attributing this to a specific zone. Patient 05 (image span = 9.22 years) achieved the fastest average growth rate across all zones in AP and ML. The fastest average growth rate was observed in zone A in AP (distal lateral) and zone F in ML (posterior distal). There is almost double the rate of average growth across all zones in AP compared with ML (0.6 mm / month comapred to 0.33 mm. These results closely mirror the bone thickness changes (Table 2.5 and Table 2.6).

Table 2.7: AP rate of cortical growth (mm/month) x 100

Patient	AP Zone						Median	CI
	A	**B**	**C**	**D**	**E**	**F**		
1	1.98	0.79	-0.79	0.00	0.40	0.79	0.59	0.74
2	0.85	0.43	-0.14	0.14	0.00	0.99	0.28	0.37
3	1.00	0.00	0.50	0.33	0.33	0.50	0.42	0.26
4	1.04	1.74	2.44	0.00	0.35	0.00	0.7	0.8
5	5.52	4.73	2.37	6.62	8.83	5.83	5.68	1.71
6	-2.51	1.25	0.00	2.51	1.88	-0.63	0.63	1.48
7	4.04	4.04	0.73	-1.10	3.30	4.77	3.67	1.84
8	4.12	0.00	4.63	2.31	1.03	0.00	1.67	1.62
9	3.05	1.39	0.69	0.97	1.94	1.25	1.32	0.68
10	0.15	0.74	1.03	0.15	0.44	0.44	0.44	0.28
11	1.47	-1.47	0.00	0.00	0.00	0.37	0.00	0.75
12	-4.11	-2.4	-0.69	-1.03	-2.74	-1.37	-1.88	1.03
Median	1.26	0.76	0.60	0.14	0.42	0.47	Average rate = 0.60 x 100 mm/month	
CI	1.55	1.13	0.88	1.19	1.57	1.19		

Table 2.8: ML rate of cortical growth (mm/month) x 100								
	ML Zone							
Patient	**A**	**B**	**C**	**D**	**E**	**F**	Median	CI
1	-1.17	-2.05	-0.88	4.11	4.69	6.16	1.61	2.85
2	0.00	0.30	-0.30	2.74	2.58	4.41	1.44	1.52
3	-0.88	-0.53	-0.71	0.35	1.06	1.41	-0.09	0.78
4	0.37	2.56	2.56	0.00	0.00	0.00	0.18	1.03
5	5.24	4.58	2.95	0.65	2.78	3.27	3.11	1.28
6	1.14	2.85	1.14	-2.85	0.00	0.00	0.57	1.52
7	3.11	0.78	-0.78	-0.78	-1.56	-1.95	-0.78	1.5
8	0.38	0.00	0.38	0.00	2.27	1.51	0.38	0.74
9	0.47	-0.47	-2.51	-1.10	0.00	2.04	-0.23	1.22
10	0.00	-0.15	0.58	0.15	0.88	0.44	0.29	0.31
11	1.07	-1.07	0.00	-2.13	0.00	-1.60	-0.53	0.95
12	1.28	-2.56	-10.67	3.84	-2.99	1.71	-0.64	4.14
Median	0.42	-0.07	-0.15	0.07	0.44	1.46	Average rate = 0.33 x 100 mm/month	
CI	0.99	1.17	1.97	1.23	1.17	1.33		

Chart 2.15 plots average cortical growth rates in each zone: there is a decrease in growth rate proximally in both planes with the slowest rate in zone D (medial proximal) in AP and in zone C (anterior proximal) in ML. The fastest growth rate is observed laterally and posteriorly. These results are similar to the growth change observations (Chart 2.14).

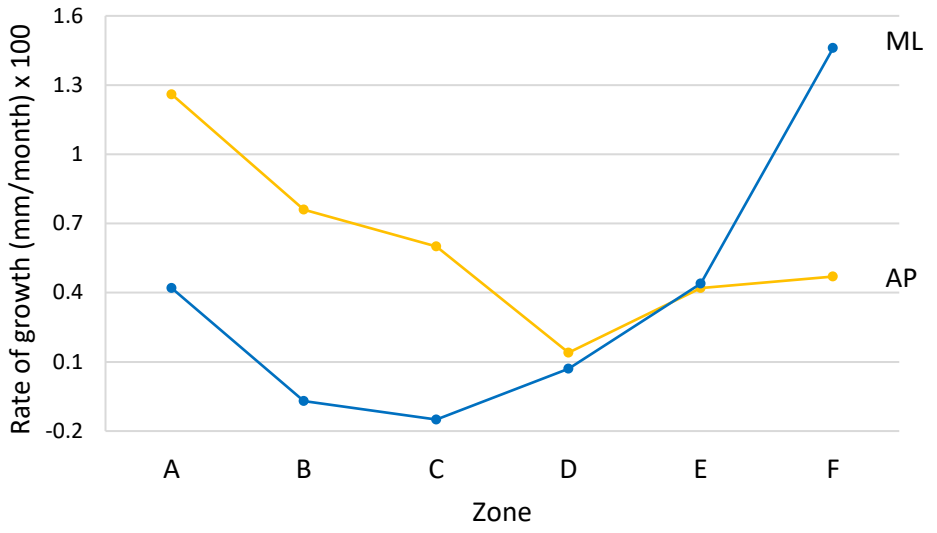

Chart 2.15: Median cortical growth rate in all zones
AP (orange) and ML (blue) over 4.98 - 11.01 years

2.3.2.3. AFcollar changes

Table 2.9 shows results of AFcollar measurements; similar to the overall bone thickness growth change and rate, the average growth rate in AP was twice that observed in ML (1.34 compared with 0.73 mm^2/month). Nine of the patients displayed a positive flare (+F) AP growth pattern (patient 05, 07, 11 did not) compared with six (patients 01, 02, 04, 05, 07, 10 did not) in ML. One patient (patient 07) grew an abnormal (A) AFcollar shape in AP whereas four were observed in ML (patients 01, 02, 04, 10). A negative flare (-F) AF growth shape was the least frequently observed growth pattern with one case in AP (patient 05) and two in ML (patients 05 and 07). Patients 09 and 10 showed the fastest rate of AFcollar growth in AP and ML respectively. Every patient's AFcollar area growth rate was positive in AP and ML indicating a net increase in distally situated cortical bone.

Table 2.9: AFcollar shape and area growth rate (mm^2/month) in AP and ML.
A = Abnormal growth shape. O = No growth shape change. - F = Flare narrow distally.
+F = Flare wide distally.

Patient	**Growth shape**		**Area growth rate (mm^2/month)**		FS SCORE
	AP	ML	AP	ML	
01	+F	A	1.27	0.92	8
02	+F	A	0.51	2.27	16
03	+F	+F	0.17	0.18	-4
04	+F	A	0.73	2.87	0
05	-F	-F	0.84	0.26	-4
06	+F	+F	2.07	1.62	16
07	A	-F	1.46	0.20	-6
08	+F	+F	3.01	0.53	-2
09	+F	+F	1.43	0.99	16
10	+F	A	0.46	0.30	7
11	O	+F	1.41	1.75	6
12	+F	+F	1.49	0.42	13
Median	-	-	1.34	0.73	
CI	-	-	0.44	0.51	

Plotting growth shapes against cortical growth rate and FS SCORE produced the following box and whiskers distributions:

Chart 2.16: *AP* collar shape vs. growth rate

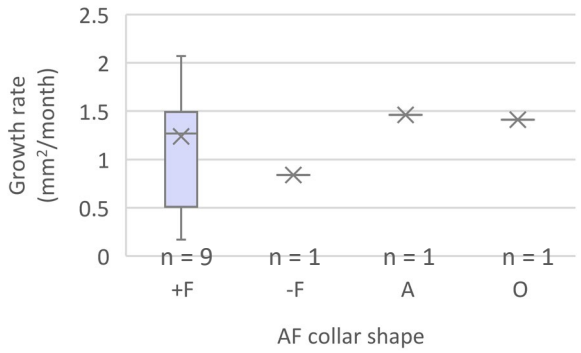

Median growth rate for +F, -F, A and O AFcollar shapes were 1.27, 0.84, 1.46 and 1.41 mm^2/month respectively although only the +F shape was present in >1 patients in this aspect (AP).

Chart 2.17: ML collar shape vs. growth rate

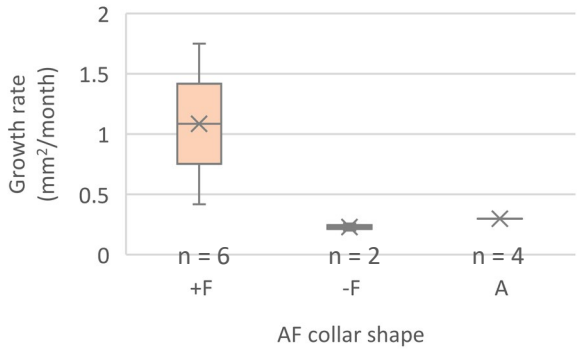

Median growth rate for +F, -F, A AFcollar shapes were 1.60, 0.76 and 0.23 mm^2/month respectively, the A shaped AFcollar displayed the largest interquartile range.

Chart 2.18: *AP* collar shape vs. FS SCORE

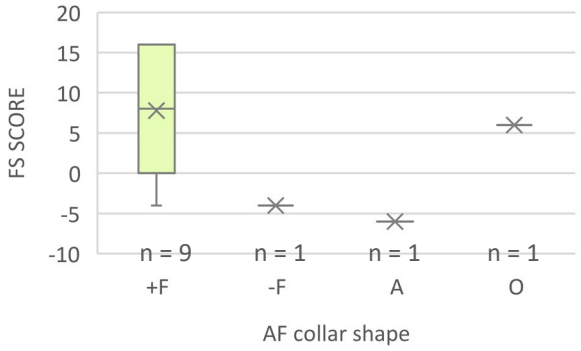

Median FS SCORES for +F, -F, A and O AFcollar shapes were 8.0, -4.0, -6.0, 6.0 respectively although only the +F shape was present in >1 patients in this aspect (AP).

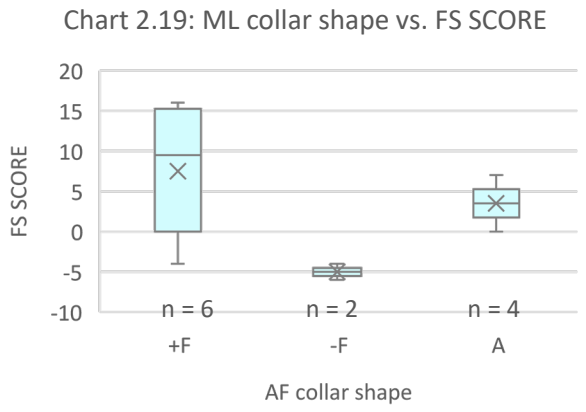

Median FS SCORES for +F, -F, A AFcollar shapes were 7.5, 9.5, -5.0 respectively, the +F shaped AFcollar displayed the largest interquartile range.

2.3.3. Non bone changes

SIW (2017) report segregated results into primary and secondary outcomes which will be summarised in the following section. Note that the data presented in this section pertains to the entire study (20 ITAP patients across two sites).

2.3.3.1. Primary outcome measures

2.3.3.1.i. Skin reaction assessments:

Results were based on six outcome measures (see Table 2.10)

Table 2.10: ITAP patients skin reaction assessment success results after 12 and 18 months

	Skin Colour	Skin Temperature	Exudate	Pain (at stump)	Swelling	Skin Adhesion (to ITAP)
No. of patients with success* score at 12 months	20	20	17	17	20	16
No. of patients with success score at 18 months	20	20	17	17	20	17

* Overall success was designated as 50% of patients achieving the defined measures in the skin assessment: Skin colour (graded 1 - 5 where 1 = normal, 5 = black), success defined as score of 2 or less. Skin temperature (graded 1 - 2 where 1 = normal, 2 = hot), success defined as score of 1. Presence/type of exudates (graded 1 - 6 where 1 = no exudate, 6 = purulent), success defined as score of 2 or less). Pain at end of stump (graded 1 - 10 where 1 = no pain, 10 = the worst pain imaginable), success defined as score of 2 or less. Swelling (graded 1 - 10 where 1 = no swelling, 10 = severe swelling), success defined as score of 3 or less. Skin adhesion to implant at surface layer (graded 1 - 10 where 1 = well adhered, 10 = no adhesion), success defined as score of 4 or less.

2.3.3.2. Secondary outcome measures

2.3.3.2.i. Microbiological assessment of the stump by standard microbiological screen:

Of the nine patients in the first cohort (one lost in follow up), three patients had their ITAP implant explanted in comparison to none of the patients in the second cohort. 15 patients (75 %) were affected by bacteria (see Table 2.11), the most common being Staphylococcus aureus.

Table 2.11: Microbiological assessment of residuum showing days since surgery for first infection to be present

	First infection presented	
Days since surgery	Cohort 1	Cohort 2
Surgery Day	0	0
Day 1 - 45	6	2
Day 46 - 90	1	2
Day 91 - 180	1	2
Day 181 - 360	1	0
Total	9	6

2.3.3.2.ii. General quality of life through the SF-36 questionnaire:

The SF-36 includes one multi-item scale that assesses eight health concepts that lead to two summary scores: The Physical Component Summary (PCS) and Mental Component Summary (MCS) scores, results of which are shown in Table 2.12

Table 2.12: SF-36 questionnaire results at intervals post-surgery

	Pre -Op	6 months post-surgery		12 months post-surgery		18 months post-surgery	
	Baseline Observed	Observed	Change from Baseline	Observed	Change from Baseline	Observed	Change from Baseline
PCS	34.88	39.69	4.81	41.50	6.62	42.05	7.17
MCS	59.04	55.40	-3.64	56.28	-2.76	56.70	-2.34

2.3.3.2.iii. Limb specific quality of life through the Q-TFA:

The Q-TFA consists of 70 questions of which 54 questions comprise four separate scores (Table 2.13):

1. Q-TFA prosthetic use score (a score of 100 indicates prosthesis normally worn every day for more than 15 hours)
2. Mobility overall score (= walking aid score + capability score + walking habits score)

3. Q-TFA problem score (a lower figure = fewer problems. Problems usually related to skin adhesion and infections)
4. Q-TFA global score

Table 2.13: Q-TFA questionnaire results at intervals post-surgery					
	Pre - Op	12 months post-surgery		18 months post-surgery	
	Baseline Observed	Observed	Change from Baseline	Observed	Change from Baseline
Prosthetic use	71	91	20	95	24
Walking aid score	89	89	0	95	6
Capability score	65	86	21	84	19
Walking habits score	41	62	21	75	34
Mobility overall score	65	79	12	85	20
Q-TFA problem score	34	9	-25	8	-26
Q-TFA global score	46	84	38	89	43

Statistical significance was tested with a student T test ($\alpha = 0.05$) and all apart from the walking aid scores and the 12 month post-operative mobility score were significant ($p < 0.05$)

2.3.3.2.iv. Limb specific measure of mobility through the SIGAM mobility grades:

The SIGAM scale is a fully validated scale of 'disability mobility grades' based on 21 questions. Patients grade themselves A - F (non-limb user, therapeutic prosthetic use only, limited/restricted, impaired, independent and normal). Results are presented in Table 2.14 and Chart 2.20.

Table 2.14: SIGAM mobility grading results at intervals post-surgery			
Disability/mobility Grade	Baseline (Pre -Op)	12 months post-surgery	18 months post-surgery
Non-limb user	1	0	0
Therapeutic prosthetic use	0	0	1
Limited/restricted	5	1	0
Impaired	5	6	8
Independent	3	3	3
Normal	6	9	8
Total	20	19	20

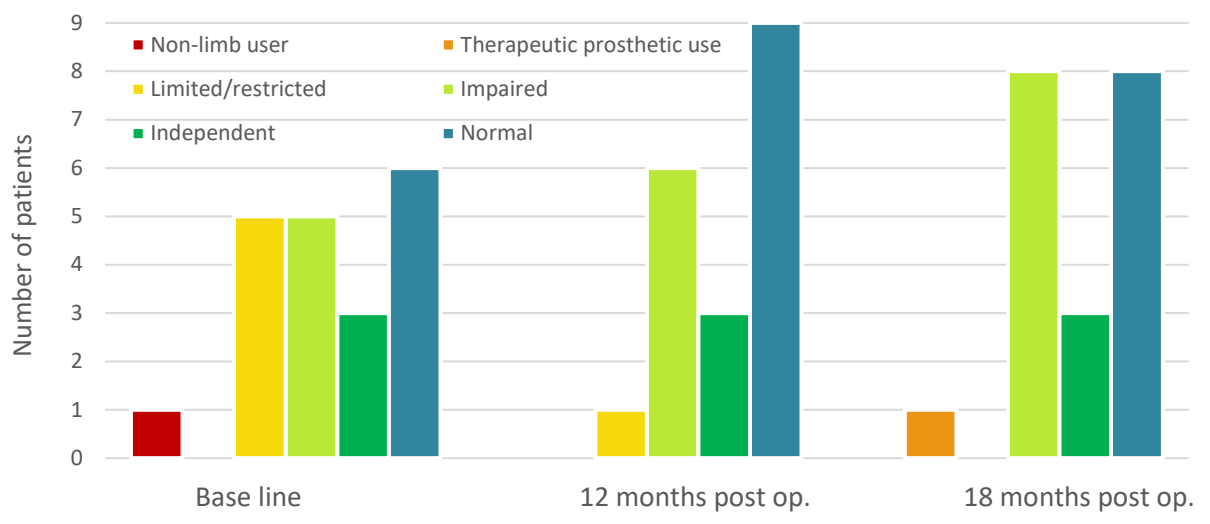

Chart 2.20: Changes in SIGAM mobility grading up to 18 months post operatively

2.4. Discussion:

Data collected from the ITAP clinical trial forms the retrospective longitudinal study for this thesis, hence is constrained by the variables available in the extant data set. The clinical trial was a single group assignment interventional model where a comparison pre and post-surgery was intended. This chapter asks the question ''which SAAP design parameters are successful'' however the clinical trial outcome measures did not consider implant design parameters. Moreover, there was no adequate control condition/group to test SAAP design parameters against and a risk of a false positive (type I error) through an exploratory analysis. In addition the sample size was relatively small for a robust statistical analysis and could be more susceptible to missing an effect that exists in the data (Type II error). Finally, retrospectively selecting features of the data to characterise dependent variables, could have distorted a resulting statistical test (double dipping). In conclusion, inter patient comparisons would have been statistically insignificant, therefore this discussion focuses on patterns as a result of implant design differences between the patients.

2.4.1. Explanation

FS SCOREs across all patients ranged between -6 to +16, suggesting that no patient obtained the worst feasible scores (on a scale -16 to 16). The patients who had their implants removed, due to a combination of infection and pain (patients 03, 05, 07), obtained the lowest FS SCOREs of -4, -4, -6. Patient 12 obtained a FS SCORE of 13, however the implant removal was uniquely a result of implant fracture. FS SCORE, therefore, is a reasonable indication of fixation success with respect to infection and pain explants. All explant patients were from cohort I with a mean implantation length of eight years.

Furthermore, all explant patients were outpatients at the RNOH, Stanmore site rather than the ROH, Birmingham; this may be due to the difference in patient numbers (RNOH n = 13 vs. ROH n = 7). It may be prudent to monitor patient 08 who is the only remaining patient with a negative FS SCORE for changes in infection/implant stability. The entire study group should be further monitored over a longer period to investigate how implant removal is correlated to the time implanted and whether any adverse fixations manifest in cohort II. In a 15 year OPRA implant follow up study by Hagberg et al. (2020) a diminishing implant survival rate from 89 % to 72 % between seven and 15 years respectively was reported.

2.4.1.1. Stem curve

As well as time implanted, the explant patients had other common features; they all received parallel stemmed, pressfit implants of which two were curved (including the one with the - 6 FS SCORE) and a below average S ratio and (R^4 - r^4) value. Since implants were pressfit they were also HA coated and had cutting fins on their distal part. A curved stem obtained a low median FS SCORE (-3) possibly due to the way it affects stress transfer compared with a straight stems. Straight stems in this study obtained a higher median FS SCORE (16) and a slightly curved stem obtained a median FS SCORE of 6. It seems the degree of curvature had a detrimental effect on FS SCORE. When curved stems have been compared with equivalent straight stems in THR variable results are reported; Callaghan et al. (1992) show no significant difference in interface micromotion under normal loads but a reduction in curved stem compared with straight stem micromotion under a large torsional load. Cristofolini et al. (2003) report that a curved cemented hip stem damages the cement surface to the point of debonding unlike a straight stem comparison and that there is more micromotion in the curved stem compared with the straight stem. Conversely, in favour of the curve stem, Meyer et al. (2019) report less periprosthetic bone loss in curved stems compared with straight stems although there is a question over the validity of their conclusion since the stems they compared were of different lengths and area moment inertias.

2.4.1.2. HA coating and cutting fins

The effect of distally coating the ITAP stems in HA was impossible to infer since there were no pressfit stems without the coating; theoretically this offers a rigid bond (osseointegration) between the bone and the implant distally while facilitating more proximal slip (not integrated) under femoral flexure. In THR, however when a direct comparison is made between identical stems with and without an HA coating there is no reported clinical advantage (Kim et al., 2003, Camazzola et al., 2009). The cutting fins (anti rotation fins) may have played a role although once more, without an equivalent comparison between patients with and without this stem feature, it is not conclusive. Patient 03 and 07 from the

explant cohort did display radiolucent lines around the cutting fins on radiographs which may have contributed to infection and/or pain but further investigation into this feature is needed.

2.4.2. Stem taper and fixation

Patient 02 uniquely received a tapered *and* pressfit stem, all other pressfit stems were parallel. The patient went on to obtain the highest FS SCORE (+16). There was a notable difference in patient 02 (R^4 - r^4) value; it was the lowest (thinnest cortex) in the study by ~ 50 %. In the remaining tapered verses parallel patients, the message was still clearly in favour of the tapered stem with respect to a higher FS SCORE.

2.4.3. Bone and implant length ratios (S ratio and F ratio)

The correlation between S ratio or F ratio with FS SCORE was apparent but low (0.321 and - 0.386 respectively). These were slightly unexpected since bending induced by any lateral external forces are a product of that force and the length of the lever. It would be reasonable to hypotheses that the greater the F ratio, the higher the bending force and thus the greater the bone apposition. Furthermore, a longer residuum tends to more 'normal' physiological patterns such as walking faster (Bell et al., 2014). The hypothesis with S ratio was that as the amount of metal in the IM decreased (through shortening and/or narrowing) the bone apposition would increase due to bone loading being greater for a greater proportion of the residuum. However, the pattern observed to achieve above zero FS SCORES determined by S and F ratios was one of a preferential ratio range; for S ratio this was between 0.47 – 0.65 and for F ratio this was between 0.41 – 0.49. One explanation for the difference in expected S ratio outcome and observed outcome is that FS SCORE is made up of a CIG rather than diaphyseal cortical thickness changes and CIG may not be affected by this. More generally it appears that if the stem occupies *at least* 47 % of the residuum length a good FS SCORE is more likely. Once more, caution in interpretation must be exercised, since S ratio alone was not the only variable that changed between patients. All patients within the 'ideal' S ratio range (01, 02, 06, 10, 11, 12) also received a tapered stem which meant they were also cemented (except for patient 02) whilst simultaneously devoid of a measurand linked to parallel stems such as an HA coating or cutting fins. Moreover, cementing lacks an interference fit/osseointegration and can be modeled by a taper slip (Mirza et al., 2010b), which may have influenced the FS SCORE. Conversely, the best F ratio scores are achieved when a residuum *below* 49 % of the original leg length remains. Long residuum's as seen in patients 05, 07 and 08 may have a curved stem (expect patient 05) because they are fixed into the curvature of the mid diaphysis, but otherwise appear not to share common features with one another.

2.4.4. Implant fit and pedestal growth

The hypothesis was that the more aligned the implant stem in the IM and the better seated the osteotomy face was on the implant collar, the closer to normal physiological function and so a more successful fixation (Cherian et al., 2014, Myers et al., 2018). The results were somewhat surprising, since both types of non-alignment (N_g and N_{ax}) produced a higher medial FS SCORE than a correctly aligned one. In patient radiographic detail notes (Appendix , A.2.2), N_{ax} patients often developed cortical thickening in the region of the stem tip since the cortex was thin. In patient 12 the N_{ax} may have also been associated with the pedestal formation. Pedestal formation in the ITAP patients reflected reported data in the literature; for example, patient 07 grew a full pedestal *with* radiolucency and was explanted after five years. Whereas pedestals in ITAP patients 02 and 09 *without* radiolucency achieved the highest FS SCORES in agreement with findings by Engh et al. (1990). Osteotomy face OH and UC did not directly influence FS SCORE, a slight pattern of increased prevalence of OH leading to a decrease in FS SCORE unless absent is noteworthy but the observation is obscured when merged with UC as a combined variable describing non-flush osteotomy/collar union at time = 0.

2.4.5. Bone changes

2.4.5.1. Radial bone thickness change and rate of change

Change in cortical bone thickness and rate display similar patterns with almost all zones increasing compared with baseline measurements (Table 2.5, Table 2.6, Table 2.7 and Table 2.8). Patient 05 experienced the most and fastest changes in both planes by approximately double the next nearest amount or speed achieved. However, the growth was due to a chronic infection with Methicillin Sensitive Staphylococcus Aureus (MSSA) and femoral osteomyelitis seven years after implantation with ‘periostitis, fluffy endosteal bone resorption and IM radiolucency’ reported by clinicians in year eight (patient radiographic detail notes A.2.2). Therefore, the patient obtained a low FS SCORE (- 4) and was explanted after eight years, illustrating the value of combining a FS SCORE with radiographic and bone changes. Patient 07 displayed the next fastest growth rate in AP, similarly this implant was removed due to infection and perhaps the bone thickness measurements were also affected in a way that did not indicate bone apposition due to strain adaptive remodelling. Patients 08 and 09 obtained the next fastest cortical growth rates although had no common implant geometries (Table 2.4) and obtained wildly different FS SCORES (- 2 and 16 respectively) but did both receive a right leg amputation and a tapered, cemented stem. The slowest growth rate in AP was observed in patient 12 who concurrently obtained a high FS SCORE, suggesting that cortical thickness change should not be the sole outcome measurand.

The median left side amputee FS SCORE was 7.5 compared with - 3 for right hand side despite there being equal numbers of right and left side amputees in the ITAP study. In the knowledge that most patients will be right side dominant, it may be that right side amputees rely on their implanted leg more than they would have if they had had their left leg amputated. This may be a consideration in a rehabilitation protocol for patients whose laterality is the same as the side that was amputated, unfortunately this cannot be confirmed in the ITAP trial as laterality was not recorded.

Bone growth change and rate along the medial and lateral sides in AP decreases moving proximally (Chart 2.14 and Chart 2.15 respectively). Bending moments come about from the femoral neck offset, muscular attachments, the bone curvature and the loading regime. It is higher in AP due to the femoral neck offset component of the resultant bending, consequently, cortical thickening is likely to be higher in AP than ML and results were in line with expectations (the hypothesis was that regions of higher bone stress will result in cortical thickening).

Medial compressive bending stress (and so cortical change) was expected to be greater than the lateral tensile bending stress. This is due to the lateral negative moment summed with external bending forces being less than the positive medial bending moment summed with the external bending forces. Across patients, zone A in AP produced the fastest rate of growth; this is a lateral zone and so somewhat unexpected. An explanation could be that remaining musculature produces an abnormal bone strain pattern and/or that there is more than just strain adaptive bone remodelling controlling cortical growth rate. Reparative remodelling through the accumulation of damage, overload and the process of surgery plus the change in patient biomechanics and mobility will all influence bone changes.

In ML the pattern of a decreasing growth change and rate moving proximally is similarly observed (Chart 2.14 and Chart 2.15 respectively) which would be expected under bending forces. The magnitude of cortical change rate is lower in ML compared with the AP which may be due to the reduction in lever arm length; growth and rate in the zones B and C are in fact negative (bone is resorbed). The only anterior zone (A, B or C in ML) which produced growth was the most distal one (A), however all posterior zones (D, E and F in ML) produced positive bone growth and rates.

2.4.5.2. AFcollar

Chart 2.16 and Chart 2.17 show that the fastest growth rates in AFcollars were observed in an A and +F shape in AP and ML respectively. Chart 2.18 and Chart 2.19 show that the highest FS SCORES were observed in patients with a +F growth shape in both aspects. There is not enough data to draw conclusions since some of the shape groups only had one patient in each aspect, however the pattern in

the observed results points towards favourable growth rate and FS SCORE with a +F AFcollar shape. The sectional area of a beam is directly related the amount of load it can support and, it appears from cortical thickness changes, that stresses are highest distally. Therefore, the greater the sectional area moving distally, will offer improved chances of implant success without breaching the bone material yield point. Although A shape AFcollar is associated to a fast growth rate the likelihood is that this is the result of reactive bone growth as this was obtained from patient 07.

2.4.6. Non-bone changes

The skin reaction assessment demonstrated exudate, skin adhesion and pain at stump in three out of 20 patients at 18 months post-surgery. The reason for stump pain was unspecified by SIW (2017); usually amputates experience stump pain as a result of either infection, neuroma, or heterotopic ossification (Neil, 2015). Heterotopic ossification was observed in 63 % of patients after traumatic amputation by Potter et al. (2010). In THR thigh pain at the level that is equal to the stem tip is common due to the high bone stress experienced in this region (Chung and Chung, 2020, Chen et al., 2021). In patient notes (not in the SIW (2017) report) sciatic nerve neuroma was observed in five of the 12 RNOH ITAP patients which is a known painful condition that feels similar to a 'pinched' nerve (Kitcat et al., 2009).

Exudate is linked to wound healing; ongoing production may indicate an inflammatory state (Weller, 2009) which is intrinsically linked to the skin adhesion state (a primary outcome measure of the ITAP clinical trial) and the microbiological assessment (a secondary outcome measure). Infection amongst the ITAP patients was an ongoing concern but despite this, the ITAP final (SIW, 2017) report concluded '…the ITAP device is a feasible method of attaching a prosthetic leg to a transfemoral amputee's residual limb and offers improved patient outcomes from conventional amputee sockets'. Furthermore, the post-surgery patient interviews offered the collective opinion that the gain in comfort, improved activity, improved emotional/social well-being was worth the risk. The SF-36 questionnaire showed an increase in the PCS and a decrease in the MCS scores at each interval post-surgery. The report offered the explanation for a decrease in MCS score to be due to 'missing mental health scores' and suggested that a comparison study for the OPRA patients also did not observe an increase in MCS score (Brånemark et al., 2014). By contrast the Q-TFA produced a statistically significant global score that almost doubled at 12 months post-surgery compared with the baseline score. The SIGAM mobility scale also showed vast improvement with a normal mobility score in eight out of 20 patients 18 months post operatively and none considered they were limited/restricted.

2.5. Conclusion

The developed FS SCORE showed reliability in the assessment of infected and painful explanted ITAPs and so achieved the first aim of this chapter. The cemented implants obtained better FS scores; it is unclear whether this was due to cementing or the absence of features related to pressfit fixation. However, reducing the volume of metal implant in the IM had a more profound effect on achieving a good FS SCORE than the method of fixation. The aim of investigating whether distal bone growth (in a +F shape) promoted good FS SCORE was achieved. Further work needs to be undertaken on why pressfit stems performed more poorly than cemented equivalents.

With respect to cortical growth, the second outcome measure reported in this study, cortical change (thickness and rate) had less impact on overall success than that which grows into the collar alone (CIG). However not all SAAPs are designed with a distal collar and so measuring CIG may not be a useful measurand for inter SAAP comparisons.

Data from ITAP patient 12 was used for the next Chapter (Three) of this thesis. The patient reported their ITAP surgery as a life changing experience. They suffered from depression post amputation and subsequent limb-socket pain was significant, resulting in narrowing of their social and general life experiences. Post ITAP the patient regained their independence and suffered negligible pain. Tragically since data was obtained from the patient they suffered an implant fracture.

CHAPTER 3

Acquisition of kinetics and kinematics from an ITAP patient

3.1. Introduction

To develop improved SAAP implants in the future, an understanding of ITAP patient biomechanics is needed. Accordingly, collection of kinetic and kinematic data from an ITAP patient is presented in this Chapter. At the time of writing, biomechanical data collected from TF SAAP patients is limited to the research outputs from one group using the OPRA (Frossard et al., 2003, Lee et al., 2007, Lee et al., 2008, Frossard et al., 2010b, Frossard et al., 2010a, Frossard et al., 2013, Vertriest et al., 2017, Frossard, 2019). The ITAP clinical was an interventional (single group assignment) clinical trial on 20 patients with the primary purpose of 'treatment' for transfemoral amputation that was conducted in two cohorts of patients in 2008 and 2013. The patients were followed up for primary and secondary outcome measurements for 18 months after implantation and thereafter for check-ups and radiographic data capture only. One of these patients was selected for biomechanical analysis in this chapter in a similar manner to the OPRA biomechanical analysis. Biomechanical analysis of the OPRA patients used a battery powered six axis load cell fixed between the patient's residual limb and prosthetic knee. This study will use a similar load cell to collect kinetic data (exact) and will simultaneously collect kinetic data (estimated) and kinematic data using an instrumented treadmill. By collecting kinetic and kinematic data from an ITAP patient I aim to achieve two outcomes:

1. To investigate gait kinetics and kinematics and compare these with OPRA patients, prosthetic socket users and non-amputated individuals.
2. To generate a set of representative forces (forces, moments and inertial forces) to be used as input in a FE model to evaluate SAAP design (Chapter Five).

The second outcome is important since the model that will be developed and validated in Chapters Four and Five are *based* on the design of an ITAP. The design differences compared to the OPRA implant are inclusion of a collar onto which the bone osteotomy sits and fixation via pressfit (line to line) or cement rather than the threaded OPRA fixture. Since force data is only available from patients using OPRA implants it is necessary to generate a *representative* set of force data to apply to the numerical model in this thesis.

3.1.1. The gait cycle

How 'well' we walk, is a useful tool to qualify general health and a gait analysis can identify deviations from normal patterns. Gait analysis is rarely used to make a medical diagnosis, but it is often used to quantitatively investigate a patient's mobility status. A gait cycle is made up of two parts; stance and swing. In stance some section of one foot is in contact with the ground (~ 60 % of the gait cycle). In

swing a limb is moving through the air and not in contact with the ground (~ 40 % of the gait cycle). The cycle is typically divided into eight phases (functional objectives); the first two are the weight acceptance phases (double legged stance), followed by two which are single legged support phases and the last four, which are the swing limb advancement phases (Fig. 3.1). Each phase has characteristic kinetics and kinematics such that any musculoskeletal dysfunction, i.e. lower limb amputation, could be identified. This is useful for a clinical team in order to develop a suitable rehabilitation program for that patient.

3.1.1.1. Functional phases of gait

Below is a summary of the eight functional phases of gait:

1. Initial contact – This phase transfers body weight to the outstretched leg which must absorb the impact of ground reaction. The knee is almost fully extended (5 ° flexion), restrained by the hamstrings and the hip has ~ 20 ° flexion, restrained by the gluteus maximus, hamstrings and adductor magnus. On impact the ankle plantar flexion is controlled eccentrically by the pretibial muscles. The shear force applied to the ground is anteriorly directed.
2. Loading response – In this phase forward progression is achieved by rocking through on the heel to forefoot under control of the pretibial muscles. The gastrocnemius and soleus deliver support at the ankle. Shock is absorbed by the knee which flexes to ~ 20 ° controlled by the quadriceps and medial hamstrings. The quadriceps produce an anterior tibial shear force. Hip orientation remains unchanged, controlled by gluteus maximum and adductor magnus. In this phase there is typically the first of two axial force peaks seen in a ground reaction force (GRF) trace.
3. Mid stance – At the start of single leg support the contralateral toe off necessitates forward progression of the body over a single stable limb. Knee flexion is 5 ° and the hip is extended to neutral under control of the posterior gluteus medius. Limb stability is dependent on eccentric actions of gastrocnemius and soleus as the ankle dorsi flexes.
4. Terminal stance – In this phase the body rolls over the forefoot and the heel rises as the hip hyperextends to 20 ° and the ankle dorsi flexes to 10 °. Gastrocnemius and soleus activity increase to counter the forward fall of the body and this phase ends as the contralateral limb contacts the floor.
5. Pre swing – There is a rocking motion through the toes putting the ankle into 15 ° flexion and a deep knee flexion (~ 40 °) in this phase as the limb starts to unload. The calf muscles recoil generating a burst of power fuelling limb push off, the second axial peak in a typical GRF trace, and there is a transfer of weight to the contralateral limb.

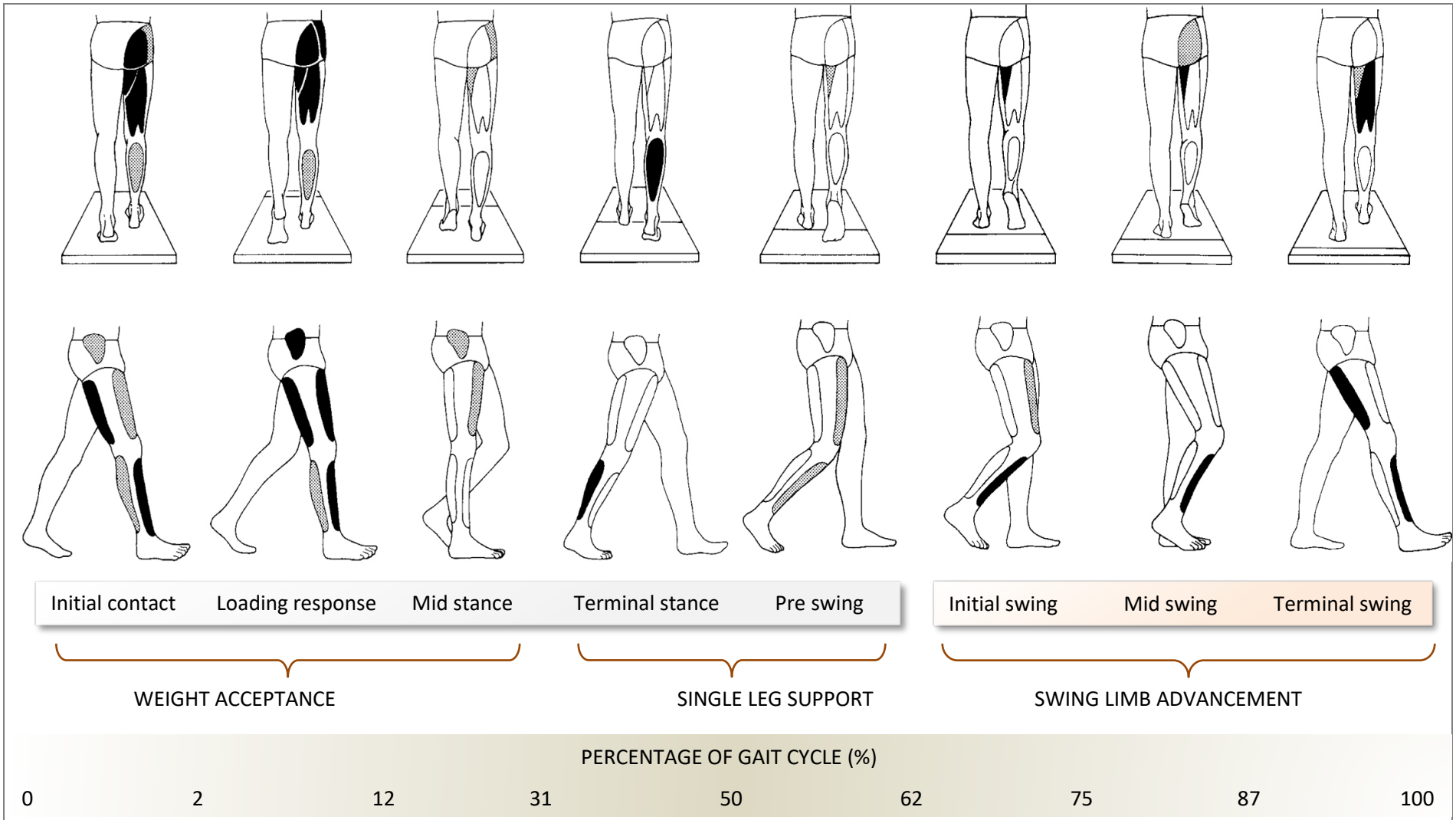

Fig. 3.1: Divisions of the gait cycle highlighting main muscle groups on one leg.
Grey tag = five stance phases, peach coloured tags = three swing phases. Adapted from Loudon et al. (2008)

6. Initial swing – Advancement of the unloaded limb starts in this phase where knee flexion increases to 60 ° to raise the foot and hip flexion increases to 15 ° to advance the thigh. The knee flexor is the biceps femoris short head and the iliacus and adductor longus are activated for the hip flexion. Pretibial muscles lift the foot and toes.
7. Mid swing – Limb advancement continues, tibialis anterior remains in control of the ankle with respect to floor clearance, hip is 25 ° flexed, knee is 25 ° flexed. Towards the end of this phase the hamstrings are recruited for the next phase.
8. Terminal swing – This phase activates the body for initial contact; the knee extends to neutral (0 ° to 5 °) and the hip retracts to 20 ° flexion. All hamstring muscles contract to restrain hip and the vastii are recruited to facilitate knee extension. There is some tibialis anterior contraction to maintain ankle dorsi flexion.

3.1.1.2. Ground reaction force

The above sequence of footfalls and associated loadbearing during the stance phase produces a typical GRF trace as measured by force plates (Chart 3.1). These are along the axial, ML and AP axes, it is the measure most commonly used in clinical diagnoses of gait pathology (Winiarski and Rutkowska-Kucharska, 2009, Chockalingam et al., 2016).

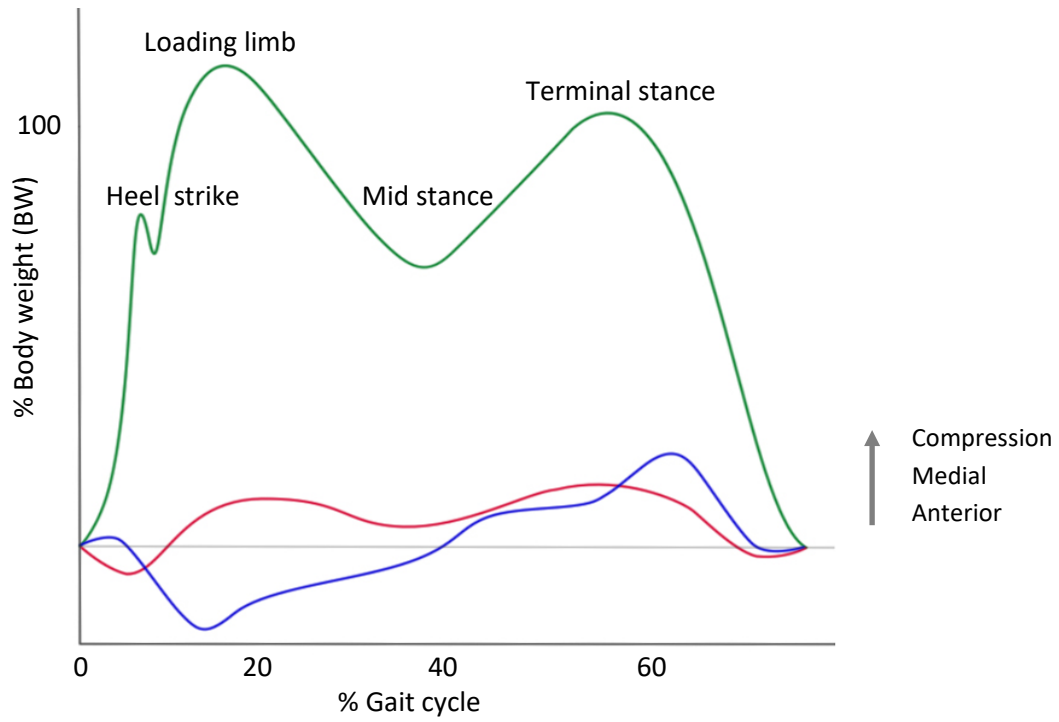

Chart 3.1: Typical GRF on flat ground in a non-amputated individual.
Positive traces show the **ground reaction** to the **applied force** as compression (green), medial (red) and anterior (blue).

3.1.1.3. Muscular control in gait

The anatomical knee joint provides stability during the stance phase of gait whereas in swing it flexes passively (Alexander et al., 2018). Prosthetic joints do not have biological muscles crossing them and so cannot be actively controlled (Morgenroth et al., 2018). This contributes to altered kinetic and kinematic patterns in TF amputees compared with non-amputees. Results in TF amputees using powered prosthetics may result in closer to non-amputated gait biomechanics, however this promising field of research is still in its infancy.

3.1.1.3.i. Non-amputated muscular control in gait

In a non-amputated individual, fourteen muscles control the knee in gait; in stance the extensors decelerate knee flexion, in swing flexors and extensors action limb progression. The five heads of the quadriceps and the upper gluteus maximus (through its iliotibial (IT) band insertion) effect knee extension and stability respectively. Three of the four hamstring muscles and the semitendinosus are primarily hip extensors. However, all hamstring muscles, in combination with the gastrocnemius and two of the hip flexors (gracilis and sartorius) are also responsible for knee flexion (Perry, 2010). The primary muscles controlling the hip are the extensors (biceps femoris long head, semimembranosus, semitendinosus, adductor magnus, lower gluteus maximus) and the abductors (gluteus medius, upper gluteus maximums and tensor fascia lata). In swing they are the flexors (adductor longus, adductor magnus, gracilis). Adductors are recruited between periods of swing and stance.

3.1.1.3.ii. TF amputation muscular control in gait

A TF amputation removes the knee joint and distal insertions of the quadriceps (knee extensors). The gluteus maximus remains but the distal insertion of the hamstrings and adductor magnus (which provides 70% of the adductor moment) are removed, thus diminishing hip extension capacity and leaving the hip abductors relatively unopposed. Gluteus medius and minimus remain but the tensor fascia lata (TFL) distal insertion is removed which weakens hip abduction power. Of the remaining musculature, the iliacus remains in use for flexion, the gluteus medius and minimus for abduction and the gluteus maximus becomes the primary hip extensor but is often overpowered by the residual flexors. Control of the prosthetic knee becomes the domain of the more proximal muscle of the pelvis and thigh. Amputation height may determine the degree of muscle transection but somewhat surprisingly the literature suggests that this makes limited difference to the muscle recruitment strategy of the TF amputee (Baum et al., 2008, Bell et al., 2014). In general, a TF amputee will rely on hip flexors (primarily iliacus) for limb advancement, some power return from more advanced prosthetic feet will augment this action. The swing begins with a fast and exaggerated hip flexion to lift the limb and after the foot advances the gluteus maximus contracts and stabilises the prosthetic knee; inertia of the

ankle/foot segment aids extension. Contact with the floor, anchors the foot and often the prosthetic knee remains extended throughout stance to avoid knee buckling and provide stability.

3.1.1.4. TF gait temporal-spatial deviations

In combination with an ill-fitting prosthesis in prosthetic socket wearing patients and/or fear of falling, some classic gait deviations are observed (S.N.Berger, 1990, Jaegers et al., 1995, Waters and Mulroy, 1999, Hof et al., 2007, Wentink et al., 2013, Mahon et al., 2017):

- Lateral trunk bending in weight acceptance towards the prosthetic leg
- Wide walking base
- Circumduction of the prosthetic leg in swing
- Vaulting using excessive plantar flexion on intact leg whilst prosthetic leg is in swing
- Standing longer on their intact leg compared with their prosthetic leg in the stance phase
- Exaggerated lumbar lordosis when prosthesis is in stance
- Higher gait energy expenditure
- Lower functional capacity

An optimal gait pattern is known to be more likely if muscle function can be retained (Gottschalk, 1999) Ward and Robinson, 2005). SAAP patients do not experience complications of prosthetic 'fit' due to direct skeletal attachment and they achieve a larger range of motion at the hip (Hagberg et al., 2005b) with temporal-spatial gait parameters more similar to healthy controls (Frossard et al., 2010b). It is hoped that biomechanical data collected from ITAP patients may also show similar changes in kinetic and temporal-spatial outcomes towards more healthy controls.

3.1.2. Collecting biomechanical data

Traditionally (forward) dynamics calculates motion from a set of initial conditions and a set of forces, however, biomechanists are usually interested in the forces and moments responsible for an observed motion. Motion is captured with systems that can record the movement of body segments and a process of (inverse) dynamics is used to produce the force and moment data.

3.1.2.1. Kinematics and kinetic data (using inverse dynamics)

Using inverse dynamics to estimate kinetics using the segmented model approach involves a few steps: First, motion of retroreflective markers attached to a patient is captured with cameras. Second, a segmented model of the patient is built. Third, kinematics are calculated by transforming the marker

movement to the relevant segment of the biomechanical model. Through a process of inverse dynamics, force and moment data can be calculated at the point of interest using the input from the segment's mass, moment of inertia, centre of gravity (COG) location, translational velocity, translational acceleration, angular velocity, angular acceleration and the external GRF data, see Fig. 3.2. By applying

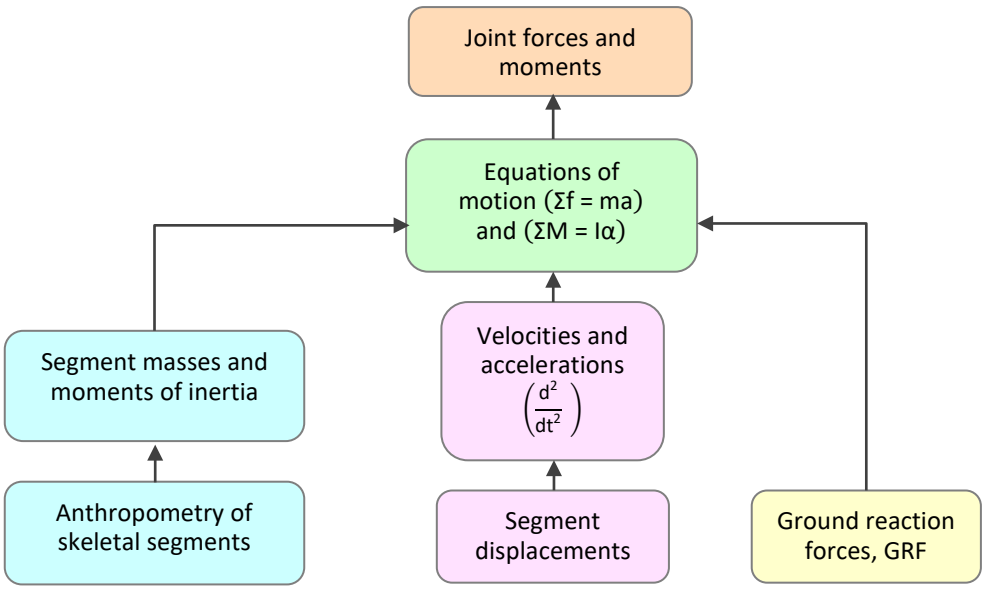

Fig. 3.2: How the segmented model approach uses inverse dynamics to estimate kinetics.

Newton's equations of motion, the known inputs in the foot segment can be used to resolve the unknowns moving proximally in the model until the segment of interest is reached. Today, commercial software are available that can relatively accurately estimate patient kinetics (Fig. 3.2) and will simultaneously collect segment kinematic data for clinical assessment (Robertson et al., 2013).

3.1.2.2. Kinetic data collection using force transducers

A force transducer (load cell) at the site of interest will report the forces that are acting upon it exactly. A force transducer transforms an electrical signal to an applied force (using inbuilt strain gauges).

3.1.2.3. Inertial forces

The *exact* kinetic data captured by the load cell only includes the inertial forces *below* the load cell at the end of the segment. In order to build accurate FE models, the inertial properties of the residuum (segment) must be applied to the COG as well as the forces and moments obtained by the load cell

(Chart 3.2). To achieve this the load cell data must be matched to the kinematic data (where the inertial forces are recorded).

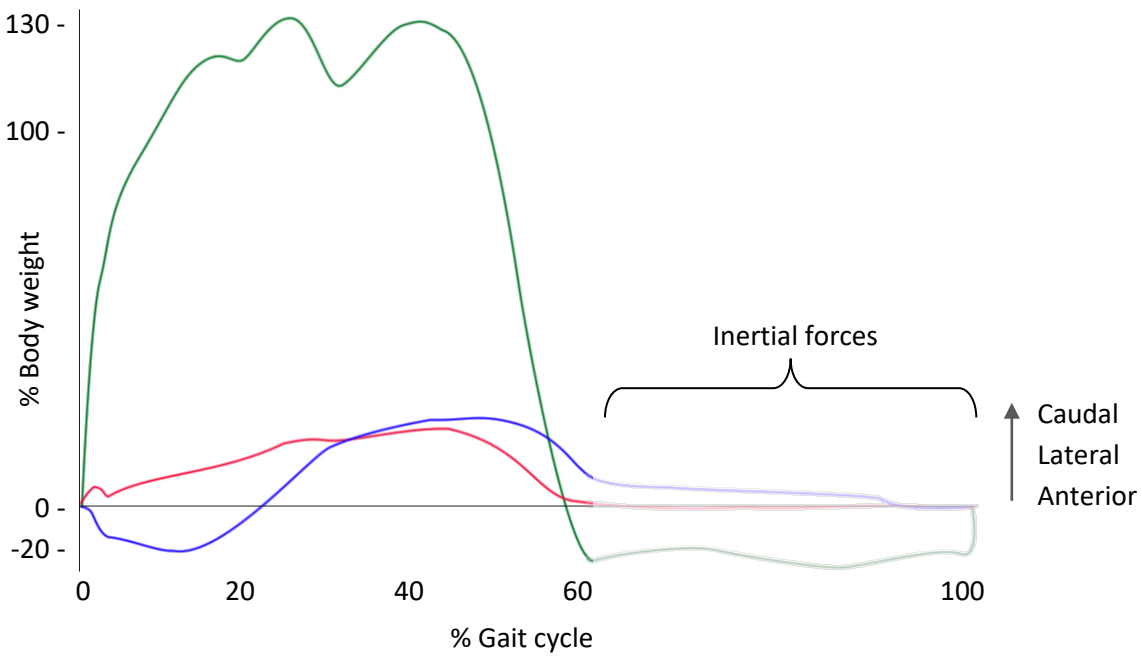

Chart 3.2 = OPRA patient force traces.
(adapted from Lee et al. (2007)). Positive traces shows the applied force as caudal/compression (green), lateral (red) and anterior (blue).

3.1.3. Chapter aims

- To collect kinetic data using a wireless six axis load cell from ITAP patient 12 (and simultaneously estimate kinetic data using an instrumented treadmill). Then compare with published kinetic data on OPRA patients, prosthetic socket users and non-amputated individuals.
- To validate the estimated kinetics using the exact kinetics and then interrogate the estimated kinetic data at points of interest to generate a set of representative moments of inertia.

3.2. Method:

Biomechanical data from ITAP patient 12 was collected via a gait analysis (with optoelectronic capture of retroreflective skin markers) on an instrumented treadmill and a bespoke wireless six axis load cell. In

addition to the kinematic data, this produced two sets of kinetic data (one exact set from the load cell output and one estimated set from the inverse dynamics calculations).

3.2.1. Mobility activities

Data collection must be harvested from activities that reflect those an ITAP patient would frequently perform for example level and variably inclined gait (running / jumping is not recommended for ITAP patients), see Fig. 3.3. Level gait data was collected at a speed chosen by the patient of (1.0 m/s) for two minutes which is slower than the average non-amputated optimum gait speed of ~ 1.4 m/s (Herr and Grabowski, 2012). Slope gradient and speed was similarly self-selected by the patient for three trials of one minute each uphill at 0.8 m/s on an 8.5 ° incline and downhill at 1.0 m/s on a – 7 ° decline.

Fig. 3.3: Photos of ITAP Patient 12 treadmill walking uphill and downhill

3.2.2. Gait analysis and inverse dynamics

The study was conducted at the RNOH, Stanmore, UK motor learning gait laboratory using the Motek Medical Grail system (Motekforce Link, Netherlands) and Vicon (Vicon Industries, USA) ten camera motion capture system. The process of data collection, patient model building and data production was semi-automated with software, Visual 3D, C-motion, USA (V3D) that was integrated with the instrumented treadmill and cameras. Full patient consent and ethical clearance was obtained for this

work (IRAS number 226799; see Appendix A.3.1). A 39 piece retroreflective skin marker set was adapted from the standard RNOH gait laboratory protocol to suit the ITAP patient and applied by the experienced RNOH gait lab manager (Fig. 3.4 and Fig. 3.5, left).

There are several popular retroreflective marker placement positions in the literature, the RNOH gait laboratory model is adapted slightly from the V3D software standard. A standing calibration provides the information to calculate the local coordinate system (LCS) of each segment. The origin of the pelvis LCS is halfway between the marker on the right and left anterior superior iliac spine. Using a hip joint centre, calculated in V3D using equations from Bell et al. (1989), the thigh LCS can be calculated. This is achieved using the axis from the virtual hip joint centre and a point midway between the femoral epicondyles and an orthogonal axis passing between the medial and lateral femoral epicondyles. The shank LCS is defined using the following landmarks: lateral and medial malleoli and lateral and medial femoral epicondyles with an origin halfway between the femoral epicondyles. Finally, the foot segment LCS origin is halfway between the lateral and medial malleoli. The corresponding computer model was adapted from the standard RNOH patient model to include an amputation of the left thigh (Fig. 3.5, right). The height of the amputation was matched to that of ITAP patient 12 (residuum = 0.201m) and the mass of the segment was estimated at 7 % body weight, BW (normal thigh segment mass in this model build is 10 % BW (Winter, 2009)). Body segments were constructed from cylindrical or truncated cones and segment anthropometric data was calculated using patient mass, height and from calibration markers. The patient was able to walk untethered and was given as much time as needed after fitting the load cell and marker set to familiarise himself with walking on the treadmill (Fig. 3.6) at a slow speed. He was offered a walking harness and made aware of the safety rails and emergency stop button.

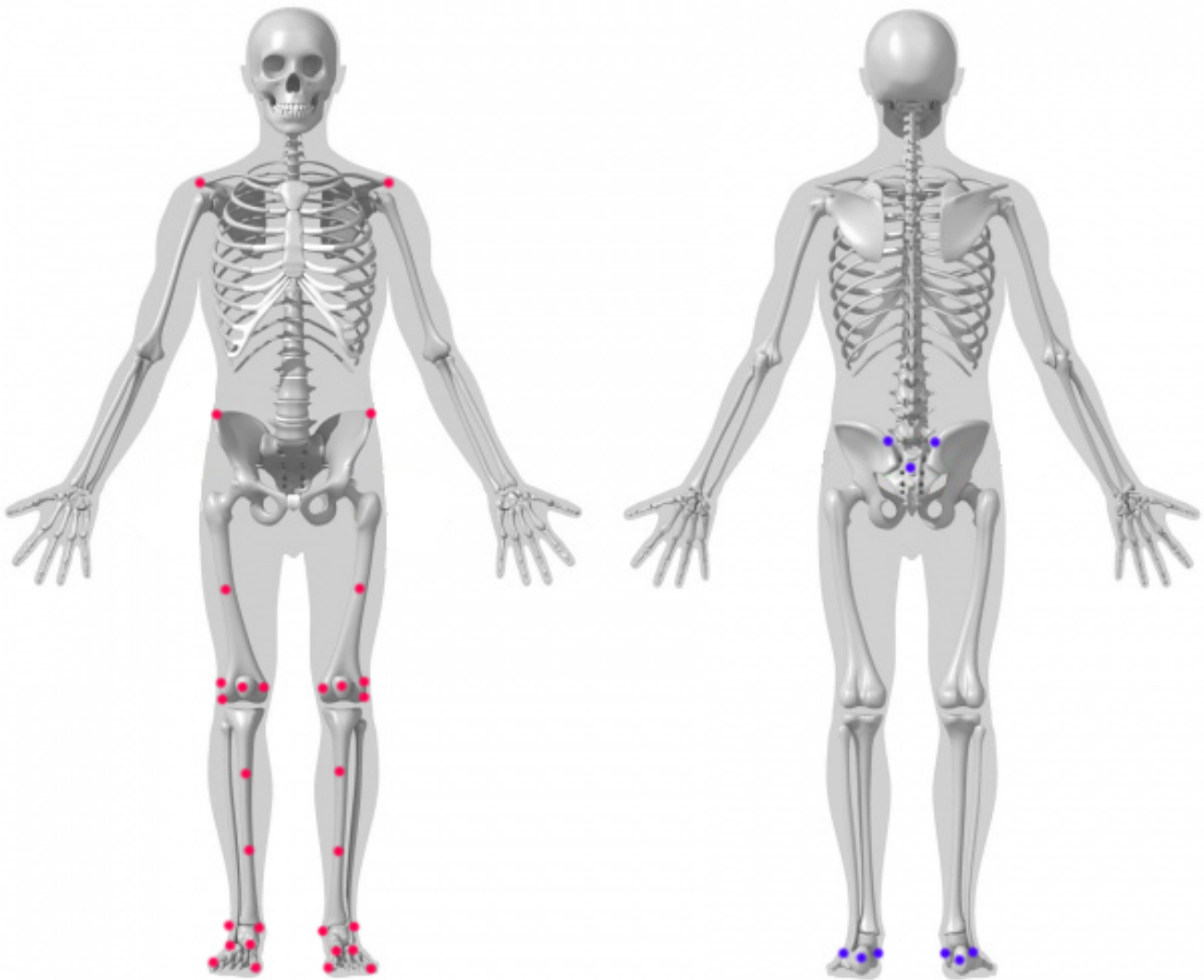

Fig. 3.4: Biomechanical marker set used.
Pink = anterior markers, Blue = posterior markers. (Two acromion markers enable V3D to calculate the body COM)

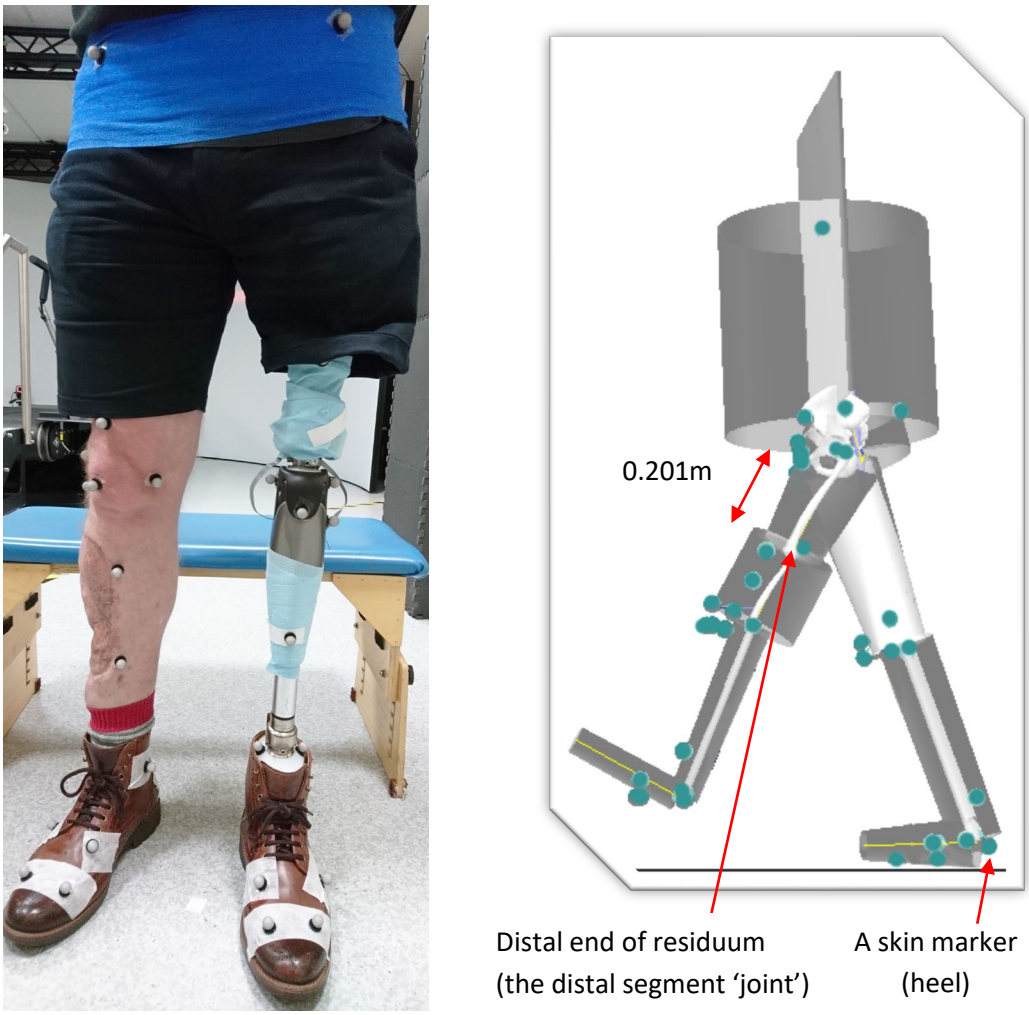

Fig. 3.5: Photo of ITAP patient 12 with retroreflective marker set and V3D equivalent model.

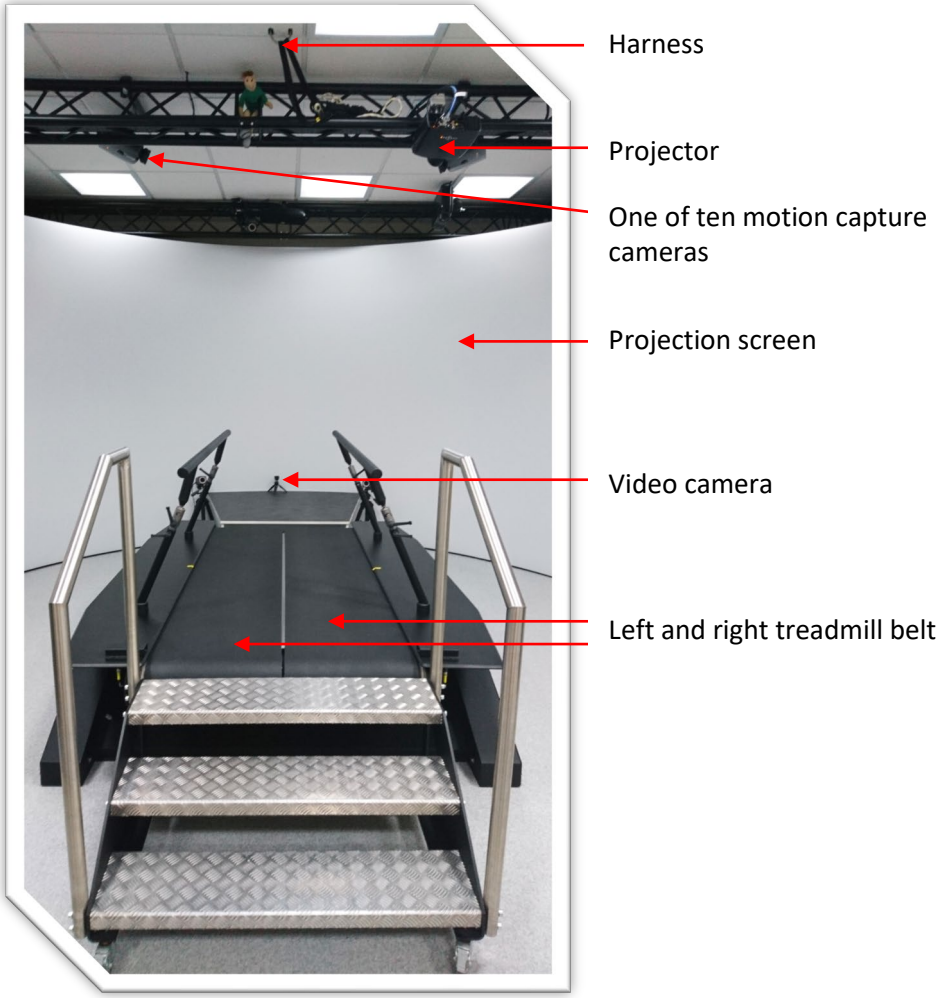

Fig. 3.6: Photo of the Motek Medical Grail treadmill at the RNOH motor learning laboratory.

3.2.3. Load cell

The load cell was designed to fit into a 110 mm gap between surfaces of male pyramid fittings on the distal face of the patient's failsafe and the proximal face of the prosthetic knee (Genium, Ottobuck, Germany), Fig. 3.7 c. The orientation of the fitted load cell replicated the patient's normal orientation (Fig. 3.7 a and Fig. 3.7 b), this was undertaken by an experienced ITAP specialist prosthetist. The load cell coordinate system vertical axis (Y) was colinear with alignment of the extended female pyramid fitting. The mediolateral, ML (X) and anterior posterior, AP (Z) axes were orthogonal to this with positive in the caudal, medial and posterior directions with respect to the patient (Fig. 3.8).

Fig. 3.7: Photos of leg components (knee, pyramid fittings and failsafe) on ITAP patient 12 before the load cell was fitted.

a = Anterior view. b = Posterior view. c = Full leg component assembly on patient.

Fig. 3.8: Photo of load cell and pyramid fittings - interposed between failsafe and prosthetic leg.

3.2.3.1. Load cell construction

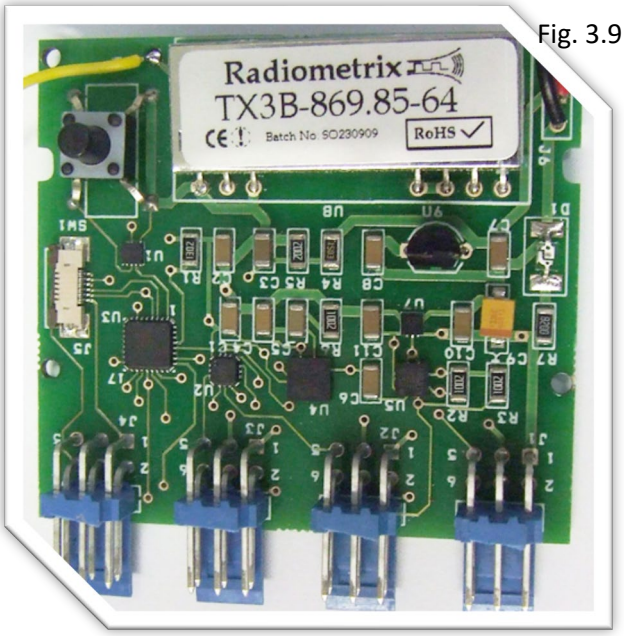

Fig. 3.9 a

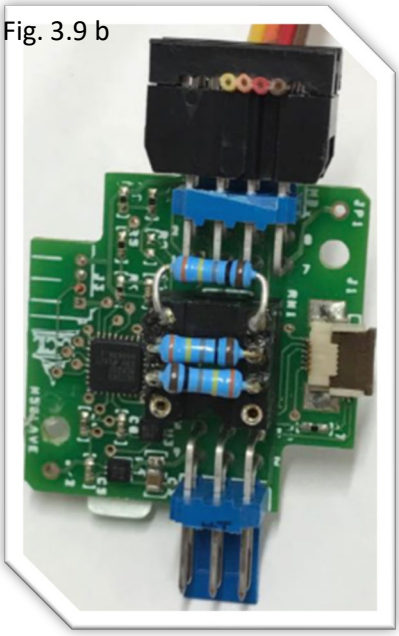

Fig. 3.9 b

Fig. 3.9 c

Fig. 3.9 d

Fig. 3.9 e

Fig. 3.9: Photos of load cell construction
a = HIPP5 PCB master. b = HIPP5 slave. c = Original force transducer showing one flat and gold wires on a flexible circuit pad. d = Force transducer protected with plastic collar and wired to the HIPP6. e = Transducer and plastic collar housed inside two female pyramid fittings.

Fig. 3.9 shows the construction development of the load cell. Note that Fig. 3.9 a + b show final PCB boards which were different to the original design shown in Fig. 3.9 d. Further details on the construction of the load cell build and calibration are in Appendix 3 (A.3.3). Data were telemetered from the subject's leg to a remote PC via UHF radio at 50 samples/sec per channel.

3.2.3.2. Load cell data processing

Data was collected over many cycles and a standard method of data processing was performed; one gait cycle was defined as initial contact (heel strike) to ipsilateral heel strike (0 to 100 %). The axial component (F_y) was used to identify the heel strike. These data segments were superimposed for each of the six DOF and processed using a bespoke algorithm developed in Excel. The algorithm either compressed or expanded a trace so that 0 and 100% of the gait cycle on each were colinear with a representative trace and the mean trace was calculated. A similar data processing method was used by Frossard et al. (2013). Two filters were incorporated into the algorithm since there were some erroneous data spikes in the resultant traces, most likely due to errors in transmission. The first was a threshold setting based on representative traces of non-polluted data along each axis. The second was the removal of any trace containing data more than 1.5 standard deviations (SD) from the mean (after the first filter had run). The resultant traces were then used to calculate the new mean.

3.2.3.3. Validating the instrumented treadmill with the load cell

The load cell was fitted distal to the failsafe device and reported exact load data at that location, whereas the V3D estimated force data at the distal end of the residuum. To validate the estimated force data with the exact force data one set needed to be transformed to the same orientation as the other. Using the load cell coordinate system as the reference there was a 0.153 m proximal and a 0.015m medial translation followed by two rotations (laterally 5 ° about the Z axis and anteriorly -2 ° about the X axis) to transform to the V3D coordinate system (see Fig. 3.10). These translations and rotations were measured from 2D photographs. This transformation was applied to the mean trace for each activity on the load cell forces and moments to compare with the V3D data (for derivation see A.3.4 in Appendix).

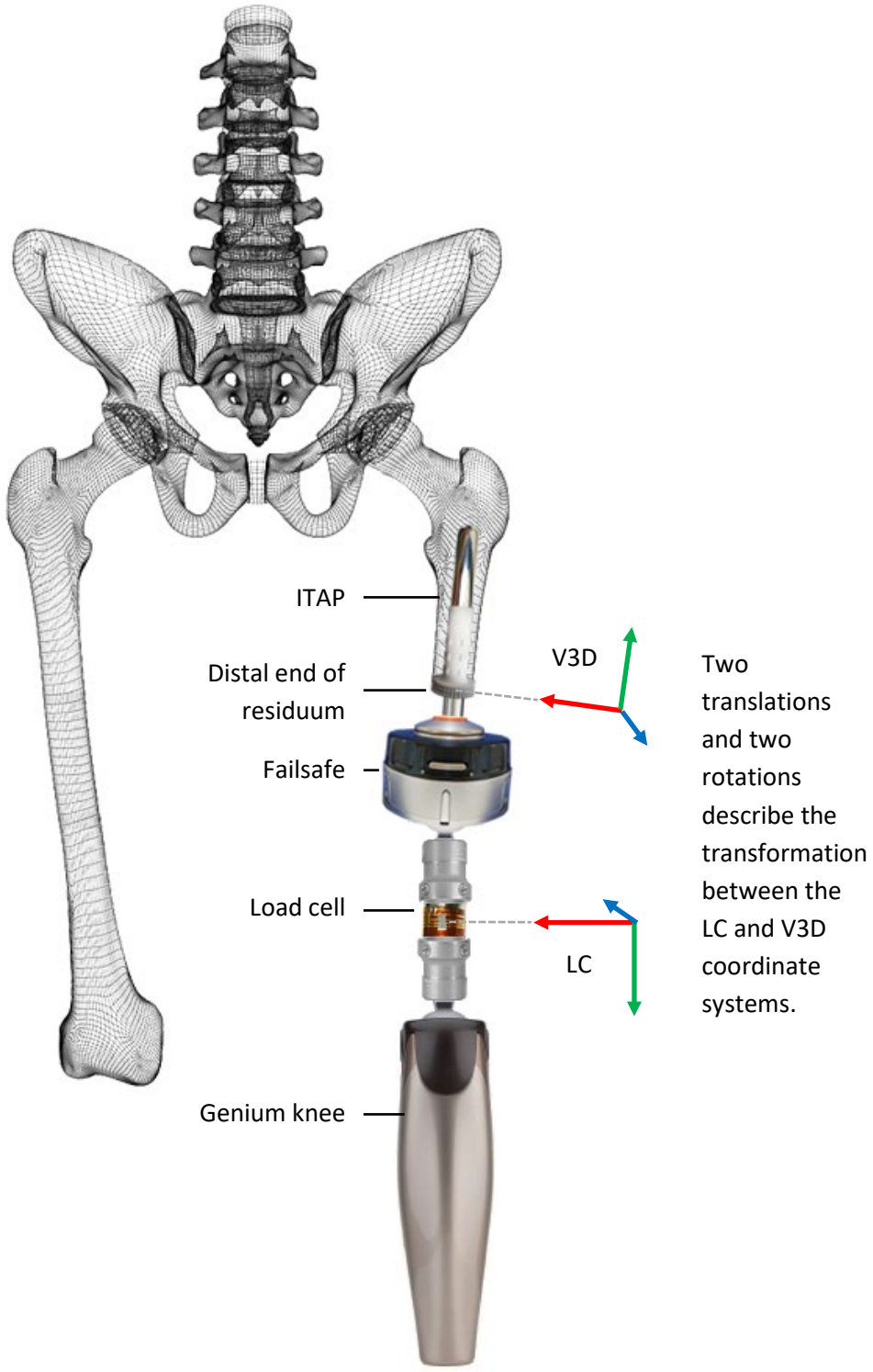

Fig. 3.10: Schematic illustrating load cell (LC) transformation to V3D coordinate system (red = X axis, green = Y axis, blue = Z axis).

3.3. Results

3.3.1. Load cell results

3.3.1.1. Raw data charts

Load cell forces and moments for walking at 1.0 m/s were processed and are plotted across one gait cycle in Chart 3.3 and Chart 3.4 respectively. From top to bottom, Chart 3.3 shows the individual and mean (red line) data for axial (F_y), ML shear (F_x) and AP shear (F_z) forces. From top to bottom, Chart 3.4 shows the individual and mean (red line) profiles for axial torque (M_y), ML bending (M_x) and AP bending (M_z) moments.

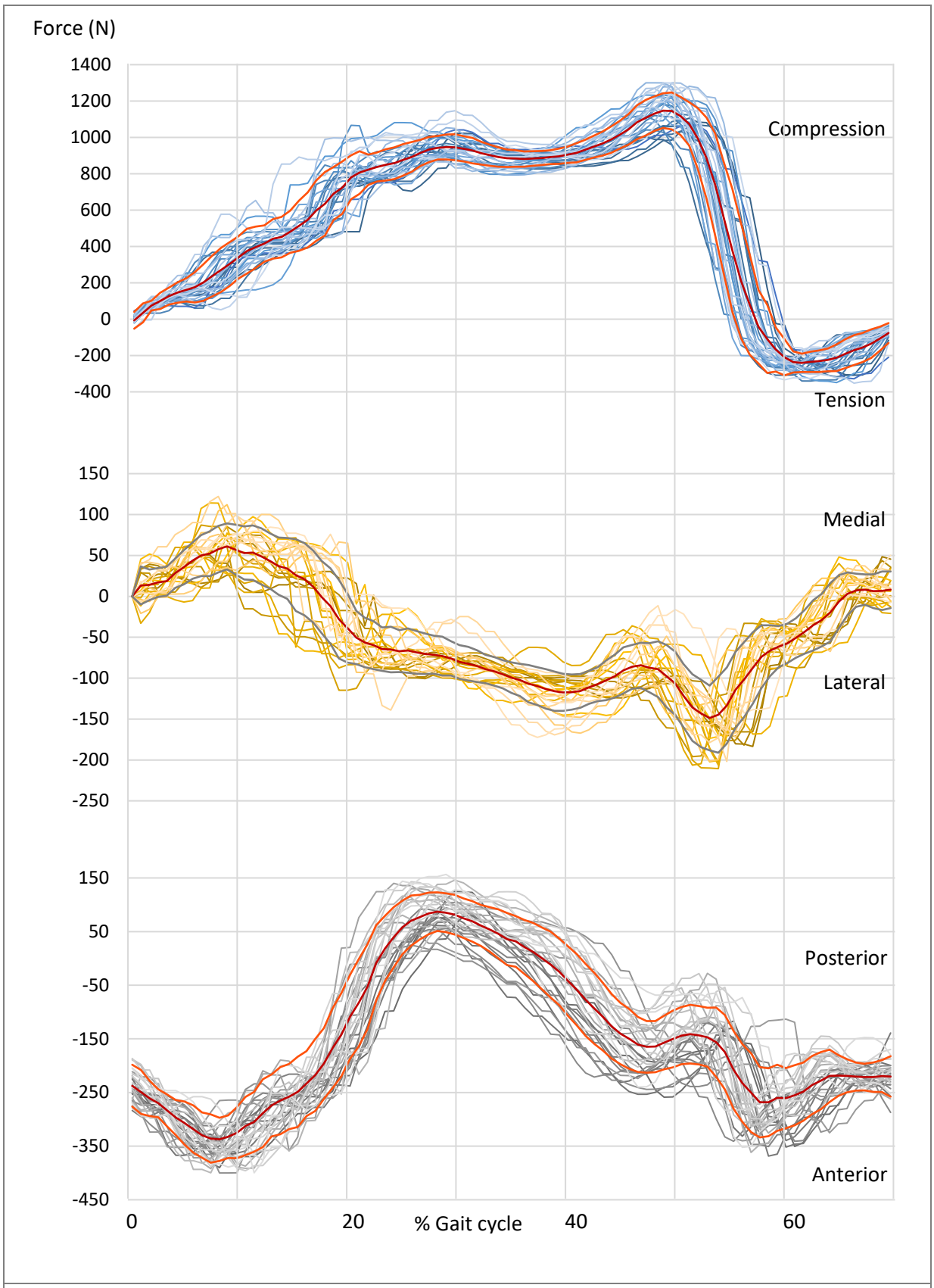

Chart 3.3: Processed raw force data from load cell
Walking at 1.0 m/s on treadmill in ITAP patient 12. Forces (N) in one gait stance cycle.
Mean (red) +/- 1 standard deviation. Top: Axial (F_y), Middle: ML (F_x), Bottom: AP (F_z)

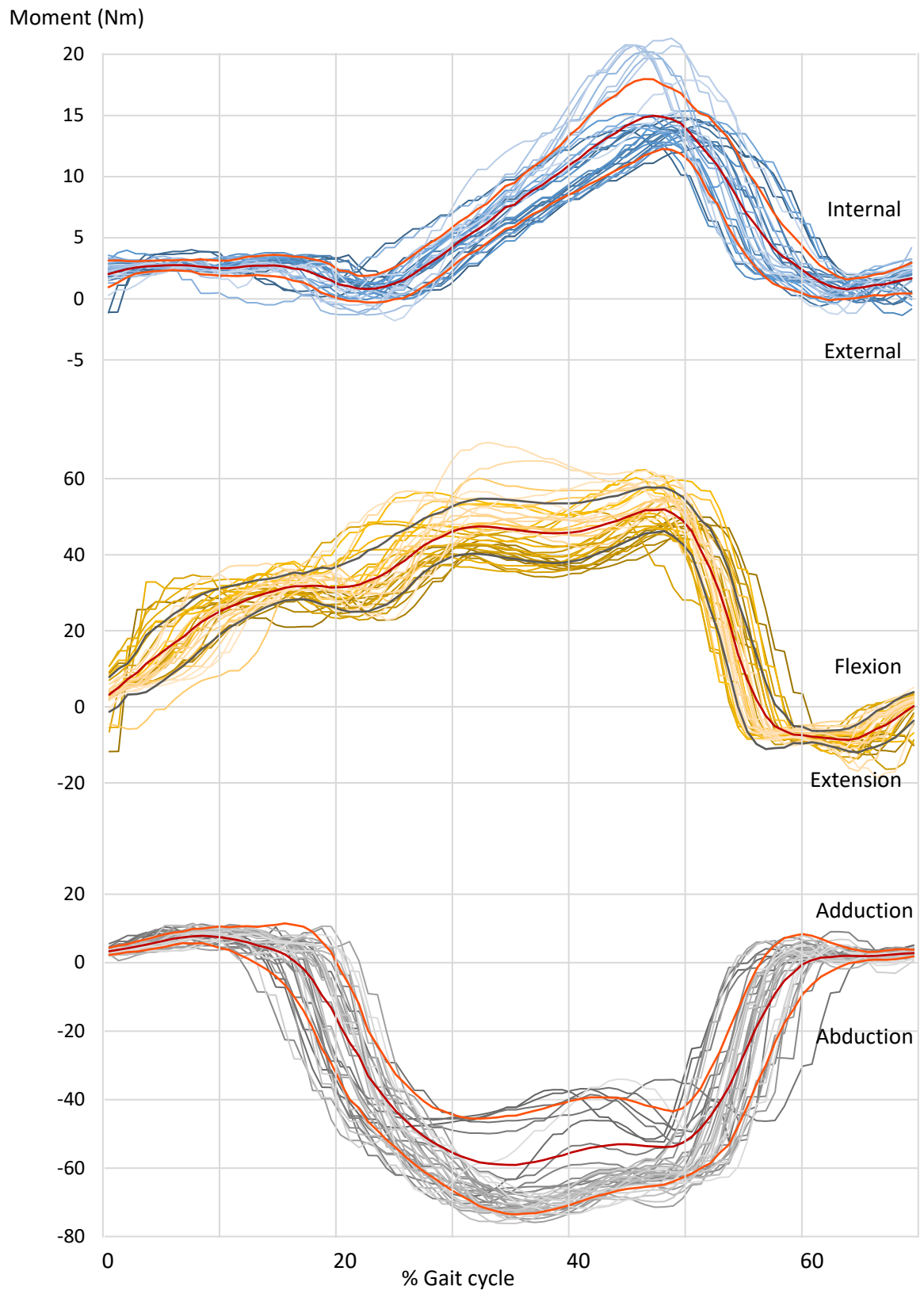

Chart 3.4: Processed raw moment data from load cell

Walking at 1.0 m/s on treadmill in ITAP patient 12. Moments (Nm) in one gait stance cycle showing mean (red) +/- 1 standard deviation. Top: Axial (M_y), Middle: ML (M_x), Bottom: AP (M_z)

3.3.1.2. Averaged data charts

All data was similarly processed and the average trace for each DOF is shown for each activity with vertical axes normalised with body weight in Chart 3.5, Chart 3.6 and Chart 3.7.

Positive forces	= Compression (F_y), Medial (F_x), Posterior (F_z)	= F_y, M_y
Positive moments	= Internal torque (M_y), Flexion (M_x), Adduction (M_z)	= F_x, M_x
%GC	= Percentage of gait cycle	= F_z, M_z

Chart 3.5: Average LC trace level walking at 1.0 m/s

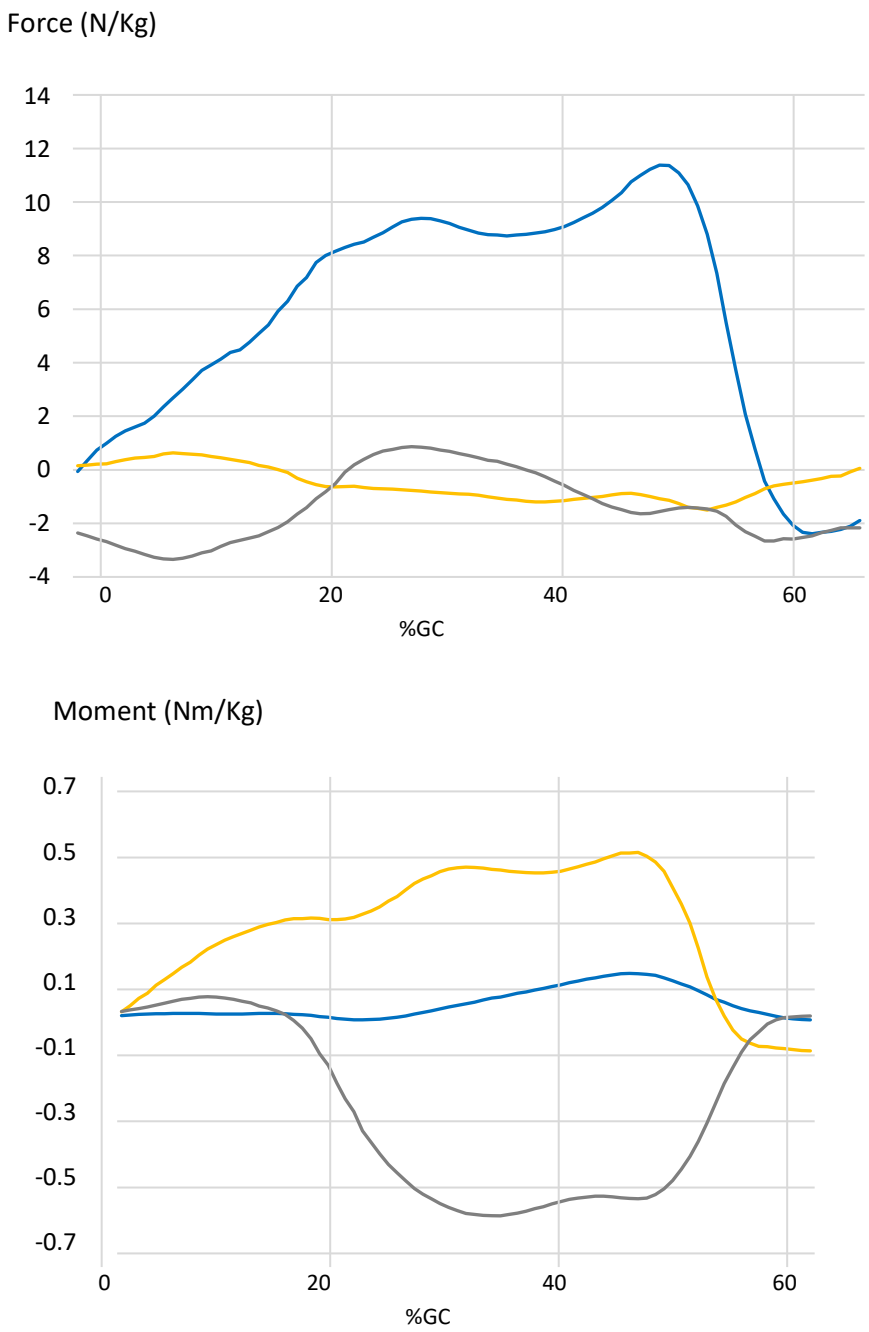

Chart 3.6: Average LC trace walking uphill (8.5 % incline, 0.8 m/s)

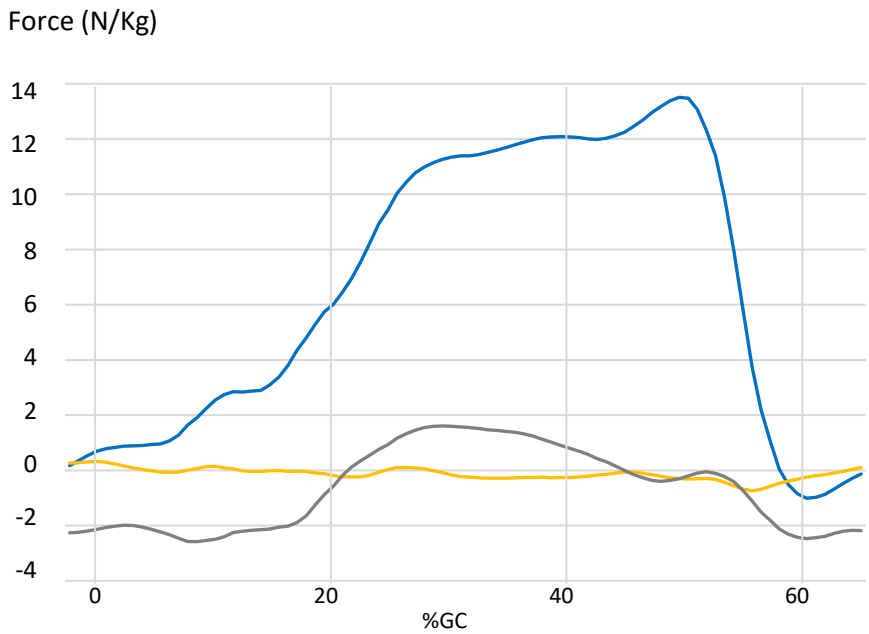

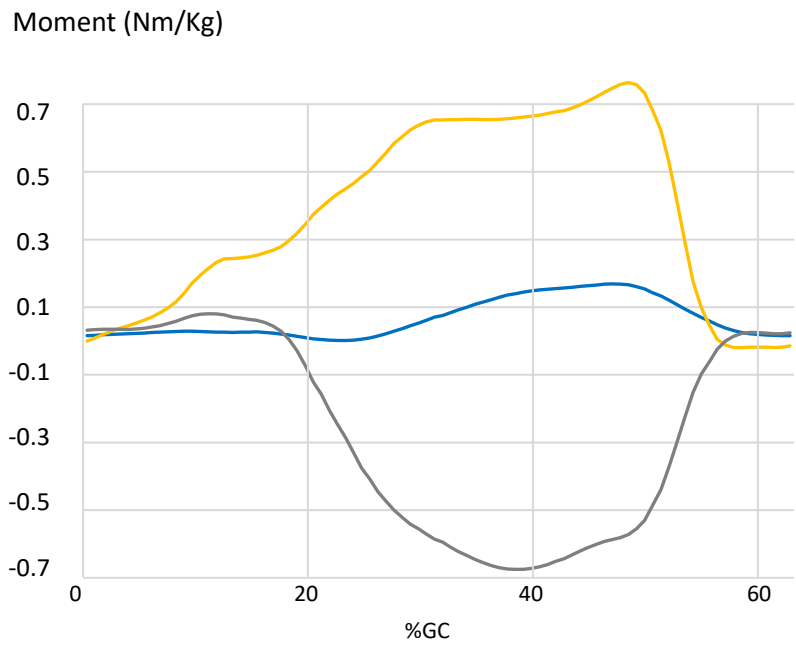

Chart 3.7: Average LC trace walking downhill (-7 % decline, 1.0 m/s)

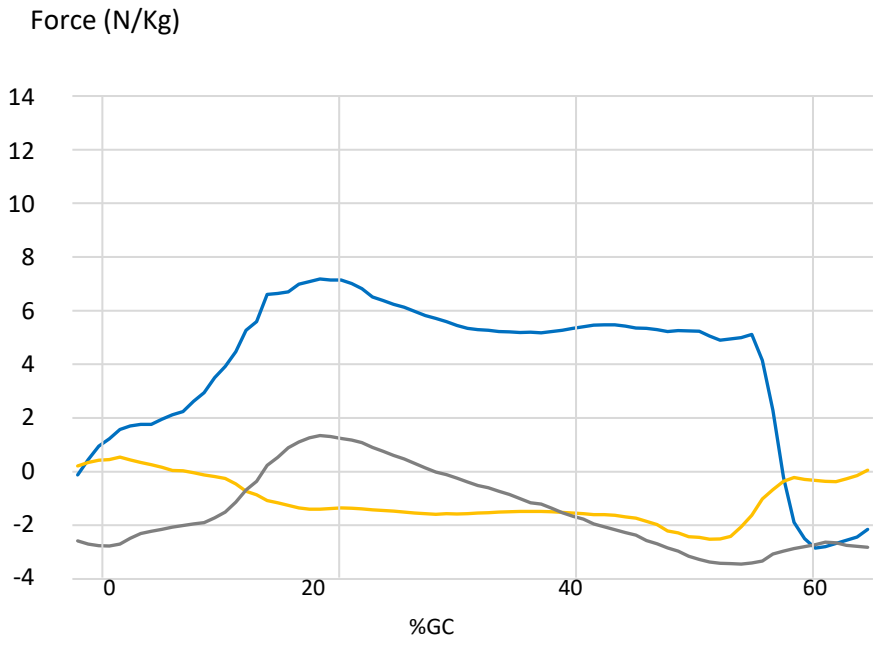

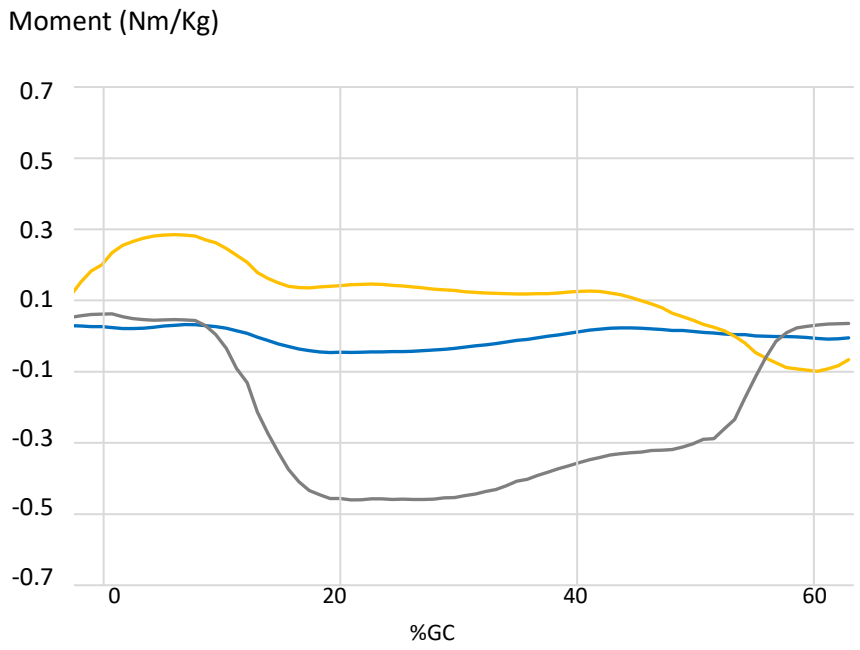

3.3.1.2.i. Walking at 1.0 m/s:

Force at the load cell in F_y was experienced caudally (as compression) with two peaks, the second larger than the first. The first peak was observed at ~ 30 % of the gait cycle (GC) at 9.39 N/kg and the second

was at ~ 50 %GC at 11.36 N/kg. Force along F_x was medially directed at heel strike but by ~ 20 %GC had turned into a laterally directed force with a peak at ~ 55 %GC of – 1.50 N/kg. Along F_z, force was anteriorly directed, peaking at – 3.35 N/kg at ~ 10 %GC, where after it decreased in magnitude until ~ 25 %GC and flipped to a posteriorly directed force, increasing to a peak of 0.84 N/kg at ~ 30 %GC. At ~ 40 %GC the force reverted to an anterior one and gradually increased in magnitude until terminal stance. The load cell reported flexion and abduction moments with both peaking at ~ 30 %GC and ~ 50 %GC which approximately corresponded to the two peaks in F_y (limb loading and terminal stance). These were 0.47 Nm/Kg and 0.52 Nm/Kg in flexion and - 0.59 Nm/Kg and - 0.53 Nm/Kg in abduction. There is negligible torque (M_y) until the limb begins to load at ~ 30 %GC thereafter an internal rotation was recorded peaking at ~ 50 %GC at 0.15 Nm/Kg.

3.3.1.2.ii. Walking uphill (0.8 m/s @ 8.5°):

As with level walking, the axial force patterns displayed two peaks. However, time in reaching the first peak was delayed and then more rapidly attained compared level walking. Both peaks were larger in magnitude than level walking; the first peak was observed at ~ 30 % GC at 11.44 N/kg followed by a gradual increase in force magnitude (unlike the midstance force magnitude dip observed in level walking) until a sharp peak at ~ 50 % GC of 13.48 N/kg. Lateral force in stance was diminished in comparison to level walking to a relatively constant - 0.25 N/kg which became slightly amplified just after push off (~ 55 %GC) to -0.69 N/kg and displayed a very small medial force at 30 %GC of 0.09 N/kg. Forces in F_z displayed a similar shape over the gait cycle (GC) to level walking but the maximum anterior force was comparatively diminished to – 2.46 N/kg at ~ 15 %GC and the maximum posterior force was approximately doubled to 1.60 N/kg at ~ 30 %GC. Moments in M_x and M_z were larger than those in level walking but generated similar shaped traces. Peaks in M_x were observed at 0.65 Nm/Kg at 30 %GC and 0.76 Nm/Kg at 50 %GC. The moment around the Z axis had one peak of - 0.68 Nm/Kg at ~ 40 % GC. M_y (torque) displayed an internal rotation peak at ~ 50 %GC at 0.17 Nm/Kg as with level walking.

3.3.1.2.iii. Downhill walking (1.0 m/s @ - 7°):

The axial force pattern displayed two peaks as with level and uphill traces. The first force peak was earlier than that observed in level walking at ~ 20 %GC and had a magnitude of 7.14 N/kg. It was larger than the second peak at ~ 50 %GC of 5.23 N/kg. Maximum peaks in lateral (F_x) force observed at ~ 20 %GC and ~ 50 %GC were larger than those seen in level or uphill walking at - 1.40 N/kg and – 2.42 N/kg respectively. Forces along the Z axis followed the posterior – anterior – posterior pattern along the GC timeline as seen in level and uphill walking. Peak anterior force at limb loading was 1.35 N/kg at ~ 20 %GC, peak posterior force in push off (~ 50 %GC) was – 3.43 N/kg which was greater than that in level or uphill walking. All moments were more lateral than those observed in level and uphill walking; M_y and

M_z displayed similar trace shapes to level walking over the GC but M_x differed. Peak flexion in M_x was 0.28 Nm/Kg and observed between initial contact and limb loading at ~ 10 %GC thereafter it steadily decreased to approximately zero at push off. M_z produced a peak abduction moment in limb loading of -0.46 Nm/Kg at ~ 23 %GC, less than that in level or uphill walking.

3.3.1.3. Forces representative of the functional stages of gait

Using the data obtained to produce Chart 3.5, Chart 3.6 and Chart 3.7, a set of forces and moments representing the stance and initial swing phases in gait at the load cell were produced (Table 3.1) using the load cell coordinate system. (i.e. resultant forces and moments at segment ends produced from the superposition of many individual forces and moments across all points of the musculoskeletal model).

Table 3.1: Forces and moments in stance and initial swing in level and slope walking.
[1] Load was recorded at the end of this phase (~ first peak in vertical force)
[2] Load was recorded at the end of this phase (~ second peak in vertical force)

Slope	Functional phase	F_x (N)	F_y (N)	F_z (N)	M_x (Nm)	M_y (Nm)	M_z (Nm)
Level	Initial contact	18.188	34.283	-249.186	5.080	2.222	3.807
	Loading response [1]	-80.075	946.841	85.055	44.744	3.492	-53.912
	Mid stance	-118.703	887.027	0.014	45.728	9.305	-57.641
	Terminal stance [2]	-108.264	1147.018	-156.872	50.792	14.699	-53.682
	Initial swing	-24.182	-231.329	-227.827	-8.549	0.886	1.910
Uphill	Initial contact	26.018	16.787	-228.039	-0.080	1.625	3.249
	Loading response	-16.466	1143.914	161.233	65.329	6.180	-57.561
	Mid stance	-26.257	1208.354	124.238	66.061	13.000	-67.572
	Terminal stance	-29.737	1361.832	-30.181	77.015	16.720	-57.663
	Initial swing	-24.246	-101.787	-249.445	-1.995	2.508	2.291
Downhill	Initial contact	21.005	-11.867	-259.794	11.473	2.934	5.313
	Loading response	-140.901	723.917	135.616	13.682	-4.123	-43.759
	Mid stance	-150.635	526.398	-137.761	12.023	-0.439	-39.465
	Terminal stance	-253.845	509.326	-339.929	4.543	1.374	-30.508
	Initial swing	-33.335	-287.299	-274.317	-9.257	-0.208	2.305

3.3.2. Validating the instrumented treadmill with the load cell

There was some association between the V3D and load cell data (Chart 3.9) in level gait; the closest agreement was observed in M_y and M_z (% RMSE = 1.38 and 2.52 respectively) with an acceptable error in F_x and M_x (% RMSE = 9.66 and 4.42). Error was higher in F_y and F_z with % RMSE = 28.90 and 18.30 respectively.

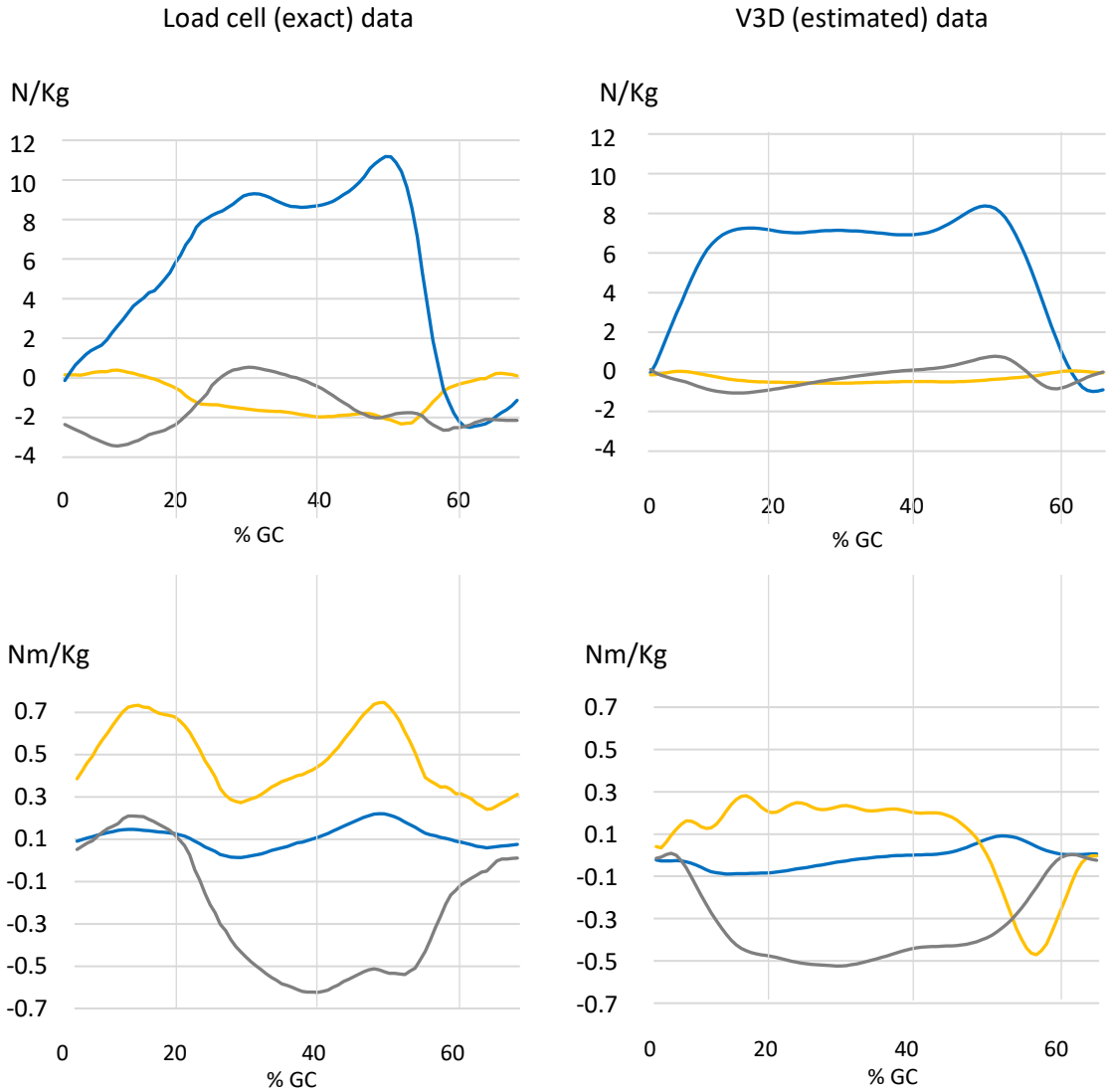

Chart 3.8: ITAP patient 12 normalised traces transformed.
Top = Stance phase forces for an average gait cycle at 1.0 m/s.
Bottom = Stance phase moments for an average gait cycle at 1.0 m/s.

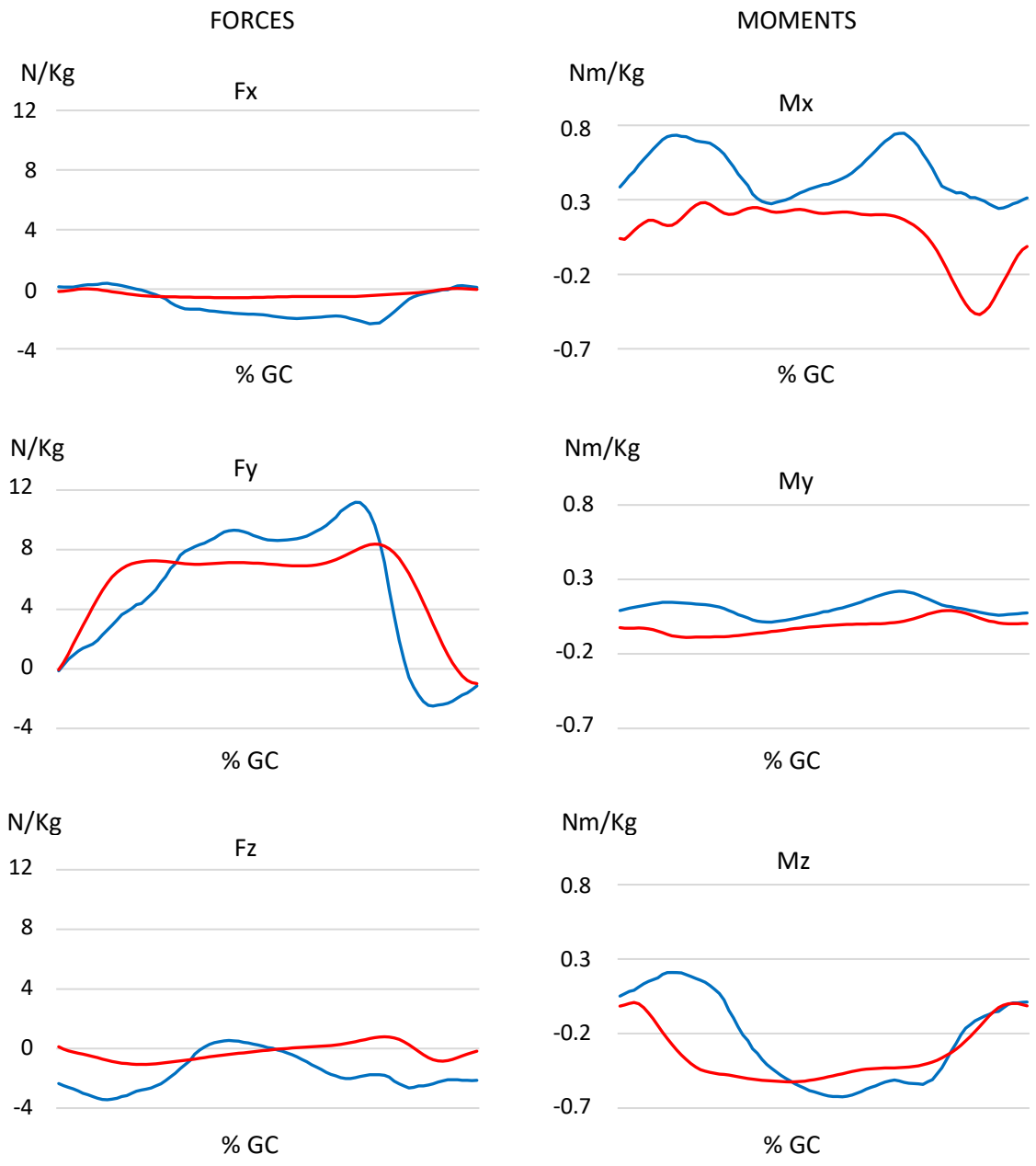

Axis	RMSE of Forces (% N/kg)	RMSE of Moments (% Nm/Kg)
X	9.66	4.42
Y	28.80	1.38
Z	18.30	2.52

Chart 3.9: V3D data (red) and load cell data (blue) stance phase forces and moments for an average gait cycle at 1.0 m/s in each axis superimposed, % RMSE underneath.

3.4. Discussion:

The ensuing discussion compares kinetic and kinematic data between different populations as well as between patients fitted with different SAAP types. Due to only being able to record biomechanical data from one ITAP patient, the comparisons made herein are qualitative in nature only.

3.4.1. Comparing ITAP patient load cell data walking at 1.0 m/s with prosthetic socket users, OPRA patients and non-amputated individuals

3.4.1.1. Forces along the longitudinal axis (F_y):

In non-amputated individuals the 'M curve' force/time graph shown in Fig. 3.1 are typical gait kinetics; the relative magnitude of the two peaks depends on gait speed (Verdini et al., 2006, Chiu and Wang, 2007). The vertical trace captured by the load cell in ITAP patient 12 showed no evidence of a heel strike transition, usually associated with the drop of the foot onto the ground. This is not always present (Perry, 2010), and it may be that the 50 Hz sampling rate was not high enough to capture it. The initial vertical GRF force trace peak in non-amputated individuals is observed during the first 100 ms in the limb loading phase and can reach 120 % BW, it is often larger than the second peak (Chart 3.1). By mid-stance, the vertical GRF drops to between ~ 65 % BW for a dynamic walk or up to ~ 100 % BW in the elderly, with most people at ~ 80 % BW (Soutas-Little, 1998).

Axial forces in this study were positive in the caudal direction making a compressive force applied to the load cell by the body (and inertial contributions) positive on the force/time graph. ITAP patient 12 generated a vertical force trace that increased throughout loading to 9.39 N/kg, dipped slightly in midstance to 8.80 N/kg and peaked at terminal stance at 11.36 N/kg, before diminishing at pre swing (Chart 3.5). This is similar to a non-amputated individual's vertical force trace (Chart 3.1) except for a comparatively diminished first force peak (< 100% BW) and a slightly increased (less dynamic gait) midstance magnitude (~ 88 % BW). This is not out of keeping with the vertical force traces of TF amputee prosthetic socket users (Nolan et al., 2003, Grimmer and Seyfarth, 2014).

Kinetic and kinematic deviations from normal gait in patients with asymmetric gait disorder such as hemiparesis (e.g. from a stroke), joint replacements and those with prosthetic limbs can display some similarities in vertical GRF depending on the resected musculature and the mechanics of the COM (Skinner and Effeney, 1985, Morita et al., 1995, Debbi et al., 2015). The effect of the split belt treadmill that was used in this study may have influenced the kinematic and kinetic deviations (Tesio and Rota, 2019). It has been suggested that treadmill data peak forces will be diminished compared with overground data (Riley et al., 2007) if the global coordinate system does not move with the treadmill belt as in this study (Van Ingen Schenau, 1980). This may offer an explanation to the first peak deviation

from 'normal'. Further investigation with EMG and COM tracking over ground rather than a split belt treadmill may help to isolate the cause of the diminished first vertical force peak in ITAP patient 12.

The OPRA biomechanical study (Lee et al., 2007, Frossard et al., 2010a) used a load cell attached to the prosthetic abutment, and patients walked over ground (not on a treadmill). There is a difference in the way their data is reported to mine; they appear to report the ground reaction on the load cell whereas I reported the forces that act upon the load cell by the body. Their vertical force data displays similarity to non-amputated individuals' traces with some including a double peak at initial loading and terminal stance (Lee et al., 2008). There was notable interpatient variability however, except for one patient, both peaks if present are less than 100 % BW and at midstance an average force of ~ 80 % BW is observed. These results are like mine albeit with slightly diminished peak values and suggests that SAAP patients do not diverge in vertical force functional phase compared with non-amputated individuals. To compare data between SAAPs study types should be more similar with respect to terrain type, outcome data needs to be clarified and there needs to be a greater number of patients.

3.4.1.2. Forces along the AP axis (F_z):

The load cell coordinate system was positive in the posterior direction. An anterior (shear) force applied by the body to the load cell was recorded in the first half of stance. This anteriorly directed shear force as the patient's heel strikes the treadmill slows the speed of movement in the anterior direction (direction of travel) in the manner of a brake. In the second half of the stance phase as the COM becomes more vertical over the leg, the direction of force changes to positive and this acts as a propulsive force and accelerates the body; by this mechanism AP shear modulates walking speed.

A metric commonly used by kinesiologists to quantify propulsion magnitude is *propulsive impulse* (Marasović et al., 2009) which is calculated by integrating the AP forces (area under the force curve). Positive and negative impulses are equal if the horizontal component of velocity is constant. In ITAP patient 12, a sizable difference between the anterior (braking) and posterior (propulsive) impulses was observed: a deceleration in the first half of stance that was greater than the acceleration in the second half acts to decrease the horizontal component of velocity. In this study both belts on the split belt treadmill were turning at the same speed and so a constant velocity that was equal on both legs would have had to be maintained. It is therefore likely that adjustments to stride length and stance time would have compensated for the impulse differences.

TF (and transtibial) prosthetic socket users are known to generate reduced propulsive and braking impulses compared with non-amputated individuals, especially at higher speeds (Silverman et al., 2008,

Schaarschmidt et al., 2012). But there is discrepancy in the literature regarding the ratio of braking to propulsive impulse at a self-selected comfortable walking speed; Rutkowska-Kucharska et al. (2018) report approximately equal impulses. Barr et al. (2012) observed similar sized impulses when patients wore a hydraulic knee unit, but a relatively larger braking impulse with a microprocessor controlled knee (MCK), that brought the braking impulse magnitude almost equal to their non-amputated control, conversely Schaarschmidt et al. (2012) report prosthetic propulsive impulses greater than braking impulses.

Results from the OPRA study showed a posterior force in the first part of stance followed by a larger anterior force in the second part of stance (Lee et al., 2007, Frossard, 2019). It must be remembered that they report reaction forces and those actioned on the load cell by the body would be equal and opposite. ITAP patient 12 did not generate as large a propulsive magnitude as the average of the OPRA patients, this may be due to the added effort required to generate push overground compared with a treadmill.

It appeared that the effect of the treadmill on the AP force compared with overground was a relatively reduction in the propulsion impulse which could be due to the belt doing part of the work in carry in the driving limb backwards in push off. This agrees with the observations of Van Ingen Schenau (1980) since a fixed coordinate system was used as the global coordinate system and also observed by Riley et al. (2007). Conversely inertial forces and the braking impulse (anteriorly directed force) are larger than that seen in overground walking.

3.4.1.3. Forces along the ML axis (F_x):

Gait ML shear is the lowest magnitude force of the three axes. Usually as the heel strikes there is a momentary medially applied force which quickly changes to laterally directed at ~ 5 % GC until the end of stance phase (John et al., 2012). As the COM shifts over to the supporting limb in double stance, abductors are important in supporting the body weight (Liu et al., 2008) and exert a lateral force on the limb. This ambulation method and muscular function, although without the TFL in the TF amputee, remains similar in this plane. In fact, in TF prosthetic socket users, there is an increase in the applied lateral force in both limbs, in most patients (Carse et al., 2020).

ITAP patient 12 experienced a predominantly laterally directed force in stance. As with non-amputated individuals this was preceded with a smaller medially directed force, however this extended beyond 5 % GC to ~ 15 % GC. Also, in a similar fashion to non-amputated individuals the trace displayed two (lateral) peaks at the beginning and the end of stance.

Comparing to the 12 OPRA patients there is stark contrast. If their data is consistent then they present reaction force values. As such the lateral force they present would be opposed by a medial force applied by the body to the load cell. This suggests that the adductor muscle forces overcame the forces generated by the lateral translation of the COM and the abductors. It is not clear why these would be opposite to the ones observed in my study other than due to the large variability along this axis.

3.4.1.4. Moments around the longitudinal axis (M_y)[1]:

Transverse plane moments at the knee in non-amputated individuals are usually dominated by an internal rotation (Malloy et al., 2016) which may be preceded by a small external rotation (Segal et al., 2011, Komnik et al., 2018). This pattern is obtained from ITAP patient 12 however the peak 0.15 Nm/Kg is comparatively reduced, which is also observed in prosthetic socket users (Fey and Neptune, 2012). The OPRA study obtained a small external rotation moment in the transverse plane of patient one, working on the premise that this is a reaction moment then by negation their data agrees with mine. The size of the moment was an order of magnitude lower than in my study at 0.08 Nm/Kg, furthermore their M_y traces varied significantly across the remaining patients and they obtained both internal and external moments in level gait. In conclusion the distribution of M_y across TF amputees is similar and despite variability in magnitudes is reduced compared to non-amputees.

3.4.1.5. Moments around the ML axis (M_x):

The initial extension observed at heel contact in a non-amputated individual is a result of two extensor mechanisms. First the heel is extended anteriorly beyond the knee axis and second muscular control by the vastii and IT band. Stance stability is optimised when the knee is extended (Perry, 2010), the same is true for a prosthetic knee (Gard, 2018). Thereafter, knee flexion develops and increases through the loading phase acting in a shock absorption capacity (Kaufman and Sutherland, 2006, Perry, 2010). One advantage of a MCK is the ability to achieve stance phase knee flexion (Kaufman et al., 2007, Schmalz et al., 2014) unlike most of the mechanical knees.

The modern prosthetic knee aims to mimic the biomechanics of natural gait; in TF amputee loading, as soon as body weight transfers to the leading limb, the knee becomes anterior to the body vector and determines a flexion moment which is the opposite situation to a non-amputated individual. However, in mid stance the TF amputee is fully weight bearing on the prosthetic limb so a knee locking strategy to prevent buckling of the knee due to flexion would be required by a strong hip extension moment (Wühr

[1] Internal and external rotations here refer to the rotational direction of the moment not whether this is an action or reaction moment

et al., 2007) in the absence of the normal hamstring and quadriceps muscular control (Arnold et al., 2005, Schmitz et al., 2017). A prosthetic knee stance yielding function is one that locks out the knee in mid stance flexion under a load and removes the requirement for an unphysiological hip extension. In ITAP patient 12 a very definite flexion moment was observed throughout the entire stance phase (including initial loading) with an extension moment observed at initial swing. The flexion moment is likely to be a combination of the removal of the distal insertion of the vastii and TFL and/or hip flexion contracture preventing normal muscular control in this phase and the 'stance yielding function' of the patients MCK (Genium knee, Ottobock, Germany). The extension moment at the start of swing is probably due to the tibia being accelerated forward; since there are no muscles spanning the load cell, this must result in a 'knee extension' (although the knee itself is flexed).

The lack of extension in loading has similarly been observed in prosthetic socket unilateral TF amputees (Segal et al., 2006, Bae et al., 2007) with Kaufman et al. (2012) demonstrating that this was more profound in patients using a MCK (presumably with a knee locking strategy) compared with a passive mechanical knee joint. Similarly, Namiki et al. (2019) observed a flexion moment in prosthetic socket unilateral TF amputees running on blades. The flexion moment usually observed from midstance until pre swing comes about as the knee joint moves anterior to the body vector and a chain of muscular contractions control knee angle. Extension moments in non-amputated individuals also occurs at this gait phase as the femur advances over the lower limb.

The OPRA patients produced a mixed moment response around the ML axis (Lee et al., 2007, Lee et al., 2008), in their coordinate system an anterior rotation was positive. Three participants produced an entirely posterior rotation throughout stance; negating this for comparison to my data suggest similar results (a flexion moment) and possibly relates to the three patients with knee stance yielding functions. The remainder of their patients exhibited the more typical extension moment preceding the stance flexion.

3.4.1.6. Moments around the AP axis (M_z):

In a non-amputated individual, the knee is abducted throughout stance and is adducted in swing with a peak of approximately 0.60 Nm/Kg (Royer and Wasilewski, 2006). The abduction is a response to the unloading and dropping of the contralateral side of the body as the COM is medial to the supporting limb. Typically, the IT band would provide a lateral counterforce at this level. In the hip, abductors including the gluteus medius, upper gluteus maximums and TFL augment the lateral counterforce. Since the TFL distal insertion is removed in a TF amputee, the remaining abductors must perform this role;

ITAP patient 12 displays that this occurs, with a clear abduction moment throughout stance with a peak magnitude approximately equal to a non-amputated individual (~ 0.60 Nm/Kg).

All OPRA patients exhibited a positive lateral rotation around the AP axis in stance; once again negating this *reaction* data to compare to my *action* data suggests a medial rotation in stance. A medial rotation in stance must refer to an adduction moment which seems unlikely in all 12 patients.

3.4.2. Comparing ITAP patient load cell data walking uphill and downhill with prosthetic socket TF amputees, OPRA patients and non-amputated individuals

Downhill walking in non-amputated individuals increases limb loading (DeVita et al., 2007) and more energy is used by ankle plantar flexors and knee extensors (DeVita et al., 2007, Franz et al., 2012) compared with level walking. Downhill walking requires controlled lowering of the COM (Franz et al., 2012) but the prosthetic limb may not be able to perform this due to the lack of muscles crossing the knee and ankle joints. It has been observed that this is overcome in amputees by increasing the loading of the intact limb (Donelan et al., 2002, Morgenroth et al., 2011, Yeom and Park, 2011, Morgenroth et al., 2018). Which can incidentally lead to secondary complications such as osteoarthritis in the intact limb (Struyf et al., 2009) or lower back pain (Mahon et al., 2017). In my study there was a marked decrease in limb loading downhill compared with level or uphill walking suggesting this tactic was employed by ITAP patient 12. Results were very similar to those obtained by Morgenroth et al. (2018) in TF prosthetic socket patients using a power knee (Ossur, Reykjavik, Iceland).

3.4.2.1. Phasing:

My results also produced a functional phase timing shift both uphill and downhill. After initial contact walking uphill took a longer time (~ 35% GC) to fully load the limb compared with level walking (~ 28% GC) whereas downhill walking loaded the limb more quickly (~ 23% GC) than level walking. This may have been due to the timing differences in lifting or lowering the body's centre of mass plus gravitational and inertial forces adding time uphill. Push off timing was less affected by gradient, therefore the single limb stance phase was compressed in ascent and extended in descent compared with level walking. The second peak (terminal stance) in level and uphill walking was larger than the first (limb loading) whereas downhill, the first peak was larger than the second. Despite which, both peaks in ascent were greater in magnitude than in level walking and lower in magnitude descending.

3.4.2.2. Forces along the longitudinal axis (F_y):

Studies overground walking suggest that in non-amputated individuals, the first vertical force peak is larger downhill compared with level and uphill walking (Kuster et al., 1995) since the speed at which the

foot strikes the ground dictates vertical force (Liu and Nigg, 2000). Although a larger first peak compared with second peak downhill was observed in my study it was not larger than either level or uphill walking. This may have been due to downward vertical component of the treadmill velocity effectively 'speed dampening' the heel impact plus the intact limb taking more of the load. Walking overground uphill the first vertical force peak of non-amputated individuals is lower than level walking or downhill (with a greater terminal stance force than level or downhill walking) in the research (Gottschall and Kram, 2005, Chan et al., 2018). Whereas it was larger in my study which, again may be due to the vertical component of the treadmill velocity effectively augmenting the impact on loading.

3.4.2.3. Forces along the AP axis (F_z):

The effect of an incline increased the length of time to fully load the limb in AP compared with level walking. The propulsive force (positively/posteriorly directed) peak was greater, and the braking force (negatively/anteriorly directed) peak was less compared with level gait. Uphill the propulsive force also acts for a longer portion of the GC (~ 26 % to 46 % GC) compared with level walking (~ 23 % to 39 % GC) or downhill walking (~ 18 % to 30 % GC). Many studies on non-amputated individuals mirror the finding that uphill walking is characterised by a greater propulsive force and downhill walking characterised by a greater braking force compared with level walking at the knee (Kuster et al., 1995, Gottschall and Kram, 2006, Lay et al., 2006, McIntosh et al., 2006). Furthermore, that an increasing ramp angle increases the deviation from level walking in all shear forces (Redfern and Dipasquale, 1997) which affords propulsion at a constant velocity. Overground, it is feasible that the lack of a posterior treadmill belt motion may lead to a reduction in propulsion, so more force would be needed, particularly in ascent. Similarly, there may be a reduction in braking force downhill overground compared with treadmill walking since no resistance against the moving belt is necessary. The literature does suggest there are statistically significant differences in GRF between the types of *level* walking environments but that they are small (Goldberg et al., 2008, Lee and Hidler, 2008). However, there was no statistically significant data available on kinetic differences between *sloped* treadmill and overground walking.

3.4.2.4. Forces along the ML axis (F_x):

Once more, the ML force trace phasing was shifted compared with level walking (walking uphill took a longer time to fully load the limb and downhill walking loaded the limb more quickly compared with level walking). Uphill there was minimal lateral force application to the load cell (average ~ - 0.25 Nm/Kg), with an equally sized medial force before and after limb loading. Conversely, downhill the lateral force recorded was up to ten fold higher than uphill (peaking at ~ 2.49 Nm/Kg) and double level gait at any point in the cycle. It is possible that instability resulting from protracted single leg stance could determine the recruitment of abductor muscles (laterally applied force) in the regulation of speed

(braking force) and/or stability downhill. Further work using EMG would be required to elucidate this conclusively.

3.4.2.5. Moments around the longitudinal axis (My):

The internal torque was observed ascending and descending as well as in level walking peaking in all cases in terminal stance. The peak was larger in magnitude walking uphill and smaller downhill compared with level walking; this variance in magnitude was also observed for both bending moments.

3.4.2.6. Moments around the ML axis (M_x):

M_x (flexion and extension) variation was pronounced uphill and downhill; walking uphill generated a 50 % increase in peak flexions at both limb loading and terminal stance, presumably as the knee joint is anterior to the body vector by a greater amount than in level walking. Descending, a flexion moment similar to level walking was observed at initial contact which peaked (0.29 Nm/Kg) before limb loading was complete and then rapidly halved in magnitude by the end of limb loading where it remained until terminal stance where it dropped to below zero in an extension moment of a similar magnitude to that seen in level walking and uphill walking. Walking downhill although the body vector will be anterior to the knee and observationally the knee will appear extended it has maintained a small flexion throughout. These observations are likely due to the control offered by the knee stance yielding function; in a study by Alexander et al. (2018) the kinematics of slope walking illustrate that the gradient determines when the patient used the knee stance yielding function. M_x in non-amputated individuals displays similar deviation from level walking; Lay et al. (2006) noted no flexion in stance in downhill and increased flexion uphill walking (at 8.5 and 21° slopes) with a greater deviation the steeper the ascent/descent at the knee. Alexander et al. (2018) observed the same pattern of increasing moment magnitude deviation from level walking the steeper the incline or decline in prosthetic socket users.

3.4.2.7. Moments around the AP axis (M_z):

M_z (adduction and abduction) displayed a ~ 13 % increase in peak magnitude uphill compared with level walking. The change downhill from level walking was more profound with a 30 % decrease in peak magnitude, however both walks observed an abduction moment. Furthermore, the peak abduction ascending is at midstance whereas in descending it is closer to limb loading.

3.4.2.8. Slope force data comparison with OPRA patients

Comparing results with ascending and descending data from the OPRA study was not straightforward; Frossard (2019) published repeat data in level and ascending. Furthermore, in publications that use the

same data set, moment results disagree; Lee et al. (2007) report an external rotation reaction moment in descent and Frossard (2019) report a mean internal rotation, both presumably reaction moments but as with level walking there was significant interpatient variation in the moment around this axis. The level walking M_y data also disagrees between the two publications but the lack of clarity as to whether Frossard (2019) has published level or ascending data compounds the ambiguity of the moments in this plane. Their M_z data suggests adduction reaction moments (Lee et al., 2007) in one publication and abduction (Frossard, 2019) in the other.

In addition it has not possible to use the data in Lee et al. (2007) for comparison since the forces have been averaged across the patients without normalising for bodyweight. This means that only the OPRA descending force data from Frossard (2019) can be used for a comparison to my data wherein a decrease in mean magnitude across the patients is observed in comparison to either their level or ascending data. This is equal to my data. Interestingly, downhill they obtained a cluster of data points on the second peak (termed local extrema in their work) i.e. at terminal stance that were the same sign as those in the first peak i.e. at initial loading. This meant that some of their patients were braking in both phases of gait, suggesting unknown alternative methods to lower the COM down the slope.

3.4.3. Validating the instrumented treadmill with the load cell

The first step toward extracting the inertial forces for the femur segment from V3D was to validate it with the load cell kinetics within margins of acceptable error. Interpretation of acceptable error, varies across the literature for example Schwarze et al. (2013) perform an estimated/exact kinetic data comparison in gait (on six prosthetic socket TF patients) and calculate % RMSE averages across their patients of F_x = 2.0 %, F_y = 5.1 %, F_z = 4.9 %, M_x = 29.9 %, M_y = 19.8 %, M_z = 19.5 %. They suggest although the estimated moments are of a lower accuracy, they are still sufficiently accurate for most clinical applications. In a similar study with nine OPRA patients, Dumas et al. (2017) present % RMSE results of F_x = 13.2 %, F_y = 6.0 %, F_z = 11.0 %, M_x = 4.5 %, M_y = 13.9 %, M_z = 6.5 % in stance (their swing % RMSE averages were ~ three times greater in each axis). Yet they state that the estimated method should be used with caution in the field of prosthetics due to the large errors. Interestingly both studies produce the least congruence between data sets in M_y whereas my results show this moment to produce the lowest % RMSE (1.38 %). With so few patients in each of these studies, only one presented here, and no clear pattern it was challenging to draw a logical conclusion. It is possible to say that there was similarity in results from the estimate forces and moments when compared with the exact data, but it may not be a reliable indication of what was being experienced by the limb.

Lack of good agreement may be the result of:

- The load cell considers the inertial properties of 'everything' below the level of the load cell whereas the V3D model includes an estimation for the inertial properties of the residual limb too.
- The V3D inertial properties were calculated using segment masses that included flesh around each segment this was different to that of the prosthetic leg and foot used by ITAP patient 12 (although this was not recorded and should be addressed in future work).
- Soft tissue motion from the skin markers on the patient can produce artefacts in joint centres, velocities, accelerations and thus joint torques (Günther et al., 2003, Faber et al., 2018). This would have been relevant to markers proximal to the load cell (pelvis, hip, thigh) and so influenced the model calibration. (Stagni et al., 2000) note that moving the coordinates of a hip joint centre by ± 30 mm can have upward of 25 % effect on the angles and moments at the hip and the knee joints.
- Modelling the body in rigid segments with idealised joint movements compounds the generalisations.
- The position of the load cell with respect to the distal end of the femur bone relied on a combination of radiographic measurements (to determine the depth of soft tissue between the distal femur and the load cell) and translation/rotation measurements taken from 2D photographs.

Achieving a validation of the load cell against the instrumented treadmill provides a potential solution to gathering biomechanical data from more ITAP patients. If patients biomechanical analyses could be conducted without a load cell then ITAP patients that could walk on a treadmill could participate. Collecting a larger data set is a primary goal for future work, however, using a treadmill rather than overground walking means comparison with the OPRA patient data set are still problematic. In order to bolster the reliability and validity of the current data set (n = 1) it is therefore necessary to resolve the experimental limitations of data collection with the load cell.

3.4.4. Study limitations

3.4.4.1. Sources of experimental error

There were a few load cell sources of error outlined in Appendix 3, A.3.5

3.4.4.1.i. Patient recruitment

Due to the geometric restrictions in repurposing the load cell it was not possible to adjust the length to less than 77.4 mm. There was only one of the 12 ITAP patients who had a space beneath their fail safe long enough to fit this in. This study on one ITAP patient may not represent the remaining ITAP patient's kinetics. Recruitment of several more patients would be ideal in future work in order to validate the data presented in this chapter. To achieve this it would be necessary to either:

- Redevelop the load cell used in this study. This may be possible if the strain gauges were designed for purpose rather than repurposed from a previous device. This is not unrealistic and a good option, however requires a full redesign and additional time which should be weighed up against the other options.
- Use a commercially available load cell such as the one used in the OPRA study that is 10 mm shorter. This would mean that more ITAP patients could fit the load cell and failsafe in the space distal to their residual limb. Whilst this is ideal, it would require a bigger budget to the one available in this study and is perhaps a consideration for new work leveraging the results obtained in this exploratory work.
- To use a commercially available *wired* load cell of which there are many much smaller types on the market. In this scenario almost all of the ITAP patients could be analysed with only a marginal increase in study budget. Data collection from a wired device means that patients would carry a power source as well as the ensuring hanging wires did not impede locomotion. This is not ideal but given the constraints is perhaps a good compromise for future work in order to collect data from the most ITAP patients.

3.4.4.1.ii. Corrupt data (post processing)

There were a few segments of data that required filtering to remove erroneous data spikes from experimental errors (see 3.2.3.2.). Achieving this by thresholding may have had an influence on the mean trace.

3.4.4.1.iii. Treadmill gradient and speed

Due to the patient self-selecting ascent and descent treadmill speeds and gradient they differed from level walking by different amounts with ascent = 0.8 m/s @ 8.5° and descent = 1.0 m/s @ - 7°. This introduces ambiguity when suggesting that ascent or descent alone may be the cause of something that perhaps would not have been discernible if the divergence from level walking were exactly equal. In

future work, as well as equating the gradient and speed of belt in ascending and descending, a range of gradients would be walked in order to assess the kinetic changes.

3.4.4.1.iv. Overground vs. treadmill

There were several factors that I viewed as advantageous in selecting the treadmill as the activity surface for this study. Principally, the ability to simultaneously collect the kinematic data for the V3D verification drove this decision. To have control over the walking surface (speed, gradient) and handrails for the patient's confidence was also very useful. However, the effect of a moving belt along the AP axis using the lab based global coordinate system may have had an effect on the kinetics. It is thought that the width of a treadmill belt may influence the ML kinetics and that the vertical force peak magnitude is influenced (Riley et al., 2007, Parvataneni et al., 2009). One must compare the results from this study with data from overground studies (such as the OPRA data) with this in mind. In further work it would be useful to repeat the exercises overground for comparison.

3.4.4.1.v. Other exercises

Several additional exercises were performed in this study including stair walking, sit to stand to sit and lateral stepping. Unfortunately, the load cell data was impossible to interpret due to both data corruption and being unable to synchronise with the V3D data. Resolving the issues surrounding the load cell construction along with a synchronised video recording of these exercises could resolve this in future work.

3.5. Conclusion

This study has successfully built a load cell that was used to collected biomechanical data from an ITAP patient that achieved an acceptable level of agreement with data from V3D and validated this Chapter's first hypothesis. There was some divergence from the biomechanics of non amputated individuals and prosthetic socket users however a direct comparison has not been straightforward since this study was conducted on a split belt treadmill. Published data from the OPRA study included many inconsistencies and was challenging to compare. There was some matching data between this study and theirs, for example a decrease in force magnitudes downhill compared with level or ascent walking and similarity in F_Y in level walking. However, it has not been possible to confirm or disprove the hypothesis that these full data sets should have been relatively similar. The Chapter has produced a reliable set of forces, moments and inertial forces that can be applied to a FE model of ITAP patient 12 implant/bone (Chapter Five). The next Chapter (four) prepares for model loading by first experimentally validating it.

CHAPTER 4

Experimental validation of a finite element model

4.1. Introduction

This Chapter aims to develop a FE model that accurately represents a SAAP cemented in a femur (*in silico)* that will be validated experimentally (*in vitro*). The cadaveric femur used for the *in vitro* work was selected as a good representation of the femoral geometry of the ITAP clinical trial patient 12 from whom kinematic and kinetic data was collected in Chapter Three. Once validated, the FE model underwent analysis in Chapter Five where the loads from Chapter Three were applied to investigate the effect of implant design on periprosthetic stress. In the discussion the term "model" describes the SAAP implanted bone as depicted computationally with the FEM, which includes all geometric discretisation's and interactions between all parts of the assembly. The term "anatomical bone" refers to the computer simulated cadaveric bone used in the FE simulation which is termed the *in silico* work. The term "bone layer" refers to the modelled layer of bone in the bone plug whereas the term "bone/implant model" refers to the three dimensional (3D) FE model of the SAAP, polymethyl methacrylate (PMMA, bone cement) and bone layer in full rather than in section or 2D.

4.1.1. Model verification and validation

The results of any type of simulation must be credible; for this there must be a standard to which the model can demonstrate its likeness to the physics of the problem. Furthermore, the maths governing the model must be correctly implemented and there must be a calibration of the accuracy of the model. With the uptake and commercialisation of software's offering FEM, there are concerns around conceptualisation errors and model limitations by the diverse group of investigators using current finite element analysis (FEA) software. The importance of model credibility in a clinical setting to draw relevant conclusions can have life changing consequences. Verification and validation (V & V) procedural standards in the publications Aeronautics and Astronautics (1998) and Roache (1998) have gained notoriety. Before those publications, the Sargent model (Sargent, 1984) illustrated a popular V & V protocol, shown in its simple form in Fig. 4.1. More latterly, the American Society of Mechanical Engineers (ASME) published a guide for V & V in computation solid mechanics (Schwer, 2007) and Marco Viceconti has provided biomechanists with a version of these salient guidelines (Viceconti et al., 2005).

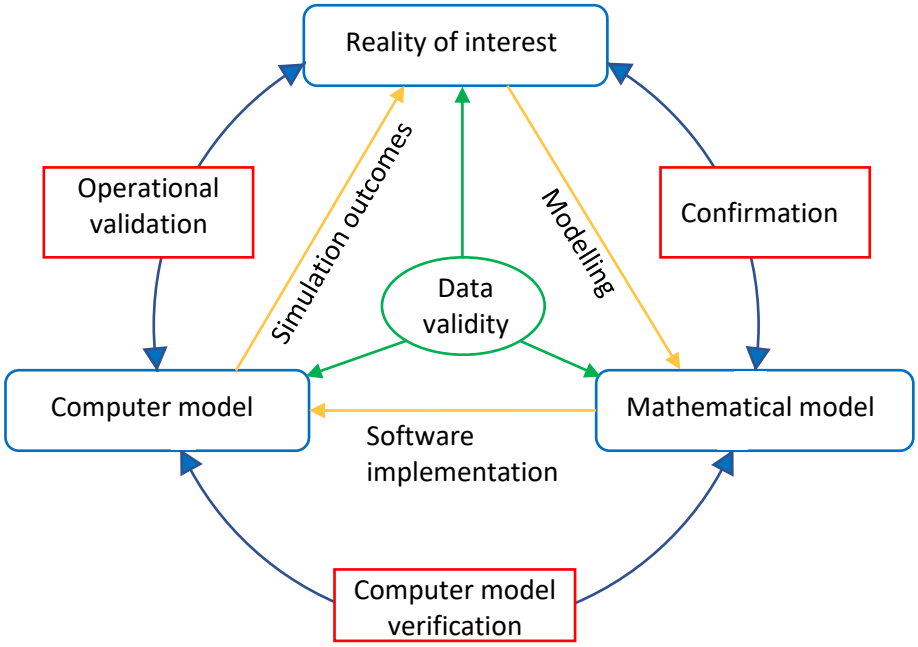

Fig. 4.1: The Sargent model
from Sargent (1984).

-Reality of interest	= Physical system for which data is being obtained
-Mathematical Model	= Partial differential equations, constitutive equations, geometry, initial conditions, and boundary conditions.
-Computer model	= Numerical discretisation, solution algorithms, convergence criteria, the computer program (code), grid size, solution options, and tolerances.
-Confirmation	= Assessing the correctness of the modelling
-Computer model verification	= Identification and removal of errors in the Software:
	Code Verification = Identification and removal of errors in the code.
	Calculation Verification = Quantification of errors introduced during application of the code to a simulation e.g. via a grid convergence study.
-Operational validation	= Quantifies the accuracy of the model through comparisons of experimental data with simulation outcomes from the computer model
-Data validity	= Ensuring the data for model building, model evaluation/testing, and conducting the model experiments to solve the problem are adequate and correct.

Verification determines that a model accurately represents the analyst's description and the solution of the model. Validation is a process by which computational predictions are compared with experimental data (the "gold standard") to assess the modelling error. Verification can be either code verification or calculation verification. The most common type of calculation-verification problem is a grid convergence

study which offers evidence of a sufficiently accurate solution. And so, the outcome of the V & V process is a quantifiable level of agreement between the experimental data and model prediction, as well as the predictive accuracy of the model.

The value of producing accurate and trustworthy models makes economic sense in the engineering industry. In medicine, where biological models are often multiscale structures of nonlinear mechanics, V & V should be critical. In addition to the long term financial advantages there is the moral question: should a FE model that has not been through the rigour of the V & V process enter the clinical market? No prototype testing process is 100 % fool proof; clinical *in vitro* work may only represent the effects of the new device/process in that organism under laboratory conditions. A biological *in silico* model cannot model all intracellular reactions that make up the biological system of interest. The overarching belief of Oreskes et al. (1994) is that it may not be possible to fully validate simulations of natural systems (as none are closed) and that "*The primary value of models is heuristic*". With this is mind, the value of the FEM in clinical developments must be carefully assessed.

FEA may be the ideal commercial tool where a clinical trial indicates that a product is unsafe, but not why nor be able to efficiently change a parameter to re-test. Commercially this may bring a trial to its end however, the FEM can simulate many iterations of the trial altering one or more variable(s) each time. The FEM offers a unique insight into the physics of a system which may not be possible analytically for example to highlight regions of possible failure, stress concentrations or damage. If accuracy and error can be quantified, then we can make an informed choice about risk to the patient. FEA is not accepted by the Food and Drug Administration (FDA) as a tool to demonstrate the physical performance of *final* orthopaedic devices. Instead, the ASTM standard it upholds, states that the estimation of stresses and strains of the static implant should be used to inform the amount of physical testing to be conducted (ASTM, 2020).

In a numerical model of the SAAP in a femur, subject to everyday stress, there are many interactions that must be considered for which the outcome is unknown. When a model with an unknown outcome is initially built for V & V there can only be best estimates in the first iteration (*operational validation* in the Sargent model). In this Chapter, a sensitivity analysis (as part of a *data validity* check in the Sargent model) is included where parameters with previously unknown influence have been varied to observe the importance/contribution to *in silico* periprosthetic bone strain.

4.1.2. Measuring deformation experimentally

Deformation of a material is linked to its constitutive equation (Hooke's law in the elastic region). Validating a FE model using deformation to describe the physics of the system is a biomechanical standard (Tayton et al., 2010, Den Buijs and Dragomir-Daescu, 2011, Helgason et al., 2014). Two methods of deformation validation have been selected in this Chapter using two deformation metrics; discrete point validation measuring strain and a full field validation measuring displacement.

4.1.2.1. Discrete point (strain gauging) measurements

In biomechanics we are mostly concerned with bone strain measurements rather than bone displacement to offer insight into the physics of bone remodelling, damage and fracture. Differentiation of the displacement will provide a strain field, but its accuracy will be comparatively diminished due to the amplification of noise in the data field. When the gradients of the displacement fields are relatively low, a small measured error may induce a large computed derivative error (Geers et al., 1996). There are further sources of inaccuracy using strain as the measurand: Experimental measurement is commonly achieved with strain gauges (Cristofolini et al., 2010, Yang et al., 2011). A gauge is a layered stack; the closest to the source (bone) is a plastic resin, next is a layer of plastic then a layer of metal foil out of which come the connection wires. The resin layer is glued to the bone surface by removing the soft tissue and scraping back the periosteum to create a well for the adhesive. A strain reading assumes the adhesive in the well is uniformly distributed and is passed to the layer of resin and then plastic and then metal foil without loss of accuracy. Furthermore, in biological specimens like bone, the surface needs to be dry (disturbing the local mechanical response of the bone), the rigidity of the adhesive is thought to affect the accuracy, and the method offers only discreet point measurements which could lead to part of the bone strain picture being unobserved and/or omitted.

There is a place for the convenience, cost effectiveness and relatively rapid measurement of strain with gauges and there are steps that can be taken to mitigate some of these sources of inaccuracy including the use of a uniaxial gauge and meticulous preparation of each recording site. This Chapter collected the periosteal bone strain at four sites considered to be most useful for strain observations (medial and lateral aspects of the bone) and validated them against the equivalent FE strain results using the bone/implant model. Gauges were placed proximally and distally on each aspect.

4.1.2.2. Full field (DIC) measurements

The ability to accurately measure changes in physical quantities, non-invasively over every point on the surface of a structure, hallmark the full field optical methods (Haddadi and Belhabib, 2008, Rastogi and Hack, 2013). These include: Moiré interferometry, the photoelastic technique (used very effectively by

Pauwels (2012)), electronic speckle pattern interferometry and Digital Image Correlation (DIC). Some of these methods can be problematic in practical application when used with biological specimens of an inhomogeneous material and often complex geometry. For example, a viscoelastic coating on fresh bone relies on the plastic acting as a witness to underlying moist bone surface. With DIC, problems such as these are mitigated (Freddi et al., 2015). DIC in biomechanics has been used extensively to validate FE models (Dickinson et al., 2011, Gilchrist et al., 2013, Grassi et al., 2014, Helgason et al., 2014) as it stands out amongst the other methods, offering detailed resolution and a good tolerance to complex geometry (Peters and Ranson, 1982, Kahn-Jetter and Chu, 1990, Thompson et al., 2007). The DIC technique accurately calculates displacement between two (or more) corresponding images - undeformed and deformed. After an initial correlation, a randomly applied pattern of object surface speckles (between two and four pixels each), generating a pixel intensity, is correlated with another image and the maximum correlation array between the subsets gives the translational shift (displacement). With two cameras a 3D model can be analysed, and the accuracy of results can be extremely good (to the order of 100s or 1000s of micro strain). In this validation method, displacement, a first order metric, gets validated with the FE model thus preserving the accuracy of the surface translations.

4.1.3. Chapter aims:

The aim of this chapter was to experimentally verify the *in silico* model within an acceptable margin of error.

4.2. Method

4.2.1. *In vitro* model

4.2.1.1. Cadaveric bone material properties

One way to ascertain bone stiffness distribution is by placing densitometry phantoms into a CT scanner with the sample in order that a linear relationship between the Hounsfield Units (HU) and the bone ash density is established (Fig. 4.2). A human cadaveric femur from a 59 year old, 86 kg male was sourced (Anatomy Gifts Registry, 7522 Connelley Drive Suite M, Hanover, MD 21076, USA) with similar geometry to ITAP patient number 12 in the clinical trial (from whom kinematic and kinetic data in Chapter Three was sourced) and scanned using a Siemens Somatom Definition AS CT scanner (slice thickness = 0.6 mm, pixel spacing = 0.35 mm x 0.35 mm, 512 x 512 matrix). The CT scanner associated 267.4 HU to the cancellous bone insert with a mineral density of 1.15 g/cm^3 and 1375.3 HU to the cortical bone insert with a mineral density of 1.82 g/cm^3. The resultant density map was converted to an elastic modulus map (Fig. 4.2) in software that converts CT scans to FE models (Scan IP, Simpleware, Synopsis, Mountain

View, California, USA), using the density/modulus power law conversion of Morgan et al. (2003): E = 15010 $\rho^{1.83}$ which illustrates the heterogenous nature of bone.

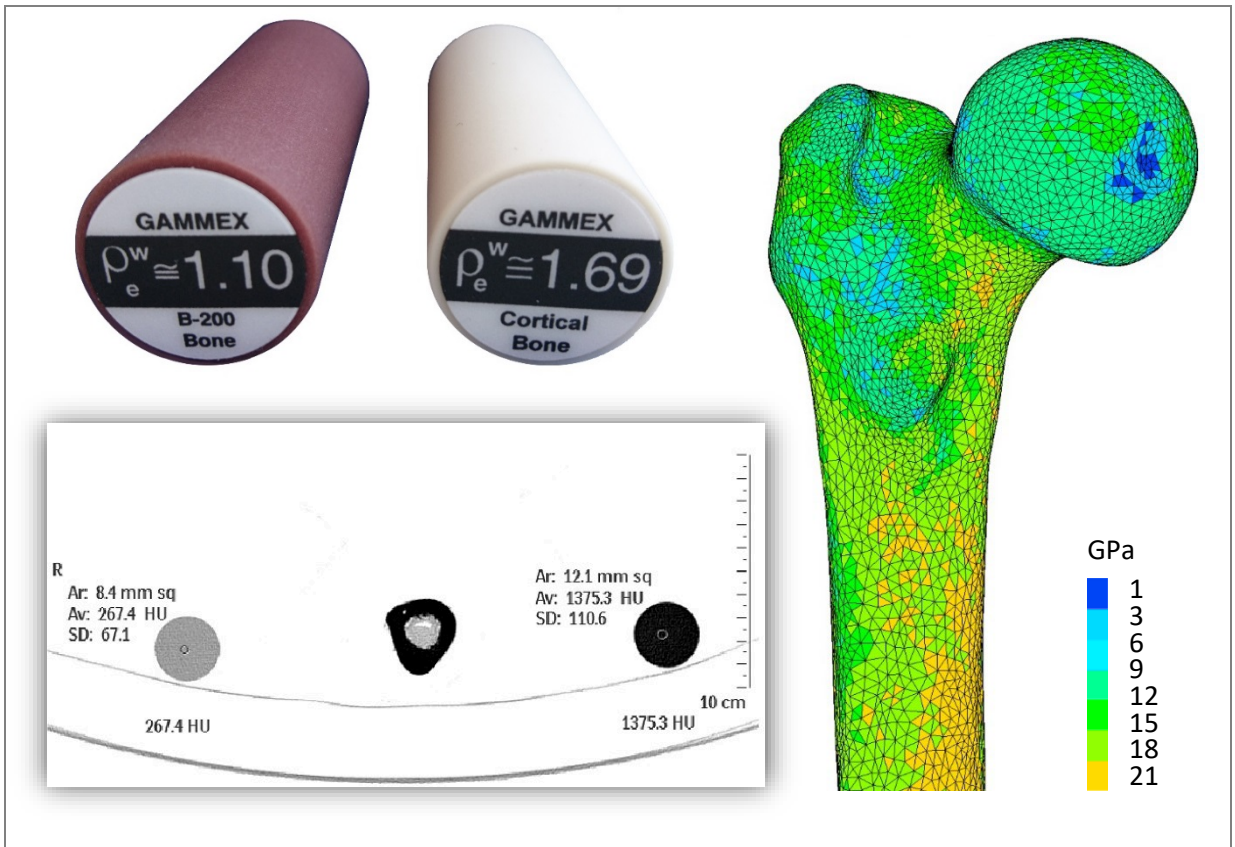

Fig. 4.2: CT bone phantoms, CT scan of bone with phantoms and Scan IP's bone stiffness map. Top left, bottom left and right respectively

4.2.1.2. The SAAP build

A computer aided design (CAD) model of a SAAP based on the ITAP design was generated (Solidworks, Dassault Systemes, France) and machined (Tritton tooling, Unit 21, Pages Industrial Park, LU7 4TZ, UK) from Ti6Al4V. The SAAP stem length was 0.12 m with a stem diameter distally of 12 mm narrowing to 9 mm proximally (dimensions equivalent to the ITAP of patient 12) allowing for a minimum of a 1 mm layer of bone cement. The collar edge shape mirrored the bone osteotomy edge and the spigot was 18 mm in diameter, the standard size used in all ITAP patients. Four cement grooves (1.5 mm deep, two radially and two longitudinally) were incorporated into the stem design as all cemented ITAP patients were of common design. No grooves were machined onto the collar surface nor was a flange added (*in vivo* these encourage bone ingrowth and soft tissue integration respectively), see Fig. 4.3.The cadaveric bone (Fig. 4.4 a) was stripped of soft tissue, the femoral anteversion angle was measured (= 12.7 °) before the bone's distal end was resected to leave 0.201 m and squared off using a calcar planer (DePuy Synthes). The fatty marrow and a small amount of cancellous bone on the endosteal surface was

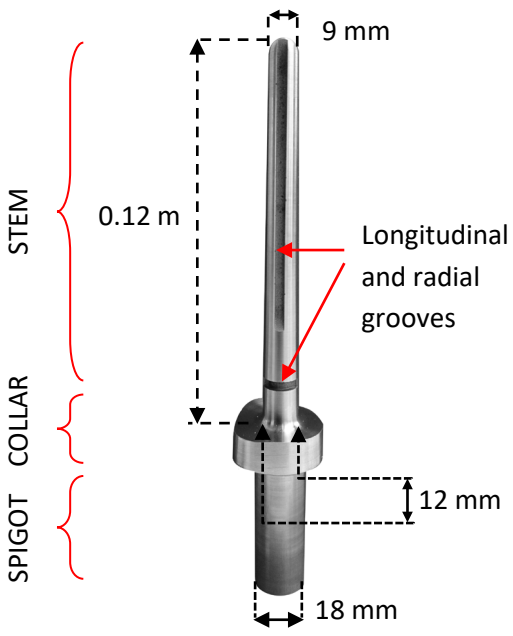

Fig. 4.3: The SAAP made for the *in vitro* study

removed, the IM canal was then washed (pulse lavage, Judd Medical, L41100, Fig. 4.4 b) and dried. A Hardinge cement restrictor was positioned in the IM canal 10 mm proximal to the stem tip and a bone cement mixing system (Cemvac™, DePuy Synthes) was used to deliver the pressurised cement in a retrograde manner (Fig. 4.4 c). The SAAP stem was inserted taking care to clean cement from osteotomy surface (Fig. 4.4 d), and the cement was left to set (Fig. 4.4 e). The SAAP spigot was inserted into a stainless-steel (T303) pot and fixed with four 6 mm grub screws (Fig. 4.5, bottom).

4.2.1.3. Strain gauges

The periosteal bone surface was cleaned, dried and smoothed with glass paper at 0.02 m and 0.11 m from the osteotomy face on each of the medial and lateral aspects. Four uniaxial gauges of 1 mm gauge length (Foil linear goblet gauge 1 mm, 11 °C STC, Tokyo Measuring Instruments Laboratory, Japan) were bonded to the bone with a flexible (1.3 GPa) adhesive (Cyanoacrylate-E, Tokyo Measuring Instruments Laboratory, Japan) along the femoral axis (Y axis in the global coordinate system), see Fig. 4.5, bottom.

4.2.1.4. Digital Image Correlation (DIC) set up

A stereo DIC system consisting of a pair of two megapixel machine vision cameras and ruggedised fixed focal length lenses (Allied Vision Technologies Marlin F-201B, Schneider Kreuznach f1.4/17 mm). The cameras were mounted on a stiff aluminium beam, and this beam mounted on a floor standing tripod. The intrinsic/internal and extrinsic/external calibration parameters of the stereo system were determined by the simultaneous photography of a calibration target containing an array of control points, and this calibration information subsequently used to determine the triaxial location in space of each correlated image speckle subset. The calibration was conducted through a control volume which fully included the whole visible region of the bone, including distance away from the camera system. Typical uncertainty measurements of this system were of the order of one micrometre per measurement point in space.

Fig. 4.4: Photos of the stages of experimental SAAP implantation into the cadaveric femur.
a = Cadaveric bone, b = Washing the IM canal, c = Filling IM canal with cement, d = Inserting implant, e = SAAP implanted

Fig. 4.5: Radiographic and photos of the SAAP in the femur

Top: ML (left) and AP (right) radiographic images of the implanted SAAP. The cement restrictor is visable at the proximal tip of the implant. The bone was stored in saline soaked cloth which is visable in the radiograph

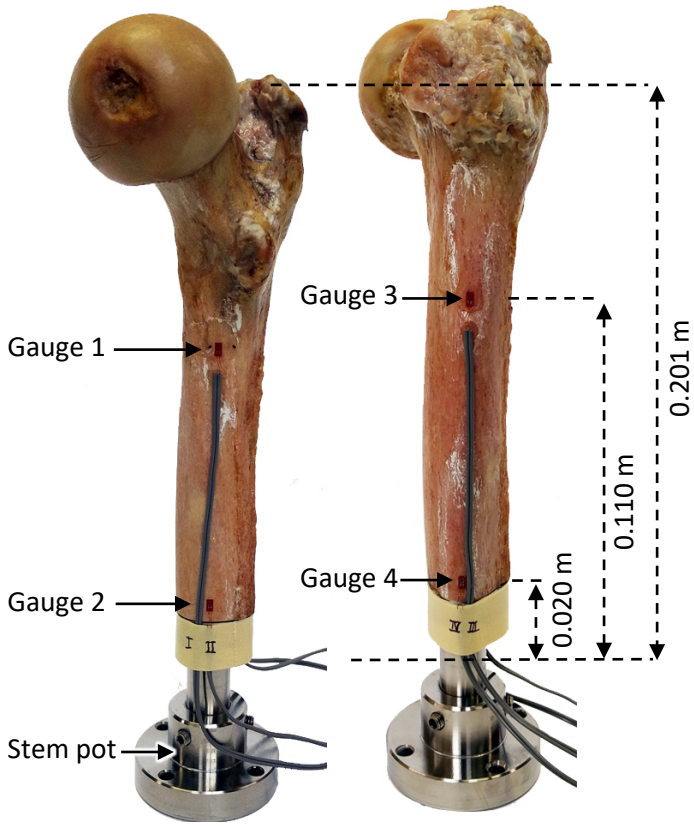

Bottom: Cadaveric femur photographed medially and laterally with SAAP implanted and potted. Showing locations of the strain gauges on the medial (left image) and lateral side (right image). Image adapted from (Ahmed et al., 2020)

Fig. 4.6: The *In vitro* model on the load test bed. Image adapted from (Ahmed et al., 2020)

4.2.1.5. Loading

The *in vitro* bone/implant model was secured to the load test bed using four M8 bolts at 6.9 ° femoral adduction, 2.0 ° flexion (and 12.7 ° anteversion) on the load test bed. Axial load was applied through planar bearings at the femoral head on a Zwick Roell, Z005, electrodynamic testing machine (Fig. 4.6). To settle the specimen a pre-load (100 N) was applied, removed and the system zeroed. Incremental loads were applied as a multiple of body weight (BW) in a range consistent with data from Bergmann et al. (2016) in steps up (loading) and down (unloading) to account for bone's viscoelastic properties from 280.9 N (0.33 BW) to 2949.8 N (3.5 BW). The desired force was maintained for three seconds in which a strain measurement at each gauge and DIC stereo image pairs were recorded from the two cameras and processed using Correlated Solutions Inc. Vic3D 8 software.

4.2.2. *In silico* model

4.2.2.1. Model concept

A method was devised to build a 'bone plug' (using the ANSYS Parametric Design Language (APDL), v.18.0, Ansys Inc., Pennsylvania, USA) inside the anatomical bone as an approach to iterate SAAP designs and run grid (mesh) refinement and sensitivity studies (Fig. 4.7). This approach made it possible to develop model complexity checking the results along the way. There was a mismatch between the exported Scan IP elements (tetrahedral) that made up the anatomical bone and the hexahedral bone plug elements. These surfaces were tied together with multi-point constraints (MPCs). Since the periprosthetic bone is the surface of interest, and there may have been some uncertainty in the transfer of stress using the MPCs, a bone layer was introduced. This method attached the exterior bone layer surface to the interior surface of the anatomical bone with the MPCs, which were not anchored to the

periprosthetic bone at all and the interior surface of the bone layer to the cement through the merging of coincident nodes (see Fig. 4.7). It also meant that the surface of interest (periprosthetic bone) was comprised of hexahedral elements (which should produce superior results, see 4.2.2.2.). Therefore, the bone plug was made of three parts; the **SAAP** was surrounded by a layer of hexahedral **cement** elements, then a layer of hexahedral **bone** elements before insertion into the anatomical bone (Fig. 4.7).

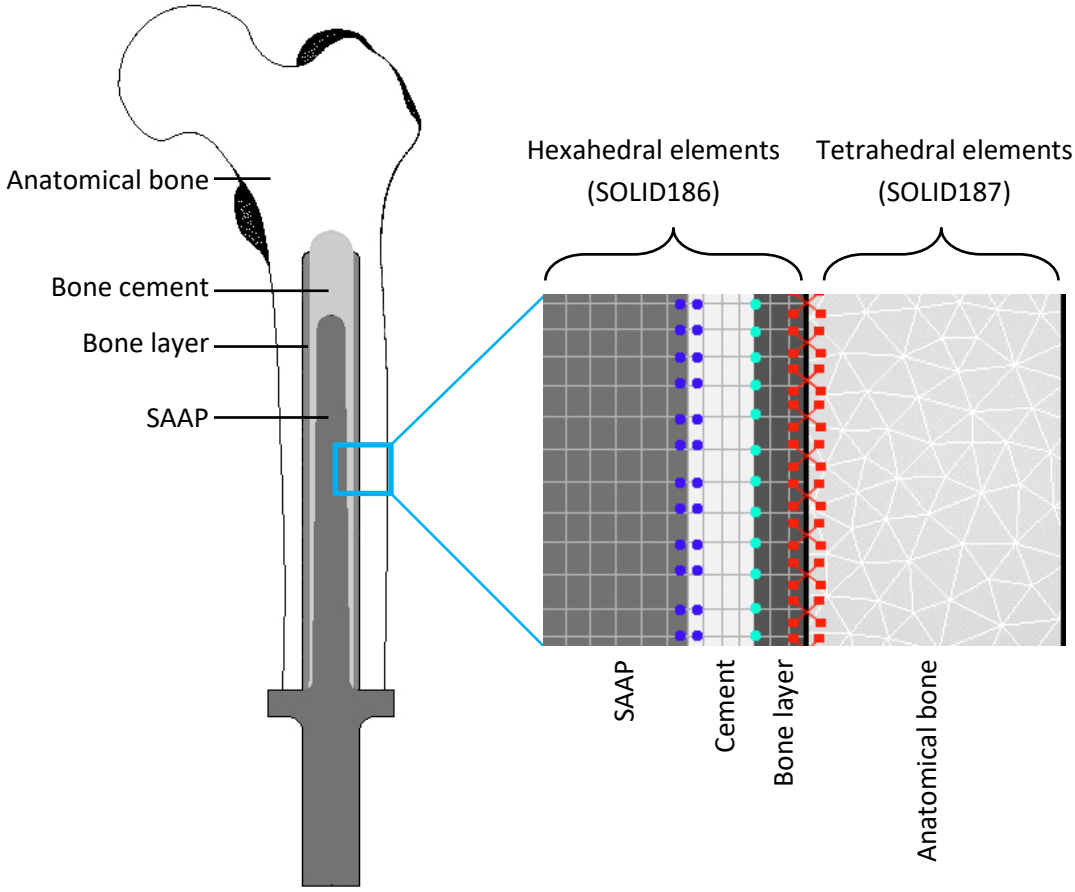

Fig. 4.7: Bone plug in anatomical bone with connections and element shapes.
Turquoise dots = merged nodes between cement and bone layers.
Blue dots = contact pair between SAAP and cement layers.
Red cross hatches = MPCs between bone layer and anatomical bone

4.2.2.2. Element choice

Hexahedral elements allowed for controlled mesh refinement through grid convergence (e.g. Richardson extrapolation, see 4.2.2.8.) furthermore, the additional nodes in the hexahedral elements allowed a higher degree and therefore better representation of the stress field being modelled. Choice of elements in biomechanical analyses vary throughout the literature, however hexahedral elements are preferred by Viceconti et al. (2000); Grecu et al. (2010) and Dickinson (2014) and in previous ITAP FEA (Newcombe et al., 2013). In the final model used for analysis, ANSYS SOLID186 elements (hexahedral)

were used; they have 20 nodes with three orthogonal translational degrees of freedom per node. The anatomical bone was built of SOLID187 elements (tetrahedral); having 10 nodes with three orthogonal translational degrees of freedom per node

4.2.2.3. Verification

Building the full 3D bone plug was performed in stages and is presented in Appendix A.4.1:

1. A 2D axisymmetric bone plug model was built to investigate the flow of forces through the assembly
2. A 3D quadrant bone plug model was built to verify consistency in the stress results with the axisymmetric model.
3. The full 3D bone plug model was built for the validation

4.2.2.4. Full bone plug (cemented) model

Build: The axisymmetric bone plug was swept through 360°. Scan IP was used to create a cylindrical cavity within the anatomical bone model with a larger diameter than the bone's intramedullary (IM) canal and was then positioned around the bone plug in a repeatable manner as follows:
The 'digital imaging and communications in medicine' (DICOM) images from the cadaveric femur CT scans were interpolated and segmented in Scan IP to produce a 3D femur model (anatomical bone) from which the distal end was resected, leaving 0.201 m (equivalent to ITAP patient 12 residual femur length). To create the cavity for the bone plug insertion a Boolean subtraction was performed in Scan IP by transforming the anatomical bone centreline to be colinear with the bone plug centre line and the global Y axis (Fig. 4.8). For details on how this was done see A.4.2.

Material properties: Using the non-homogeneous element material properties calculated from the density modulus conversion in Scan IP (see 4.2.1.1.) in the FE model may have introduced some uncertainty to the analysis. This is due to the way that finite elements handle stress transfer across boundaries of differing stiffness (Maunder et al., 1996), see Appendix A.4.3 for more. Real bone, whilst non-homogeneous, has a continuously varying elastic modulus rather than one that step changes at element boundaries. Therefore, in order to perform a FEA of bone where all approximations are known, an idealised homogenous material model should be used. Real bone is stronger in its long axis than radially or circumferentially (Bartel et al., 2006); and if the packing of the haversian systems was perfectly ordered there would not be any difference between the transverse stiffness moduli. The slightly unordered packing of the haversian systems in natural bone leads to a small difference between the transverse moduli; the circumferential direction modulus is greater than the radial direction stiffness (Ashman et al., 1984). A transversely isotropic or orthotropic material lends itself well to

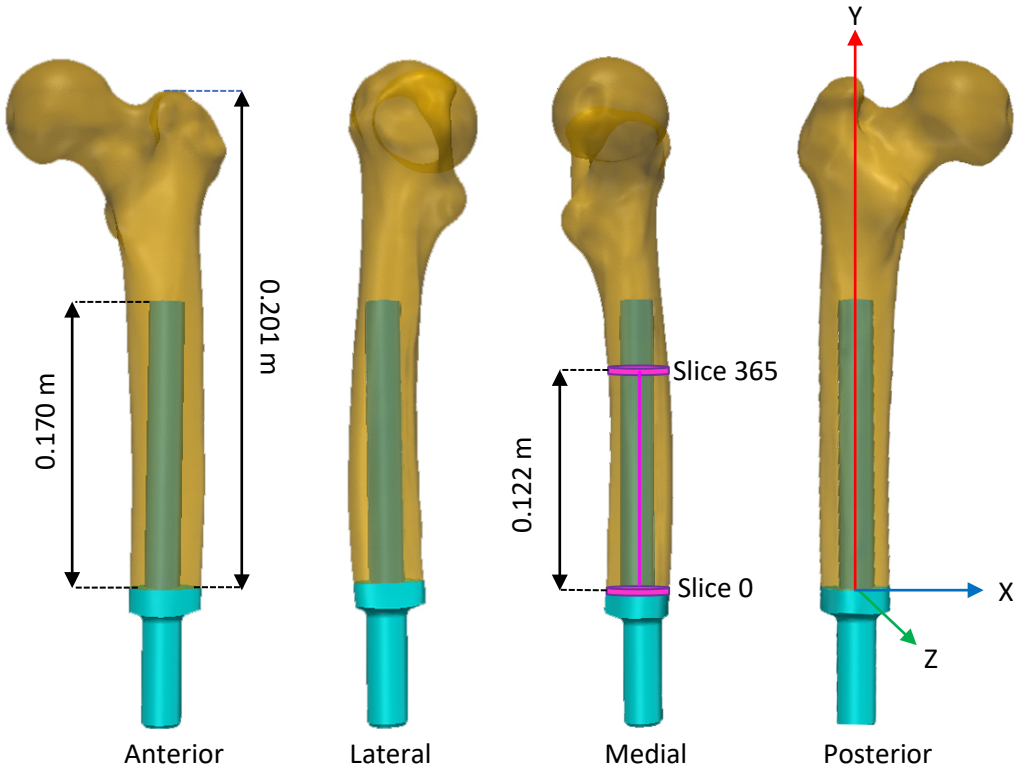

Fig. 4.8: Scan IP anatomical bone model
Showing the bone plug is aligned in all aspects (blue placeholder is shown but is not exported)

modelling cortical bone. Geraldes and Phillips (2014) discuss the merits of implant assessment using orthotropic bone properties, and others (Pidaparti and Turner, 1997, Cuppone et al., 2004, Turner et al., 1999) demonstrate experimentally an orthotropic assumption the closest approximation to the heterogenous nature of bone. Many published studies employ isotropic models, these have been shown to misrepresent bone strain when compared with orthotropic models (Peng et al., 2006). Since Scan IP does not offer orthotropic material properties the exported ANSYS file (.ans) was read into ANSYS and then written out as a .DAT file for editing. A cylindrical element coordinate system was defined where X = radial, Z = circumferential, Y = axial and orthotropic properties (Ashman et al., 1984) were attributed to the anatomical bone elements (and the bone layer elements for which a cylindrical coordinate system was scripted and appropriately invoked in the FE build):

Young's modulus	Poisson's ratio	Shear modulus
EX = 12.00 GPa	vXY = 0.22	GXY = 5.61 GPa
EY = 20.00 GPa	vYZ = 0.35	GYZ = 6.23 GPa
EZ = 13.40 GPa	vXZ = 0.38	GXZ = 4.53 Gpa

Bone cement material properties:

E = 2.00 GPa	v = 0.40

The SAAP was modelled using the ITAP material (TiAl6V4) with material properties:

E = 115.00 GPa	ν = 0.30

No cancellous bone was modelled (see results of sensitivity analysis section 4.2.2.9.)

Changes made for validation:

- The SAAP stem was tapered, since all ITAP patient cemented stems were tapered in the clinical trial. The cement layer at the distal end was 1 mm thick and increased proximally, and the bone layer was uniformly 2 mm thick (see Fig. 4.9).
- Contacts between both bone parts and the SAAP collar: Successful SAAP surgery assumes osseointegration (fully bonded surfaces) of the distal bone faces (bone layer and anatomical bone) and the SAAP collar. *In vitro* this is not the case, and the slip between the distal bone parts and the SAAP collar was modelled *in silico* by contacts two and three (see Fig. 4.9).

Interactions:

- The cement layer was fully bonded (nodes merged) to the bone layer.
- The bone layer was tied to the anatomical bone with MPC equations, i.e. fully bonded
- All contact friction was considered isotropic with a coefficient of 0.30
- Three contact surfaces were modelled:

1. Between the SAAP stem and the cement layer: Contact **one**.
2. Between the anatomical bone (osteotomy face) and the SAAP collar: Contact **two**.
3. Between the bone layer (distal face) and the SAAP collar: Contact **three**.

Boundary conditions (BC) and Load Case (LC)

BC: Four nodes on the face of the SAAP spigot were fully restrained

LC: An early stance (initial loading) LC without muscular contribution was applied as a distributed proximal load at the femoral head with the anatomical axis of the femur colinear with the global Y axis. An 842.8 N axial load (1.0 BW) was transformed (see A.4.4) to reflect osseointegrated transfemoral alignment of 6.9 ° adduction and 2.0 ° flexion (as measured with fluoroscopy by Sullavin and Zahedi (2018)), producing:

FX	FY	FZ
lateral (+) / medial (-) shear	proximal (+) / distal (-) force	anterior (+) / posterior (-) shear
+ 101.19 N	- 836.19 N	+ 29.20 N

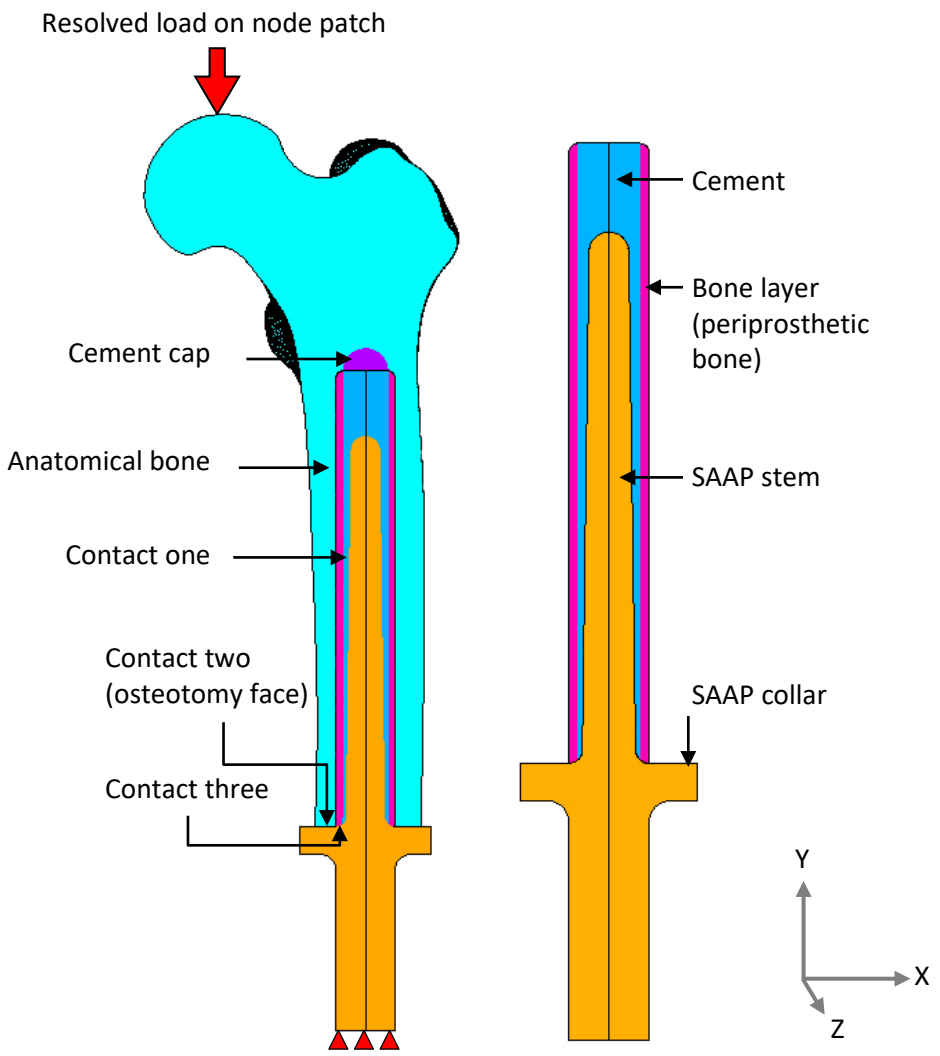

Fig. 4.9: Longitudinal section of the *in silico* model assembly
Left = Showing the bone plug inside the anatomical bone (purple cap = cement material elements, fully bonded to cement layer and anatomical bone). Right = The full bone plug. Image from (Ahmed et al., 2020)

4.2.2.5. Measurements

Strain gauge node selection: Surface nodes surrounding the central node corresponding to the centre of each strain gauge *in vitro*, were selected and the mean axial strain was calculated for the validation.

DIC node selection: To validate the *in silico* displacement, surface nodes attached to the elements representing the bone DIC visible region were selected. The nodal displacement range falling within a 95 % confidence interval (to omit any outlying nodal displacements) was calculated.

4.2.2.6. Outputs

Validation: The outputs from the *in vitro* strain gauges were compared with *in silico* strain in the longitudinal global (Y) axis and agreement was measured using the bivariate analysis, Lin's concordance correlation coefficient (CCC) (Lin and Torbeck, 1998).

The *in vitro* DIC displacement maps were compared (a.) visually and (b.) as a span of displacement (m) to the corresponding field of view *in silico,* agreement was quantified using CCC.

4.2.2.7. Transfemoral alignment for *in silico* models

When taking alignment orientation measurement from radiographs of the ITAP patients it seemed that the majority were **ab**ducted and in flexion, however it was not clear in all the radiographs whether patients were non-weight bearing or standing. Instead, I used the experimental measurements presented by Sullavin and Zahedi (2018) which showed SAAP patients in double support in **add**uction and flexion from fluoroscopy data. Thus, for the sake of the validation, I have assumed that the orientation of the patient femur in initial loading is similar to double support.

4.2.2.8. Mesh Convergence

Richardson's extrapolation (Richardson and Gaunt, 1927) was used to estimate the error in the solution in a log-log convergence plot of axial stress and element edge length.

Table 4.1: Results of Richardson's extrapolation for the bone plug with a constant refinement ratio

$r = \left(\frac{h_3}{h_2} = \frac{h_2}{h_1} = \text{constant}\right)$ and the observed convergence rate obeying: $p = \frac{\log\left(\frac{f_3 - f_2}{f_2 - f_1}\right)}{\log r}$ such that

$f.exact \approx f_1 - \frac{f_2 - f_1}{r_{21}^{p} - 1}$

		Most coarse mesh		Most fine mesh
Normalised Element Edge Length, *h*		2.000	1.000	0.500
Maximum stress in Y axis (Pa), *f*		1421900.000	1422700.000	1422800.000
Element Edge Length Refinement Ratio, *r*			2.000	2.000
Relative Error, *e*			0.056%	0.007%
Error to Exact Solution			0.008%	0.001%
Grid Convergence Index, *GCI*			0.010%	0.001%
95% Confidence Interval	lower bound		1422557.143	1422782.143
	upper bound		1422842.857	1422817.857
Estimate of Exact Solution, *f.exact*			1422814.286	1422814.286

for the bone plug model with normalised element edge lengths of 0.5, 1 and 2. A relative error of < 1 % at normalised element edge length of one (0.625 mm) was calculated and so used (Table 4.1). Anatomical bone tetrahedral element edge lengths were matched to 0.625 mm, total assembly (bone plug + anatomical bone) element count was 385,080.

4.2.2.9. Sensitivity analysis

In order to generate model credibility, the effect with which parameters that cannot be experimentally validated such as contact stiffness have on the performance indicator should be assessed. A parametric sensitivity study was used to investigate interaction sensitivities on the FE model results one parameter at a time. These were bone material properties (stiffness and material orientation) and contact properties between parts. The performance indicator was axial (Y axis) bone strain at four locations on the periosteal bone, each was the same as the four strain gauges used in the *in vitro* work (see 4.2.1.3.) results are shown in Table 4.2.

Sensitivity tests:

Isotropic baseline	……	E = 18 Gpa +/- sensitivity of 30 %
Transversely isotropic baseline	……	EX = 12 Gpa, EY = 20 Gpa, EZ = 12 Gpa +/- sensitivity of 10 %
Orthotropic baseline	……	EX = 18 GPa, EY = 20 GPa, EZ = 16 GPa +/- sensitivity of 10 %
Inhomogeneous		
ANSYS contact type	……	‘standard’, ‘no separation’, ‘bonded’ or ‘rough’
Friction baseline	……	0.3 +/- sensitivity of 20 %

Results were normalised by calculating one standard deviation (SD) as a percentage of the mean strain (at each gauge mean) of each parameter on every model (Table 4.2).

Table 4.2: Results of sensitivity study

	Location 1	Location 2	Location 3	Location 4
Bone stiffness (isotropic baseline)	12.2 %	8.8 %	12.6 %	11.0 %
Bone material orientation (transverse, orthotropic or inhomogeneous)	33.7 %	21.2 %	37.5 %	69.7 %
ANSYS contact type	3.7 %	2.9 %	4.7 %	3.3 %
Friction	3.1 %	1.0 %	2.8 %	14.2 %

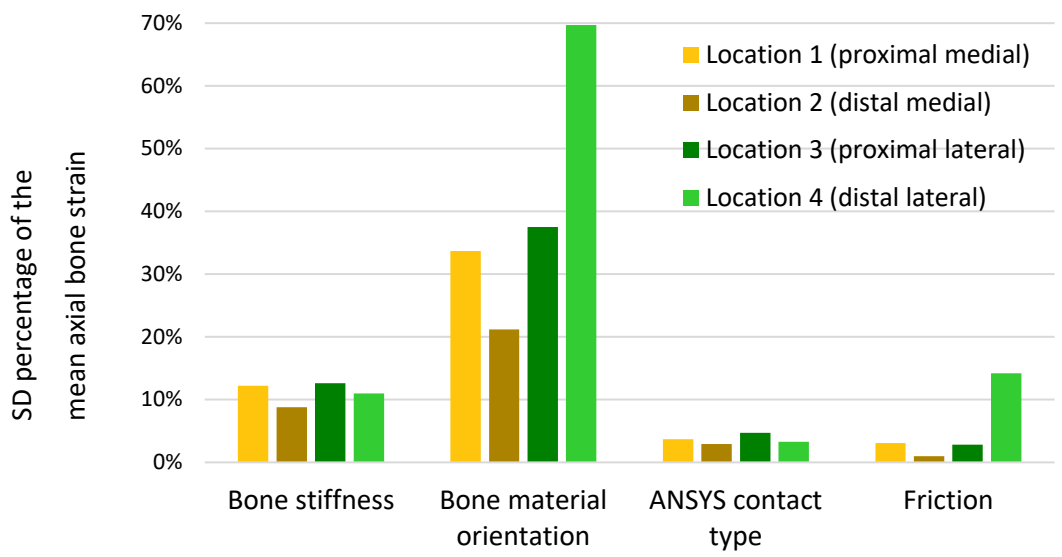

Chart 4.1: Parameter sensitivity plotted as an SD percentage of the mean axial bone strain obtained at each location for each parameter.

Axial bone strain was highly sensitive to bone material orientation at all four periprosthetic locations, in particular location four (distal lateral) where the SD was almost 70 % of the mean of the values obtained. Axial bone strain was also sensitive to absolute bone stiffness with a more equal dispersion around the mean across all four sites. The type of contact algorithm that ANSYS used and the friction coefficient exhibited much less sensitivity except for at location four where relative sensitivity (14.2 %) was observed. The large degree to which bone stiffness and material orientation influenced axial strain results is due to their effect on bone tissue deformation. Most transfemoral amputees present with osteopenic bone through disuse (Fromme et al., 2017) so the correct bone material and orientation is critical for accurate FE models. Overall, the lateral aspect of the model displayed a higher sensitivity at all four locations compared to the medial aspect, which may be due to differences between bone in compression and tension.

Cancellous bone: Each model was run with and without a cancellous bone part (proximal to the full bone plug) in the anatomical bone. Results at all four locations were the same as those without the cancellous bone part (i.e. if the femoral head was filled with cortical bone material) and so was omitted from the final model.

4.3. Results

4.3.1. Validation

4.3.1.1. Strain Gauge Validation

The CCC produced a correlation ρ_c = 0.934 between the four mean *in silico* and *in vitro* strain gauge results. *In silico* strains corresponding to gauge positions one, three and four (error = 12.17 %, 10.62 % and 9.58 % respectively) were closer to their corresponding mean *in vitro* strains than gauge two (error = 30.79%), Table 4.3.

4.3.1.2. DIC Validation

Investigating the span of displacement *in vitro* and *in silico*, generated acceptable agreement (Table 4.3: error = 3.27 %, 5.85 % and 11.79 % for displacement in X, Y and Z respectively) with a CCC of 0.997 (Chart 4.2, bottom). Fig. 4.10 illustrates the full field displacement data *in vitro* and *in silico*:

Y axis: Displacement along the Y-axis was maximum (positive) along the lateral edge and maximum (negative) along the medial edge of the bone DIC record *in silico* and *in vitro*.

X axis: The largest displacements *in silico* and *in vitro* along the X-axis were proximal and decreased distally.

Z axis: Along the Z-axis, maximum (negative) displacement was recorded at the greater trochanter *in vitro* and *in silico* and decreased in a diagonal fashion to a minimum at the femoral head *in vitro* and *in silico*.

Table 4.3: Mean strain (με) (top). Displacement (mm) (bottom)
in vitro and *in silico* (SD in brackets)

Strain (με)	**Gauge 1**	**Gauge 2**	**Gauge 3**	**Gauge 4**
Mean in vitro	-619.0 (5.2)	-388.5 (8.5)	460.5 (2.9)	36.5 (12.7)
Mean in silico	-543.65	-508.12	411.58	39.99
Error (%)	12.17	30.79	10.62	9.58
Displacement (mm)	**X axis**	**Y axis**	**Z axis**	
In vitro range	0.795	0.530	0.067	
In silico range	0.821	0.561	0.0749	
Error (%)	3.27	5.85	11.79	

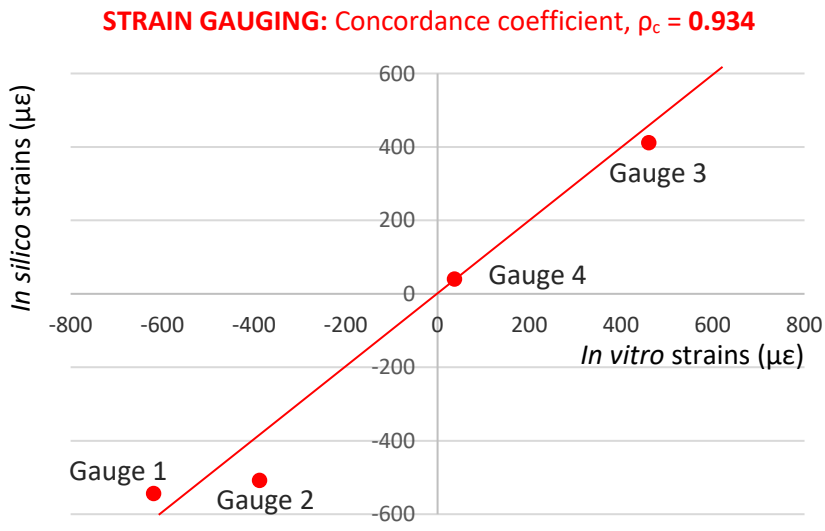

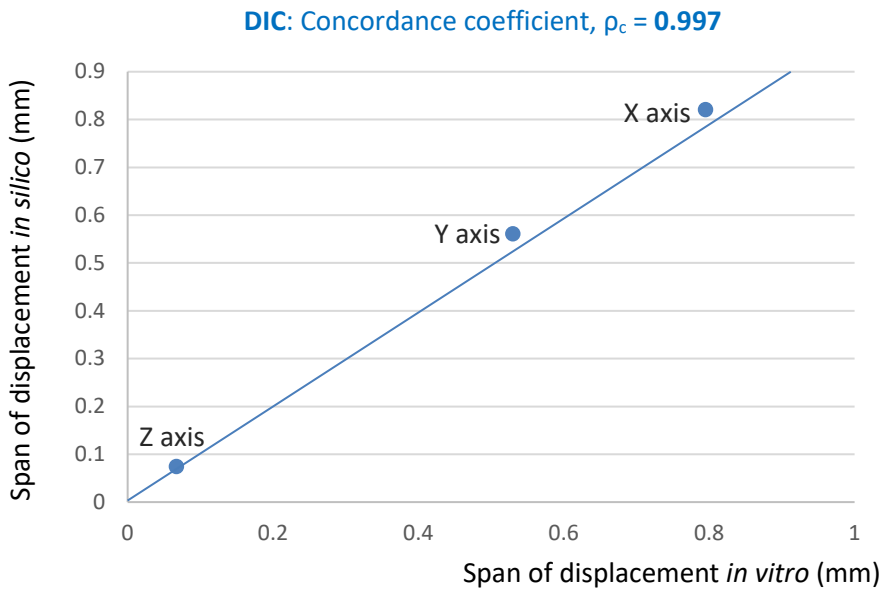

Chart 4.2: Plot *in vitro* against *in silico* strain (top) and displacement (bottom).

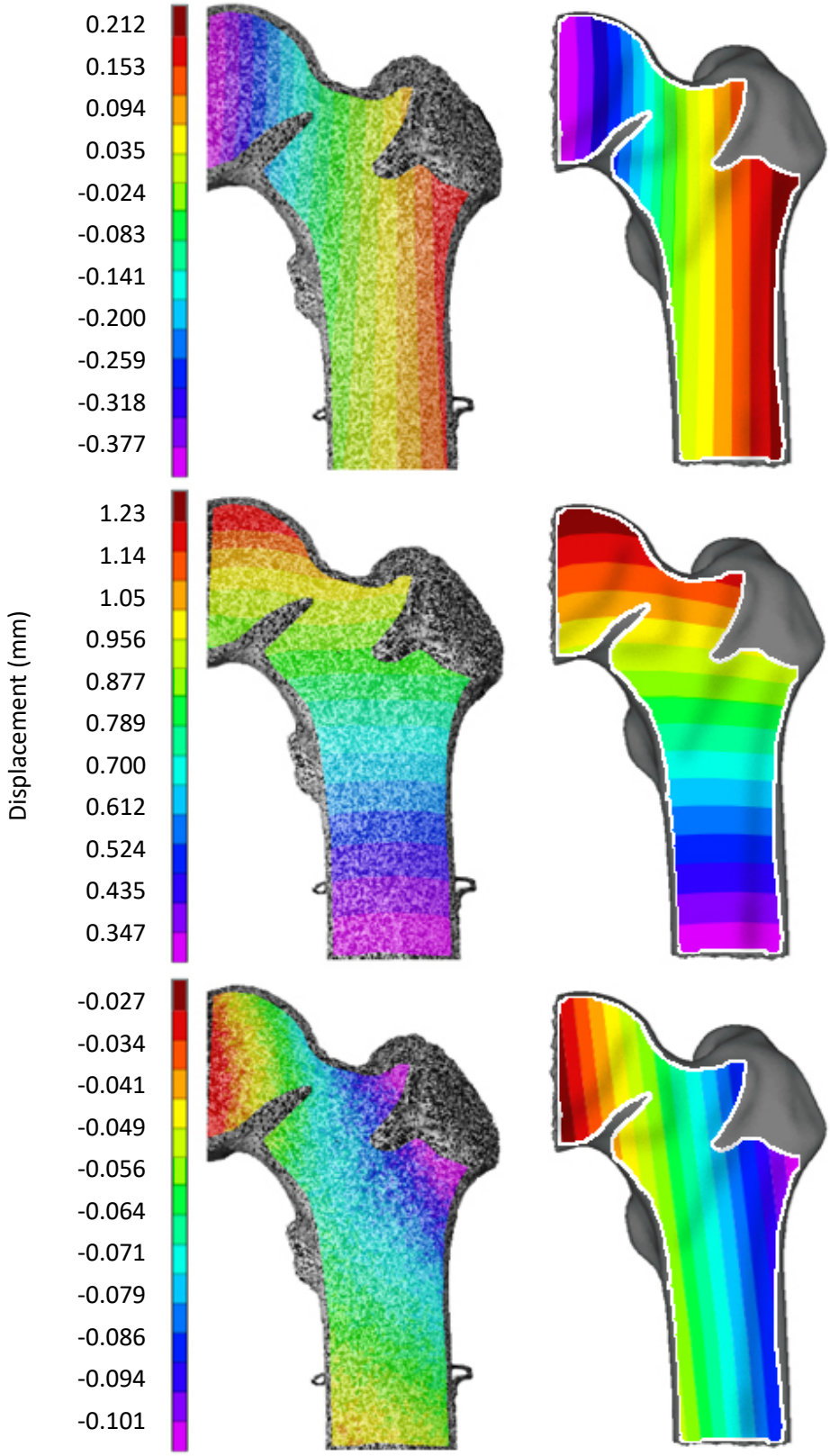

Fig. 4.10: Left = *In vitro* displacement (mm), Right = *in silico* displacement (mm). The white line on the *in silico* plots bounds the equivalent DIC camera area. Top = Y axis, Middle = X axis, Bottom = Z axis. Image from (Ahmed et al., 2020)

4.4. Discussion

A robust discrete point strain validation corroborated by a full field displacement validation of the FE model (full bone plug + anatomical bone) has been presented.

4.4.1. Strain gauge validation

Difficulties obtaining reliably accurate results strain gauging biological specimens has been outlined in section 4.1.2. The single-grid uniaxial strain gauge coupons used in this study records the *in vitro* strain in one direction. To avoid the possibility of misalignment with respect to the Y axis, a stacked rosette gauge may seem attractive. However, this introduces sources of inaccuracy; since three gauge grids are superposed onto the same measurement location which results in a thick gauge coupon, is difficult to adhere to a curved bone surface and may affect the strain readings. On balance, acceptable *in silico* agreement was observed with a CCC of 0.934; discrete point gauge discrepancies and correlations of this order are similar to those of comparable biomechanical studies (Bougherara et al., 2010, Moazen et al., 2013). There were a few sources of validation discrepancy:

- Strain gauge discrepancies could have been introduced by the visual placement of the uniaxial gauge on the bone being subject to misalignment with respect to the Y axis.
- Using an idealised bone material may have introduced a source of inaccuracy
- As mentioned in 4.1.2 differentiating the displacement values to obtain strain values suffers from the magnification of noise in the data

4.4.2. DIC validation

Displacement information from the DIC method is of attractive precision and high signal to noise ratio. Since the full surface displacement fields are available from the *in silico* model presented here, a direct comparison has been made between displacement fields, thus avoiding the inaccuracies associated with the calculation of the second order strain data from the first order displacement information. The displacement field span demonstrates good agreement with slightly larger displacements *in silico* in all axis compared with *in vitro*, with an average error of 7 % and a CCC of 0.997. It is possible that the discrepancy between the *in vitro* and *in silico* displacements in the Z axis were the result of a torsion that was not calculated by the *in silico* model. A possible reason for this may have been the way that the force was applied or accuracy of the measured angle of anteversion, none the less discrepancies of this magnitude are not unexpected in comparable DIC biomechanical studies (Dickinson et al., 2011, Grassi et al., 2013).

4.4.3. V & V in computational biomechanics

A biological tissue numerical model represents a part of a bigger living system, therefore despite a diligent V & V protocol, we must remember that there are limitations on the absolute validity of an *in silico* model. In examples such as medical devices or drug delivery models, these question marks might lead us to investigate the patient risk and assess the models sensitivity (Dar et al., 2002). Not only because the transfer of information to the patient from these types of models is rarely possible but also due to the ethical implications. In the case of a parametric study of a bone remodelling response to geometry changes in a SAAP I am comparing differences between design. The model is one step removed from a direct treatment for the patient and instead is offered as a design guide. This minimises the questions of patient risk in the balance with benefit and provides significant weight to the value of the investigation.

The validation experimental approach should reproduce the physics of the biological system and the performance indicator must be suited to the proposed use of the model (Anderson, 2006). Throughout the literature, SED as a bone remodelling indicator, was not commonly reported despite Huiskes et al. (1987) using it in their vastly cited and impactful work. To generate a higher level of model credibility, strain data was supplemented with first order displacement measurements in this study. Displacement data is not a metric that is frequently reported in the computational biomechanics literature and the increased accuracy afforded by the analysis in this study therefore sets it apart from the rest of the literature. This resulted in the V & V of the *in silico* model in this chapter being well represented by the experimental approach.

Furthermore, the FEA on TF amputee implant and bone are limited; while Xu and Robinson, 2008 did look at both the bone and implant (OPRA) response to applied loads, they measured Von Mises stress in both materials and did not experimentally validate the model (although an analytical model was presented for comparison). Tomaszewski et al., 2012a presented a bone failure implant type comparison again looking at the bone Von Mises stress but lacking validation. More recently, Thesleff et al., 2018a presented a FEA of the OPRA implant which collected the Von Mises stress and was not validated. The lack of comparable standards in the computation biomechanics literature should not set this study apart from the field but sadly it does and it is hoped that it will encourage an improved standard for future analysts.

4.5. Conclusion

This study aimed to experimentally verify and validate an *in silico* model within an acceptable margins of error. The build and test process produced a good level of agreement, as well as predicting the accuracy of the model. Future research could compare between the experimentally derived displacements and those predicted by simulation, which could be further improved by the introduction of discrete points of comparison between the two data fields. This study should provide the reader with confidence in using this model for further FEA.

CHAPTER 5

A Finite Element Analysis: how SAAP design influences bone Strain Energy Density

5.1. Introduction

To answer the question of what SAAP design features promote successful implant fixation a FEA is presented in this Chapter by building on fixation success outcomes in the ITAP clinical trial (Chapter Two). Results indicated that ITAP design variables of value for further investigation were stem taper and radius, S ratio (stem**:**residuum length) and fixation type. Using the validated FE model from Chapter Four, plus ITAP patient load cases from Chapter Three, a parametric FE study of SAAP design on periprosthetic bone is presented in this Chapter. The results will be compared with the results of the clinical trial presented in Chapter Two.

5.1.1. Hypotheses:

It is expected that geometrical changes to the SAAP stem and method of fixation to the bone will have significant effects on periprosthetic bone stress. More specifically:

- The more narrow, more tapered, shorter SAAP stems without a cortical plate will generate the greatest periprosthetic bone SED.
- A pressfit stem will generate a significantly different periprosthetic bone SED distribution compared with a cemented stem.

5.2. Method

5.2.1. Load application

Load cell results from Chapter Three provided the five FE load case (LC) inputs:

= Initial contact

= Loading response

= Mid stance

= Terminal stance

= Initial swing

Nodal load was applied using a bespoke software application (Ramsay, 2018) which loads a cloud of nodes surrounding the central node (to mitigate potential stress concentrations) with a statically equivalent set of nodal forces. The rotational and translational accelerations (inertial forces) were

calculated on the segment of interest (the bone residuum) by the kinematic software (V3D) and added to each LC (see A.5.1), the workflow summary was:

1. Marry the load cell (kinetic data collected in Chapter Three) gait stage forces LC1 – LC5 with the equivalent frame in V3D by a visual interpretation of the force graphs.
2. Collect the loads (forces and moments) at the distal and proximal ends of the V3D segment.
3. Enter V3D distal and proximal segment loads into inertial forces calculator (bespoke algorithm, see Appendix A.5.1)
4. Collect the translational and rotational accelerations at each of the five frames of interest.
5. Add the appropriate material density and the five accelerations to the five load cases applied to the ANSYS bone part (calculation of mass, centre of mass and the inertial tensor are automated in ANSYS).
6. The full load case (LC1, 2, 3, 4, 5) was then applied sequentially to four nodes of the SAAP spigot in an automated manner.

Node coordinates were consistently:

Node	X	Y	Z
N1	0.000	-0.625E-001	0.000
N2	0.000	-0.625E-001	-0.563E-003
N3	-0.520E-003	-0.625E-001	0.215E-003
N4	0.520E-003	-0.625E-001	0.215E-003

Similarly, restraints on the femoral head were consistently:

Restraint	X	Y	Z
R1	-4.450E-02	2.208E-01	8.930E-03
R2	2.400E-03	2.109E-01	-1.370E-02
R3	5.780E-03	2.078E-01	3.300E-03

5.2.2. Building models for loading

A total of 81 models (Fig. 5.1 and Appendix Table A.5.2) were built in a repeatable way as described in section 4.2.2.4. When designing the cortical plate, experienced human and veterinary orthopaedic surgeons were consulted. Plating the bone aspect under tension is the standard, therefore the lateral aspect of the bone was plated (as bone is weaker under tension than compression). Cortical plates are

typically fixed using locking screws, therefore modelling the union between the plate and the screws was considered fully bonded (Caiti et al., 2019). Furthermore, complete osseointegration is expected between the cortical plate and the periosteal bone and so a fully bonded union between these surfaces was modelled (coincident nodes merged). Finally, the plates were modelled using current techniques in patient specific design whereby a Boolean subtraction operation of the bone from the plate shapes it to perfectly hug the bone periosteum contours.

Pressfit models (which cannot be independently validated due to the reliance on osseointegration between the SAAP stem and periprosthetic bone) were built in the same way as the cemented equivalents except the cement layer was modified to cortical bone properties (effectively thickening the bone layer). In order to not deviate into a different class of problems, and therefore validate, the question of how to model the pressfit interaction arose. Clinically, the ITAP is manufactured as a line to line fit with the diameter of the IM canal of the bone layer. An interference fit is introduced by the plasma spray coating of HA on the stem (150 -200 µm). Ideally the SAAP stem would have been modelled as line to line with the bone layer and the HA coating would have been modelled as a separate layer around the SAAP stem, thus allowing the interference mechanics of the problem to be modelled by compressing the HA layer. Instead, a radial interference fit (Equation 5.9) was applied as follows: A thermal expansion was applied directly to the SAAP stem using the coefficient of thermal expansion for Ti6Al4V (8.6 e^{-6} °C $^{-1}$), the radius of the stem, and a 50 µm displacement was used which pertains to the ideal interference of a titanium alloy hip stem (Abdul-Kadir et al., 2008).

$$u = r\,\alpha\,\Delta T$$

T = temperature (°C)
u = displacement (m)
r = SAAP stem radius (m)
α = coefficient of thermal expansion (°C^{-1})

Eqn. 5.9

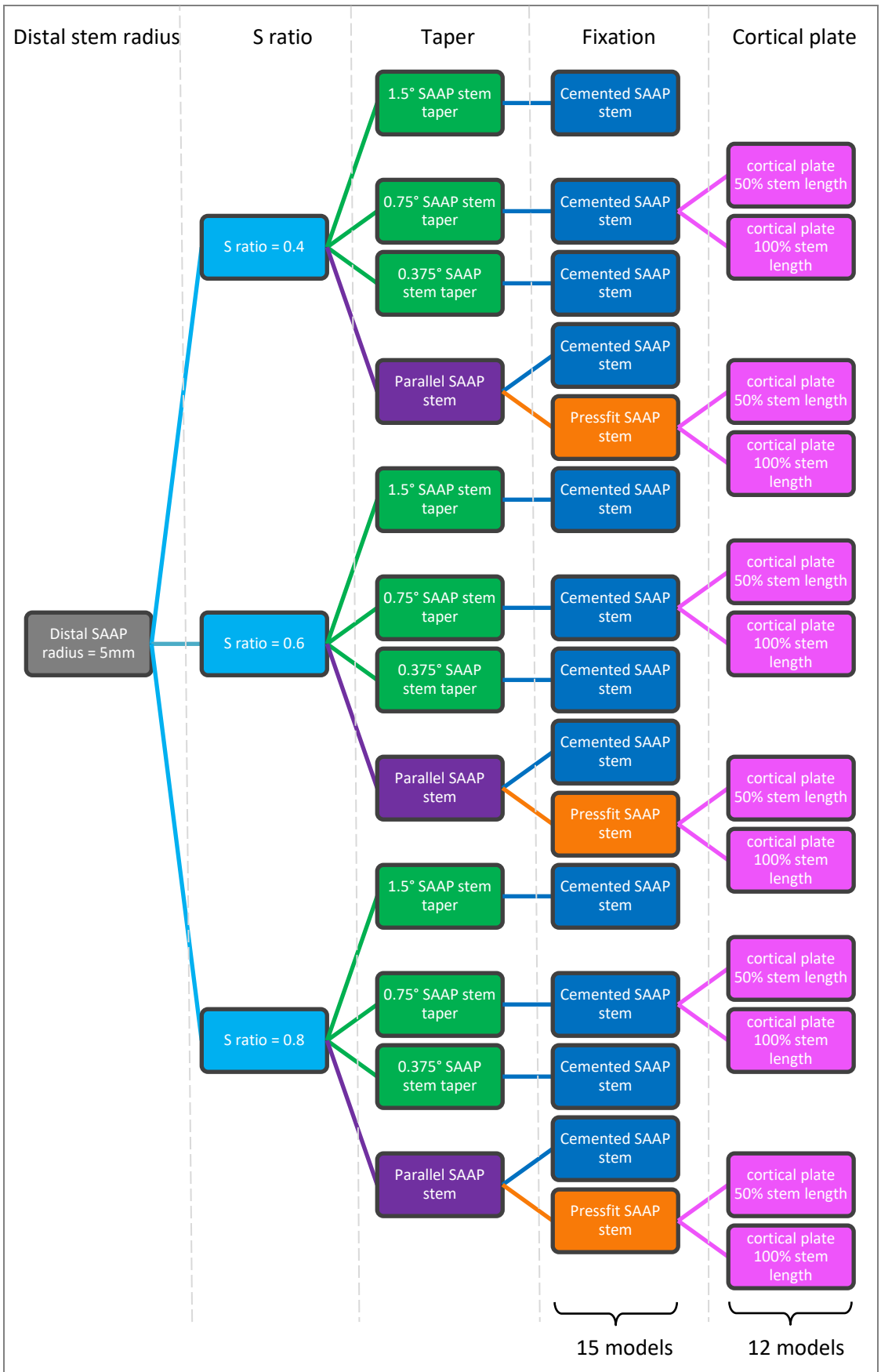

Fig. 5.1: All SAAP models built for a 5 mm distal radius SAAP stem.
The same models were run for a 6 mm and 7 mm distal radius stem. Total models = 81.

5.2.3. Adapting the validated model to represent clinical conditions

Contacts: After model validation (Chapter Four), two of the three contacts (the distal tips of the bone layer / SAAP collar and the anatomical bone osteotomy face / SAAP collar (contacts 2 and 3 in Fig. 4.9)) were replaced with a tied interaction (nodes merged). Bone in these regions is modelled as osseointegrated with the SAAP collar; in the strictest sense this is not a time = 0 occurrence. None the less, to comparatively analyse models with different fixation methods this approximation was assumed.
Density: Osteopenia and osteoporosis differ only in the amount that they diverge from the average bone mineral density (BMD) for that population (sex, age, race) (Kanis et al., 2000). A number of studies publish the characteristic findings of osteoporosis in radiographs of patients with lower limb amputations (Benichou and Wirotius, 1982, Kulkarni et al., 1998). The condition arises as a result of disuse atrophy (or strain adaptive bone resorption) and has some of the hallmarks of osteoporosis observed in the elderly including absence of osteocytes and concentric joint space narrowing. The material density of both the bone layer and the anatomical bone were reduced by 30 % (to 1.203 gcm^{-3}) to reflect this (Rush et al., 1994, Sherk et al., 2008, Tomaszewski et al., 2012b).
Material stiffness: Further signs of osteoporosis in the ageing patient are increased bone porosity, changes in the material distribution in space (e.g. an increase in the inner and outer cortex geometry (Tong et al., 2015)) and physiological changes associated with ageing such as mineral composition (Currey, 2003). Bone *strength* is influenced by all of these factors (Osterhoff et al., 2016) and so must be accounted for in FE models. It has been calculated that the effect of osteoporosis in ageing bones degrades in material *stiffness* by ~ 2 % per decade (Burstein et al., 1976). Osteoporosis as a result of atrophy disuse, rather than ageing, only accounts for 60 % of these effects (Ammann and Rizzoli, 2003). Therefore, in conjunction with a decrease in bone density in my FE model a 1.2 % decrease in material stiffness was applied (in all directions) to the material model in use (Ashman et al., 1984) to give:

Young's modulus	Poisson's ratio	Shear modulus
EX = 11.86 GPa	vXY = 0.22	GXY = 5.54 GPa
EY = 19.76 GPa	vYZ = 0.35	GYZ = 6.13 GPa
EZ = 13.24 GPa	vXZ = 0.38	GXZ = 4.48 Gpa

5.2.3.1. Data acquisition

Each model was run with five load cases and stored as a results file with five load steps solutions. All nodes along a centreline of each longitudinal aspect (lateral, medial, anterior, posterior) from the base of the stem to the tip, on the (periprosthetic) bone layer were obtained and placed into a selection. SED (Jm^{-3}) was calculated at each node (Equation 5.1) and stored as a result for that aspect with its

corresponding distance (m) along the SAAP stem (Y axis). Charts were produced with SED (Jm^{-3}) along the Y axis and distance along the SAAP stem (m) along the X axis (see results).

$$\frac{\left((\sigma_x \times \varepsilon_x) + (\sigma_y \times \varepsilon_y) + (\sigma_z \times \varepsilon_z) + (\sigma_{xy} \times \varepsilon_{xy}) + (\sigma_{yz} \times \varepsilon_{yz}) + (\sigma_{xz} \times \varepsilon_{xz})\right)}{2} \qquad \textit{Eqn. 5.1}$$

5.2.3.2. Grouping

Three model groups were created (see Fig. 5.2). The tapered group were all cemented, the parameters investigated were stem taper, length and radius. The parallel group parameters investigated were stem fixation type, radius and length. The cortical plated group parameters investigated were fixation type and a plated model verses a non-plated equivalent. The models for each comparison and SETS they are in are presented in Appendix Table A.5.3.

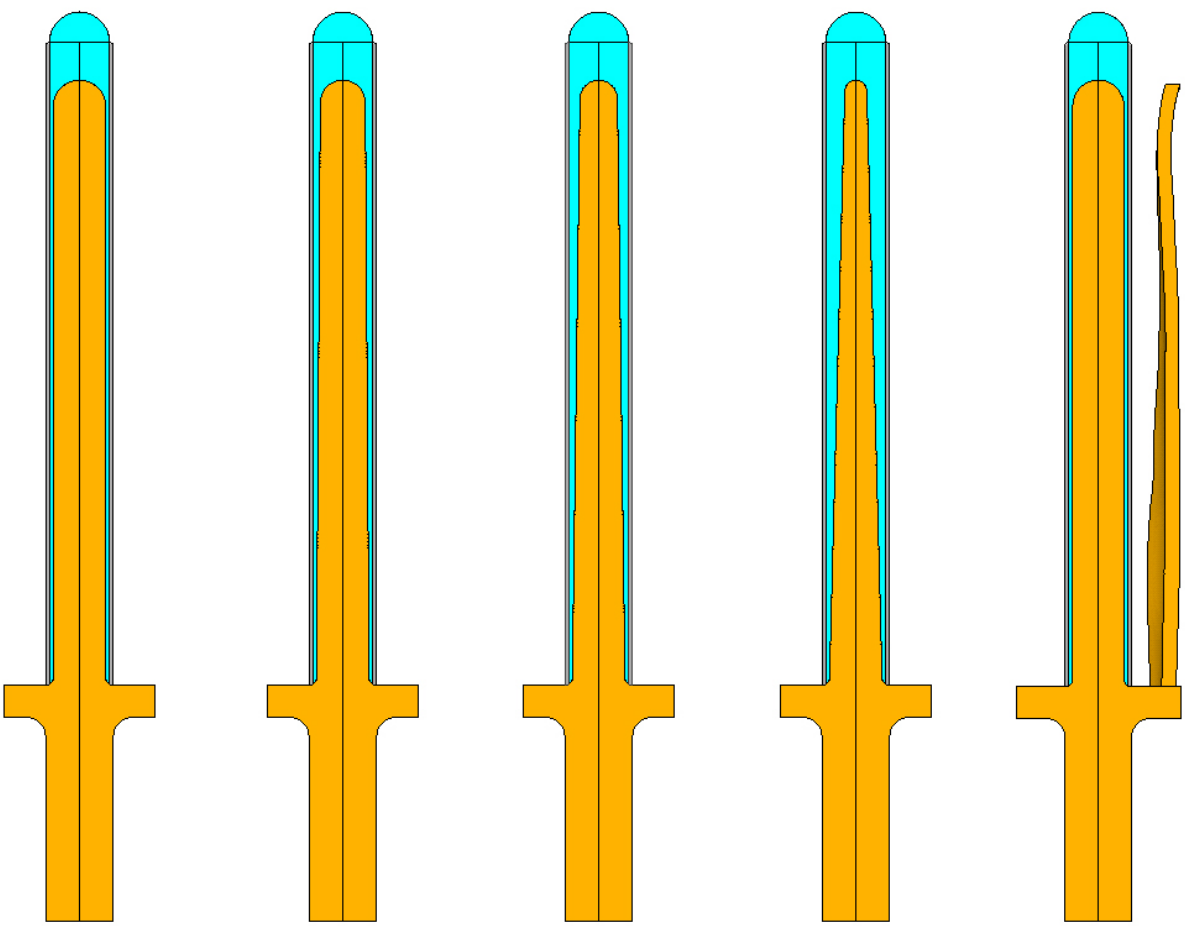

Fig. 5.2: longitudinal sections of 7 mm radius, 0.16 m stemmed, cemented FE bone plug models from left to right: parallel, 0.375 ° , 0.75 °, 1.5 ° stem taper, full length cortical plate. Orange = SAAP, turquoise = cement, grey = bone layer

5.2.4. Statistical methods

A one way analysis of variance (ANOVA) was used to determine statistical significance between the means of three or more groups at $\alpha = 0.05$ where the null hypothesis (H_0) assumed no significant difference. When a comparison between two distributions was required the student T test was used assuming unequal variances at $\alpha = 0.05$ where the null hypothesis (H_0) assumed no significant difference between pairs. When the ANOVA delivered a non-significant result, a post hoc T test between each pair in the group was run to determine what the relationship between pairs were.

5.3. Results

SED result charts for the parameters under investigation

A representative chart for each SET is displayed in the results. All results and discussion will cover all charts from all SETS in each group (tapered, parallel and cortical plated models).

Key for charts: Each governing colour (dark red, blue or green) has one or two supplementary colours of the same (but lighter) hue. Together these form a ***colour gradient***.

Key for tables: Each of the three groups of implants (tapered, parallel and cortical plated) are presented in the tables below. Each table is coloured depending on the group of implant and the text thereafter is bound by the same colour (the same colour also carries through to the discussion). The table colours are completely unrelated to the colours used in the presentation of the data on the charts. For the tapered implants the table is cyan, for the parallel implants the table is fuchsia and for the cortical plated implants the table is mustard coloured. Under the table group heading is a list of the SETS of models and metric that is being compared in bold text. The non-bold text states which of these SETS have been selected as representative and are displayed. All charts are presented in all four aspects with the title of each chart stating the aspect and the load case shown. Underneath the last aspect chart is the key for the data plotted. Following the last chart is a statistical analysis for that data set followed by the results section.

Chart 5.1 compares tapered stem taper and stem length

(Chart 5.2 is a magnification of the lateral aspect of Chart 5.1)

Chart 5.3 compares tapered stem radii

Chart 5.4 compares parallel stem fixation

(Chart 5.5 is a magnification of the lateral aspect of Chart 5.4)

Chart 5.6 compares parallel stem radii

Chart 5.7 compares plated (2 lengths) to non-plated implants

5.3.1. TAPERED STEM GROUP

Stem taper and stem length (SETS A (or D), B (or E) , C (or F))

Comparing stem tapers and lengths in all model result SETS A – C and D – F (stem radius 5 – 7 mm).

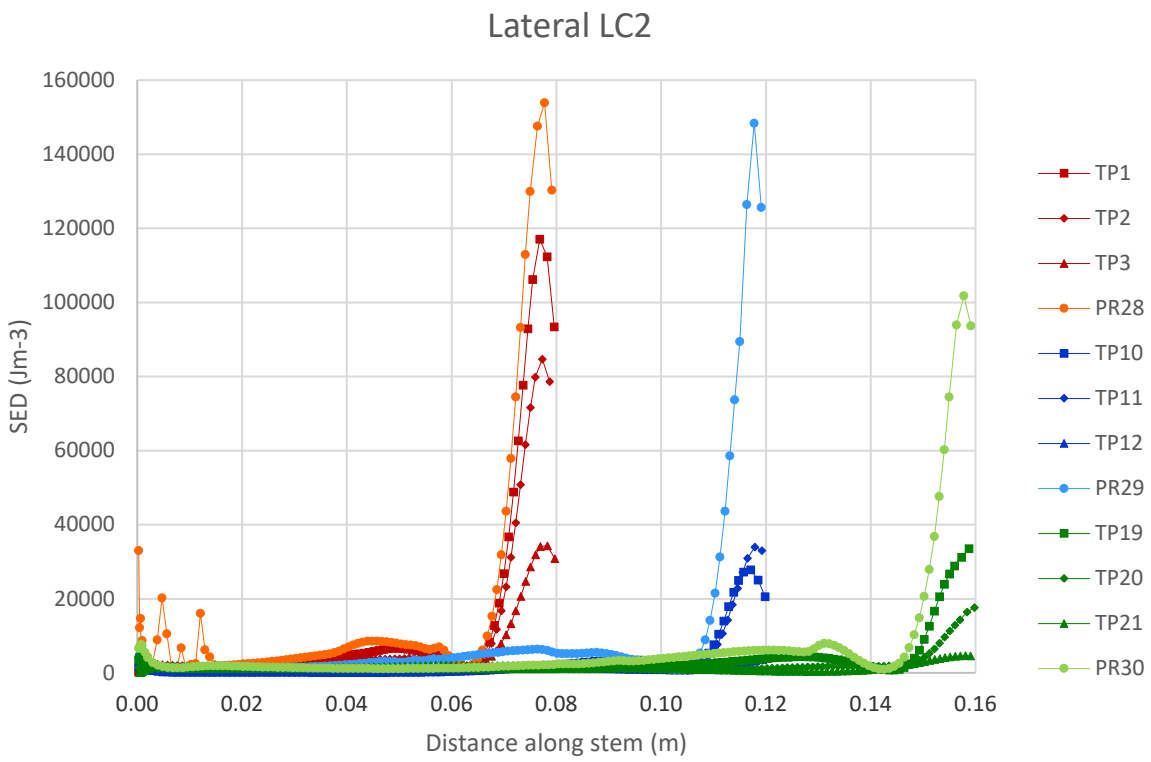

Chart 5.1 (lateral): SED to compare **taper** in periprosthetic bone under LC2

SET A in tapered, cemented stems:

Governing colour: Red = 0.08 m, blue = 0.12 m, green = 0.16 m stem length

Line markers: Circle = parallel, square = 0.375 °, diamond = 0.750 °, triangle = 1.500 ° stem taper

Colour gradient: Stem taper (dark = tapered, light = parallel)

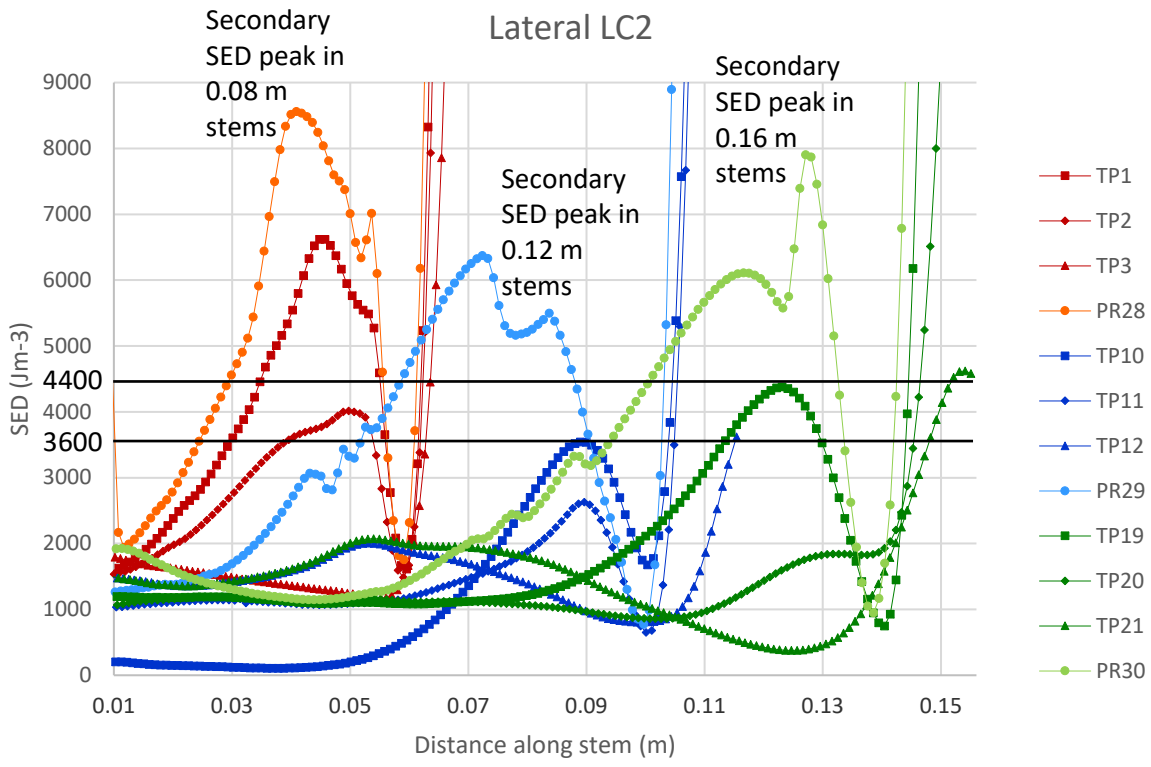

Chart 5.2 (above only): Magnified scale SED to compare **taper** in the lateral aspect in periprosthetic bone under LC2 SET A in tapered, cemented stems

<u>In the lateral aspect</u>

SED distribution & magnitude: Distribution was dominated by a relatively large primary periprosthetic bone SED peak in all stems at the stem tip. A secondary periprosthetic bone SED peak was also observed ~ 2/3 proximal to the stem base (Chart 5.2). All load cases elicited a similar periprosthetic bone SED distribution to each other, but magnitudes varied; the primary peak under LC1 and LC5 was the same order of magnitude as the secondary peak in all stems. Under LC2 – LC4 the primary periprosthetic bone SED peak was at least one order of magnitude greater than the periprosthetic bone SED of the secondary peak.

Stem taper parameter: As taper increased from circle → square → diamond → triangle line marker, the primary peak periprosthetic bone SED decreased. All stems apart from the 1.5 ° tapers (and the 0.75 ° taper in the 0.16 m stem) elicited a secondary peak, which similarly decreased as stem taper increased.

Stem length parameter: Periprosthetic bone SED magnitude decreased as stem length increased in otherwise equivalent stems under LC2 – LC4 at the primary periprosthetic bone SED peak (except for SET A (or D) under LC4 where the 0.12 m parallel stem primary peak periprosthetic bone SED was greater than the 0.08 m equivalent stem). Under LC1 and LC5 the periprosthetic bone SED was

greatest in the 0.12 m > 0.08 m > 0.16 m stems at the primary periprosthetic bone SED peak except for in SET C (or F) under LC1 where periprosthetic bone SED decreased with increased stem length. At the secondary periprosthetic bone SED peak, all stems under all load cases generated a periprosthetic bone SED *increase* as stem length increased.

Remodelling threshold: In SET A, all 0.08 m stem primary peak periprosthetic bone SED values and the secondary peak periprosthetic bone SED values of the parallel and 0.375 ° taper stem was above the homeostatic remodelling threshold (0.0044 MPa or 4400 Jm^{-3}). The 0.75 ° tapered stems secondary periprosthetic bone SED peak fell within the homeostatic periprosthetic bone SED range and the 1.5 ° tapered stem secondary periprosthetic bone SED peak fell below the homeostatic remodelling threshold (3600 Jm^{-3}). All 0.12 m stems primary peak periprosthetic bone SED values and the parallel stemmed secondary periprosthetic bone SED peak was above the homeostatic remodelling threshold (4400 Jm^{-3}), with the remaining secondary periprosthetic bone SED peaks of the more tapered stems below the homeostatic remodelling threshold (3600 Jm^{-3}). All 0.16 m stems primary peak periprosthetic bone SED values and the parallel stemmed secondary peak periprosthetic bone SED, were above the homeostatic remodelling threshold (4400 Jm^{-3}). The 0.375 ° tapered stem secondary periprosthetic bone SED peak fell within the homeostatic bone SED range and the 0.75 ° and 1.5 ° tapered stems secondary periprosthetic bone SED peak fell below the homeostatic remodelling threshold (3600 Jm^{-3}). Similar secondary periprosthetic bone SED peak distribution results were observed in SETS B and C; as radius increased more of the secondary peak periprosthetic bone SED values were above the homeostatic remodelling threshold. In SET C, all secondary peak periprosthetic bone SED values were above 4400 Jm^{-3}.

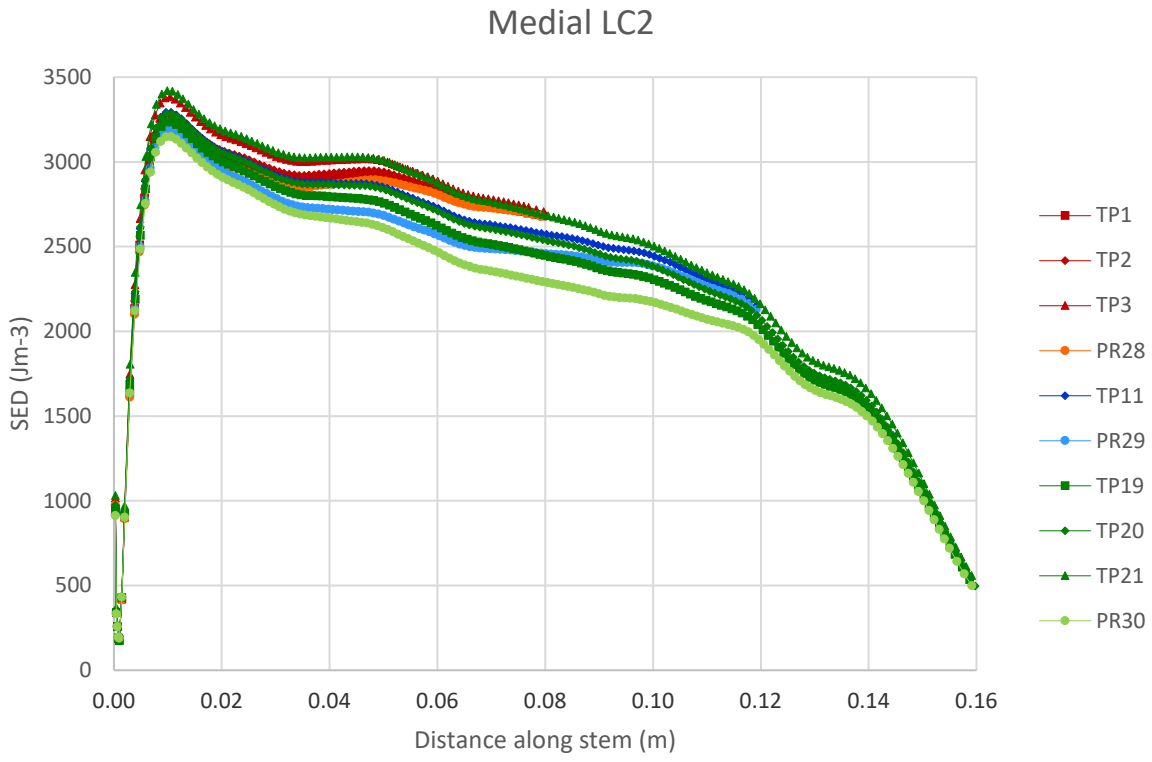

Chart 5.1 (medial): SED to compare **taper** in periprosthetic bone under LC2
SET A in tapered, cemented stems:
Governing colour: Red = 0.08 m, blue = 0.12 m, green = 0.16 m stem length
Line markers: Circle = parallel, square = 0.375 °, diamond = 0.750 °, triangle = 1.500 ° stem taper
Colour gradient: Stem taper (dark = tapered, light = parallel)

<u>In the medial aspect</u>

SED distribution & magnitude: Under LC1, the 0.08 m and 0.12 m stems elicited a gradually increasing periprosthetic bone SED from distal to proximal, the 0.16 m stem followed this distribution with a more rapid rise in periprosthetic bone SED from 0.12 m to a peak at 0.14 m followed by a rapid periprosthetic bone SED reduction to the stem tip. The distribution was very similar under LC5 however the 0.12 m stems also elicited a decrease in periprosthetic bone SED (from 0.08 m to the stem tip). Under LC2 – LC4, after an initial spike at 0.01 m from the stem base, 0.08 m stems elicited a gradually increasing periprosthetic bone SED from halfway along the stem length after a slight dip in periprosthetic bone SED (except under LC2 in SET A which gradually decreased). A similar initial periprosthetic bone SED distribution was obtained in the 0.12 m and 0.16 m models but in all, after 0.08 m, a decrease in periprosthetic bone SED was observed. The decrease was more pronounced in the 0.16 m stems than the 0.12 m stems, where it dipped to almost the starting periprosthetic bone SED (~ 500 Jm^{-3}) at the stem tip.

Stem taper parameter: In all stems under LC2 – LC4, an increased stem taper led to an increased periprosthetic bone SED along the length of the stem (opposite result from the lateral aspect). Under

LC1 and LC5 the distribution as a result of stem taper were mixed; predominantly an increased stem taper led to a decreased periprosthetic bone SED.

Stem length parameter: In general, the periprosthetic bone SED magnitude decreased as stem length increased. The 0.08 m stems under all load cases produced a higher periprosthetic bone SED than the longer stems apart from the most tapered (1.5 °) 0.12 m and 0.16 m stems up to 0.04 m from the stem base.

Remodelling threshold: Under LC3 and LC4 the distal length of all stems was within or above the remodelling threshold in SET A but all stems were under the remodelling threshold under LC1, LC2 and LC5. In SET B under LC2 the entire length of the 0.08 m stems was within or above the remodelling threshold. This was also observed in SET B under LC3 and LC4 in all stem lengths, LC1 and LC5 in SET B in all stems were under the remodelling threshold. In SET C, all stems except for the parallel 0.16 m stem under LC 2 – 4 produced periprosthetic bone SED within or above the remodelling threshold. SET C under LC1 and LC5 similarly fell below the remodelling threshold in all stems.

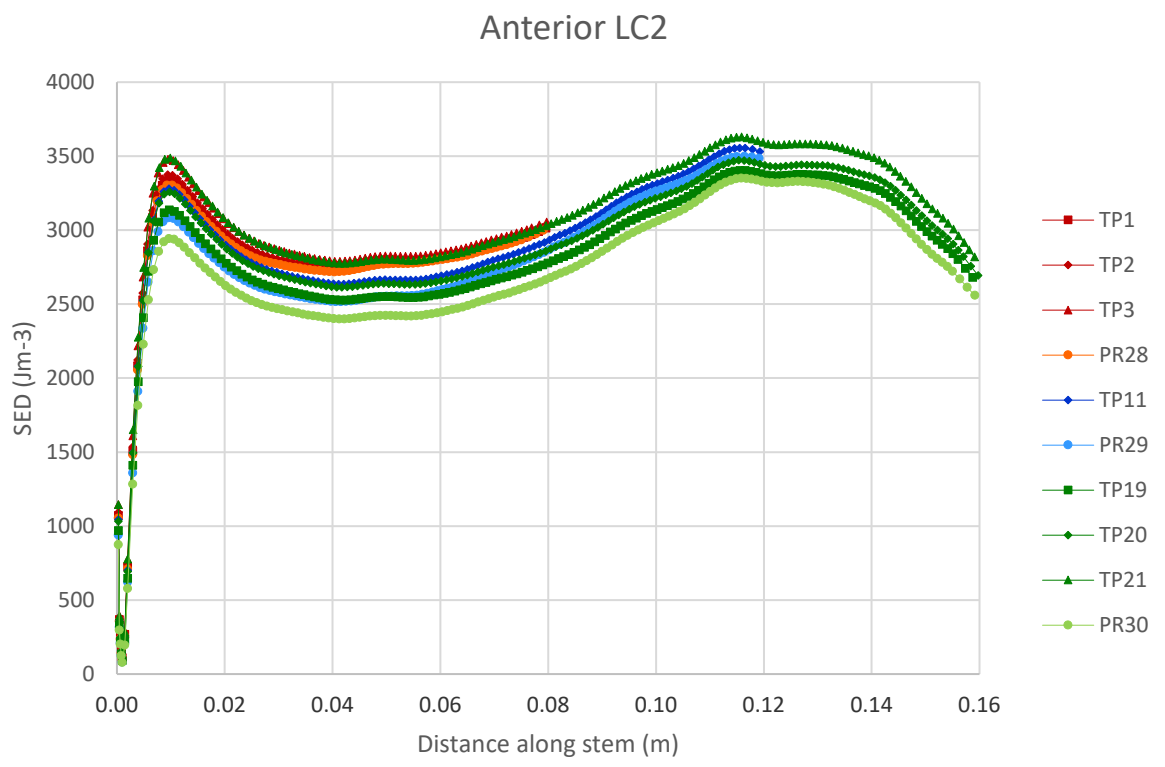

Chart 5.1 (anterior): SED to compare **taper** in periprosthetic bone under LC2
SET A in tapered, cemented stems:
Governing colour: Red = 0.08 m, blue = 0.12 m, green = 0.16 m stem length
Line markers: Circle = parallel, square = 0.375 °, diamond = 0.750 °, triangle = 1.500 ° stem taper
Colour gradient: Stem taper (dark = tapered, light = parallel)

<u>In the anterior aspect</u>

SED distribution & magnitude: In 0.08 m and 0.12 m stems under LC1 and LC5 there was an incremental increase in periprosthetic bone SED from distal to proximal where the 0.12 m stems elicited ~ triple the periprosthetic bone SED at the stem tip. Similarly, the 0.16 m stems elicited an increasing periprosthetic bone SED until 0.14 m wherein a peak was reached. In LC2 – LC4 after an initial SED spike at 0.01 m along the stem the distribution either gradually increased (under LC2), stayed constant (under LC3) or decreased (under LC4) until the step tip in the 0.08 m and 0.12 m stems. The same was observed in the 0.16 m stems, however towards the tip the periprosthetic bone SED distribution peaked at its highest (LC2) or lowest (LC4) value at ~ 0.12 m along the stem from the most distal point. Thereafter the periprosthetic bone SED decreased, plateaued or increased (LC2, LC3, LC4 respectively) to the stem tip. Most 0.08 m stems elicited the highest SED in the periprosthetic bone; this observation was marginal under LC1 and LC5 and more pronounced in LC2 – LC4.

Stem taper parameter: In all stems under LC2 – LC4, an increased stem taper led to an increased periprosthetic bone SED along the length of the stem. Under LC1 and LC5 there was little

differentiation in periprosthetic bone SED values between stems of different taper, except for the 0.16 m stems that clearly displayed a greater periprosthetic bone SED with an increased taper. All distributions under LC1 and LC5 produced a periprosthetic bone SED increase along stems from distal to proximal.

Stem length parameter: The 0.16 m stems produced slightly lower periprosthetic bone SED values than the 0.12 m stems with the exception of the 1.5 ° taper 0.16 m stem under LC2 – LC4 which elicited higher periprosthetic bone SED than all 0.12 m stems and some 0.08 m stems (those of SET A (or C) under LC2, LC3 and LC4).

Remodelling threshold: Periprosthetic bone SED in SET B and SET C models fell below the remodelling threshold (3600 Jm^{-3}) under LC1 and LC5 except SET C under LC5 in the proximal (0.10 m to stem tip) part of the 0.12 m and 0.16 m stems which were above the bone remodelling threshold. This was also observed in SET B under LC5. In SET B, 0.08 m stems under LC2 and SET C, 0.08 m and 0.12 m stems apart from the parallel and 0.375 ° taper under LC2 and LC3 fell within or above the remodelling threshold proximal to 0.02 m from the stem base. In SET C under LC3 all 0.08 m and 0.12 m stems (plus the 1.5 ° taper 0.16 m stem) were within or above the bone remodelling threshold. In SET C under LC4 this was only observed at the initial periprosthetic bone SED spike and up to 0.02 m from the stem base in all stems apart from the parallel 0.16 m one. Under LC5 in SET C all 0.12 m and 0.16 m stems were above the bone remodelling threshold from 0.10 m along the stem from the most distal point. This was also observed in SET B under LC5 but only proximal of 0.11 m from the most distal point.

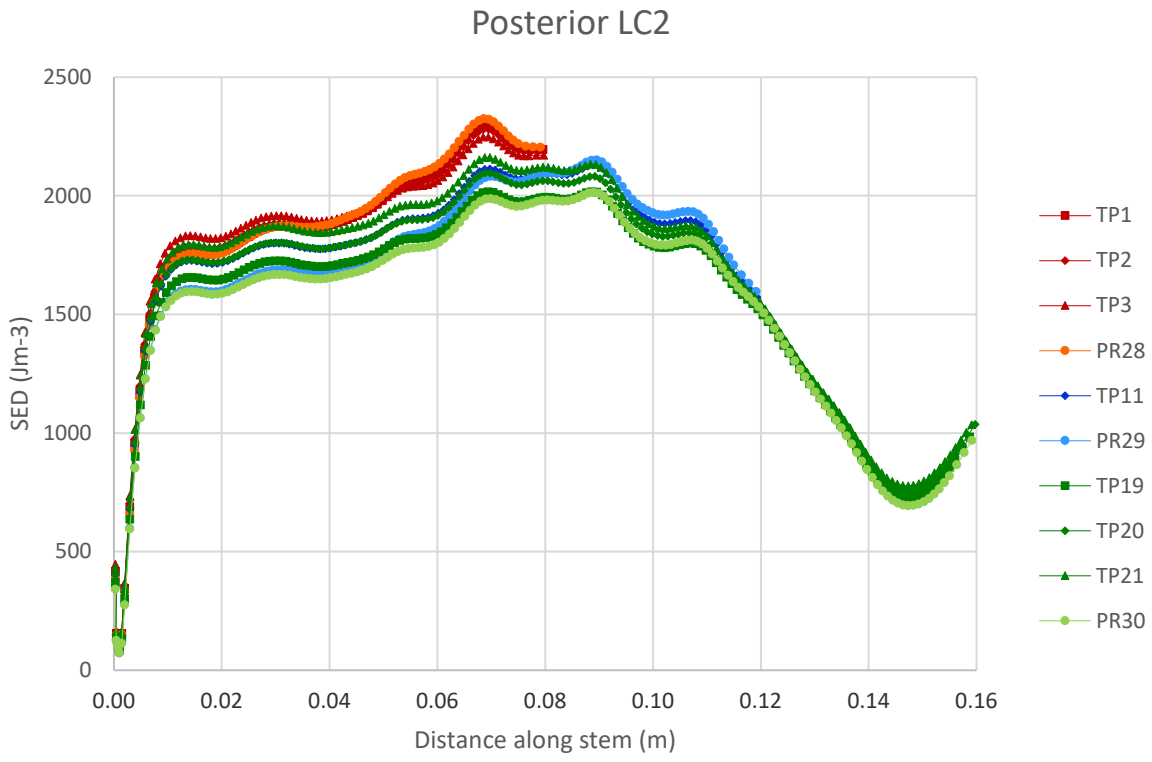

Chart 5.1 (posterior): SED to compare **taper** in periprosthetic bone under LC2
SET A in tapered, cemented stems:
Governing colour: Red = 0.08 m, blue = 0.12 m, green = 0.16 m stem length
Line markers: Circle = parallel, square = 0.375 °, diamond = 0.750 °, triangle = 1.500 ° stem taper
Colour gradient: Stem taper (dark = tapered, light = parallel)

<u>In the posterior aspect</u>

SED distribution & magnitude: The periprosthetic bone SED distribution under LC1 and LC5 in 0.08 m stems increased from distal to proximal. In the 0.12 m stems under LC1 and LC5, this periprosthetic bone SED distribution was also observed until a peak at ~ 0.08 m from the stem base was reached and followed by a fall in periprosthetic bone SED to the stem tip. In the 0.16 m stems under LC1 and LC5 the same periprosthetic bone SED distribution as the 0.12 m stems was observed, however the decrease in periprosthetic bone SED values above 0.12 m continued until it dropped to ~ 100 Jm^{-3} at the stem tip. Under LC2 – LC4 there was an initial increase in periprosthetic bone SED at a rate similar to that observed medially and anteriorly until 0.01 m along the stem from the stem base. Once this point was reached, all stems under LC2 continued to elicit an increase (at a much reduced rate) in periprosthetic bone SED whereas under LC3 the stems elicited a plateau in SED and under LC4 a decrease until 0.08 m from the stem base. Thereafter, there was a decrease in periprosthetic bone SED in the 0.12 m and 0.16 m stems until 0.12 m and after that there was an increase in periprosthetic bone SED until the tip of the 0.16 m stems (under LC2 – LC4).

Stem taper parameter: Taper differences follow a similar pattern under LC2 – LC4; an increased taper elicited an increased periprosthetic bone SED until ~ halfway along the stem in the 0.08 m and 0.12 m stemmed models, thereafter the increase in taper resulted in a decreased periprosthetic bone SED. In the 0.16 m stems the increased taper generated an increased periprosthetic bone SED along the whole stem length.

Stem length parameter: The 0.08 m stems elicited a higher periprosthetic bone SED than the longer stems, this was particularly evident under LC2 – 4. Under LC1 and LC5 the periprosthetic bone SED of the 0.08 m stem were matched by the 1.5 ° taper 0.16 m stem. Most of the 0.12 m stems elicited a higher periprosthetic bone SED than the 0.16 m stems, in particular the proximal halves, often with the exception of the 1.5 ° taper 0.16 m stem.

Remodelling threshold: Apart from SET C stems under LC2 and LC3 in the 0.08 m and 0.12 m, all stem's periprosthetic bone SED distribution in the posterior aspect fell below the remodelling threshold (3600 Jm^{-3}).

Table 5.1 (below): Statistics for (tapered cemented) stem **taper**
ANOVA: Each row tests four models (three tapered and one parallel).
T test: Each pair within each taper group; six unique permutations per cell for four tapers.
Black text = P values in a one way ANOVA test comparing stem tapers.
Grey cells = accept H_0, white cells = reject H_0
Grey text in brackets = number of stem taper comparisons where H_0 is rejected in a T test.

	Lateral	Medial	Anterior	Posterior	ANOVA Significant incidences	ANOVA SET sig. incidences
SET A, 5 mm, 0.08 m LC2	< 0.05	0.73 (0)	0.85 (0)	1.00 (0)	1	8
SET A, 5 mm, 0.12m LC2	< 0.05	< 0.05	< 0.05	< 0.05	4	
SET A, 5 mm, 0.16 m LC2	< 0.05	< 0.05	< 0.05	0.18 (1)	3	
SET B, 6 mm, 0.08 m LC2	0.22 (0)	0.07 (3)	< 0.05	< 0.05	2	10
SET B, 6 mm, 0.12 m LC2	< 0.05	< 0.05	< 0.05	< 0.05	4	
SET B, 6 mm, 0.16 m LC2	< 0.05	< 0.05	< 0.05	< 0.05	4	
SET C, 7 mm, 0.08 m LC2	0.23 (0)	0.70 (5)	< 0.05	0.48 (4)	1	8
SET C, 7 mm, 0.12 m LC2	< 0.05	< 0.05	< 0.05	0.40 (0)	3	
SET C, 7 mm, 0.16 m LC2	< 0.05	< 0.05	< 0.05	< 0.05	4	
ANOVA significant incidences	7	6	8	5		

Table 5.2 (below): Statistics for (tapered stem) stem **length**
ANOVA: Each row tests three models (0.08 m, 0.12 m, 0.16 m). A group of tapered stems (median taper size = 0.75 °) was compared with a group of parallel stems.
T test: Each pair within each stem group; three unique permutations per cell for three lengths.
Black text = P values in ANOVA comparing stem length. Grey cells = accept H_0, white cells = reject H_0
Grey text in brackets = number of stem length comparisons where H_0 is rejected in a T test.

	Lateral	Medial	Anterior	Posterior	ANOVA Significant incidences	ANOVA GROUP sig. incidences
SET D, 5 mm, 0.75 ° taper LC2	< 0.05	< 0.05	0.46 (0)	< 0.05	3	10
SET E, 6 mm, 0.75 ° taper LC2	< 0.05	< 0.05	0.94 (0)	< 0.05	3	
SET F, 7 mm, 0.75 ° taper LC2	< 0.05	< 0.05	< 0.05	< 0.05	4	
SET D, 5 mm, parallel, LC2	< 0.05	< 0.05	0.88 (0)	< 0.05	3	11
SET E, 6 mm, parallel, LC2	< 0.05	< 0.05	< 0.05	< 0.05	4	
SET F, 7 mm, parallel, LC2	< 0.05	< 0.05	< 0.05	< 0.05	4	
ANOVA significant incidences	6	6	3	6		

Stem radius (sets G, H, I)

Comparing stem radius in all model result SETS G – I (0.08 m – 0.16 m stem length).

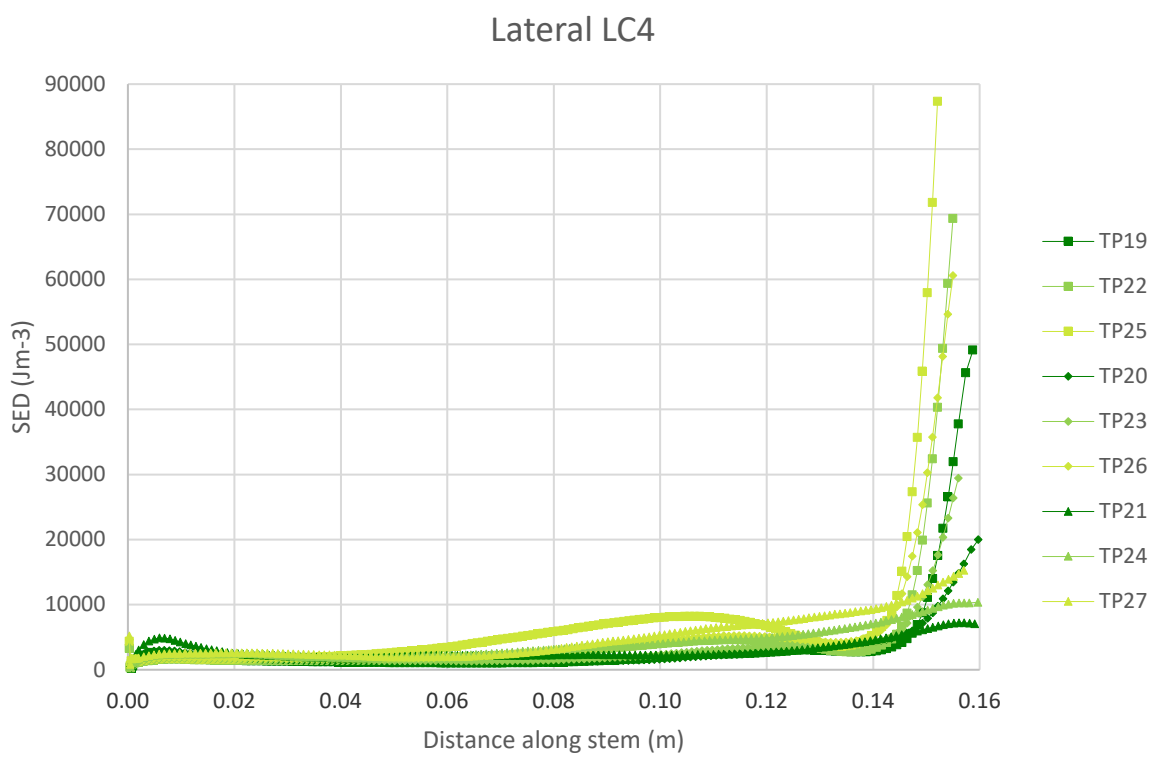

Chart 5.3 (lateral): SED in periprosthetic bone comparing stem **radius** under LC4, SET I in cemented stems

Governing colour: Green = 0.16 m stem length

Line markers: Square = 0.375 °, diamond = 0.750 °, triangle = 1.500 ° stem taper

Colour gradient: Stem radius (dark = 5 mm, mid = 6 mm, light = 7 mm)

In the lateral aspect

Stem radius parameter: Both the primary (at the stem tip) and secondary (2/3 way along the stem from the stem base) periprosthetic bone SED peaks displayed increased magnitude with increased stem radii under all load cases and stem tapers.

Remodelling threshold: All stems exceeded the bone remodelling threshold in SET G under LC2 – LC4 in the primary and secondary periprosthetic bone SED peak except for the 5 mm radius, 1.5 ° tapered stem. All stems were below the remodelling threshold under LC1 and LC5. All primary periprosthetic bone SED peaks and 6 mm and 7 mm radii, 0.375 ° and 0.75 ° tapered stems secondary peaks are within or above the remodelling threshold under LC1 – LC5 in SET H. All primary periprosthetic bone SED peaks and the 7 mm radius, 0.375 ° and 0.75 ° tapered stems of the secondary periprosthetic bone SED peaks under LC1 and LC5 of SET I were within or above the bone remodelling thresholds. The same stems were within or above the remodelling threshold under LC2 – LC4 plus the 6 mm radius, 0.375 ° tapered ones.

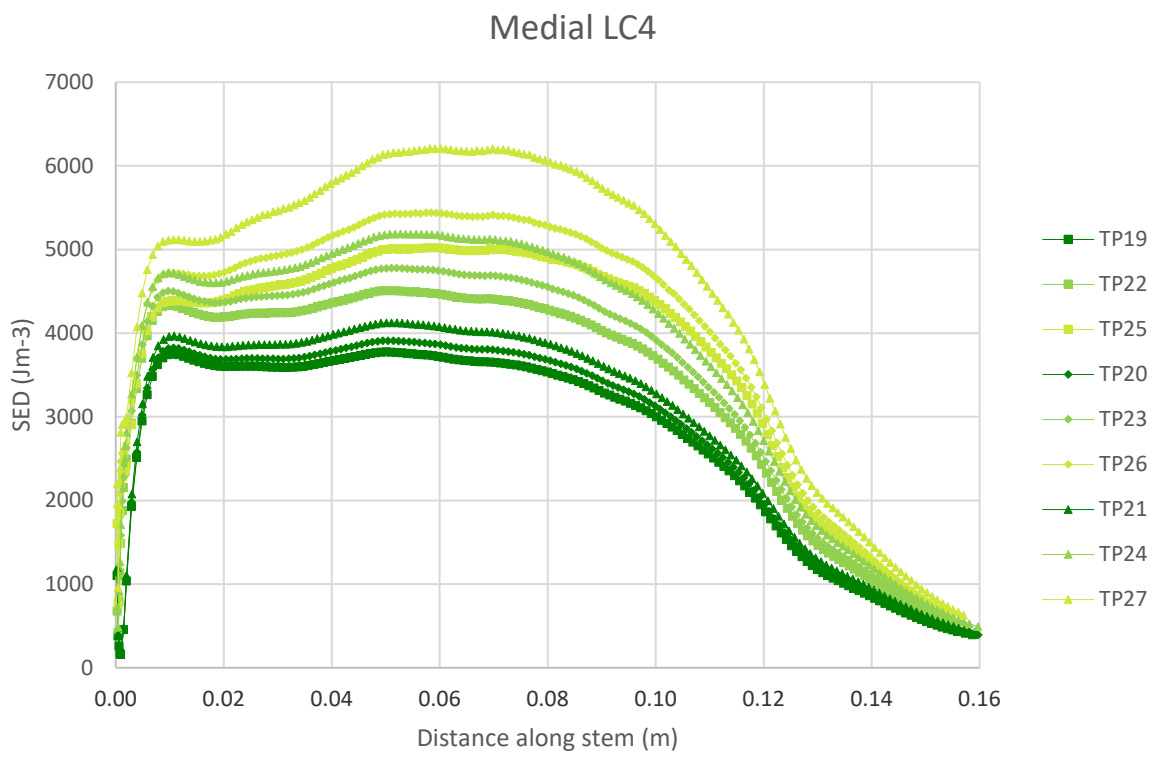

Chart 5.3 (medial): SED in periprosthetic bone comparing stem **radius** under LC4, SET I in cemented stems

Governing colour: Green = 0.16 m stem length

Line markers: Square = 0.375 °, diamond = 0.750 °, triangle = 1.500 ° stem taper

Colour gradient: Stem radius (dark = 5 mm, mid = 6 mm, light = 7 mm)

<u>In the medial aspect</u>

Stem radius parameter: An increased stem radius elicited an increased periprosthetic bone SED in all SETS (except for the 0.375 ° tapered 7 mm stem which fell below the 1.5 ° tapered 6 mm stem).

Remodelling threshold: In SET G, under LC2 – LC4, all stems were above or within the remodelling threshold except for the 5 mm stems under LC2 and all stems fell below the remodelling threshold under LC1 and LC5. In SET H, under LC 2 – LC4, all stems were above or within the remodelling threshold expect for the 5 mm stems under LC2 and LC3 and all stems fell below the remodelling threshold under LC1 and LC5. In SET I, under LC2 – LC4, all stems were above or within the remodelling threshold from the most distal point to ~ 0.08 m along the stem except for the 5 mm stems under LC2 (which fell below the remodelling threshold). Between 0.08 – 0.16 m all 5 mm stems fell below the remodelling threshold. Between 0.11 – 0.16 m the 6 mm and 7 mm radii stems also fell below the remodelling threshold. All stems fell below the remodelling threshold under LC1 and LC5 in SET I.

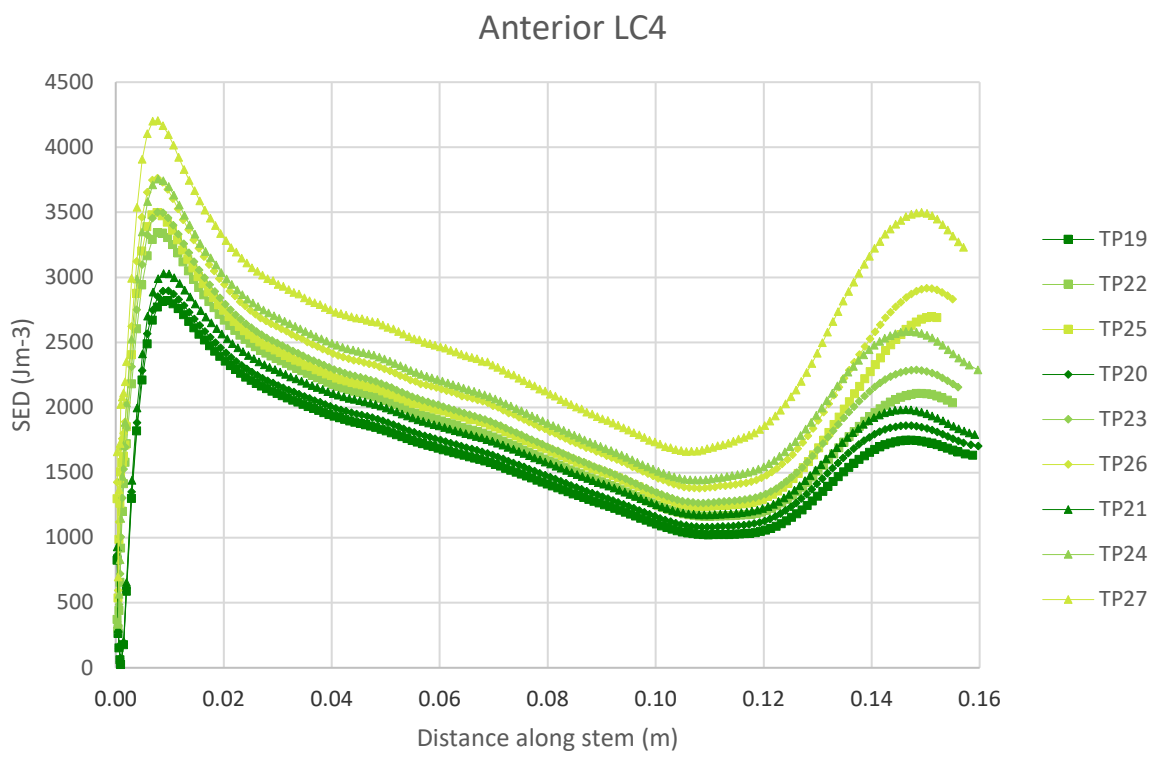

Chart 5.3 (anterior): SED in periprosthetic bone comparing stem **radius** under LC4, SET I in cemented stems

Governing colour: Green = 0.16 m stem length

Line markers: Square = 0.375 °, diamond = 0.750 °, triangle = 1.500 ° stem taper

Colour gradient: Stem radius (dark = 5 mm, mid = 6 mm, light = 7 mm)

<u>In the anterior aspect</u>

Stem radius parameter: In all stems in all SETS as the radius increased the periprosthetic bone SED increased except for the 1.5 ° tapered 6 mm stem under LC4 in SET H (which elicited higher periprosthetic bone SED than the 0.375 ° tapered 7 mm radius stem).

Remodelling threshold: All stems in all SETS under LC2 – 4 were within or above the bone remodelling threshold in the initial periprosthetic bone SED peak between 0.01 – 0.02 m along the stem from the stem base. Thereafter, only the 7 mm stems in all SETS remained within or above the remodelling threshold as well as the 6 mm stems in SET I under LC2. Under LC1 all stems fell below the remodelling threshold, however under LC5 the 7 mm stems in SET G and both the 7 mm and 6 mm stems of SET I elicited periprosthetic bone SED above or within the remodelling threshold between 0.12 – 0.15 m along the stem from the stem base.

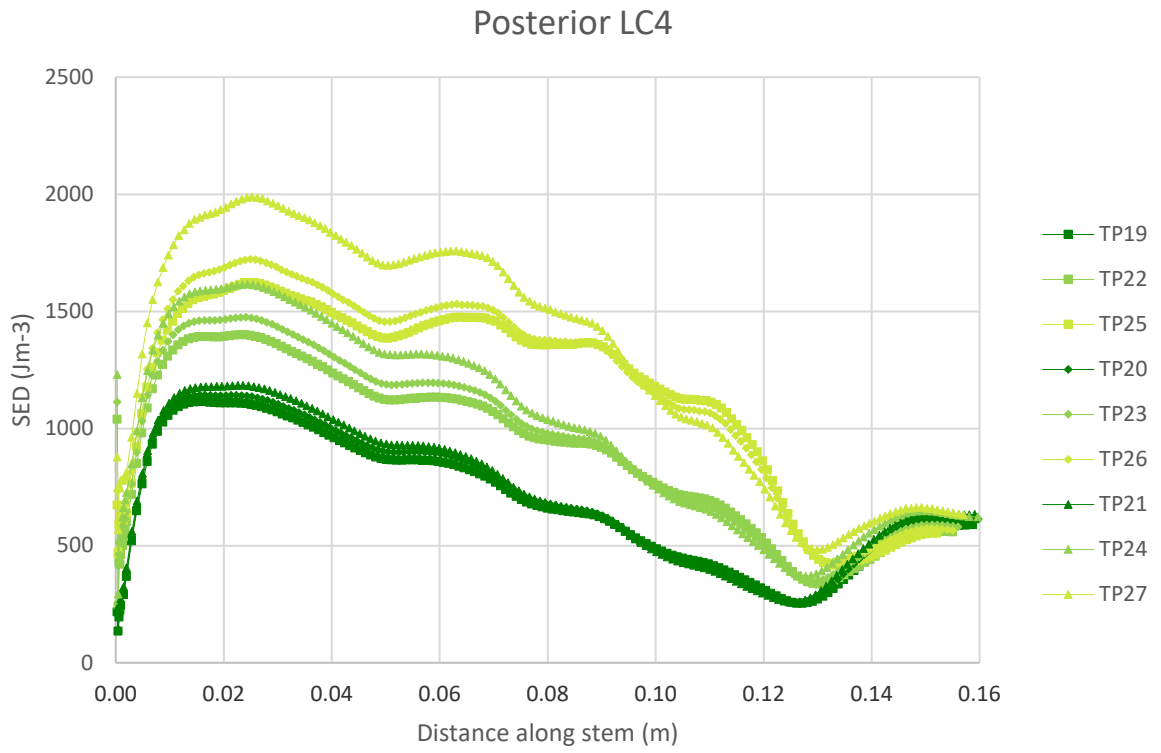

Chart 5.3 (posterior): SED in periprosthetic bone comparing stem **radius** under LC4, SET I in cemented stems

Governing colour: Green = 0.16 m stem length

Line markers: Square = 0.375 °, diamond = 0.750 °, triangle = 1.500 ° stem taper

Colour gradient: Stem radius (dark = 5 mm, mid = 6 mm, light = 7 mm)

<u>In the posterior aspect</u>

Stem radius parameter: In all stems in all SETS under LC1 – LC5, the greater the stem radii the greater the periprosthetic bone SED.

Remodelling threshold: All stems in SET G fell below the remodelling threshold under all load cases. In SET H, all stems fell below the remodelling threshold under LC1, LC3 and LC4, under LC2 and LC5 the 7 mm stems were within or above the remodelling threshold otherwise the rest remained below. In SET I, all stems fell below the remodelling threshold under LC1, LC3 and LC4, under LC2 and LC5 the 7 mm stems were within or above the remodelling threshold otherwise the rest remained below.

Table 5.3 (below): Statistics for (tapered cemented) stem **radius**
ANOVA: Each row tests three models (5 mm, 6 mm, 7mm).
T test: Pairs within each SET; there are three unique permutations per cell for three radii.
Black text = P values in ANOVA comparing stem radii. Grey cells = accept H_0, white cells = reject H_0
Grey text in brackets = number of stem radii comparisons where H_0 is rejected in a T test.

	Lateral	Medial	Anterior	Posterior	ANOVA Significant incidences
SET G, 0.08 m, 0.75 ° taper, LC4	< 0.05	0.69 (3)	< 0.05	< 0.05	3
SET H, 0.12 m, 0.75 ° taper, LC4	< 0.05	< 0.05	< 0.05	< 0.05	4
SET I, 0.16 m, 0.75 ° taper, LC4	< 0.05	< 0.05	< 0.05	< 0.05	4
ANOVA significant incidences	3	2	3	3	

5.3.2. PARALLEL STEM GROUP

5.4.1.1Fixation (set J)

Comparing stem fixation type in all model result SETS J.

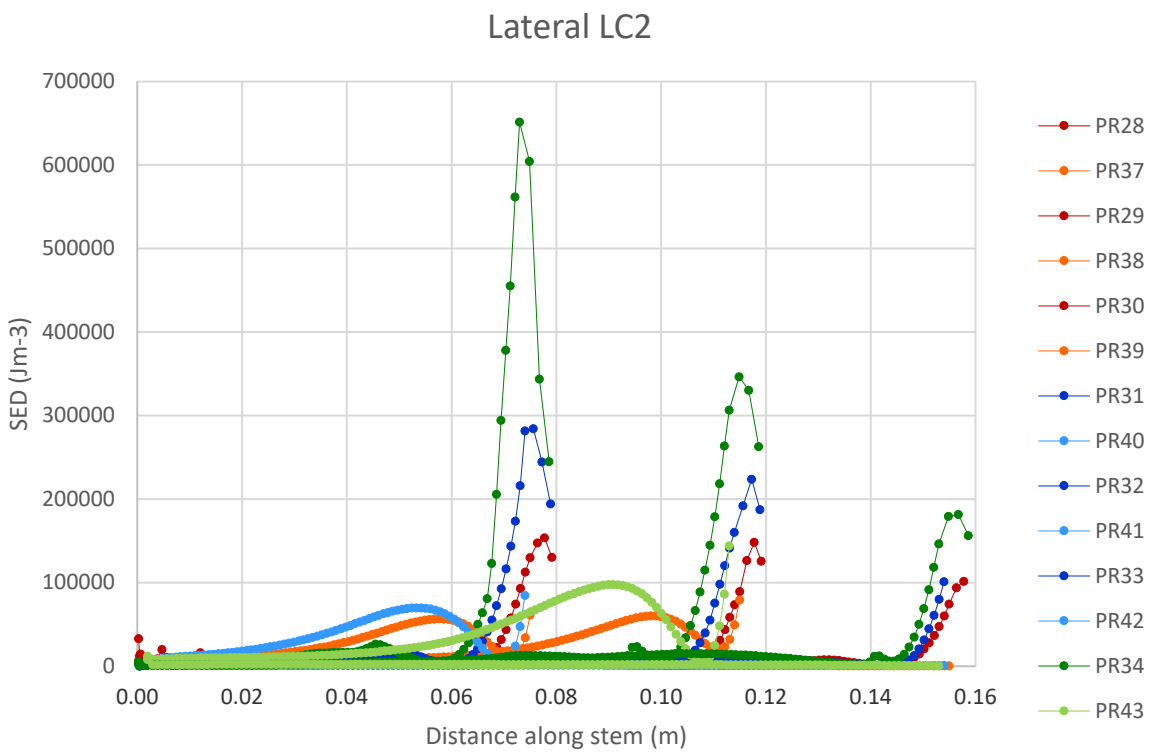

Chart 5.4 (lateral): SED comparing **fixation** in parallel stems periprosthetic bone under LC2, SET J

Governing colour: Red = 5 mm, blue = 6 mm, green = 7 mm stem radius

Colour gradient: Fixation (dark = cemented, light = pressfit)

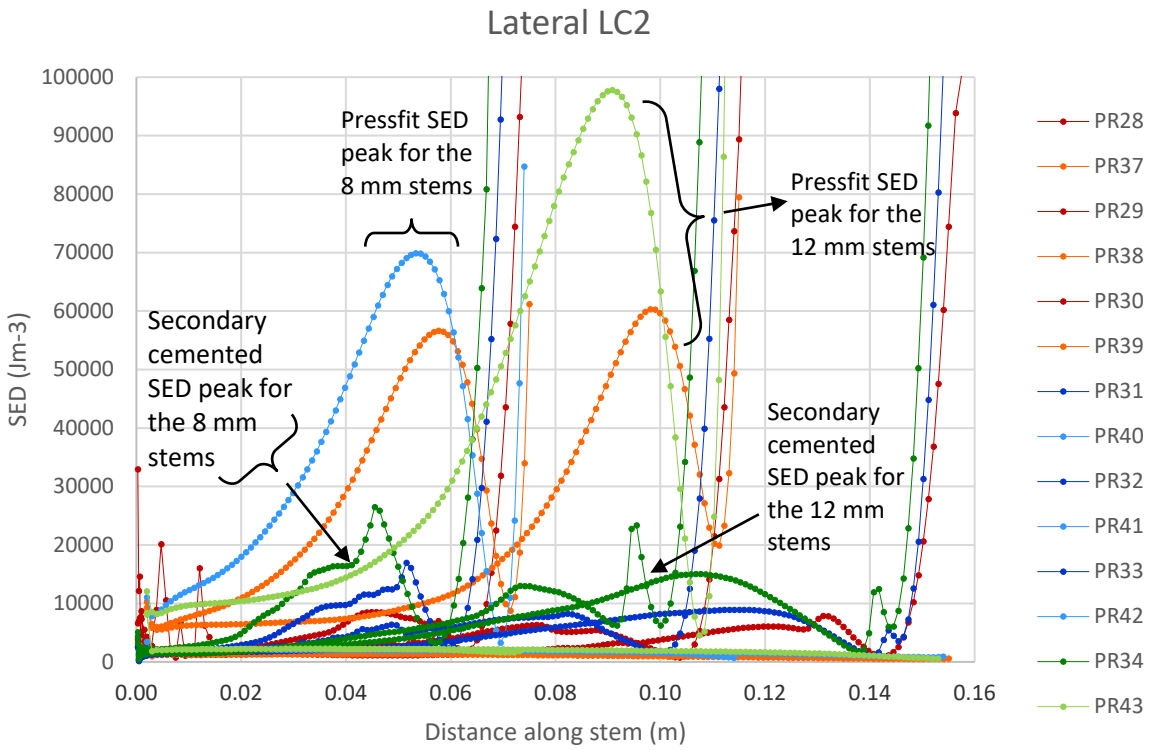

Chart 5.5 (above only): Magnified scale SED comparing fixation (lateral aspect)
In periprosthetic bone under LC2, SET J. Governing colours are cemented stems and their lighter hues are the equivalent pressfit stems.

<u>In the lateral aspect</u>

SED distribution & magnitude: The shape of the pressfit periprosthetic bone SED distribution under all load cases is ~ unchanging and as follows: at ~ 2/3 up from the stem base (= cemented stems secondary periprosthetic bone SED peak), the pressfit stems peak (Chart 5.5) and then dip to ~ initial periprosthetic bone SED values at the stem base. After the periprosthetic bone SED dip moving proximally, the periprosthetic bone SED steeply rises in all stems to the stem tip under all load cases. The periprosthetic bone SED magnitude at the tip of the pressfit stems is similar to the magnitude at the preceding (more distal) SED peak. This is below the primary periprosthetic bone SED peak of the cemented stems in LC2 – LC4, however under LC5 the peak periprosthetic bone SED in all pressfit stems is similar to cemented equivalent stems and under LC1 it is greater than cemented equivalents.

Fixation parameter: Under LC2 – LC4 the difference stem fixation has on the peak periprosthetic bone SED magnitudes is ~ threefold (cemented primary periprosthetic bone SED peak > pressfit peak).

Remodelling threshold: Under LC1 – LC5 all pressfit stems were within or above the bone remodelling threshold although under LC1 and LC5 this was only for the most proximal half of the stems whereas under LC2 – LC4 this was for the whole of the stem's length.

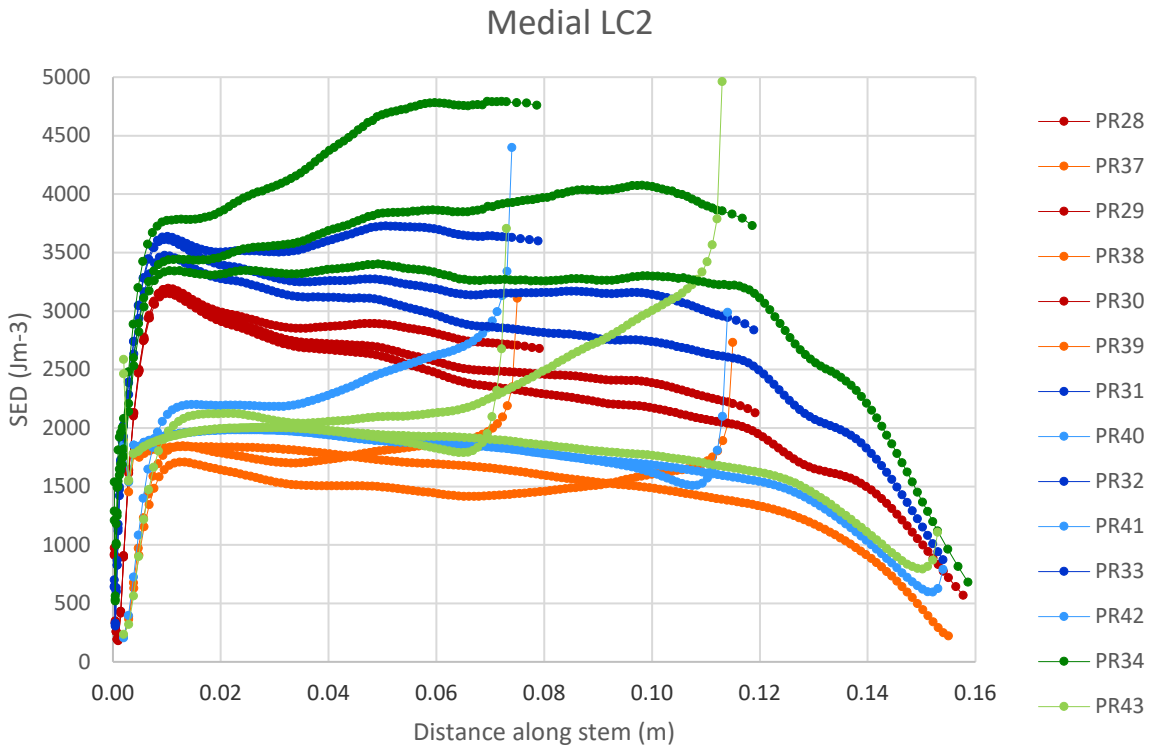

Chart 5.4 (medial): SED comparing **fixation** in parallel stems periprosthetic bone under LC2, SET J

Governing colour: Red = 5 mm, blue = 6 mm, green = 7 mm stem radius

Colour gradient: Fixation (dark = cemented, light = pressfit)

<u>In the medial aspect</u>

SED distribution & magnitude: The pattern of distribution in the pressfit stems mirrored the cemented stems up to 0.01 m from the most distal point with a sharp rise in periprosthetic bone SED albeit ~ 50% lower in magnitude then any equivalent cemented stems at the same point. For the length of the pressfit stems thereafter until 0.01 m before their tips, both the 0.08 m and 0.12 m stems periprosthetic bone SED were relatively constant. At 0.07 m and 0.11 m in the 0.08 m and 0.12 m pressfit stems respectively there was a sharp increase in periprosthetic bone SED such that the periprosthetic bone SED at the tip of the stems in cemented and pressfit were ~ equal. The 0.16 m pressfit stems elicited a similar periprosthetic bone SED distribution as the shorter stems until 0.11 m from the stem base. Thereafter the periprosthetic bone SED gradually decreased to the stem tip such that periprosthetic bone SED in cemented and pressfit stems were equal at ~ 500 Jm^{-3}. Under LC1 and LC5 the pressfit stems also elicited a lower periprosthetic bone SED distribution than their cemented equivalents except for 5 mm and 6 mm 0.16 m pressfit stems which in both cases elicited higher periprosthetic bone SEDs than all stems regardless of fixation or length for the distal half of their length.

Fixation parameter: Under LC2 – LC4 all pressfit stems elicited a lower periprosthetic bone vSED distribution than their cemented equivalents.

Remodelling threshold: All pressfit stems under all load cases fell below the remodelling threshold except for stem tips of all 0.08 m stems and 7 mm radius 0.12 m stems under LC2 – LC4.

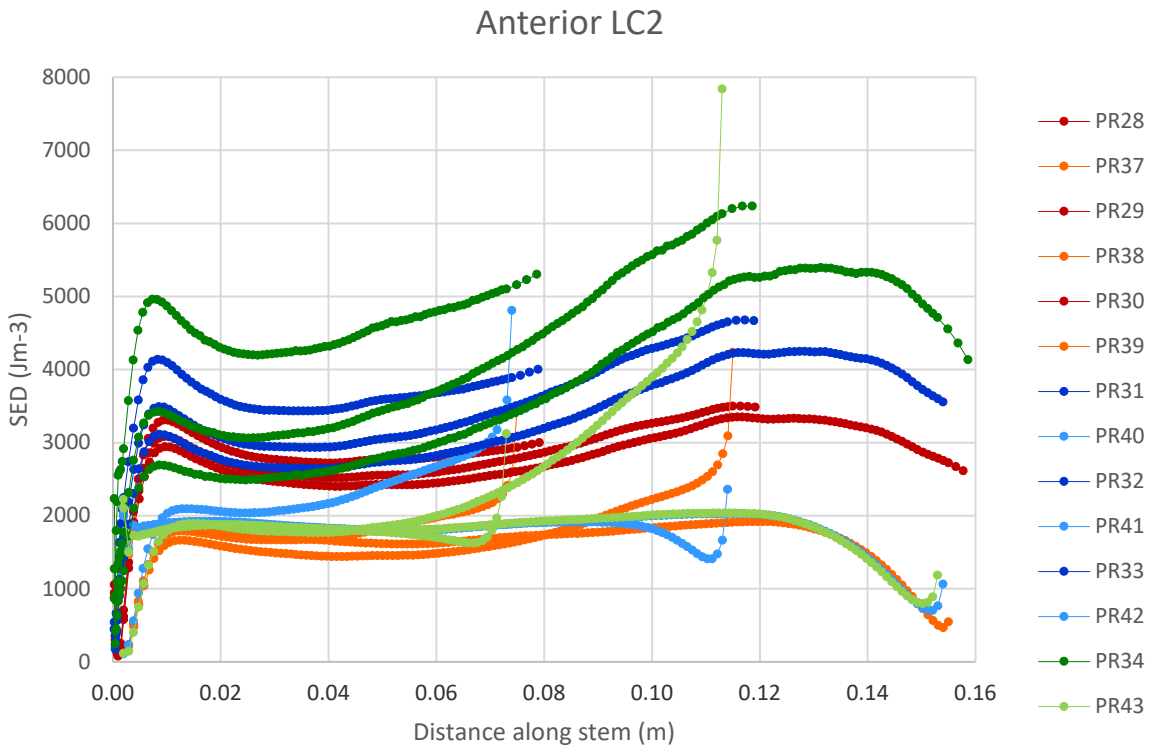

Chart 5.4 (anterior): SED comparing **fixation** in parallel stems periprosthetic bone under LC2, SET J

Governing colour: Red = 5 mm, blue = 6 mm, green = 7 mm stem radius

Colour gradient: Fixation (dark = cemented, light = pressfit)

<u>In the anterior aspect</u>

SED distribution & magnitude: The periprosthetic bone SED distribution in the pressfit stems under LC1 and LC5 were similar in all stems albeit with a slight increase in periprosthetic bone SED at the stem tips in the 0.08 m and 0.16 m pressfit models. Under LC2 – LC4 this increase in periprosthetic bone SED at the stem tips was more apparent. The 5 mm pressfit stems under all load cases elicited the lowest periprosthetic bone SED; the larger diameter pressfit stems elicited similar periprosthetic bone SED values along all stem lengths.

Fixation parameter: Under all load cases the periprosthetic bone SED was lower in the pressfit stems compared with the cemented counterparts, this was less apparent under LC1 and LC5.

Remodelling threshold: All pressfit stems under all load cases fell below the remodelling threshold.

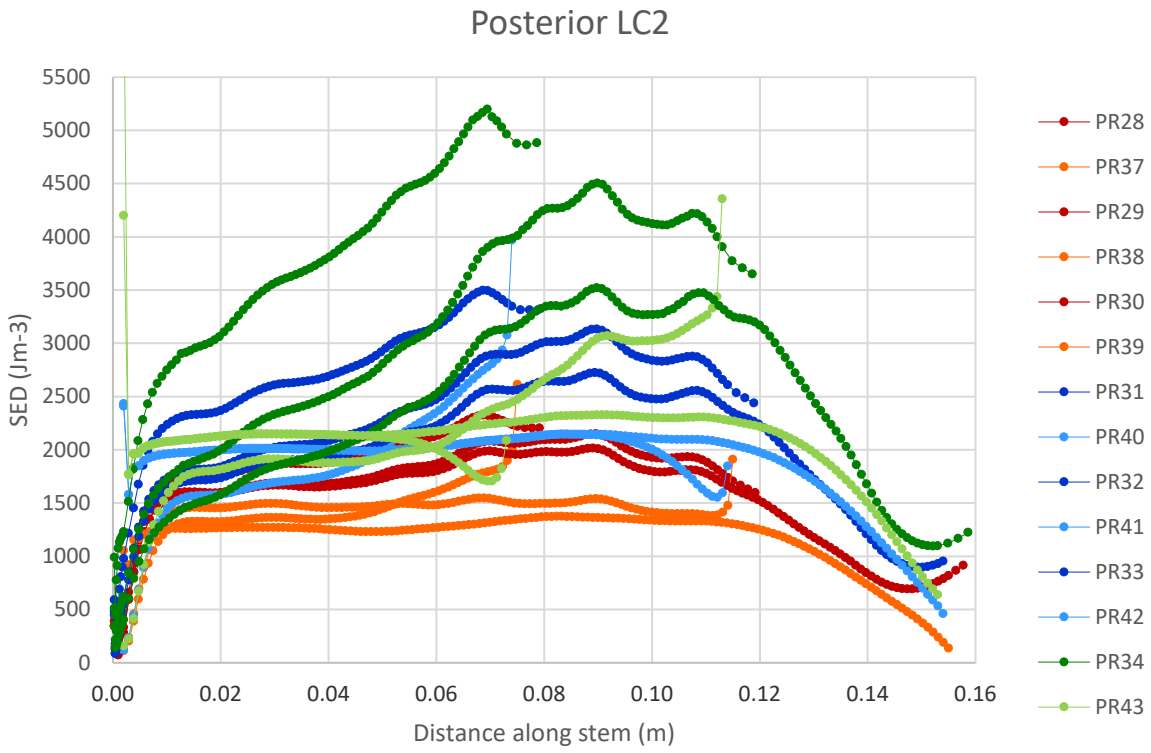

Chart 5.4 (posterior): SED comparing **fixation** in parallel stems periprosthetic bone under LC2, SET J

Governing colour: Red = 5 mm, blue = 6 mm, green = 7 mm stem radius

Colour gradient: Fixation (dark = cemented, light = pressfit)

<u>In the posterior aspect</u>

SED distribution & magnitude: In pressfit fixations the 0.08 m and 0.12 m stems gradually increased in periprosthetic bone SED until 0.01 m before the stem tip, followed by a steep increase in periprosthetic bone SED to the stem tip. The periprosthetic bone SED magnitude of the pressfit and cemented 0.08 m and 0.12 m stems at the stem tip was similar in equivalent stems. In the 0.16 m pressfit stems there was a gradual increase in periprosthetic bone SED until 0.12 m along the stems from the stem base followed by a gradual decrease until the stem tip. The periprosthetic bone SED magnitude of the pressfit and cemented stems at the 0.16 m stem tip was similar in equivalent stems. Under LC2 – LC4 in the 0.08 m and 0.12 m pressfit stems after an initial increase to 0.01 m along the stem length from the stem base there was a relative periprosthetic bone SED plateau until 0.01 m before the stem tip then a sharp increase in periprosthetic bone SED to the tip (similar to the anterior aspect periprosthetic bone SED distribution). In the 0.16 m pressfit stems after 0.12 m along the stem length from the stem base, the periprosthetic bone SED gradually decreased and in all pressfit stem cases the periprosthetic bone SED value at the tip was similar to the cemented stem equivalent. The only exception to this pattern was under LC4 where the 0.16 m pressfit stems gradually decreased in

periprosthetic bone SED after the initial spike in periprosthetic bone SED at 0.01 m all the way to the stem tip.

Fixation parameter: Under LC1 and LC5 the pressfit stems elicited a periprosthetic bone SED lower than all cemented stems. Under LC2 – LC4 most of the periprosthetic bone SED elicited by the pressfit stems was lower than the cemented stems, however there was considerable overlap between the 7 mm pressfit stems (the highest magnitude periprosthetic bone SED of the pressfit stems) and the 5 mm cemented stems (the lowest magnitude of the cemented stems).

Remodelling threshold: Except for the 7 mm radius 0.12 m pressfit stem at the tip and base and the 7 mm radius 0.08 m pressfit stem at the base only under LC2, all pressfit stems fell below the bone remodelling threshold.

Table 5.4: Statistics for (parallel) stem fixation
T test: Each row tests two models (cemented or pressfit); there is one permutation per cell
Number of incidences where the p value < 0.05 comparing stem fixation.

	Lateral	Medial	Anterior	Posterior	T test significant incidences
SET J, 0.08 m, 5 mm radius, LC2	1	1	1	1	4
SET J, 0.12 m, 6 mm radius, LC2	1	1	1	1	4
SET J, 0.16 m, 7 mm radius, LC2	1	1	1	1	4
SET J, 0.08 m, 5 mm radius, LC2	1	1	1	1	4
SET J, 0.12 m, 6 mm radius, LC2	1	1	1	1	4
SET J, 0.16 m, 7 mm radius, LC2	1	1	1	1	4
SET J, 0.08 m, 5 mm radius, LC2	1	1	1	1	4
SET J, 0.12 m, 6 mm radius, LC2	1	1	1	1	4
SET J, 0.16 m, 7 mm radius, LC2	1	1	1	1	4
T test significant incidences	9	9	9	9	

5.4.1.2 Stem radius and length (SET K, L, M)

Comparing parallel stem radii and length in model result SETS K, L, M (cemented and pressfit).

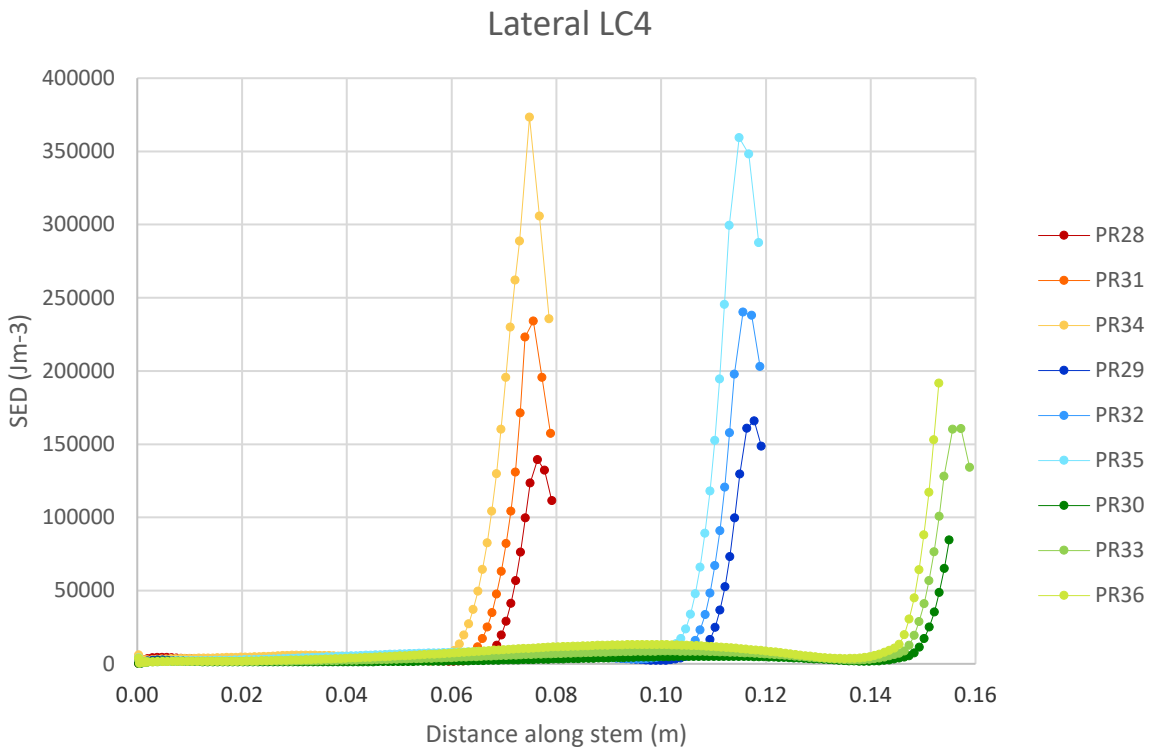

Chart 5.6 (lateral): SED in periprosthetic bone comparing stem **radius** in the parallel models Results from SET K under LC4

Governing colour: Red = 0.08 m, blue = 0.12 m, green = 0.16 m stem length

Colour gradient: Stem radius (dark = 5 mm, mid = 6 mm, light = 7 mm)

In the lateral aspect

SED distribution & magnitude: The shorter stemmed implants elicited a higher periprosthetic bone SED in equivalent (radius) stems in SET K except for in the secondary periprosthetic bone SED peak where the opposite was observed. Uniquely, the shorter stemmed implants elicited a lower periprosthetic bone SED in equivalent (radius) stems in SET L.

Stem radius parameter: The periprosthetic bone SED distribution increased with increasing stem radius in SET K (cemented) and SET L (pressfit).

Remodelling threshold: SET K bone remodelling: Under LC2 – LC4 all primary and secondary periprosthetic bone SED peaks were within or above the bone remodelling threshold. Under LC1 all secondary periprosthetic bone SED peaks were under and all primary periprosthetic bone SED peaks were within or over the bone remodelling threshold. Under LC5 the 7mm radius 0.12 m and 0.16 m stems in the secondary periprosthetic bone SED peak (the rest were below) and all stems primary periprosthetic bone SED peaks were within or above the bone remodelling threshold. SET L bone remodelling: Under all load cases all stems were above the bone remodelling threshold.

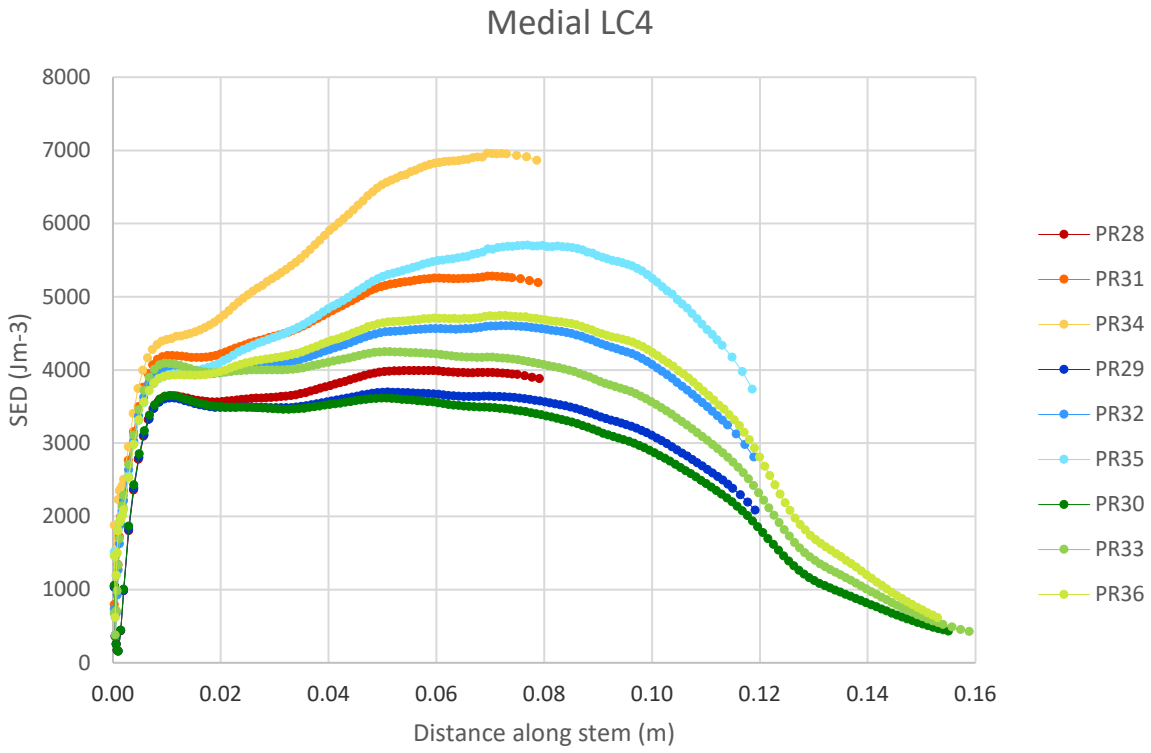

Chart 5.6 (medial): SED in periprosthetic bone comparing stem **radius** in the parallel models
Results from SET K under LC4
Governing colour: Red = 0.08 m, blue = 0.12 m, green = 0.16 m stem length
Colour gradient: Stem radius (dark = 5 mm, mid = 6 mm, light = 7 mm)

<u>In the medial aspect</u>

Stem radius parameter: The periprosthetic bone SED distribution increased with increasing stem radius in SET K (cemented) and SET L (pressfit).

Stem length parameter: The shorter stemmed implants elicited a higher periprosthetic bone SED in equivalent (radius) stems in SET K and SET L.

Remodelling threshold: SET K bone remodelling: Under LC2 the 6 mm and 7 mm radius, 0.08 m stems and the 7 mm, 0.12 m stem were within or above the bone remodelling threshold. The remaining stems were below the remodelling threshold. Under LC3 and LC4 all 0.08 m stems and the distal half of all 0.12 m and 0.16 m stems were within or above the remodelling threshold. Under LC1 and LC5 all stems were below the remodelling threshold. SET L bone remodelling: Under LC2 – LC4 only the stem tips of the 0.08 m, 6 mm and 7 mm radius and 0.12 m 7 mm radius stems were within or above the bone remodelling threshold. Under LC1 and LC5 all stems were below the bone remodelling threshold.

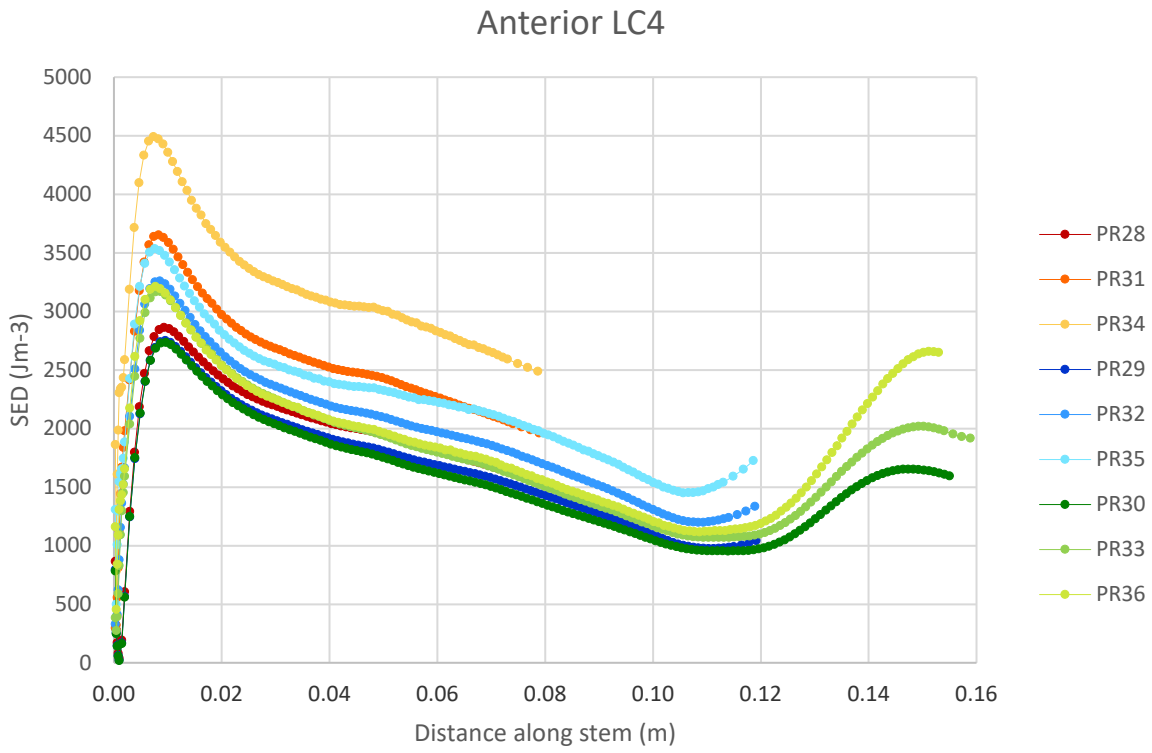

Chart 5.6 (anterior): SED in periprosthetic bone comparing stem **radius** in the parallel models
Results from SET K under LC4
Governing colour: Red = 0.08 m, blue = 0.12 m, green = 0.16 m stem length
Colour gradient: Stem radius (dark = 5 mm, mid = 6 mm, light = 7 mm)

<u>In the anterior aspect</u>

Stem radius parameter: The periprosthetic bone SED distribution increases with increasing stem radius in SET K (cemented) and SET L (pressfit).

Stem length parameter: The shorter stemmed implants elicited a higher periprosthetic bone SED in equivalent (radius) stems in SET K and SET L.

Remodelling threshold: SET K bone remodelling: Under LC1 all stems were under the bone remodelling threshold. Under LC2 the proximal halves of all 6 mm and 7 mm radius stems were within or above the bone remodelling threshold. Under LC3 and LC4 only the initial periprosthetic bone SED peak of the 7 mm radius 0.08 m stem and all of the 6 mm radius 0.08 m stem were within or above the bone remodelling threshold. Under LC5 only the stem tips of the 6 mm and 7 mm radius 0.12 m stems and the proximal half of the 0.16 m stems were within or above the bone remodelling threshold. SET L bone remodelling: Most of all stems were below the bone remodelling threshold under all load cases except for the stem tips of the 6 mm radius, 0.08 m stem and the 7 mm radius 0.12 m stem under LC2 and LC3 as well as the 7 mm radius 0.12 m stem tip under LC5.

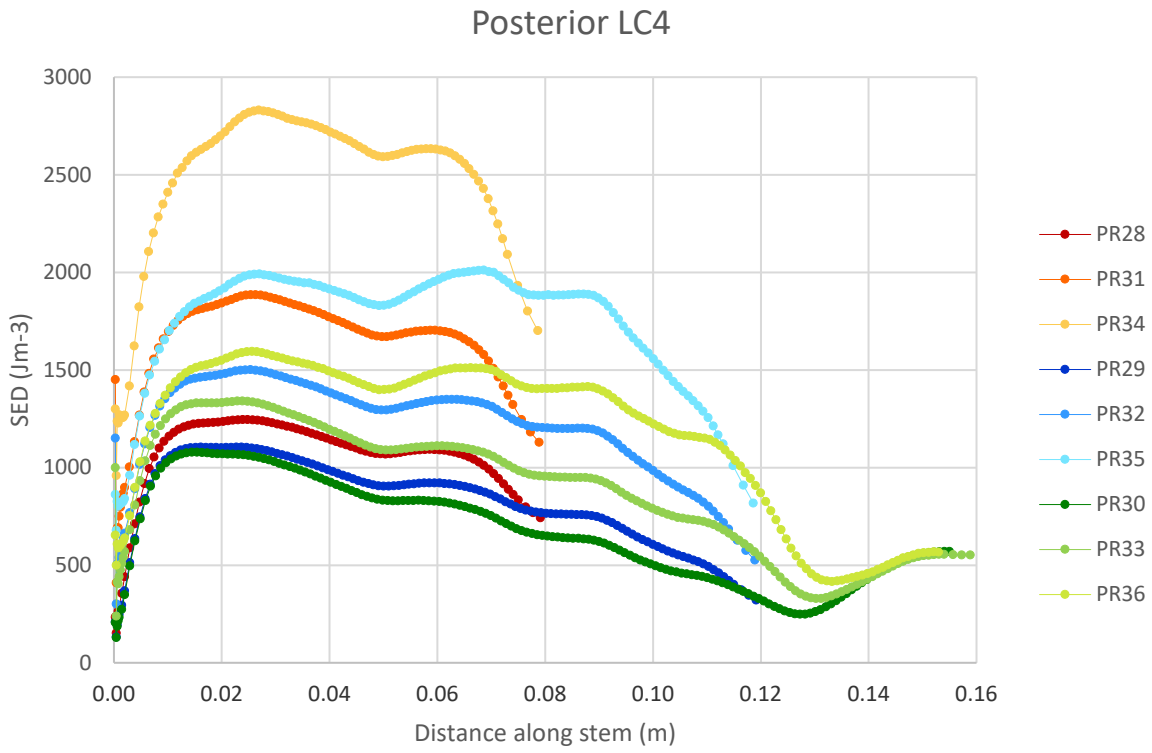

Chart 5.6 (posterior): SED in periprosthetic bone comparing stem **radius** in the parallel models
Results from SET K under LC4
Governing colour: Red = 0.08 m, blue = 0.12 m, green = 0.16 m stem length
Colour gradient: Stem radius (dark = 5 mm, mid = 6 mm, light = 7 mm)

<u>In the posterior aspect</u>

Stem radius parameter: The periprosthetic bone SED distribution increased with increasing stem radius in SET K (cemented) and SET L (pressfit).

Stem length parameter: The shorter stemmed implants elicited a higher periprosthetic bone SED in equivalent (radius) stems in SET K and SET L.

Remodelling threshold: SET K bone remodelling: Under LC1 all stems fell below the bone remodelling threshold. Under LC2 – LC5 all stems fell below the bone remodelling threshold except for the proximal part of the 7 mm radius 0.08 m and 0.12 m stems. SET L bone remodelling: All stems under all load cases fell below the bone remodelling threshold except for the 6 mm radius 0.08 m stem and the 7 mm radius 0.12 m stem tips which fell within the bone remodelling threshold under LC2 and LC3.

Table 5.5 (below) : Statistics for (parallel) stem **radius**
ANOVA: Each row tests three models (5 mm, 6 mm, 7mm)
T test: There are three unique permutations per cell
Black text = P values in a one way ANOVA test comparing parallel stem radius.
pf = pressfit, cm = cemented fixation. Grey cells = accept H_0, white cells = reject H_0
Grey text in brackets = number of stem length comparisons where H_0 is rejected in a T test.

	Lateral	Medial	Anterior	Posterior	ANOVA Significant incidences	ANOVA GROUP sig. incidences
SET K, 0.08 m, parallel, cm, LC4	< 0.05	< 0.05	< 0.05	< 0.05	4	11
SET K, 0.12 m, parallel cm, LC4	0.11 (0)	< 0.05	< 0.05	< 0.05	3	
SET K, 0.16 m, parallel, cm, LC4	< 0.05	< 0.05	< 0.05	< 0.05	4	
SET L, 0.08 m, parallel, pf, LC4	< 0.05	< 0.05	< 0.05	< 0.05	4	11
SET L, 0.12 m, parallel, pf, LC4	< 0.05	< 0.05	< 0.05	< 0.05	4	
SET L, 0.16 m, parallel, pf, LC4	< 0.05	< 0.05	0.25 (0)	< 0.05	3	
ANOVA significant incidences	5	6	5	6		

Table 5.6 (below) : Statistics for (parallel) stem **length**
ANOVA: Each row tests three models (0.08 m, 0.12 m, 0.16 m)
T test: On each pair within each SET. There are three unique permutations per cell.
Black text = P values in ANOVA comparing parallel stem length.
Grey cells = accept H_0, white cells = reject H_0
Grey text in brackets = number of stem radii comparisons where H_0 is rejected in a T test.

	Lateral	Medial	Anterior	Posterior	ANOVA Significant incidences
SET M, 5 mm, parallel, pf, LC2	< 0.05	< 0.05	0.168 (1)	< 0.05	3
SET M, 6 mm, parallel, pf, LC2	< 0.05	< 0.05	< 0.05	0.153 (1)	3
SET M, 7 mm, parallel, pf, LC2	< 0.05	< 0.05	< 0.05	0.194 (2)	3
ANOVA significant incidences	3	3	2	1	

5.3.3. CORTICAL PLATED GROUP

5.4.1.1Plated vs. non-plated (SETS Q, R, S, T, U, V)

All cortical plate lengths are either 50% or 100% relative to the stem length of that model. Results from SET Q (0.08 m stems), LC4 are presented.

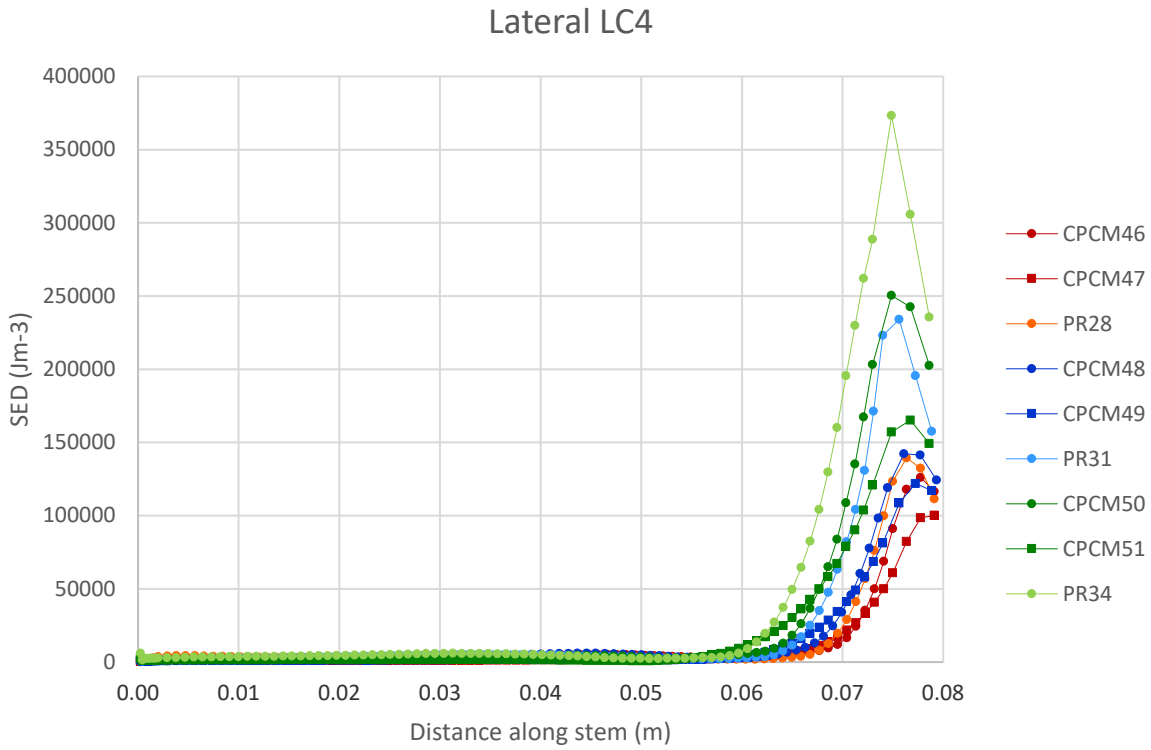

Chart 5.7 (lateral): SED in periprosthetic bone in cortical plated, parallel, cemented stems comparing plated to non-plated stems
LC4, SET Q (0.08 m stems)
Governing colour: Red = 5 mm, blue = 6 mm, green = 7 mm stem radius
Line markers: Circle = cortical plate is half stem length, square= cortical plate is full stem length
Colour gradient: Plate (dark = plated, light = non-plated)

In the lateral aspect

SETS Q, R and S (cemented):

SED distribution & magnitude: Periprosthetic bone SED distribution between the plated and non-plated models was similar; the primary and secondary periprosthetic bone SED peaks observed in previous (non-plated) models was obtained in the plated models too.

Cortical plating parameter: Primary periprosthetic bone SED peaks in all plated models were less than non-plated models under LC1 – LC5. In the 0.08 m stems (SET Q), non-plated primary periprosthetic bone SED peaks were up to double the plated values. Secondary periprosthetic bone

SED peak differences were greater between the full plate and non-plated than the half plate and non-plated stems under LC2 – LC4, these differences were not present under LC1 and LC5 (periprosthetic bone SED values were similar between the three classes of models at the secondary peak).

SETS T, U, V (pressfit):

SED distribution & magnitude: Periprosthetic bone SED between plated and non-plated models differed tremendously in magnitude and distribution under all load cases. Plated model periprosthetic bone SED under LC2 – LC4 remained below 750 Jm^{-3} in half plated models from the stem base to the plate tip, thereafter there was a sharp hike in periprosthetic bone SED magnitude until the stem tip, but this value remained below the non-plated equivalent stem periprosthetic bone SED values. In the full plated stems, the periprosthetic bone SED value remained below 500 Jm^{-3} for the entire length of all stems under LC2 – LC4.

Cortical plating parameter: Once again, the periprosthetic bone SED magnitude difference between the plated and non-plated stems was greatest in the shorter stems (SET T and U) where peak periprosthetic bone SED values differed by up to 50 fold under LC1 – LC5. In the 0.16 m stems (SET V) this large difference in peak periprosthetic bone SED between the plated and non-plated equivalent models was not observed under LC1 – LC5, however the non-plated stems still resulted in higher periprosthetic bone SED along the entire length.

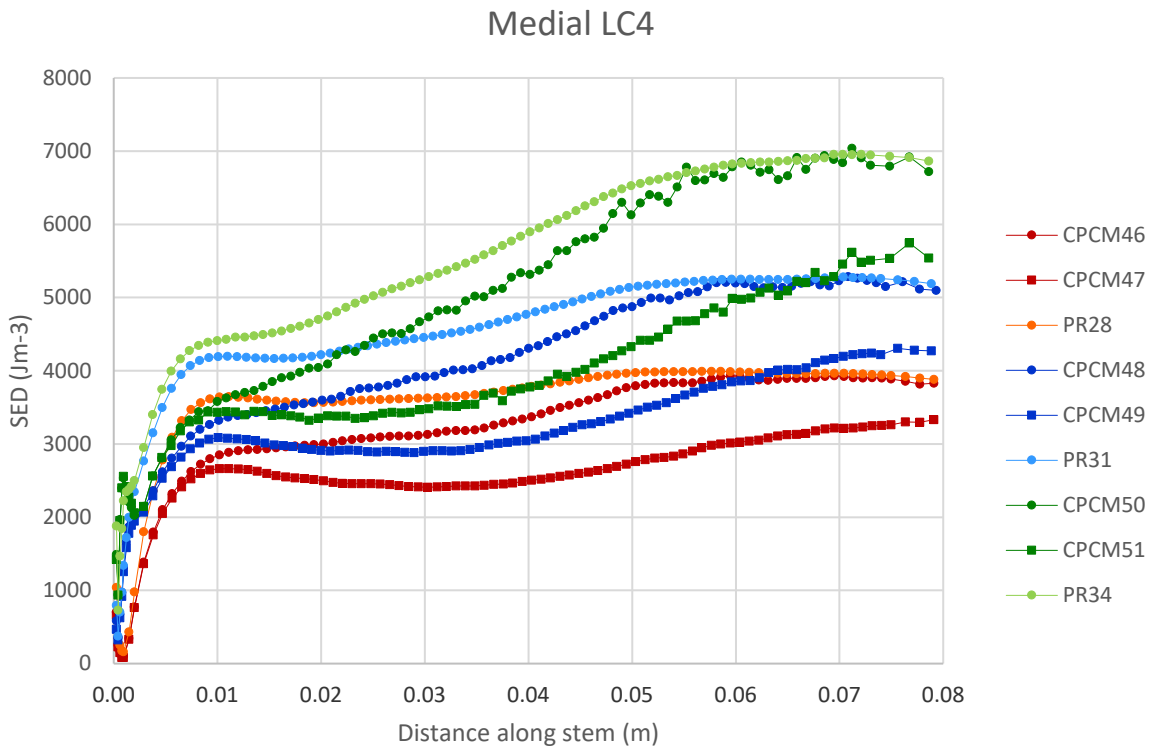

Chart 5.7 (medial): SED in periprosthetic bone in cortical plated, parallel, cemented stems comparing plated to non-plated stems
LC4, SET Q (0.08 m stems)
Governing colour: Red = 5 mm, blue = 6 mm, green = 7 mm stem radius
Line markers: Circle = cortical plate is half stem length, square= cortical plate is full stem length
Colour gradient: Plate (dark = plated, light = non-plated)

<u>In the medial aspect</u>

SETS Q, R and S (cemented):

SED distribution & magnitude: In all plated stems there was minimal difference in periprosthetic bone SED distribution and magnitude compared with non-plated equivalents under all load cases.

In SETS T, U, V (pressfit):

SED distribution & magnitude: Periprosthetic bone SED in non-plated models was relatively constant 0.01 m above the stem base and below the most proximal point of data collected. This distribution was not completely mirrored in the plated models under any load case although the proximal half (proximal to the plate tip) of the half plated models did come close to the non-plated periprosthetic bone SED magnitude and distribution. In the distal half of the half plated models and all of the full plated models, periprosthetic boneSED was ~1/3 that of non-plated equivalents under LC2 – LC4. At the proximal end of the full plated models in the 0.08 m and 0.12 m stems there was a sharp increase in periprosthetic bone SED to the stem tip so that the periprosthetic bone SED value in all plated and

non-plated models was equal under LC2 – LC4. This was the opposite in the 0.16 m stems where there was a decrease in all plated stems from 0.12 m from the most distal point to the stem tip, although once again the periprosthetic bone SED value in all plated and non-plated models was equal under LC2 – LC4.

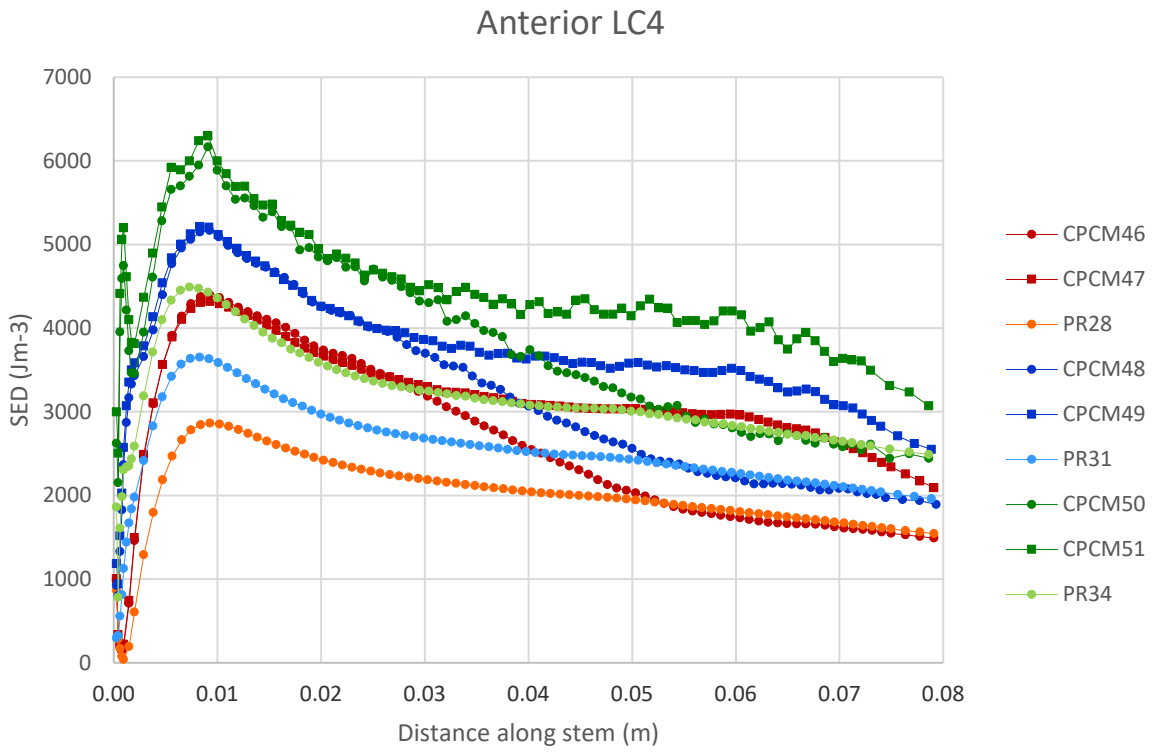

Chart 5.7 (anterior): SED in periprosthetic bone in cortical plated, parallel, cemented stems comparing plated to non-plated stems
LC4, SET Q (0.08 m stems)
Governing colour: Red = 5 mm, blue = 6 mm, green = 7 mm stem radius
Line markers: Circle = cortical plate is half stem length, square= cortical plate is full stem length
Colour gradient: Plate (dark = plated, light = non-plated)

<u>In the anterior aspect</u>

SETS Q, R and S (cemented):

SED distribution & magnitude: Periprosthetic bone SED distribution in plated stems was similar to non-plated equivalent stems. The periprosthetic bone SED magnitude in the plated models was *higher* than the non-plated equivalent models under LC2 – LC4. The difference was only upheld in the proximal half of the plated models in those that had a full plate; half plated models resulted in periprosthetic bone SED magnitude ~ equal to non-plated models proximal to the plate tip.

SETS T, U, V (pressfit):

SED distribution & magnitude: Periprosthetic bone SED distribution and magnitude in plated stems was similar to non-plated equivalent stems with the exception of the proximal part of the full plated models in the 0.16 m stems (SET V) that produced a *rise* in periprosthetic bone SED above the half and non-plated stems under LC2 – LC4.

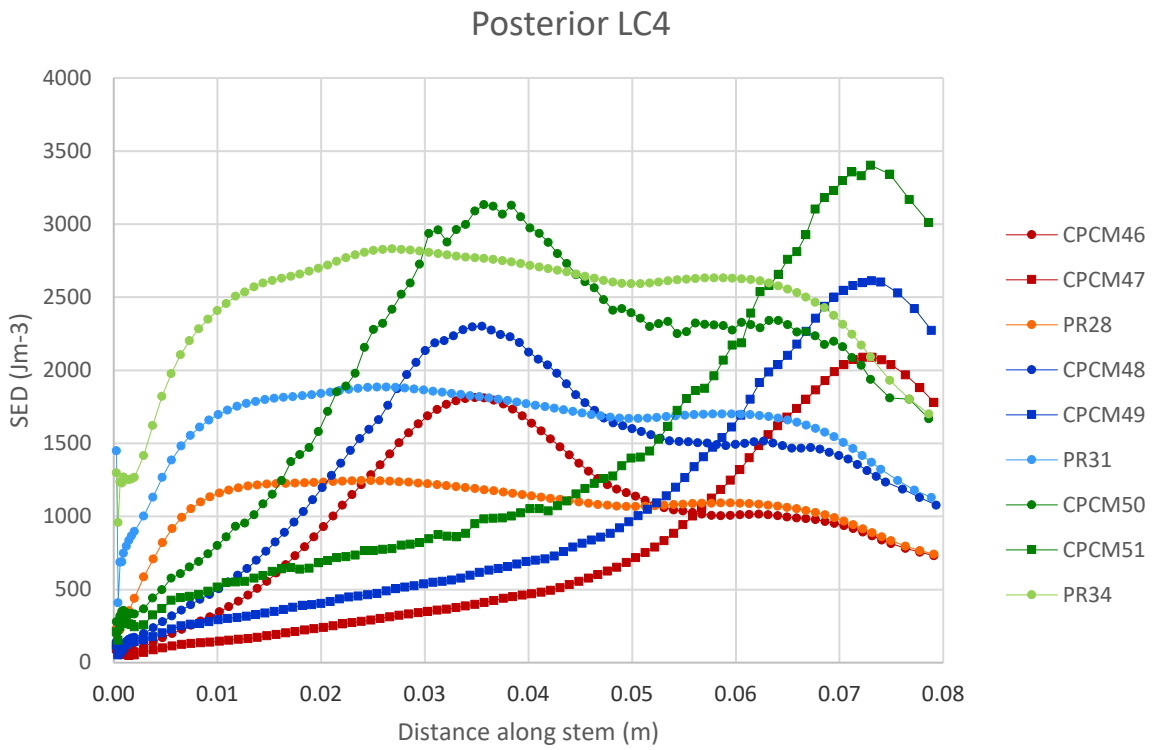

Chart 5.7 (posterior): SED in periprosthetic bone in cortical plated, parallel, cemented stems comparing plated to non-plated stems
LC4, SET Q (0.08 m stems)
Governing colour: Red = 5 mm, blue = 6 mm, green = 7 mm stem radius
Line markers: Circle = cortical plate is half stem length, square= cortical plate is full stem length
Colour gradient: Plate (dark = plated, light = non-plated)

<u>In the posterior aspect</u>

SETS Q, R and S (cemented):

SED distribution & magnitude: Periprosthetic bone SED distribution in all plated stems was lower in plated models than non-plated equivalent models and lower in full plated than half plated models. Plated stems elicited a gradual increase in periprosthetic bone SED from distal to proximal, in half plated models this was characterised by a periprosthetic bone SED rate change (plateau) at the plate tip where it ~ matched the periprosthetic bone SED of the non-plated models under LC2 – LC4 thereafter. Full plated models periprosthetic bone SED continued to increase in the proximal half and culminated in periprosthetic bone SED values similar to the non-plated and half plated models by the stem tip under LC2 – LC4.

SETS T, U, V (pressfit):

SED distribution & magnitude: Periprosthetic bone SED distribution in plated stems was similar to non-plated equivalent stems under LC2 – LC4 with the exception of the proximal part of the half

plated models in the 0.16 m stems (SET V) that elicited a slight periprosthetic bone SED hike at the plate tip until the stem tip. Periprosthetic bone SED magnitude was ~ double the non-plated equivalent models under LC2 – LC4 but not under LC1 or LC5.

Table 5.7: Statistics for (parallel) cortical plated vs. non-plated models
ANOVA: Each row tests three models (half-length plate, full length plate, no plate)
T test: Pairs within each triplet within the SET. There are three unique permutations per cell.
Black text = P values in a one way ANOVA test comparing cortical plated to non-plated model.
pf = pressfit, cm = cemented fixation. Grey cells = accept H0, white cells = reject H0
Grey text in brackets = number of stem length comparisons where H0 is rejected in a T test.

	Lateral	Medial	Anterior	Posterior	ANOVA Significant incidences	ANOVA GROUP sig. incidences
SET Q, 5 mm, 0.08 m, cm, LC4	0.49 (2)	< 0.05	< 0.05	< 0.05	3	9
SET Q, 6 mm, 0.08 m, cm, LC4	0.17 (1)	< 0.05	< 0.05	< 0.05	3	
SET Q, 7 mm, 0.08 m, cm, LC4	0.12 (2)	< 0.05	< 0.05	< 0.05	3	
SET R, 5 mm, 0.12 m, cm, LC4	< 0.05	< 0.05	< 0.05	< 0.05	4	10
SET R, 6 mm, 0.12 m, cm, LC4	0.45 (0)	< 0.05	< 0.05	< 0.05	3	
SET R, 7 mm, 0.12 m, cm, LC4	0.13 (1)	< 0.05	< 0.05	< 0.05	3	
SET S, 5 mm, 0.16 m, cm, LC4	0.59 (0)	< 0.05	< 0.05	< 0.05	3	10
SET S, 6 mm, 0.16 m, cm, LC4	0.23 (0)	< 0.05	< 0.05	< 0.05	3	
SET S, 7 mm, 0.16 m, cm, LC4	< 0.05	< 0.05	< 0.05	< 0.05	4	
Cemented significant incidences	2	9	9	9		
SET T, 5 mm, 0.08 m, pf, LC4	< 0.05	< 0.05	0.09 (1)	< 0.05	3	10
SET T, 6 mm, 0.08 m, pf, LC4	< 0.05	< 0.05	< 0.05	< 0.05	4	
SET T, 7 mm, 0.08 m, pf, LC4	< 0.05	< 0.05	0.09 (2)	< 0.05	3	
SET U, 5 mm, 0.12 m, pf, LC4	< 0.05	< 0.05	< 0.05	< 0.05	4	11
SET U, 6 mm, 0.12 m, pf, LC4	< 0.05	< 0.05	< 0.05	< 0.05	4	
SET U, 7 mm, 0.12 m, pf, LC4	< 0.05	< 0.05	0.12 (1)	< 0.05	3	
SET V, 5 mm, 0.16 m, pf, LC4	< 0.05	< 0.05	< 0.05	< 0.05	4	12
SET V, 6 mm, 0.16 m, pf, LC4	< 0.05	< 0.05	< 0.05	< 0.05	4	
SET V, 7 mm, 0.16 m, pf, LC4	< 0.05	< 0.05	< 0.05	< 0.05	4	
Pressfit significant incidences	9	9	6	9		
ANOVA total significant incidences	11	18	15	18		

5.3.3.1. Fixation on cortical plated models cemented or pressfit

(SET N, O, P)

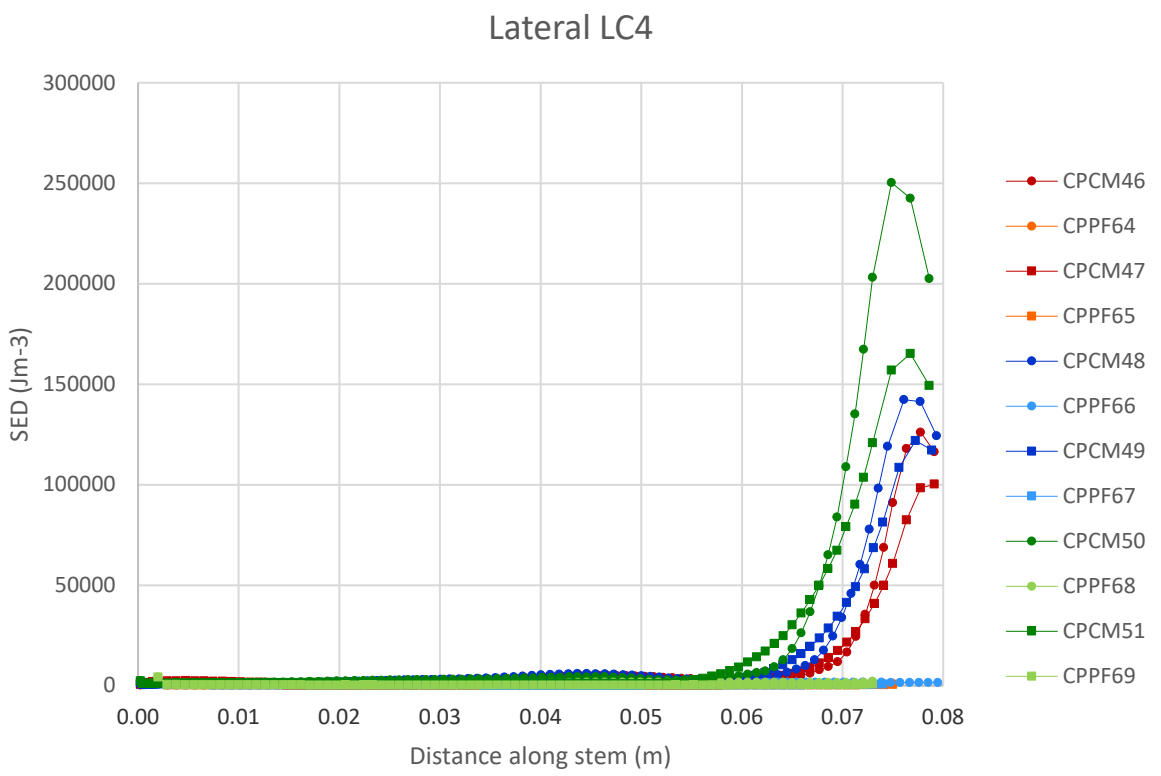

Chart 5.8 (lateral): SED in periprosthetic bone cortical plated parallel stems comparing fixation In LC4, SET N

Governing colour: Red= 5 mm, blue = 6 mm, green = 7 mm stem radius

Line markers: Circle = cortical plate is half stem length, square = cortical plate is full stem length

Colour gradient: Fixation (dark = cemented, light = pressfit)

In the lateral aspect:

SED distribution & magnitude: The periprosthetic bone SED magnitude increased in the proximal half of the pressfit half plate models came close to that of the cemented full plate models between the secondary and primary periprosthetic bone SED peaks under LC2 – LC4. Final (stem tip) periprosthetic bone SED magnitudes in the two fixation types are ~ three orders of magnitude apart.

Fixation parameter: Under LC1 – LC5 all pressfit stems elicited a lower periprosthetic bone SED than the cemented stems.

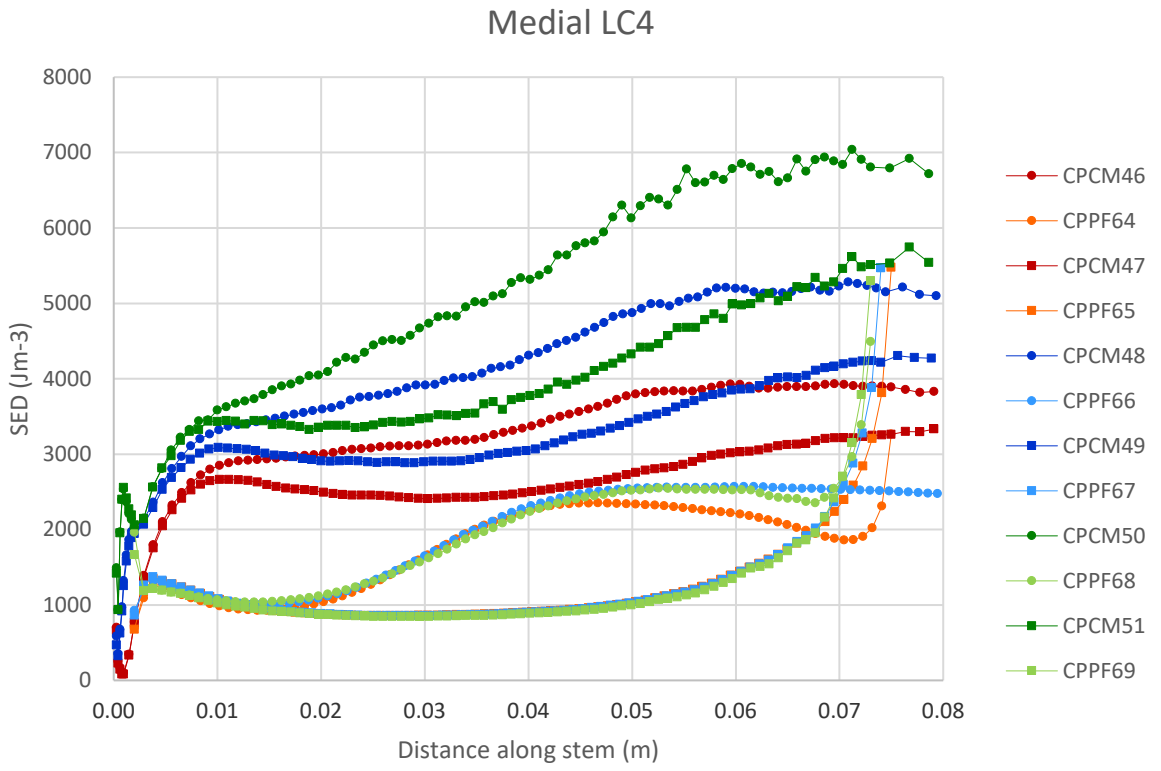

Chart 5.8 (medial): SED in periprosthetic bone cortical plated parallel stems comparing fixation In LC4, SET N

Governing colour: Red= 5 mm, blue = 6 mm, green = 7 mm stem radius

Line markers: Circle = cortical plate is half stem length, square = cortical plate is full stem length

Colour gradient: Fixation (dark = cemented, light = pressfit)

<u>In the medial aspect:</u>

SED distribution & magnitude: The periprosthetic bone SED magnitude increased in the proximal half of the pressfit half plate models and reached the cemented full plate model periprosthetic bone SED magnitude in SETS O and P under LC2 – LC4 and mirrored the distribution until the stem tip. In SET N the pressfit half plate model came close to that of the cemented full plate models periprosthetic bone SED magnitude. Final periprosthetic bone SED magnitudes are very similar in the two fixation methods in models with the same plate length under LC2 – LC4. Under LC1 and LC5 the final periprosthetic bone SED magnitudes are not similar in the two fixation methods at ~ one order of magnitude apart.

Fixation parameter: Under LC1 – LC5 all pressfit stems elicited a lower periprosthetic bone SED than the cemented stems.

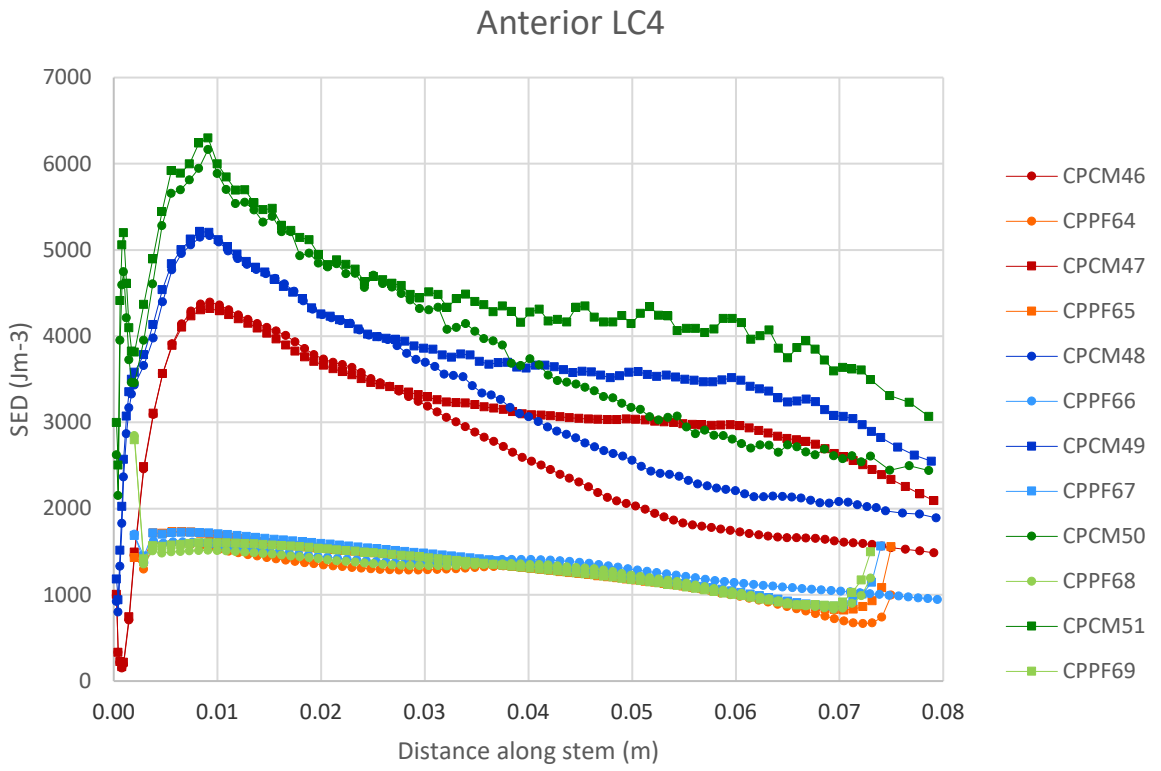

Chart 5.8 (anterior): SED in periprosthetic bone cortical plated parallel stems comparing fixation In LC4, SET N

Governing colour: Red= 5 mm, blue = 6 mm, green = 7 mm stem radius

Line markers: Circle = cortical plate is half stem length, square = cortical plate is full stem length

Colour gradient: Fixation (dark = cemented, light = pressfit)

<u>In the anterior aspect</u>

Fixation parameter: Under LC1 – LC5 all pressfit stems elicited a lower periprosthetic bone SED than the cemented stems.

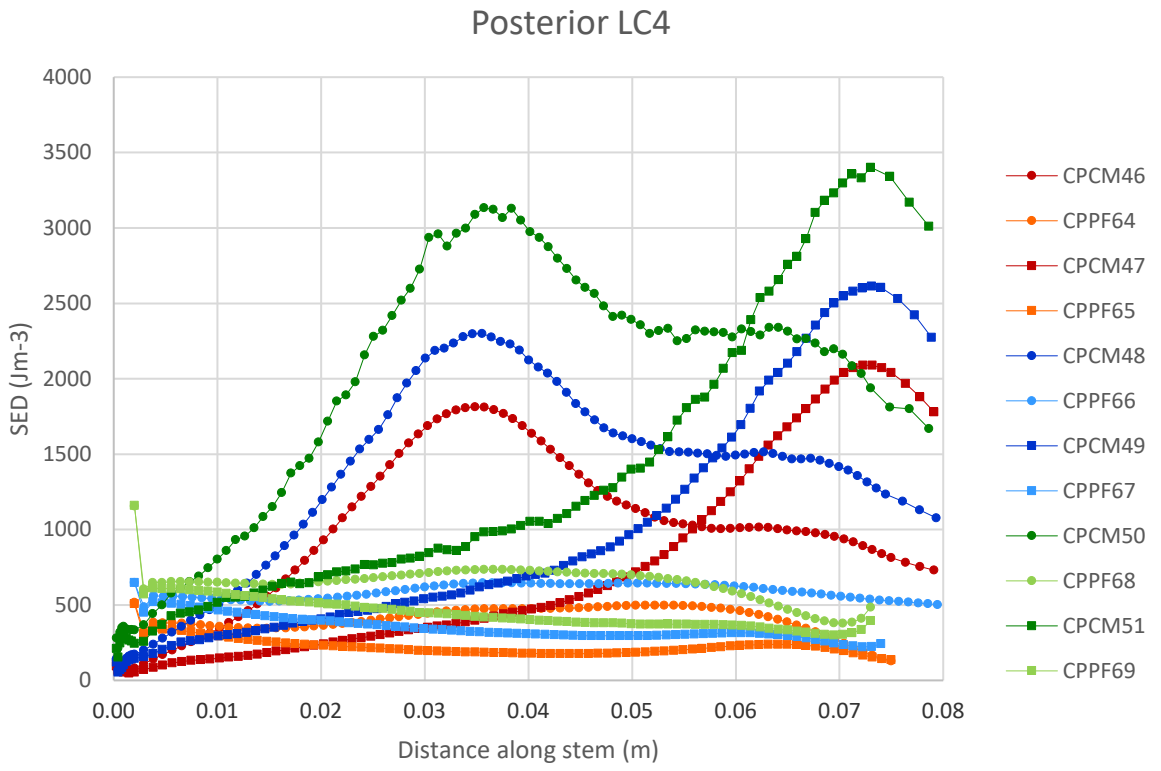

Chart 5.8 (posterior): SED in periprosthetic bone cortical plated parallel stems comparing fixation In LC4, SET N

Governing colour: Red= 5 mm, blue = 6 mm, green = 7 mm stem radius

Line markers: Circle = cortical plate is half stem length, square = cortical plate is full stem length

Colour gradient: Fixation (dark = cemented, light = pressfit)

<u>In the posterior aspect</u>

Fixation parameter: Under LC1 and LC5 all pressfit stems elicited a lower periprosthetic bone SED than the cemented stems in SET N and O. In SET P, the proximal half of all pressfit stems elicited a higher periprosthetic bone SED under LC1 and LC5. Under LC2 – LC4 differences in periprosthetic bone SED magnitude between fixation types were marginal; the proximal half of the pressfit half plate models reached the cemented full plate model periprosthetic bone SED magnitude in all models apart from SET O under LC4 and in SET N under LC3 and LC4 it was the distal half of the pressfit half plate models that reached the cemented full plate model periprosthetic bone SED magnitude. Final periprosthetic bone SED magnitudes were different in the two fixation methods with cemented stems ~ four times the periprosthetic bone SED magnitude of equivalent pressfit models.

Table 5.8 (below): Statistics for (parallel) cortical plated fixation models
T test: Each row tests two models (cemented, pressfit) therefore there is one permutation per cell. Number of incidences where the p value < 0.05 in a T test comparing stem fixation in cortical plated parallel stemmed models. cp = cortical plate length in metres

Stem fixation	Lateral	Medial	Anterior	Posterior	T test Significant incidences
SET N, 0.08 m, 5 mm radius, 0.04 cp, LC4	1	1	1	1	4
SET N, 0.08 m, 5 mm radius, 0.08 cp, LC4	1	1	1	1	4
SET N, 0.08 m, 6 mm radius, 0.04 cp, LC4	1	1	1	1	4
SET N, 0.08 m, 6 mm radius, 0.08 cp, LC4	1	1	1	1	4
SET N, 0.08 m, 7 mm radius, 0.04 cp, LC4	1	1	1	1	4
SET N, 0.08 m, 7 mm radius, 0.08 cp, LC4	1	1	1	1	4
SET O, 0.12 m, 5 mm radius, 0.06 cp, LC4	1	1	1	1	4
SET O, 0.12 m, 5 mm radius, 0.12 cp, LC4	1	1	1	1	4
SET O, 0.12 m, 6 mm radius, 0.06 cp, LC4	1	1	1	1	4
SET O, 0.12 m, 6 mm radius, 0.12 cp, LC4	1	1	1	1	4
SET O, 0.12 m, 7 mm radius, 0.06 cp, LC4	1	1	1	1	4
SET O, 0.12 m, 7 mm radius, 0.12 cp, LC4	1	1	1	1	4
SET P, 0.16 m, 5 mm radius, 0.08 cp, LC4	1	1	1	1	4
SET P, 0.16 m, 5 mm radius, 0.16 cp, LC4	1	1	1	1	4
SET P, 0.16 m, 6 mm radius, 0.08 cp, LC4	1	1	1	1	4
SET P, 0.16 m, 6 mm radius, 0.16 cp, LC4	1	1	1	1	4
SET P, 0.16 m, 7 mm radius, 0.08 cp, LC4	1	1	1	1	4
SET P, 0.16 m, 7 mm radius, 0.16 cp, LC4	1	1	1	1	4
T test Significant incidences	18	18	18	18	

5.4. Discussion

Three groups (tapered, parallel and cortical plated) of experimentally validated FE models with variable parameters (stem taper, length, radius, fixation method or cortical plate) were run in 81 quasi static, non-linear (friction contact) simulations under five load cases (LC1 – LC5). Periprosthetic bone SED was recorded in all aspects (lateral, medial, anterior and posterior). The outcome goal was to promote successful SAAP stem fixation by avoiding periprosthetic bone resorption and so aseptic loosening. A periprosthetic bone SED between or above the thresholds for strain adaptive bone remodelling (3600 - 4400 Jm^{-3}) offer the best chance of implant stability with respect to minimising aseptic loosening. Patterns in the distribution and magnitude of periprosthetic bone SED were observed in all groups and key observations will be discussed with relation to their effect on strain adaptive bone remodelling. If an analytical stress analysis is discussed I have assumed that an increase in stress leads to an increase in periprosthetic bone SED (within the elastic limits of bone, see Equation 5.1).

5.4.1 Tapered stem group

Cemented stemmed models with lengths of 0.08 m, 0.12 m, or 0.16 m, radii of 5 mm, 6 mm or 7 mm and tapers of 0 °, 0.375 °, 0.75 °, 1.5 ° were compared in SETS A - C and SETS D - F (12 permutations) providing data on stem taper and length and then SETS G - H (12 permutations) were compared with provide data on stem radius (see Appendix Table A.5.3). Pressfit tapered stems were not modelled, despite being used in some THRs, since the wedge that they create in the bone requires osseointegration for mechanical stability. Because the taper is inverted relative to the bone in a SAAP patient, initial fixation may not sufficiently anchor the SAAP while osseointegration is underway and so they were not included in the ITAP clinical trial.

5.4.1.1. Stem taper

Each of the SETS in this comparison (A, B and C) contained one of each of the three implant stem lengths with equal distal radius; each SET differed in stem distal radius size (see Appendix Table A.5.3). A stem taper comparison is made in the sectional diagram in Fig. 5.3.

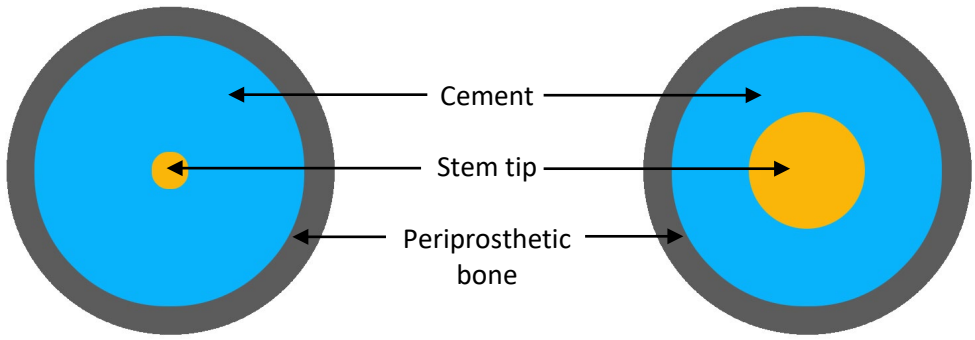

Fig. 5.3: Illustration of a SAAP stem tip in a bone plug with different taper angles
Not to scale. Left = A high taper angle and lower R_r. Right =A low taper angle and higher R_r.

Except for the lateral aspect SED peaks (primary and secondary), an increase in stem taper (more pointed) resulted in an increased periprosthetic SED. Analytically (using composite beam theory) this was expected; from Appendix A.1.1, we know that increasing R_r leads to a decrease in torsional and bending stress ratios, and a constant axial stress ratio (Appendix Chart A.1.1), remembering that:

$$R_r = \frac{\text{stem radius}}{\text{bone radius}} \text{ and } R_{stress} = \frac{\text{bone stress}}{\text{stem stress}}.$$

Then if stem taper increases, then stem radius decreases (Fig. 5.3) and, R_r decreases and so R_{sbend} and R_{stor} increase and since these are ratios of $\frac{\text{bone stress}}{\text{stem stress}}$ they define a relative increase in bone stress as was observed in the medial, anterior and posterior aspects. This effect is harnessed clinically; a tapered stem in a cemented collarless THR is often selected to function as a 'taper slip model'. Over time (most subsidence will occur in the first year) it gradually subsides and forms a tighter and tighter wedge within the cement mantle of the host bone (Mirza et al., 2010a). Subsidence and torsional resistance have been shown to be proportional to increasing implant stem taper and implant success (Pierson et al., 2015), although success depends heavily on the quality of the cement technique as well as the geometry of the stem (Hussain and Finlayson, 2008). Petrie and Williams (2005) also generated favourable (increased) (crestal) bone strain results for (increased) stem tapers.

The lateral aspect results cannot be similarly explained, the periprosthetic SED distribution is dominated by the primary and secondary SED peaks. Here an increased stem taper led to *decreased* periprosthetic bone SED. An explanation for the lateral SED peaks are a combination of the high shearing forces due to the taper slip (Huiskes, 1990, Keaveny and Bartel, 1993, Keaveny and Bartel, 1994, Mirza et al., 2010a) along with the stress concentration at the stem tip (the stem tip acts as a stress riser due to the irregularity in geometry from a stem being present to not present). Sometimes this can lead to bone fracture in thin bone cortices and is cited as the second leading cause for revision surgery in THR patients (Beals and Tower, 1996).

In the radiographs of the ITAP clinical trial, several patients presented with cortical bone thickening along the lateral aspect of the implant stem (ITAP patients 01, 02, 03, 04, 05, 06, 08, 09, 11), furthermore, patient 07 exhibited cortical thickening at the stem tip in the lateral aspect. It is likely that this is the result of the comparatively large SED magnitude observed along the whole stem in this aspect: the primary SED peaks are in excess of the upper homeostatic bone remodelling threshold (4400 Jm^{-3}) and the majority of the secondary SED peaks (apart from those elicited by the longer, more tapered ones) are within or above bone remodelling threshold.

Under the load cases presented here, the magnitude of the peak SED was within the structural capacity of bone (yield point and ultimate failure of cortical bone is 9.9×10^5 and 26.4×10^5 Jm^{-3} respectively (Horch et al., 2011)), thus damage was unlikely (the largest SED primary peak was 1.54×10^5 Jm^{-3}). However, there is a risk of damage to the bone under a greater load case such as that experienced during a fall, bone fracture at the stem tip, as was the case in ITAP patient 06, may occur. The bony pedestals in radiographs of ITAP patients 03, 08 and 12 at the stem tip, indicate questionable stability in this region (Agathangelidis et al., 2014) which may be associated with the stress concentrations experienced by the bone.

The effects of stem taper changes under LC2 in the ANOVA test generated significant evidence for this parameter to affect the periprosthetic SED. When testing the means of the taper groups with an ANOVA, if results were insignificant then the results from the T tests produced significant difference in four out of ten comparisons. Of these, the significant paired comparisons were obtained with stem tapers at the extremes of the range tested i.e. 1.5 ° or parallel, bolstering evidence for the significance of taper influencing periprosthetic SED.

Since bone stress is a function of cross sectional material distribution these results should be normalised with respect to bone dimensions before making implant design recommendations. The mean diaphyseal bone radius in the FE model was 0.016 m, using this outer radius for a hollow cylinder with a stem (inner) radius of 5 mm, 6 mm or 7 mm, area moment inertias are 5.10×10^8, 5.05×10^8 and 4.99×10^8 m^4 respectively (see Eqn. 2.4).

The following <u>stem taper conclusions</u> can be drawn (in a 0.201 m long residuum):

- An increase in stem taper significantly increases periprosthetic SED in the medial, anterior and posterior aspects. Some exceptions may be observed posteriorly in models with lowest and highest area moment inertias and in the medial aspect of the 0.08 m stems. These results

confirm part of my first hypothesis (*''the more narrow, more tapered, shorter SAAP stems without a cortical plate will generate the greatest periprosthetic bone SED''*).

- An increase in stem taper significantly decreases periprosthetic SED in the lateral aspect. Some exceptions may be observed in 0.08 m models with lower area moment inertias. This does not support my first hypothesis

5.4.1.2. (Tapered) stem length

Since bone length in the FE model remained fixed, varying the stem length changed the S ratio only. These results produced a very clear case for decreasing stem length on increasing periprosthetic SED. The same models were used to investigate the effect of stem length as were used for stem radius but grouped as SETS D – F. Each SET contained one of each of the three implant stem lengths with equal distal radius; each SET differed in stem distal radius size. Each SET either had a 0.75 ° stem taper (median stem taper) or a parallel stem (Appendix Table A.5.3). SED magnitude significantly decreased as stem length increased in ANOVA in all aspects except the half of the anterior aspect comparisons. No statistically significant paired stem length comparisons in the T test were obtained.

Mechanically, the application of an axial force at the femoral head will induce bending as a product of force x perpendicular distance from line of force (plus that resulting from bone curvature if present). This moment arm will be the distance along the femoral neck from the point of load application to the mechanical axis of the femur. Bending is also induced when a translational force is applied to the femoral head; in this case the moment arm is the distance from the point of load application to the most distal level of the bone (residuum length). The total bending moment experienced by the implant/bone assembly is the sum of all bending. When comparing equivalent models implanted with different stem lengths, neither the force, point of application, nor the moment arm change. The proportion of the bending moment that is carried by the bone depends on the height at which the cross section is being taken. In a shorter stem, more of the bending moment will be experienced by bone alone, whereas a longer stemmed model shares the load with the more flexible bone, thus the bone implanted with a longer stem will carry less force. In a longer residuum (lower amputation), the femoral neck moment arm remains unchanged and so bending as a result of axial force remains the same. However, the bending moment will increase in the application of a translational force since the residuum bone moment arm is longer. The total bending experienced in a longer residuum will be greater than a shorter residuum (higher amputation and greater bone curvature). Given that the height of the amputation is dictated by the surgical team, only the S ratio need be evaluated when making SAAP design decisions.

Clinically currently, short stemmed THR implants are popular (Gustke, 2012, Tatani et al., 2020) since they tend to load the proximal femur in a more physiologically normal manner (Feyen and Shimmin, 2014, Razfar et al., 2016), thereby reducing stress shielding (Ong et al., 2009, Bishop et al., 2010, Cilla et al., 2017). In pressfit THR a shorter stem may compromise primary stability (unlike tapered cemented stems) (Feyen and Shimmin, 2014) although others report stress shielding without compromising primary stability (Arno et al., 2012, Bieger et al., 2012), furthermore the incidence of fracture in short pressfit stems is lower (Molli et al., 2012).

Since bone stress is a function of the ratio of the stem height to the residuum lever arm length (S ratio) and S ratios for the 0.08 m, 0.12 m and 0.16 m stems were 0.4, 0.6 and 0.8 respectively then the following stem length conclusions can be drawn:

- An increase in S ratio significantly decreases periprosthetic SED, some exceptions may be observed anteriorly in models with lower area moment inertias. These results confirm part of my first hypothesis (''*the more narrow, more tapered, shorter SAAP stems without a cortical plate will generate the greatest periprosthetic bone SED*'').

In the ITAP patients an S ratio range of 0.47 – 0.76 produced optimal (positive) FS scores, with the rest between 0.50 – 0.62. Despite the difficulty in distilling comparable clinical results across the full range of variables under investigation an interesting result was obtained comparing patients 08 and 11. Both received similar implant geometries, had a similar bone radii and fixation methods (cemented) and resulted in the same radiolucent zone prevalence score (-2), however obtained very different FS scores (-18 and 6 respectively). The noteworthy difference between these patients was their S ratio (0.42 and 0.62); patient 08 had an S ratio falling outside the optimal S ratio range (as measured by FS score) whereas patient 11 had an S ratio within the optimal range.

5.4.1.3. (Tapered) Stem distal radius

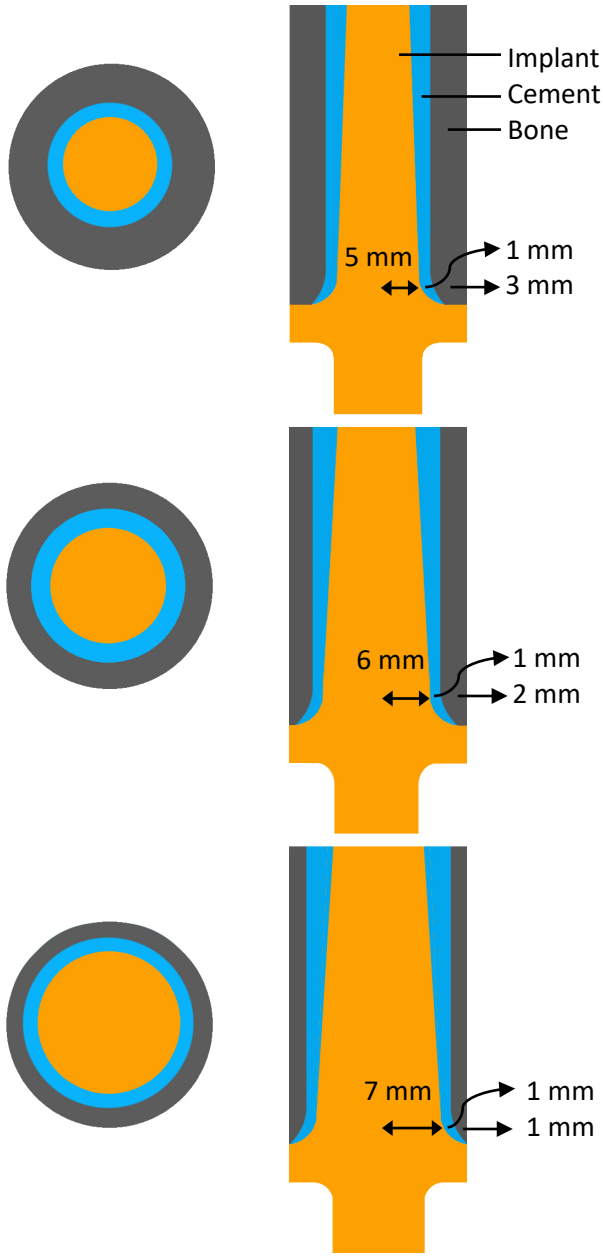

Fig. 5.4: A distal stem transverse and longitudinal cross section of three stem radii
Stems are equal length, 0.75 ° stem taper bone plug models with a 5 mm, 6 mm or 7 mm distal radius. (note a consistent distal cement mantle thickness of 1 mm and a bone layer of 3 mm, 2 mm, or 1 mm respectively.)

Fig. 5.4 illustrates a changing stem radius. Each of the SETS in this comparison (G, H and I) contained one of each of the three implant stem tapers with an equal stem length; each SET differed in stem length (see Appendix Table A.5.3). In all aspects, an increase in stem radius (towards a thinner bone cortex) resulted in an increase in periprosthetic SED. The results were statistically significant in all aspects in the comparison of the SET means (ANOVA) except for the shortest stem in the medial aspect, despite this

the T test produced statistically significant difference in all paired comparisons (TP2:TP5, TP2:TP8, TP5:TP8).

The numerical results were not modelled well analytically by composite beam theory which calculated the opposite behaviour (increase in R_r would cause a decrease in R_{stress}). There are several reasons why this mismatch could have been unexpectedly obtained: The assumption that an increase in stress leads to an increase in periprosthetic bone SED (Eqn. 5.1) may be an oversight and the contribution from the strain component caused a divergence from the analytical expectation. Another reason for the results not agreeing with analytical prediction is that the taper design feature and the outer radius of the anatomical bone changes along the length and so may not meet the conditions of beam theory (as discussed in Section 1.2.3.1). Finally, since stress transfer in a cemented implant will differ from a pressfit (see 5.4.2.1) there may be some contribution to the numerical periprosthetic SED result from the increased hoop stresses experienced in thinner bone cortices. Clinically, hoop stresses in periprosthetic bone have been observed in cemented THR patients (Bell et al., 2007). Equation 5.2 shows how these increase with an increase in stem radius.

$$\sigma_H = \frac{Pd_i}{2t} = \frac{Pr_2}{r_1 - r_2}$$

P = Internal pressure
d_i = Internal diameter of bone
t = bone cortex thickness

Eqn. 5.2

The following <u>stem radii conclusion</u> can be drawn (in a 0.201 m long residuum):

- An increase in cemented stem radii significantly increases periprosthetic SED in all aspects. Exception may be observed medially in models with a low S ratio (0.4). These results do not confirm my first hypothesis (*''the more narrow, more tapered, shorter SAAP stems without a cortical plate will generate the greatest periprosthetic bone SED''*).

In ITAP patient results; a weak positive pearsons correlation was obtained (0.4) between the implant radius and FS score but it was insignificant (p value = 0.2) and there was no correlation between the RL score and implant radius. Importantly, the correlation between second moment area and FS score was not strong (0.2) nor significant (p value = 0.7). These results suggest that either the sample size was too small to produce statistically meaningful outcomes or that, as suggested by Petrie and Williams (2005) and Cilla et al. (2017), other parameters influencing the FS score masked the effect of the section properties in the cemented implant patients.

5.4.2. Parallel stem group

5.4.2.1. Fixation type

SET J made nine comparisons between two equivalent parallel stems (since there were no tapered pressfit models only parallel stems were compared) using either press fit or cemented fixations under LC2 (see Appendix Table A.5.3). In all aspects, in all stems, the method of fixation generated a significantly different periprosthetic SED.

In pressfit parallel stems, modelled well analytically by composite beam theory, load is transmitted along the implant predominantly to the stem tip and flows into the host bone (Shen, 1998). The pressfit periprosthetic SED distribution under all load cases in all stems in all aspects produces a sharp uptick in magnitude at the stem tip (~ proximal 0.01 m of the stem) reflecting this. The flow of force does not completely bypass the periprosthetic bone in the pressfit stems; but a SED less than cemented equivalents was observed. The SED magnitude in the pressfit stems was relatively constant along the length of the periprosthetic bone proximal to 0.01 m from the stem base, albeit below the remodelling threshold under most load cases. The beam theory analysis is not influenced by length (since the length constant drops out of the equation in the derivation of the stress flow) and so a constant periprosthetic stress was expected. Similarly, a constant hoop stress is expected along the length of the periprosthetic bone (which also results from section properties rather than lengths) in a parallel stemmed cemented implant. There was slight variability in the SED magnitude in periprosthetic bone of the parallel cemented implants, which suggests additional mechanics to those dependant on section properties.

The following stem fixation conclusion can be drawn (in a 0.21 m long residuum):

- A cemented implant stem produces a significantly different periprosthetic SED distribution from a pressfit equivalent in all aspects under all load cases. This result confirms my second hypothesis.

Except for the lateral aspect and the bone at the tip (in all aspects), most periprosthetic SED in the pressfit stems fell below the remodelling threshold under all load cases. Although activities of daily living will include load cases greater than those applied here, walking will be the predominate loading regime and so substantial bone resorption would be expected in these patients. Of the four pressfit ITAP patients from the clinical trial, three had parallel stems (patients 03, 05 and 07) and although they all developed an increased cortical thickness laterally (particularly at the stem collar), there were severe problems in this patient cohort. Two developed a radiolucency (patients 03 and 07), suggesting a poor

union between the bone and implant; this was further illustrated in patient 03 who grew a stem tip pedestal. Pedestal formation (often with other signs) can indicate loosening (Pluot et al., 2009a). Patient 07 developed sciatic nerve neuroma and an untreated mild infection that ultimately led to implant removal. Similarly, patient 05 had their implant removed (after eight years of implantation) due to femoral osteomyelitis.

Since all cemented fixations had a stem taper in the ITAP clinical trial (taper slip models) there are no equivalent clinical results from the trial however there was one tapered pressfit stem patient (02) who achieved a high FS score (16). Considering the method of stress transfer in this pressfit patient such a good fixation may seem surprising. However, from section 5.4.1.1. where a reduction in taper (to 0°) was shown to increase periprosthetic SED in the lateral aspect there is a chance that bone remodelling in this aspect adequately anchored the implant. Furthermore, the patient had a low S ratio (0.50) and the lowest area moment inertia of all the ITAP patients (1.519 e-8 m^4) – both features that the numerical analysis results suggested may be exceptions to the trend observed and so potentially result in a successful fixation.

The debate as to whether cement or not is ongoing in the orthopaedic community; often there is no choice but to cement, for example in patients with porotic bone and/or a thin bone cortex. Cementing is a more affordable option because the stem does not rely on a costly porous coating or plasma spraying hydroxyapatite (HA) used to promote osseointegration in the pressfit stems. In a recent meta-analysis by Phedy et al. (2017) which analysed 27 clinical studies in terms of THR implant survival rates and adjusting for patient age, surgeon skill and implantation length, pressfit implants had a higher revision rates than cemented. This high rate of survival can in part be attributed to recognising the value of excellent cement penetration and pressurization (Ling et al., 2010, Maggs and Wilson, 2017).

5.4.2.2. (Parallel) stem radius

Each of the SETS in this comparison (K, L,) contained one of each of the three implant stem lengths with either a cemented (SET K) or pressfit (SET L) stem fixation; within each group of stem lengths were three models differing in stem radius (see Appendix Table A.5.3). In most aspects, an increase in stem radius elicited an increase in periprosthetic bone SED. The results were statistically significant in all aspects in ANOVA except for the 0.12 m stem in the lateral aspect and the 0.16 m stem in the anterior aspect (the T test failed to provide pairwise significance).

The numerical results were not modelled well analytically by composite beam theory which calculated the opposite behaviour (increase in R_r would cause a decrease in R_{stress}). As with the tapered group,

further work needs to be undertaken to investigate why this may be. In the ITAP patients the correlation between radius and FS score was very weak (0.34) and not significant (0.28) at $\alpha = 0.05$.

The following (parallel) stem radius conclusion can be drawn (in a 0.201 m long residuum):

- A thicker parallel stem, or an increase in R_r, whether pressfit or cemented, produced a significantly higher periprosthetic SED distribution than narrower stemmed equivalents. There may be some exceptions in stems with an S ratio > 0.6. These results do not confirm my first hypothesis (''*the more narrow, more tapered, shorter SAAP stems without a cortical plate will generate the greatest periprosthetic bone SED*'').

5.4.2.3. (Parallel) Stem length

SET (M) compared models PR37 – PR45 (these were the pressfit parallel models, the cemented ones were included in the tapered comparison as a 0 ° taper); each of the three radii groups in the SET contained implants that differed in stem length (see Appendix Table A.5.3). As with the tapered equivalents (section 5.4.1.2.) a decreasing SED was observed in the longer stemmed models. Results were statistically significant in almost all aspects testing with the ANOVA; however, the SED results were not as statistically significant along the AP axis compared with the ML axis.

The insertion of a stem into a bone, despite the method of fixation, will lead to a share of the flow forces through the composite and inevitably a reduction in bone stresses. (Jasty et al., 1994, Kim et al., 2001). In terms of how short a stem can be in a SAAP patient will depend on the condition of the bone stock and the height of the amputation. In THR stems as short as 50 mm have been used resulting in near physiologically normal bone loading (Østbyhaug et al., 2013). Similarly in proximal humeral pressfit FEA, similar results were found as stems decreased in length, with a 'stemless' implant producing the most physiologically normal stresses (Razfar et al., 2016).

5.4.3. Cortical plated group

5.4.3.1. Plated vs. non-plated

Each SET in this comparison (Q, R, S) contained three models; models in each triplet differed from one another by their cortical plate presence/length. Triplets differed from one another by their radii. SETS differed from one another by their stem lengths. All stems were cemented. SETS T, U, V were divided similarly but all stems were pressfit (Appendix Table A.5.3).

Although there were some exceptions, the broad SED picture in both fixation types showed a decrease in SED magnitude with the addition of a cortical plate; a full plate shielding the bone from stress to a greater degree than a half plate. Most models in most aspects, proximal to the cortical plate and close to the stem tip produced an SED that matched the non-plated equivalents.

Cemented

The non-plated models produced significantly different (higher) SED values in the medial and posterior aspects under LC4 compared with the plated models, thus illustrating the stress shielding effect of the plate. Whereas in the anterior aspect, the non-plated models produced significantly different (lower) mean SED values under LC4. Under this load case (terminal stance) there was the highest flexion moment (M_x) of the gait cycle combined with a propulsive force (- F_z), see Table 3.1, causing an anterior compression. In plated models, flexure is restricted due to the lateral plate; the surface restriction under a compressive force may increases the hoop stress (Equation 5.2) and so result in the increased SED observed anteriorly. In the lateral aspect, results were not significantly different in an ANOVA (although a T test showed a significantly different SED distribution between more pairs in the shorter stemmed models). This was somewhat surprising since there was a clear graphical difference (see lateral Chart 5.7) and the full field FE stress picture showed an obvious shielding underneath the plate (Fig. 5.5 d - f). However, due to plated models retaining the lateral primary SED peak observed in the non-plated equivalents (albeit somewhat reduced in magnitude) there was not a significant difference. Introducing a plate introduces a new stress riser on the anatomical bone surface (Fig. 5.5 e); the stress shielding effect of the plate is still apparent on the bone layer (Fig. 5.5 f).

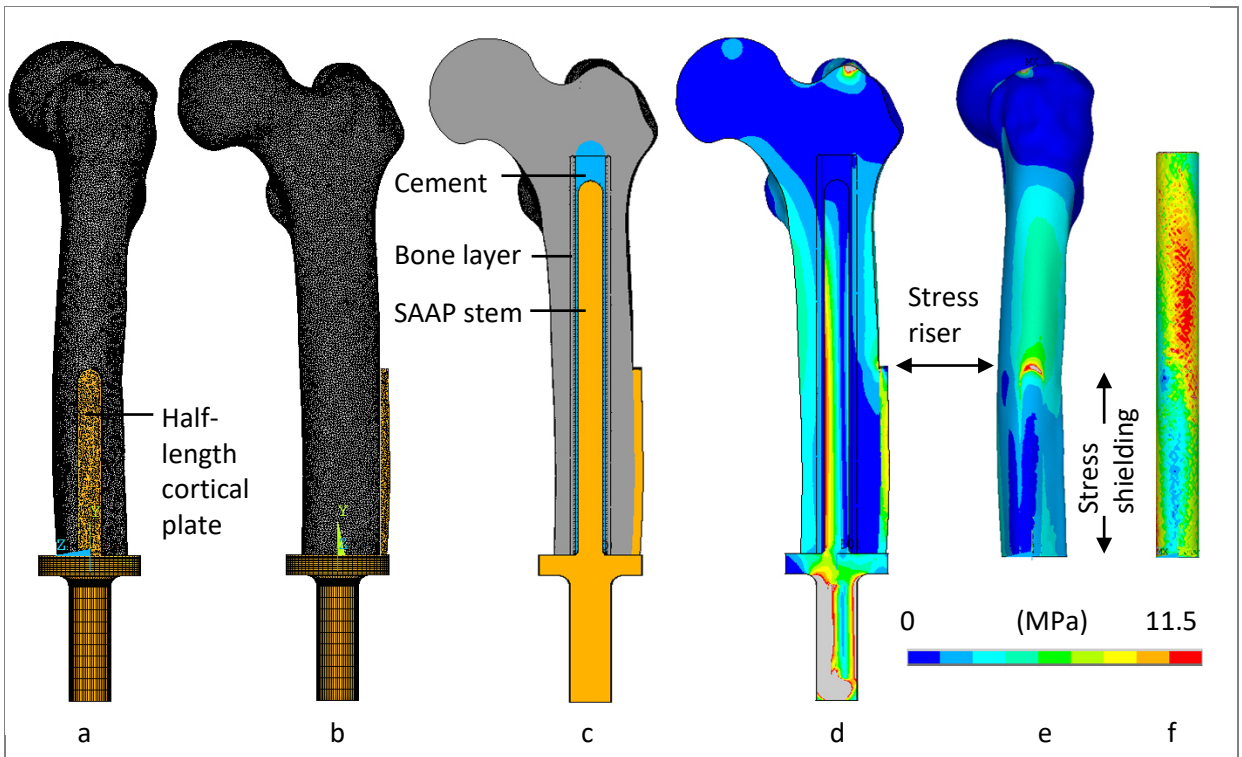

Fig. 5.5: FE bone plug models meshed and simulated
a = FE meshed model anterior view
b = FE meshed model lateral view
c = Longitudinal cross section of full FE model
d = Longitudinal cross section of full FE model with equivalent von Mises stress under LC4
e = Lateral view of FE model anatomical bone component equivalent von Mises stress under LC4
f = Lateral view of FE model bone layer equivalent von Mises stress under LC4

However, the only verified conclusion that can be drawn between <u>(cemented) plated vs. non plated</u> models (in a 0.201 m long residuum) is that:

- A plated stem significantly alters the periprosthetic bone SED distribution, predominantly by decreasing it in the medial and posterior aspect and increasing it in the anterior aspect compared with non-plated equivalents (see the effect of this in Fig. 5.5 d). There may be some exception to this in the lateral aspect. These results confirm part of my first hypothesis (*''the more narrow, more tapered, shorter SAAP stems without a cortical plate will generate the greatest periprosthetic bone SED''*).

<u>Pressfit</u>

Within the pressfit group, the non-plated models produced statistically significant different (higher) mean SED values in the lateral and medial aspects under LC4 in an ANOVA. Whereas in the posterior aspect the difference in group means resulted in the non-plated models producing significant different (lower) SED values in an ANOVA. In the anterior aspect results were not statistically significant using an

ANOVA, a pairwise T test produced significantly different SED distributions between more pairs in the shorter stemmed models. In the lateral aspect, due to stress transference being predominantly straight to the stem tip (due to the rigid bond), the effect of the plate significantly subdues the SED (to a greater degree and for more of the bone with the longer plate). At an SED magnitude of ~ 750 Jm^{-3} or 500 Jm^{-3} in the short and long stems respectively, these plates put the bone into a resorptive state in this aspect. Similarly, in the medial aspect SED magnitude decreased to ~ 1/3 that of the non-plated equivalents, suggesting that the lateral cortical plate had an influence on the degree of ML bending resulting from the axial component of LC4 (F_y).

The following conclusion between (pressfit) plated vs. non plated models (in a 0.201 m long residuum) is that:

- A plated stem significantly alters the SED distribution, predominantly by decreasing it in the lateral and medial aspect and increasing it in the anterior aspect compared with non-plated equivalents. There may be some exception in the anterior aspect. These results confirm part of my first hypothesis (*''the more narrow, more tapered, shorter SAAP stems without a cortical plate will generate the greatest periprosthetic bone SED''*).

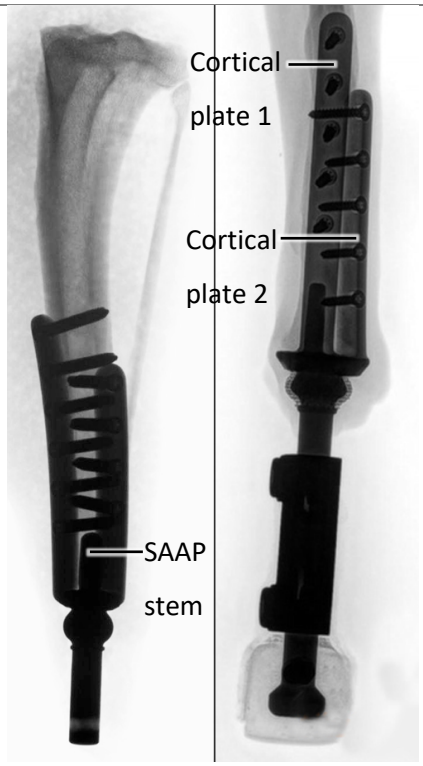

Fig. 5.6: Radiographs of planted SAAPs in companion animals
L = A canine tibial two locking plate canine SAAP used *in vitro* testing. R = feline radial two locking plate SAAP

Clinically, cortical plates whether cemented or pressfit, were not implanted in the ITAP patients as it was considered detrimental to detach muscle to plate the bone in an already muscularly compromised limb. A SAAP plate can provide rigidity, stability and prevents rotation of the stem. The stress shielding effect of the plate (Fig. 5.5 d and f) can be modulated by geometry and material (Ramakrishna et al., 2004, Haase and Rouhi, 2010, Saidpour, 2006, Bagheri et al., 2014, Al-Tamimi et al., 2017). Plate-induced osteopenia can also be reduced using a non-rigid connection to the anatomical bone surface such as a locking plate; (Cheal et al., 1983, Greiwe and Archdeacon, 2007). Most cortical plates used clinically are involved in bone fracture repair, however in some companion animals they have been used in conjunction with a SAAP, Fig. 5.6 (Fitzpatrick et al., 2011).

5.4.3.2. (Cortical plated) fixation

SETS in this comparison (N,O,P) differed from one another by their stem lengths. Each SET contained six pairs of models; there were two pairs of each stem radii, pairs of the same stem radii differed by their plate length (full or half). Models within each pair differed from one another by their fixation method, since there were no tapered pressfit models only parallel stems were compared (Appendix Table A.5.3). In all aspects, in all stems, the method of fixation generated a statistically different periprosthetic SED. The plated model's fixation type results in a similar discussion to the un-plated equivalent discussed in section 5.4.2.1.

The following conclusion between (plated) fixation type models (in a 0.201 m long residuum) is that:

- Fixation method in cortically plated SAAPs significantly alters the SED distribution. These results confirm my second hypothesis .

5.4.4. Comparison between clinical and FE results

Clinically, the most cortical growth and rate change were observed in AP and ML in distal zones A and F. This was twice as prolific in AP (corresponding to numerical model aspects medial and lateral) compared with the ML plane (corresponding to numerical model aspects anterior and posterior). Correspondingly, numerically SAAP models produced a distal medial periprosthetic bone SED peak approximately 0.01 m from the most distal measurement point (except for the plated models). Laterally this was similarly observed in the numerical models (the secondary periprosthetic bone SED peak) although in a slightly more proximal location than observed clinically (closer to zone B than zone A). To a lesser degree, the large distal anterior and posterior clinical cortical growth and rate change were well matched numerically. In these aspects there was often an periprosthetic bone SED distribution with a distal magnitude spike, however this was sometimes accompanied by a slight proximal magnitude increase that was not observed clinically.

5.4.5. Summary

This study considered the effects of implant design feature changes (stem radius, length, taper, fixation and cortical plate) with respect to the effect they had on bone remodelling. Most FE results indicated that minimising the geometry of the implant increased periprosthetic bone SED, thus minimises the chance of bone resorption. Practically, this must be balanced with implant strength requirements. However there were some unexpected results when looking at the effect of SAAP radii on periprosthetic bone SED that require further investigation. Not plating a bone meant that distal bone SED remained high laterally, a future design consideration is that plating should be carefully considered in patients, especially those with a (distally) thin cortex (since bone SED reduces as cortex decreases). Since the FS

SCORE showed improvements in patients with a +F distal cortical growth shape, risking cortical growth and collar ingrowth in this region does not seem wise. A shorter implant stem, despite fixation method, promoted increased periprosthetic bone SED and a reduction in parallel stem radius yet an increase in tapered stem radius also promoted increased periprosthetic bone SED. A cemented fixation generated higher periprosthetic bone SED compared with pressfit models; this was likely due to the taper slip effect introducing cortical hoop stresses. These results are summarised in Table 5.9

Table 5.9: Summary of SED outcomes (without the exceptions)

Group	SED Outcome summary
Tapered stem taper	An increase in stem taper significantly increases periprosthetic SED except for in the lateral aspect
Tapered stem length	An increase in S ratio significantly decreases periprosthetic SED
Tapered stem radii	An increase in cemented stem radii significantly increases periprosthetic SED
Parallel stem fixation	A cemented implant stem produces a significantly different periprosthetic SED distribution from a pressfit equivalent.
Parallel stem radius	A thicker parallel stem, whether pressfit or cemented, significantly increases periprosthetic SED distribution compared with a narrower stem.
Parallel stem length	An increase in S ratio significantly decreases periprosthetic SED
Plated vs. non plated (parallel)	A plated stem of either half or full length, cemented or pressfit significantly alters the SED distribution, predominantly by decreasing it.
Plated fixation type (parallel)	Stem fixation method in cortically plated SAAPs still produces a significantly different SED distribution

5.5. Conclusion

This Chapter presents a FEA looking at the effects of SAAP geometry changes on periprosthetic bone SED using a validated model from Chapter Four. Bone remodelling thresholds based on the theory of strain adaptive bone remodelling indicate the effectiveness of a parameter change. As periprosthetic bone SED dips below remodelling threshold and bone resorption is initiated, long term fixation success diminishes. The overriding FE message was one of aiming to reduce the amount of metal in the bone in order to minimise bone resorption (except when considering the SAAP radius in both the parallel and tapered group). Finally, all groups observed a significantly different (increased) periprosthetic SED using a cemented fixation as oppose to pressfit. Understanding how to design SAAPs in TF patients to minimise resorption is critical and it is hoped that the results from this FEA will go some way to guide future designs.

CHAPTER 6

6.1. Conclusions, limitations and future work

A TF amputation along with the ITAP, disturbs the flow of forces experienced by the femur as compared with an intact unimplanted bone. The physiological bone stress flow in the intact unimplanted bone, is well documented; literature describes remodelling theories, thresholds, and how changes in activity levels and evolutionary demands influence it. There is also literature on the changes in bone stress distributions in TF amputees fitted with a prosthetic socket and how this brings about ipsilateral limb osteopenia and contralateral limb osteoarthritis. However, there is a gap in the current knowledge regarding how the stress disturbances affect patients fitted with SAAP (of which the ITAP is one type), both in terms of implant success and bone remodelling thus linking to implant design. This thesis brings together outcomes from the ITAP clinical trial with a kinetic and kinematic study and uses the results to inform and build a parametric numerical model comparing the effect of implant design on periprosthetic bone remodelling. In doing so it closes the gap in our understanding of the effects on periprosthetic bone remodelling around SAAPs. Moreover, a SAAP design guide has been developed in order to address strain adaptive periprosthetic bone resorption; regularly observed with the use of current SAAP designs (Xu and Robinson, 2008, Haket et al., 2016, Thomson et al., 2019, Örgel et al., 2020).

SAAP design research tends to focus on the mechanical stresses (often Von Mises stress) experienced by the implant (or the bone) (Xu and Robinson, 2008, Tomaszewski et al., 2012a, Tomaszewski et al. (2012b, Thesleff et al., 2018a). The literature predominantly reports outcome metrics associated with the mechanical requirements of the implant and/or compares the effects of SAAP designs on periprosthetic bone (Von Mises) stress. Von Mises stress is a theoretical value commonly used to determine if yielding will occur in an isotropic and ductile metal (achieved when components of stress acting on it are greater than the criterion):

$$\sigma_{\text{von mises}} = \sqrt{\frac{(\sigma_1 - \sigma_2)^2 + (\sigma_2 - \sigma_3)^2 + (\sigma_3 - \sigma_1)^2}{2}}$$

Although these are useful outcome metrics to compare the merits of one implant against another post hoc, or to assess the structural integrity of the implant material, they do not describe the adaptive bone tissue reaction to the effects of a fluctuating load since they do not quantitively address strain adaptive periprosthetic bone resorption. Furthermore, physiological load cases applied in the aforementioned simulations are frequently harvested from published data, primarily the OPRA data set discussed in Chapter three (Frossard, 2019, Lee et al., 2007). Applying load cases from the literature, introduces unknown sources of simulation error in addition to the uncertainties discussed in Chapter three with

this dataset. The novel work in this thesis takes patient specific data from the only ITAP clinical and applies it to validated FEA models to fill this gap in the literature and provides a direct clinical translation for SAAP design in future TF amputees.

In Chapter One, after a review of the biological processes associated with bone remodelling, current SAAP devices available to patients globally are presented. The ITAP is one of only two devices that have undergone the rigour of a full scale clinical trial (the OPRA being the other). The problems and failures of the devices reviewed tend to be connected to the issue of infection rather than unsuccessful osseointegration. Avoiding infection by addressing the soft tissue seal around SAAP implants as they exit the body requires further work to match the success of implant integration with the bone. Wide scale development and adoption of SAAPs are held up by this; future work could involve cross referencing natural analogues of keratinised epithelium breach designs (e.g. deer antler). The second obstacle in SAAP development is the lack of a dependable (universal) safety connection device. Of the current devices none are without problem(s) and many leave patients without adequate protection; future work developing a reliable failsafe device is needed.

The results of the ITAP clinical trial are presented in Chapter Two of this thesis. The importance of an FS score, similar to that used in the assessment of hip implants is identified and generated. Patient outcome using the developed FS score along with cortical bone change, the second outcome measure is assessed. The clinical trial was a single group assignment interventional model where a comparison pre and post-surgery was intended. Outcome measures did not consider implant design parameters, rendering inter patient comparisons statistically insignificant. Therefore, I reported *trends* in fixation success and bone changes as a result of implant design differences between the patients. Despite the small population (n = 12) and lack of clearly differentiated implant design features, this study demonstrated that an ideal S and F ratio range and a straight, tapered stem and +F collar growth shape were beneficial, whereas one or more of the parameters pertaining to the pressfit fixation was detrimental. With respect to cortical growth, diaphyseal cortical change (thickness and rate) had less impact on overall success than that which grew into the collar in a distally flared manner (+F) alone.

These results demonstrate the need for further investigation with increased patient numbers to determine statistical significance. Ideally, matched patients would be recruited and implanted with a SAAP that differed in one parameter only. If a multivariate analysis was deemed necessary (due to the limitations of recruitment and/or surgical need) then a future study must ensure that the number of patients in each subgroup is enough to generate statistical significance. The results of such a trial could offer valuable insight into deviations from numerical models that may have been overlooked or where approximations did not offer a clear picture. Furthermore, a bigger and statistically relevant clinical trial

would mean that the numerical simulations of Chapter Five could be treated as a pre-clinical analysis and implants for the trial could be engineered accordingly.

Another limitation of the work presented in Chapter Two was that in developing an outcome measuring scale it was not possible to weight the contributions from the two sub scores (CIG and RL) in an informed way. With a larger patient group in a future trial as described, it would be possible to develop the FS SCORE to represent outcome success more accurately. This could then act as a feedback loop on the clinical fixation success; it should be noted that the process of calibrating SAAP implant success will be an evolution as the richness of data increases. A final limitation of the FS SCORE is that one of the sub scores (CIG) results from cortical bone growth around a SAAP collar. Collars are a design feature in all SAAP designs *except* the OPRA, therefore in order for the scoring system to be universal an equivalent sub score for these implants must be found in the future.

Chapter Three captured kinetic and kinematic data from an ITAP patient fitted with a wireless six axis load cell and a retroreflective marker set. The load cell kinetic data was used to validate the kinetic data produced by the principles of inverse dynamics in the commercial biomechanical software. Results showed the greatest disparity in the axial force component (F_Y) and the moment around the AP axis (M_x) but in summary offered an acceptable level of agreement. The necessity for agreement was to verify that extracting inertial forces from the biomechanical software at matched gait stages was valid. Load cell results from patient 12 produced kinetic data that was similar in distribution to non-amputated gait with some deviations in phasing and magnitude attributed to the split belt treadmill and/or the transected muscles. In future work it would be beneficial to perform the same study overground.

The kinetic data obtained from the patient walking downhill differed from that of a non-amputated individual but matched prosthetic socket data; this may be due to the preferential loading of the intact limb. A load phasing difference was observed on slope gait compared with level gait and this was likely to be due to the positioning of the body's COM. Comparing data with the OPRA patient kinetic data was challenging and this should be addressed in future work. Ideally, a study would take groups of patients with different SAAP designs and look at biomechanical approaches and deviations from non-amputated gait to level and sloped overground gait. To augment this, activities of daily living should be included in particular stair ascent and descent. It would be interesting in future work to apply the load cases to the FE model from the full original study plan to investigate the effects on periprosthetic bone. These included sloped walking, stair walking, sit to stand to sit and lateral stepping. This study was limited by the use of the split belt treadmill and n = 1 for the load cell study. In addition, some of the load cell build complications may have added experimental error.

Chapter Four was a precursor to Chapter Five where the former presented an experimental validation of a FE model for analysis in the latter. The FE verification was made using experimentally produced displacement data obtained with DIC and discrete point strain gauge data. One of the limitations in this study was that I compared FE and DIC displacement *spans* and this was potentially reductive as the variability between directly compared nodal coordinates was omitted. Future work should address this by introducing discrete points of comparison between the two data fields.

Chapter Five used the validated model from Chapter Four and the load cases from Chapter Three to investigate bone SED in a FE model representing a SAAP in a femur modelled on an ITAP patient. Analytical results predicted the effects of changing SAAP design features on periprosthetic bone SED well for S ratio (length), cortical plating and taper. Moreover the chapter's second hypothesis regarding the expected difference in periprosthetic bone SED between SAAPs fixed in the bone differently was met. There was an unexpected lack of agreement with analytical results when investigating changes in SAAP radius which may have been due to unmet beam theory governance, none the less requires further investigation. Applying the results of the FEA more globally to the question of bone remodelling, these matched well the clinical results. The match with such a small clinical population was a success and in future work a bigger clinical trial could provide opportunity for statistical comparison between results obtained numerically and that observed clinically. It would be useful run a univariate analysis on fixation method to get a clearer picture on the advantages and disadvantages of each method in this population. Furthermore, it might be interesting to remove the FE model interference fit approximation and include a layer of HA line to line with the inner bone layer surface. This would mean that the material properties of the mineral would determine the resultant interference and may shed further light on the unexpected radius change model results.

Both the numerical and the clinical study suffered from data reduction by investigating bone remodelling along aspect lines or from 2D radiographs rather than full field. In future work it may be useful to produce periprosthetic bone SED maps of the inner surface of the bone layer to compare with equivalent CT maps. A CT map of this nature would be a Boolean subtraction map between the two timescales under investigation. The next evolution of SAAPs will establish a direct connection between the limb and the user's skeleton, nerves, and muscles. The bidirectional communication between external prostheses and implanted electrodes will allow more natural prosthetic function with improved outcomes. It is therefore of clinical importance that the SAAPs of today are designed to minimise unwanted bone remodelling (resorption) to prepare for the SAAPs of tomorrow. The results of this thesis demonstrate how, with patient specific data, FE models can reasonably predict periprosthetic bone outcomes of different SAAP designs. The power of this preclinical analysis could be transformative to counter the deleterious effects of strain adaptive periprosthetic bone resorption.

Appendices

Appendix 1

A.1.1 Analytical stress analysis of a SAAP stem in bone

The composite beam analysis can discount the cement layer since it had a negligible effect on bone and implant stress transfer as shown in Table A.1.1. These results were obtained from two FE beam models; a pressfit (two material composite) and cemented (three material composite) model comprising two and three elements respectively. Material properties were considered elastic and isotropic (Fig. A.1.1). Restraining nodes at the distal end in all six DOF and applying a force (100 N) at the proximal end (nodes merged) to produce torsional, bending and axial stress resulted in the tabulated reaction solutions at the two supports (distal nodes).

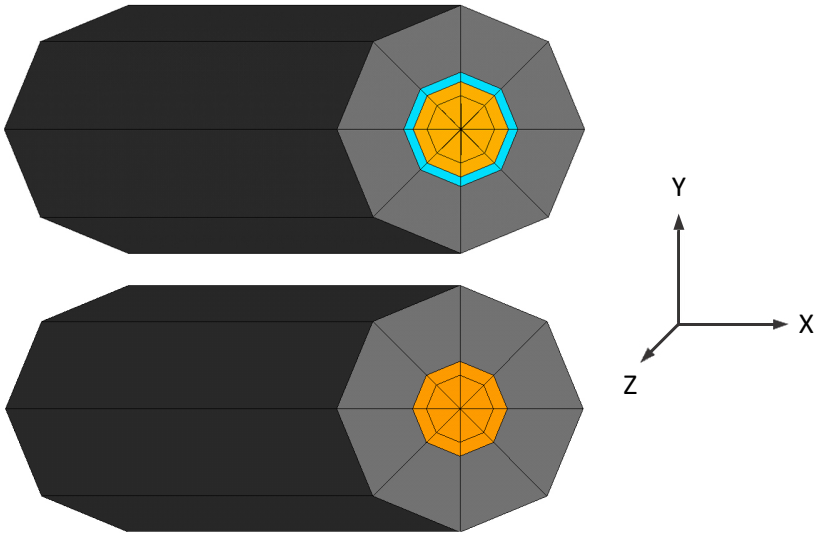

Fig. A.1.1: Beam models of a pressfit (top) and cemented (bottom) implant stem in a bone diaphyses. Grey = cortical bone (inner radius = 5 mm, outer radius = 13 mm, E = 18 Gpa, ν = 0.3). Turquoise = bone cement (inner radius = 5 mm, outer radius = 6 mm, E = 2 Gpa, ν = 0.4). Orange = SAAP stem (radius = 5 mm, E = 115 Gpa, ν = 0.3)

Table A.1.1: Reaction solution resulting from a torsion, bend and axial load application (M_x, M_y, F_x respectively) in cemented and pressfit FE beam models.				
		Implant	Cement	Bone
Torsion (Pa)	Cemented	12.75	0.22	87.03
	Pressfit	12.51	-	87.49
Bending (Pa)	Cemented	12.74	0.24	87.02
	Pressfit	12.51	-	87.49
Axial (Pa)	Cemented	54.34	0.42	45.25
	Pressfit	15.90	-	84.10

The first step in developing a non-dimensional beam analysis that represents a two material composite is to consider the bone and the implant as two parallel springs fixed distally with a force applied proximally. The force in each one will be proportional to a stiffness constant, K, where:

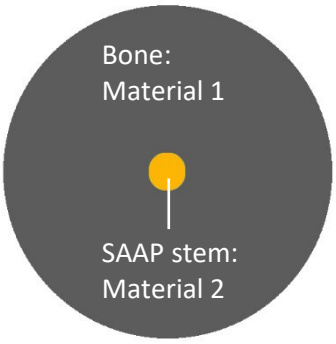

Fig. A.1.2: A cross section through a two material composite beam model.

$$K = \frac{AE}{L}$$

A = Section area
E = Stiffness modulus
L = Length

Eqn. A.1.1

And since:

$$F = Kx$$

F = Force
K = Stiffness constant
x = Displacement

Eqn. A.1.2

Which can be expressed as:

$$F_i = \frac{K_i}{K_1+K_2} \cdot F$$

Where i is 1 or 2 and
$F = F_1+F_2$ is the total
force in materials one and two.

Eqn. A.1.3

Then the ratio of forces is equal to the ratio of stiffnesses in the two materials:

$$\frac{F_1}{F_2} = \frac{K_1}{K_2}$$

F_1 = Force in bone
F_2 = Force in implant
K_1 = Stiffness constant for bone
K_2 = Stiffness constant for implant

Eqn. A.1.4

To investigate the (non-dimensional) distribution of stresses the following ratios were assumed:

$$R_r = \frac{\text{Radius of material two, } \mathbf{r_2}}{\text{Radius of material one, } \mathbf{r_1}}$$

$$R_E = \frac{\text{Stiffness modulus of material one, } \mathbf{E_1}}{\text{Stiffness modulus of material two, } \mathbf{E_2}}$$

$$R_F = \frac{\text{Force in material one, } \mathbf{F_1}}{\text{Force in material two, } \mathbf{F_2}}$$

$$R_{Sax} = \frac{\text{axial stress material one}}{\text{axial stress material two}}$$

$$R_{Sbend} = \frac{\text{bending stress material one}}{\text{bending stress material two}}$$

$$R_{Stor} = \frac{\text{torsional stress material one}}{\text{torsional stress material two}}$$

Note that R_r uniquely has material two as the numerator in the ratio so that $0 < R_r < 1$

If axial stress = $\frac{F}{A}$

then substituting from equation A.1.1:

$$R_{Sax} = \frac{\frac{A_1 E_1}{\frac{L}{A_1}}}{\frac{A_{2E_2}}{\frac{L}{A_2}}} = \boxed{R_E}$$

Eqn. A.1.5

If bending stress = $\frac{M_y}{I}$

where y is the distance to the neutral axis (the radius in this case), and I the second moment of area, then substituting from the bending stiffness relationship where M = EIθ gives:

$$R_{Sbend} = \frac{E_1 I_1}{E_2 I_2} \times \frac{\frac{Y_1}{I_1}}{\frac{Y_2}{I_2}} = \boxed{\frac{R_E}{R_r}}$$

Eqn. A.1.6

And if torsional stress = $\frac{Tr}{J}$

then substituting from the torsional stiffness relationship where

$$T = \frac{JG\phi}{L}$$

gives:

$$R_{Stor} = \frac{J_1 G_1 \phi}{J_2 G_2 \phi} \times \frac{\frac{r_1}{J_1}}{\frac{r_2}{J_2}} = \boxed{\frac{R_G}{R_r}}$$

Eqn. A.1.7

Plotting R_{Sax}, R_{Sbend} and R_{Stor} using the relationships derived from equations A.1.5, A.1.6 and A.1.7 produces Chart A.1.1 which shows the difference in distribution and magnitude between bending or torsion and axial stress ratios $\left(\frac{\text{bending or torsion or axial stress material one}}{\text{bending or torsion or axial stress material two}}\right)$. *In vivo* strain measurements in mammalian and avian bones show bending and torsional strains to be the most prevalent during peak loading (Lieberman et al., 2003, De Margerie et al., 2005).

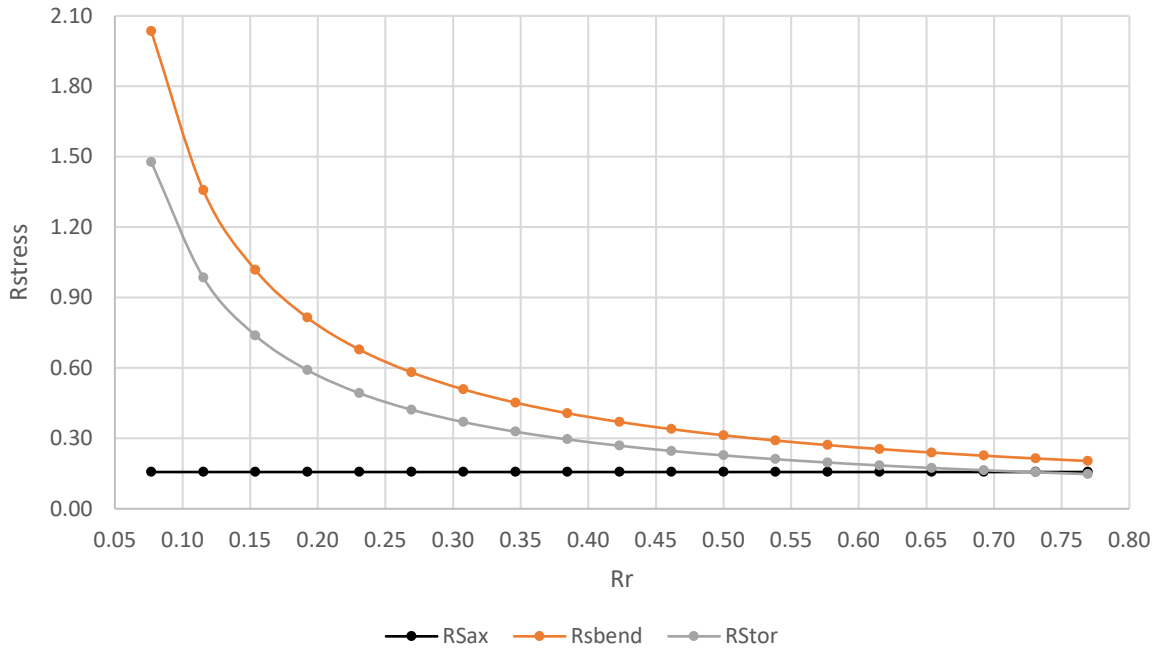

Chart A.1.1: Plot showing relationship between the ratio of stresses (R_{stress}) in three planes (axial, bending and torsion) and the ratio of radii between bone and implant when:

Bone	Implant
E_1 = 1.80E+10 Pa	E_2 = 1.15E+11 Pa
G_1 = 5.00E+09 Pa	G_2 = 4.40E+10 Pa

This analysis concludes that as the R_r increases in magnitude (towards a thinner cortex):

- That R_{sax} remains unchanged
- And R_{sbend} and R_{stor} change (decreases) non-linearly

A.1.2 Units of strain energy and strain energy density

Strain energy:

$$\frac{\text{stress x strain x volume}}{2} = \text{Nm}$$

$$\frac{\text{force x displacement}}{2} = \text{Joule}$$

Strain energy density (SED):

$$\frac{\text{stress x strain}}{2} = \text{N/m}^2 \,*$$

$$\frac{\text{force x displacement}}{\text{2 x volume}} = \text{Joule/m}^3 = \text{Pa}$$

* Where stress and strain are summed from all axes i.e.:

$$\frac{\left((\sigma_x \times \varepsilon_x) + (\sigma_y \times \varepsilon_y) + (\sigma_z \times \varepsilon_z) + (\sigma_{xy} \times \varepsilon_{xy}) + (\sigma_{yz} \times \varepsilon_{yz}) + (\sigma_{xz} \times \varepsilon_{xz})\right)}{2}$$

A.1.3 Failsafe designs

Failsafe interventions are required for any SAAP to prevent loading the bone beyond yield point and causing fracture e.g. in the event of a fall or the artificial limb leg getting trapped. A personalised bone/implant model calculating stress flow from patient kinetic data would be the ideal information for the design of a failsafe connection to protect the bone from overload. This is not feasible for every patient and in addition patient bone density changes (increases) over time which affects the failsafe detachment thresholds. The requirement for this flexibility has not been accounted for in the currently available designs. Three devices are on the market at the time of writing; the AXOR II, used in patients with the OPRA implant, the failsafe designed by Stanmore Implants Worldwide (SIW) for use with patients in the ITAP clinical trial and the Click Safety Adapter used in patients with the ILP and OPL implants. All are factory set to release at pre-determined thresholds but have the capability to be increased or decreased. Literature regarding the method of failsafe threshold calculations is not published.

AXOR II (for OPRA implants)

The AXOR II supersedes the OPRA ROTASAFE system with the introduction of a bending response to overload. It detaches from the OPRA abutment in the event of torque overload and opens itself in the event of bending overload in the AP plane (Fig. A.1.3, right). The device is factory set to torque release at 15 ± 2 Nm and AP bending at 70 ± 5 Nm (Integrum A.B.), however both releases are controlled by spring tension mechanisms that can be factory adjusted to suit outside of these ranges. Problems with the failsafe have been reported in 89 % of patients in a study by Zaid et al. (2019c) involving difficulties donning and doffing their limb and noise using the failsafe. The bending response in AP is limited to only catering for a backwards fall, a comprehensive safety device would prevent bending overload in all degrees of freedom.

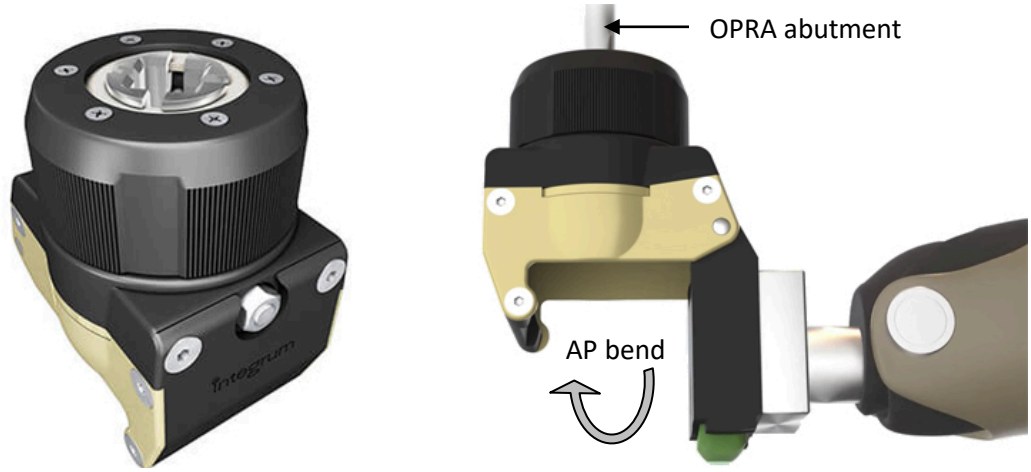

Fig. A.1.3: AXOR II. Image on the right shows the device response to bending overload in AP plane

SIW failsafe (for ITAP implants)

The SIW failsafe device (Fig. A.1.4) offers detachment in the event of overload in bending and torque. The torque release is controlled by a frictional clutch plate shown in red/green in the parts blow up diagram in Fig. A.1.4, held in place by springs (not shown). Overcoming the spring tension causes the two halves of the failsafe to rotate freely against each other. The six radially placed spring loaded jaws shown on the right image of Fig. A.1.4 clip to the proximal half of the failsafe. If bending force overcomes the tension of a jaw spring it unclips and pushes upward against the distal surface of one of the clutch plates (the green one) to detach the top from the bottom half of the device. Settings for detachment of the failsafe can be adjusted (by the manufacturer) by altering stiffness of the jaw springs, clutch plate springs and the springs within a preload cell. There is no published literature regarding the effectiveness of the SIW failsafe device. Verbal feedback from prosthetists at the RNOH is that the device offers a substandard safety solution: It detaches on occasion when it should not, tension

adjustments are not possible by the prosthetist and the length of time it takes to receive the device after sending it off for adjustment is impractical for patients.

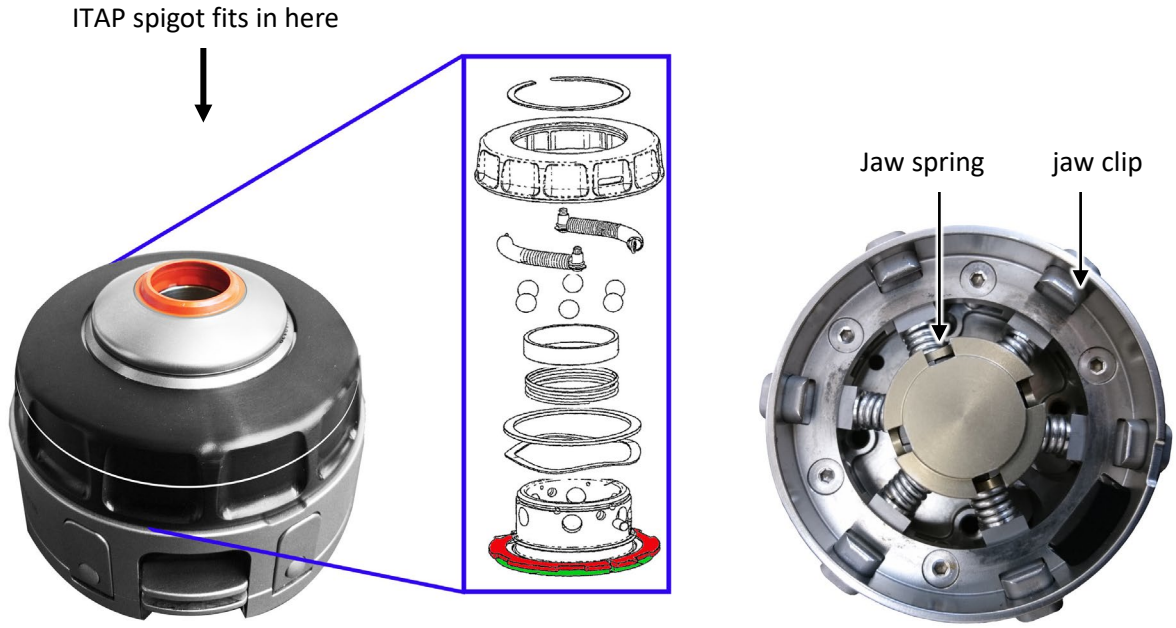

Fig. A.1.4: SIW failsafe. Left = Failsafe with the end cap inserted. The ITAP spigot fits into the end cap. Exploded internal view of the proximal part of the device showing the clutch plates (red and green) against which torque release is controlled. Right = View from the top of the distal half of the failsafe once detached in which the bending release control is housed (six spring loaded jaws)

Click Safety Adapter (for ILP/OPL implants)

The ILP/OPL failsafe device (manufactured by Xilloc, formerly OTN) detaches only in the event of torque overload. Detachment is controlled by two pins which act as material failsafe; shearing off when a torque exceeds a threshold. In the latest version of the adapter (the Nexus, not yet available) the connector accepts an ILP/OPL implant distal 16/18 taper *or* an OPRA abutment (Xilloc Medical B.V., 2019). Fracture of the bone due to overload is rare suggesting that overall, the devices do a good job, however some patient experiences suggest that threshold settings have not been calculated correctly or changed as the bone remodels.

Fig. A.1.5: Click safety adapter by Xilloc. Left and centre image: current version.
Right image: The Nexus

Appendix 2

A.2.1 Montages of ITAP patients 01 -12

Patient 01 (AP montage above each ML montage)

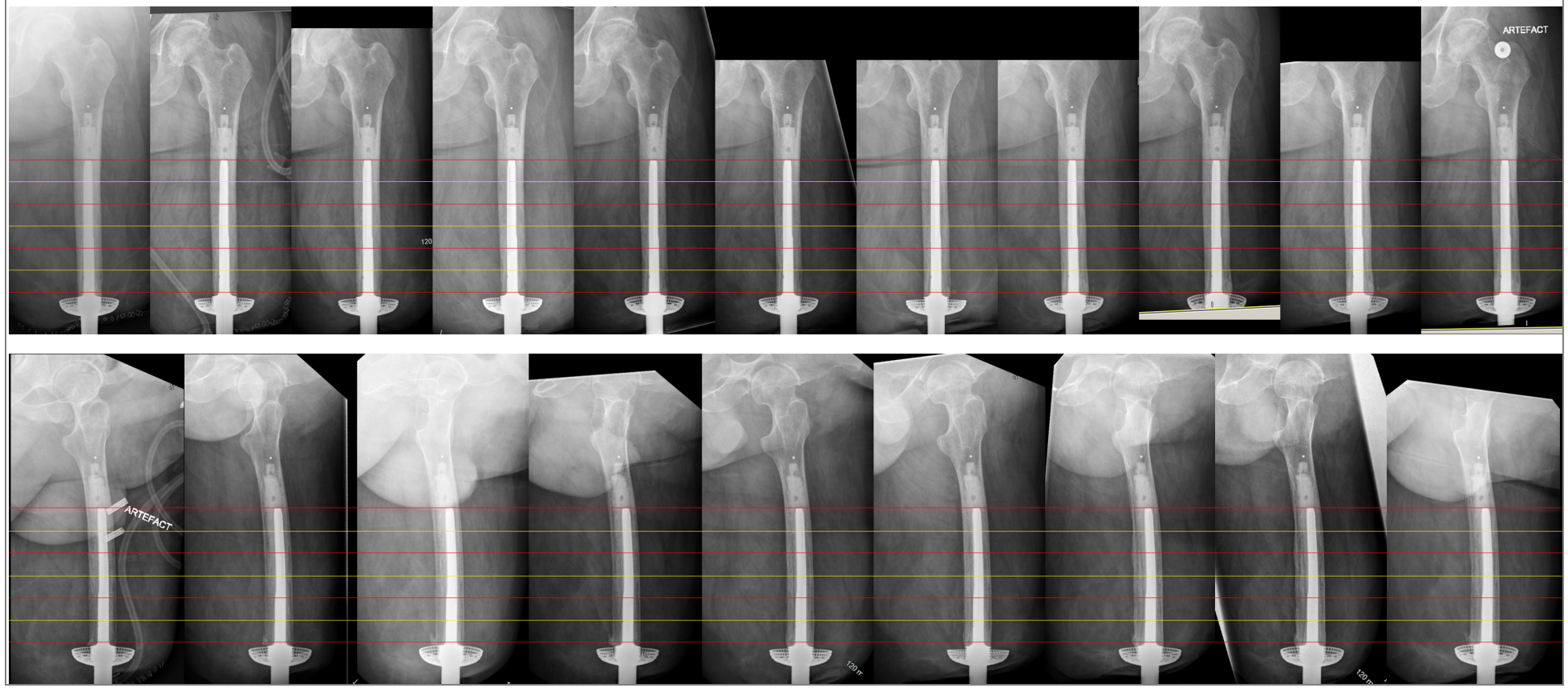

Patient 02

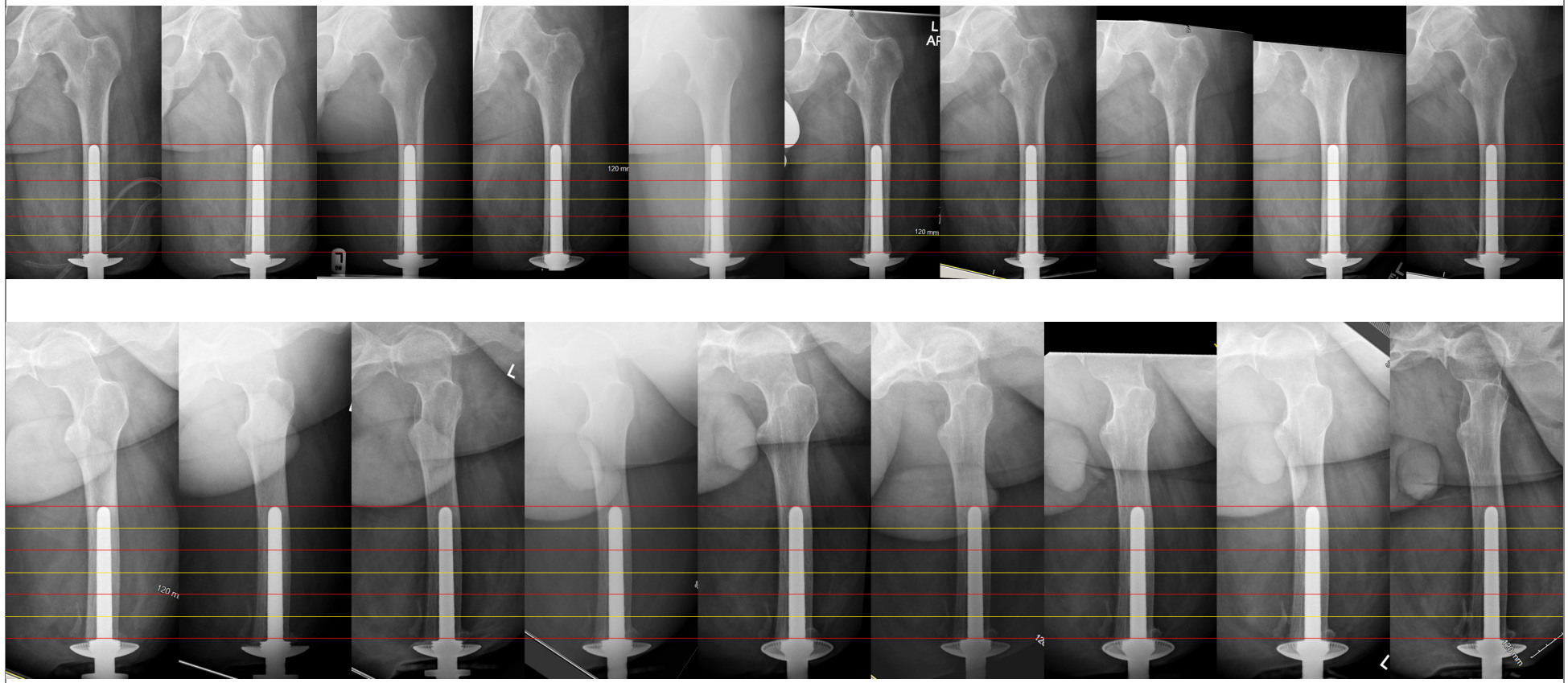

Patient 03

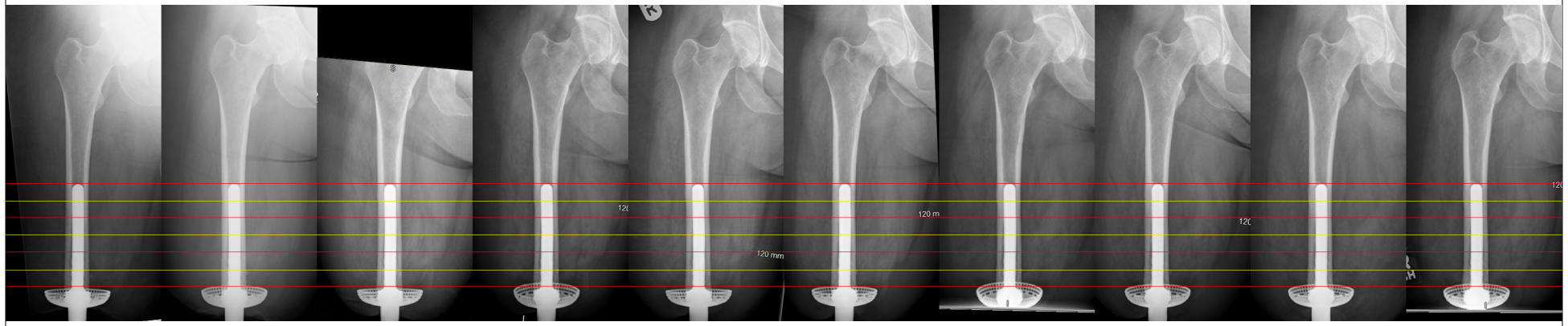

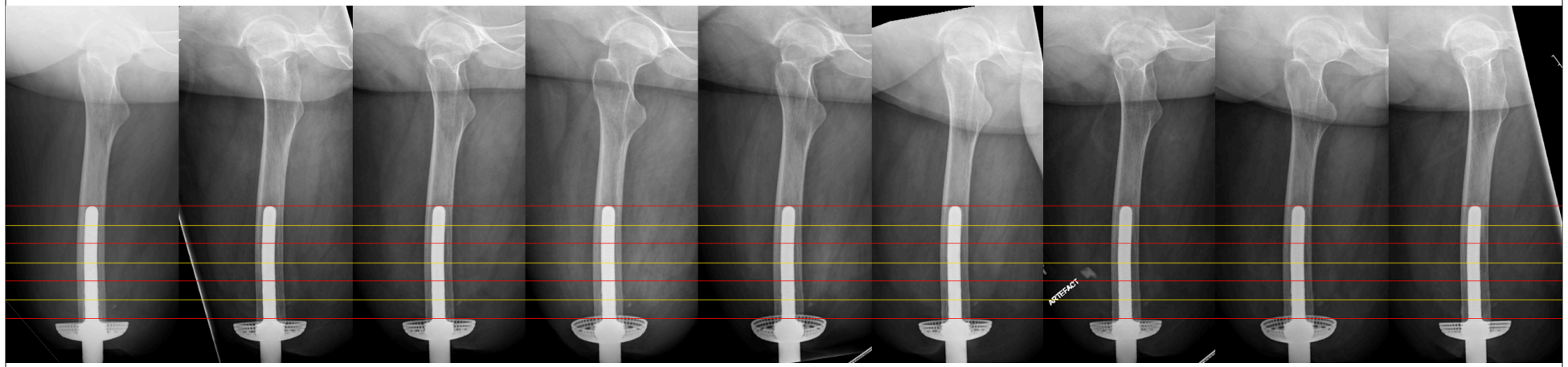

Patient 04

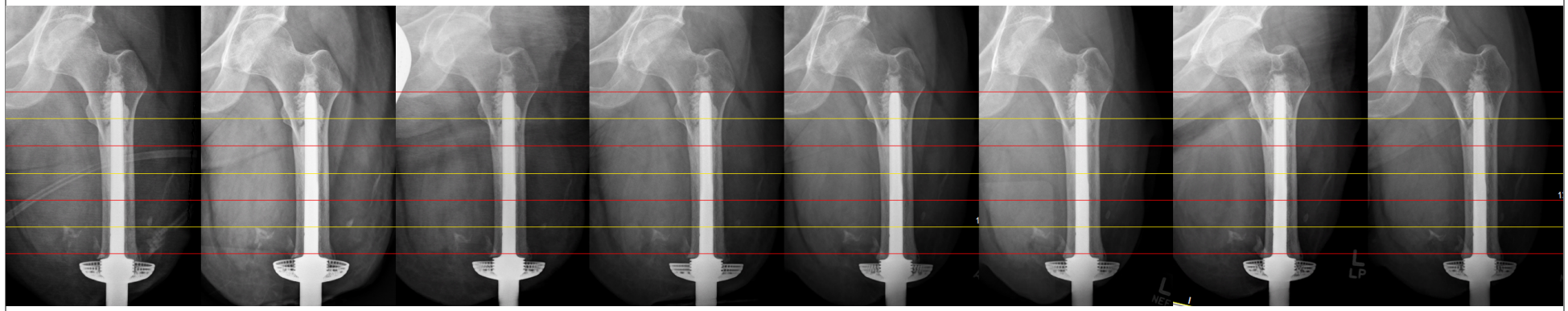

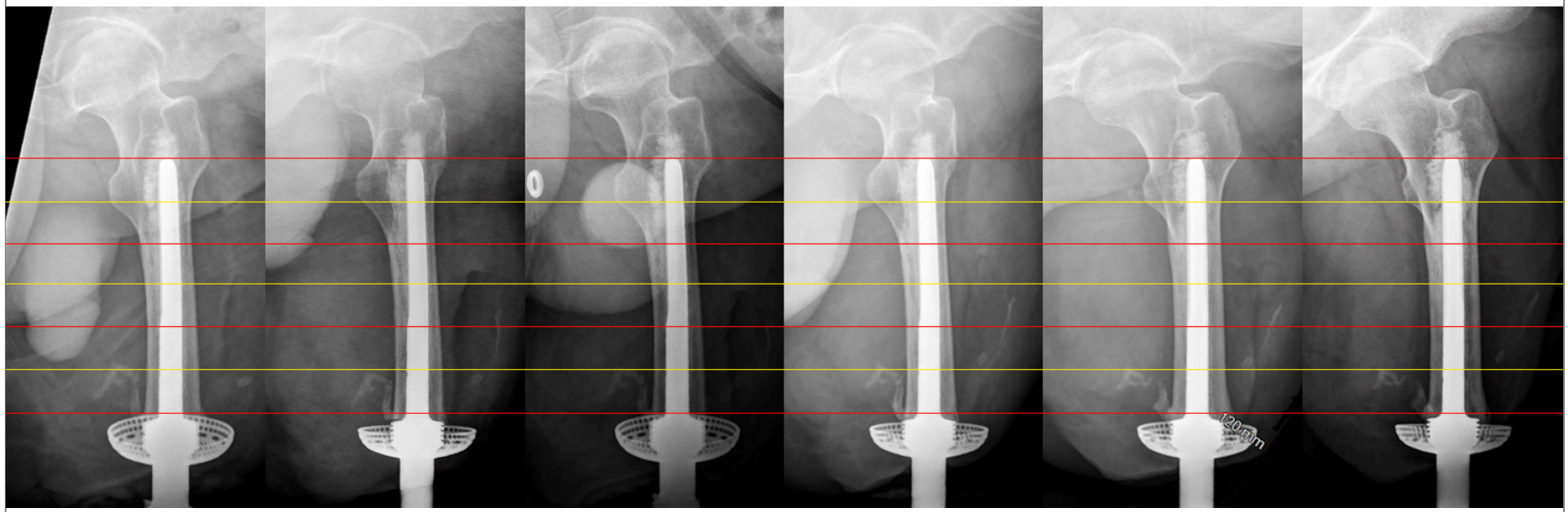

Patient 05

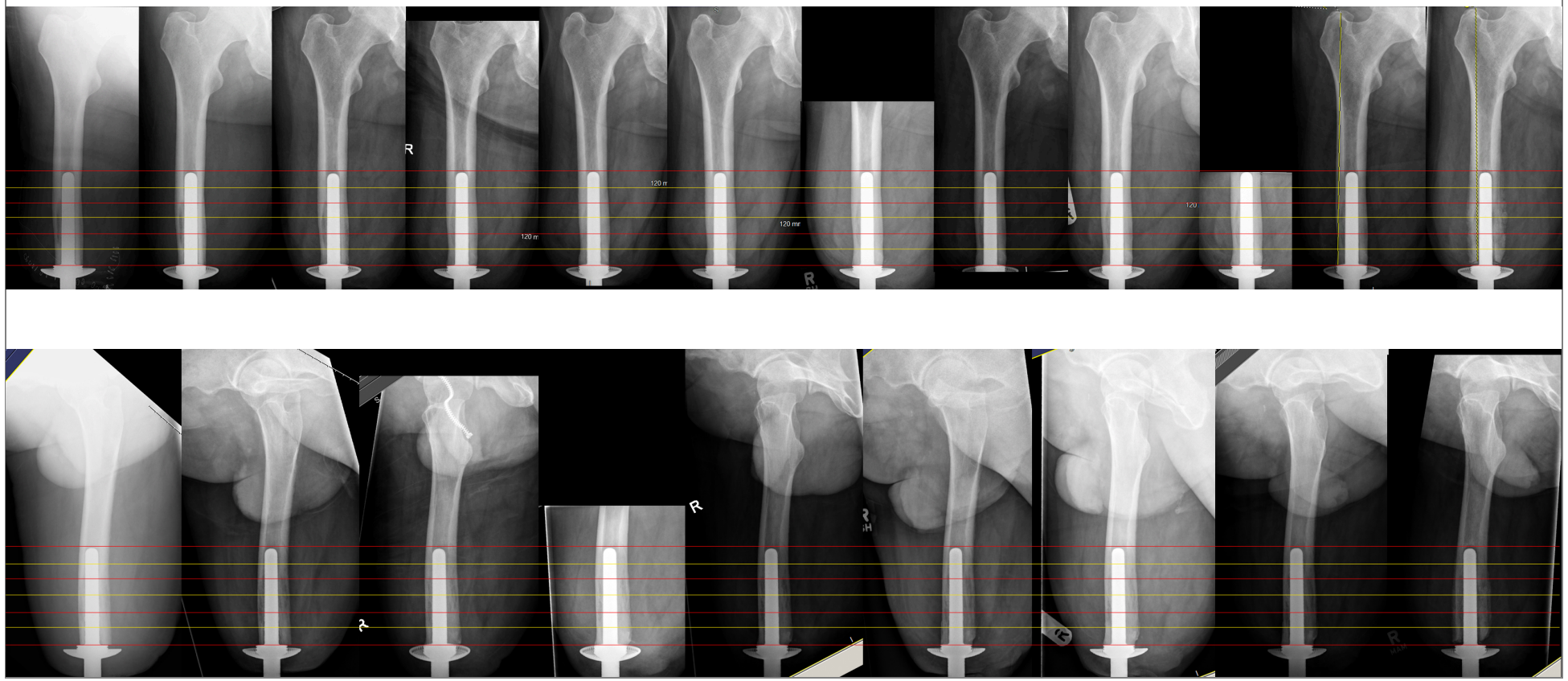

Patient 06

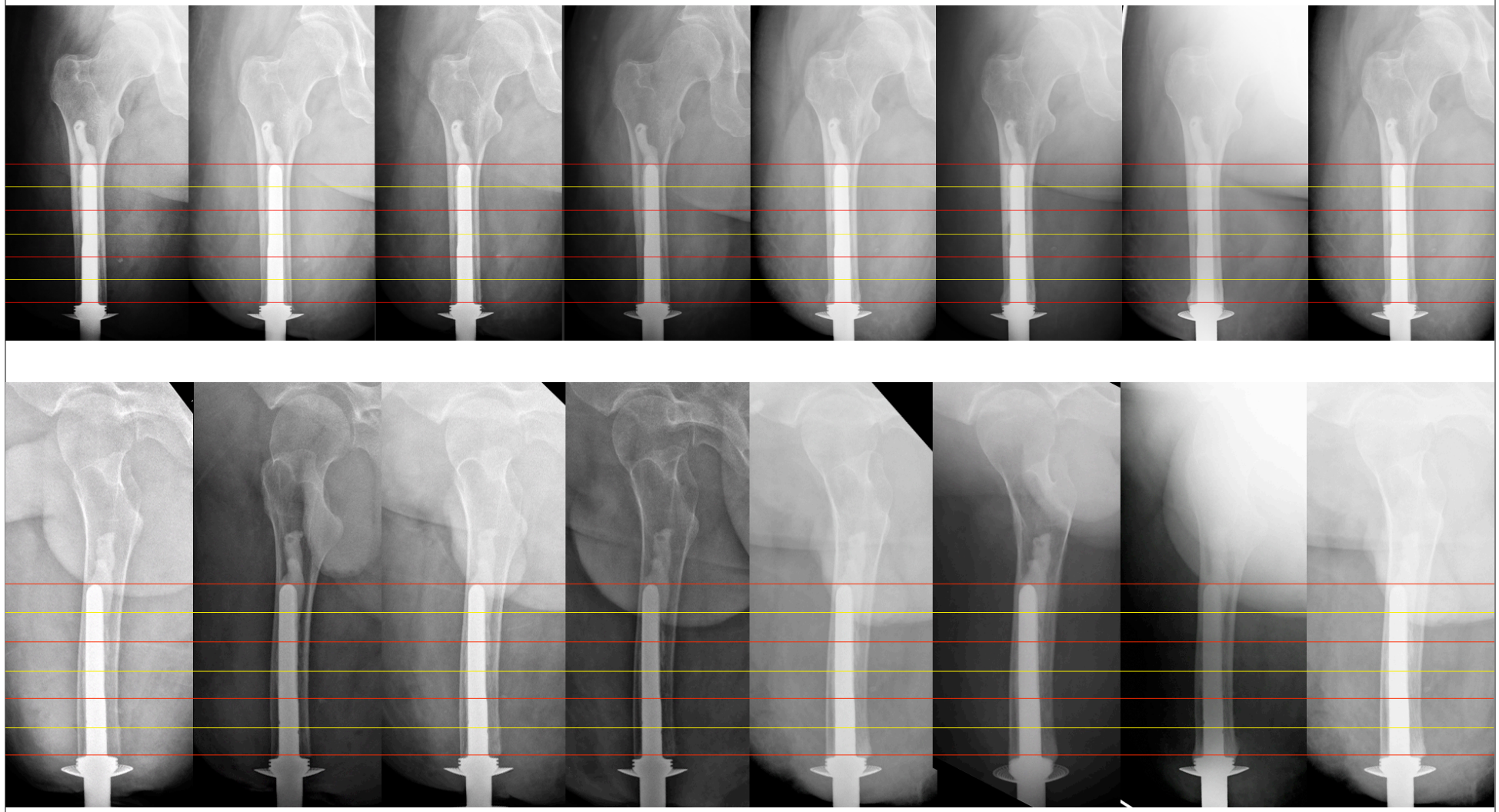

Patient 07

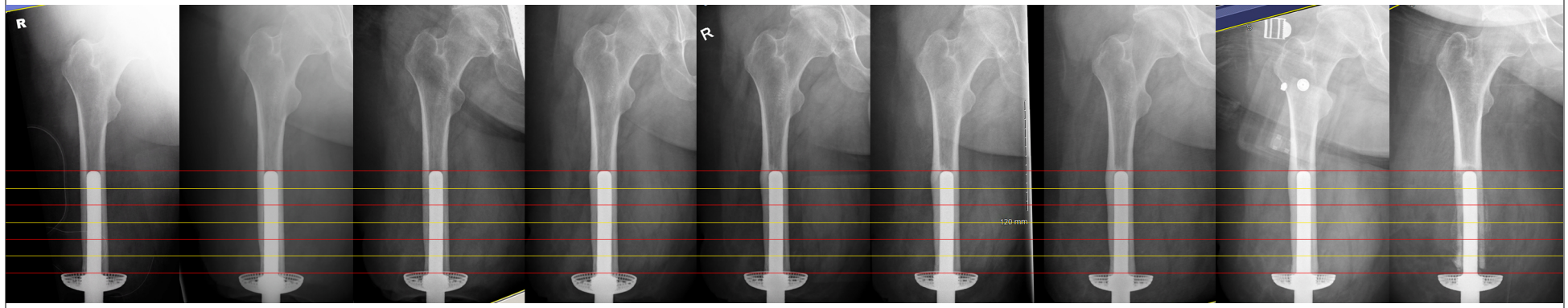

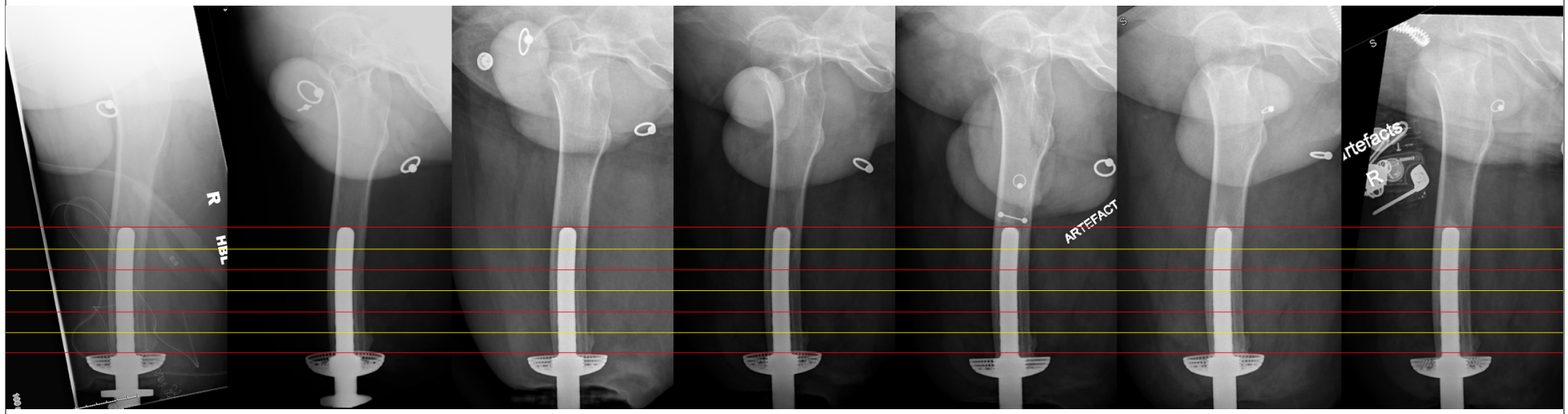

Patient 08

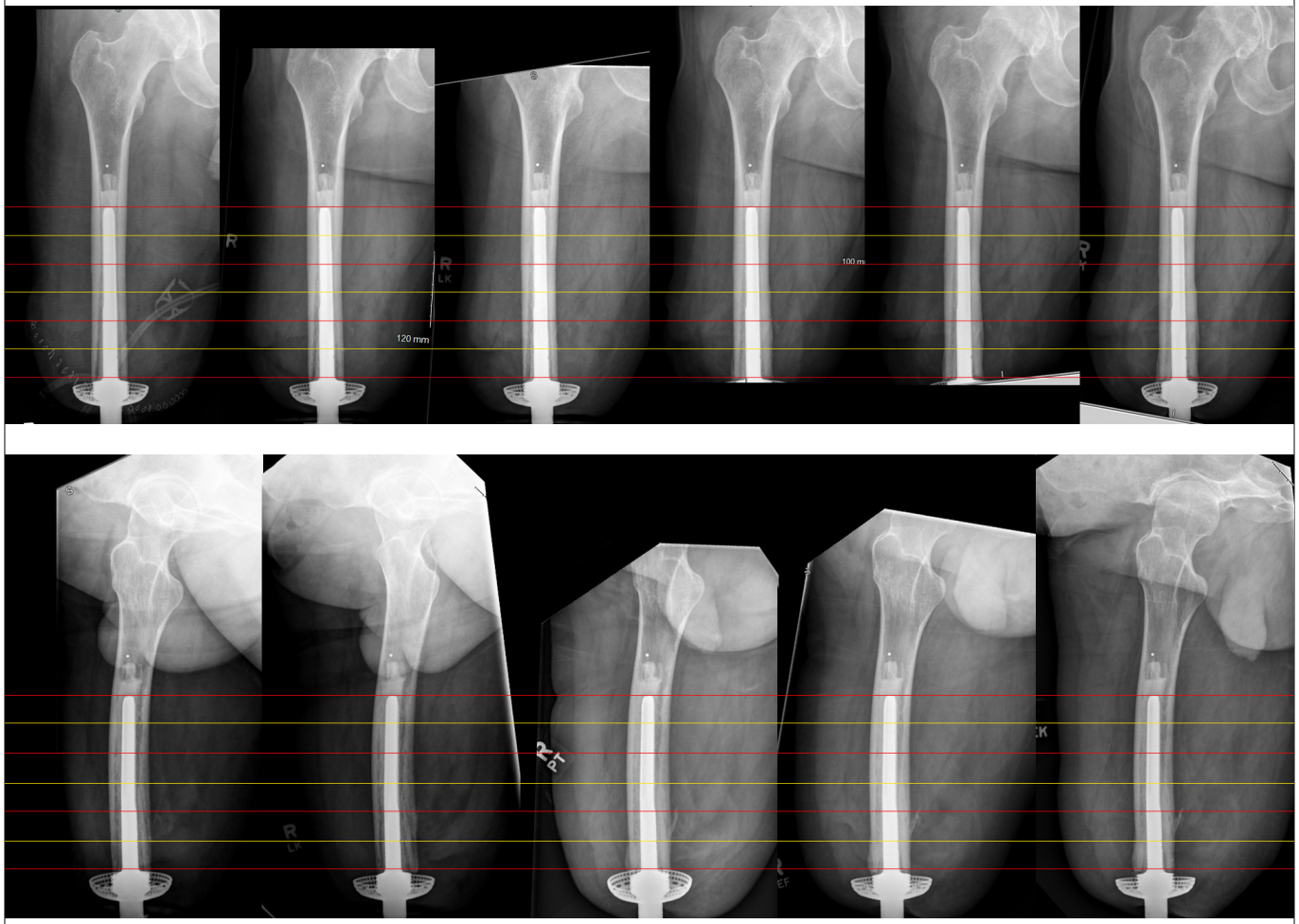

Patient 09

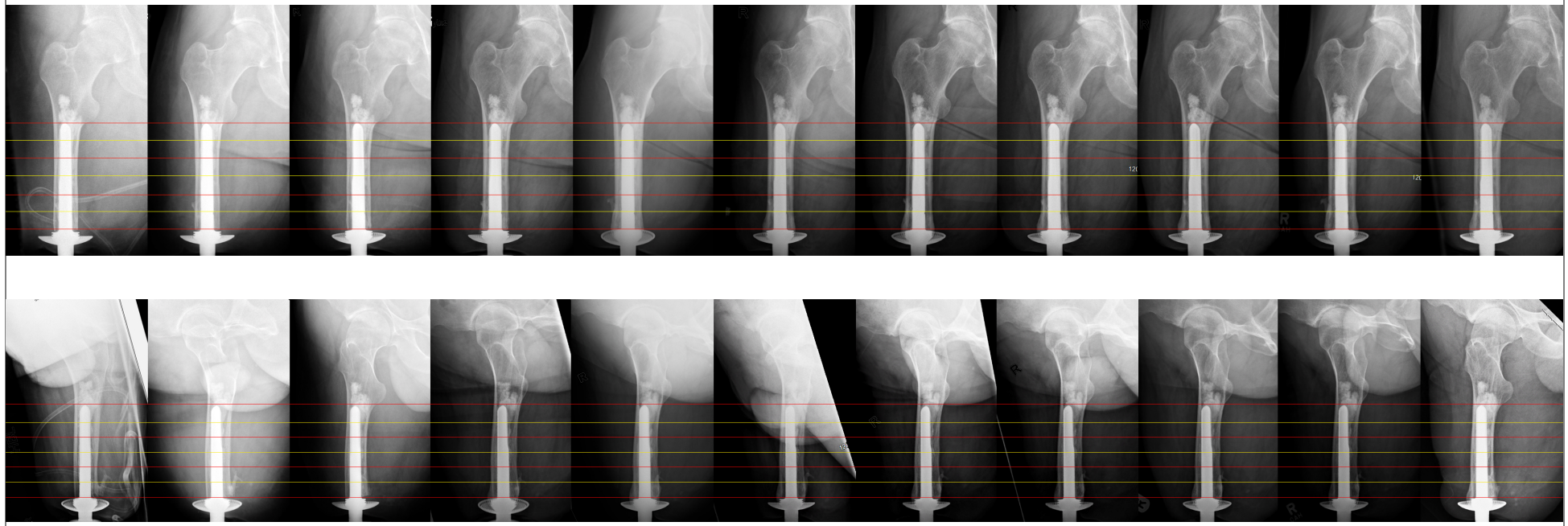

Patient 10

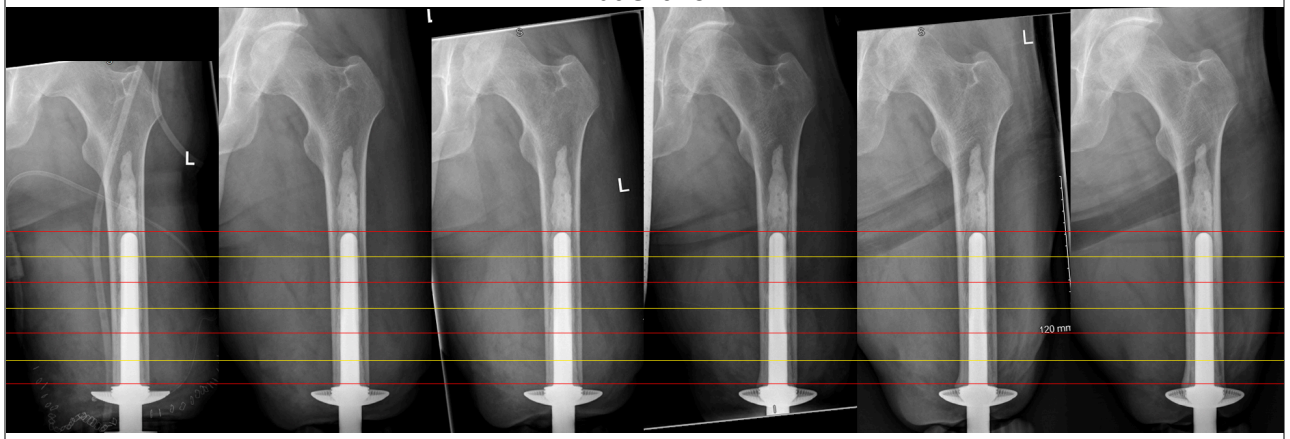

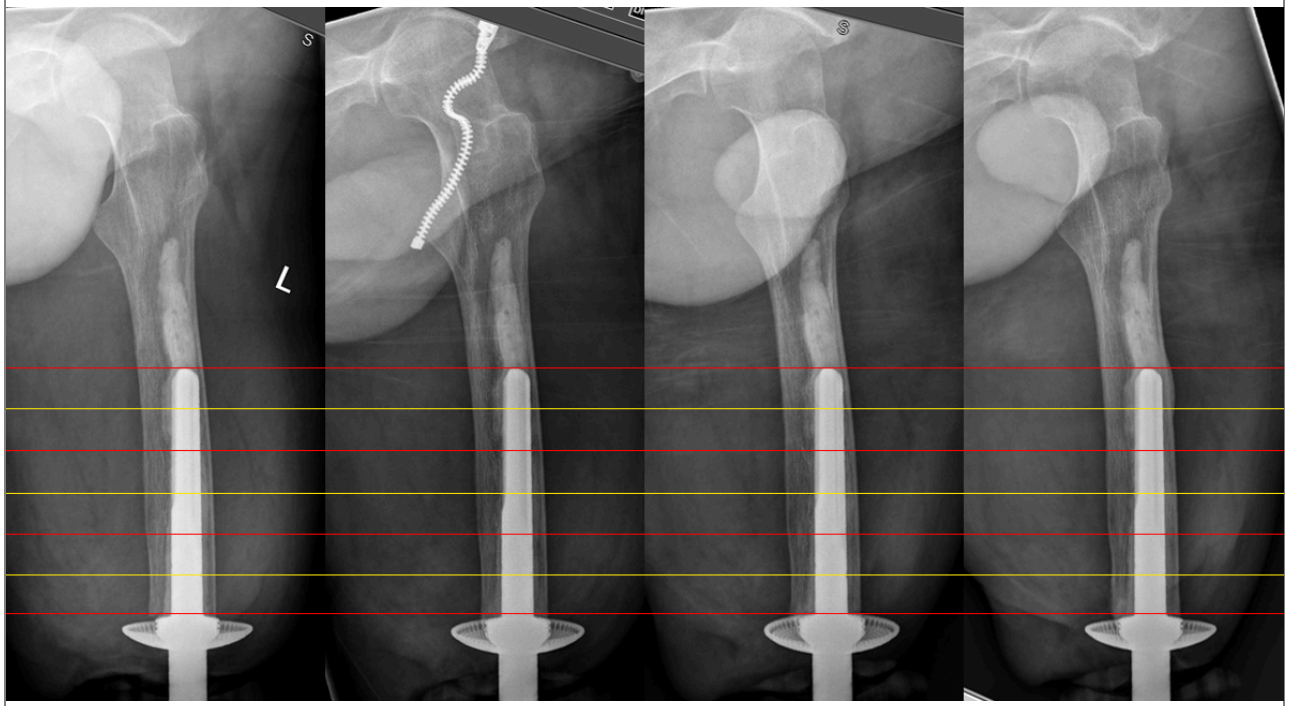

Patient 11

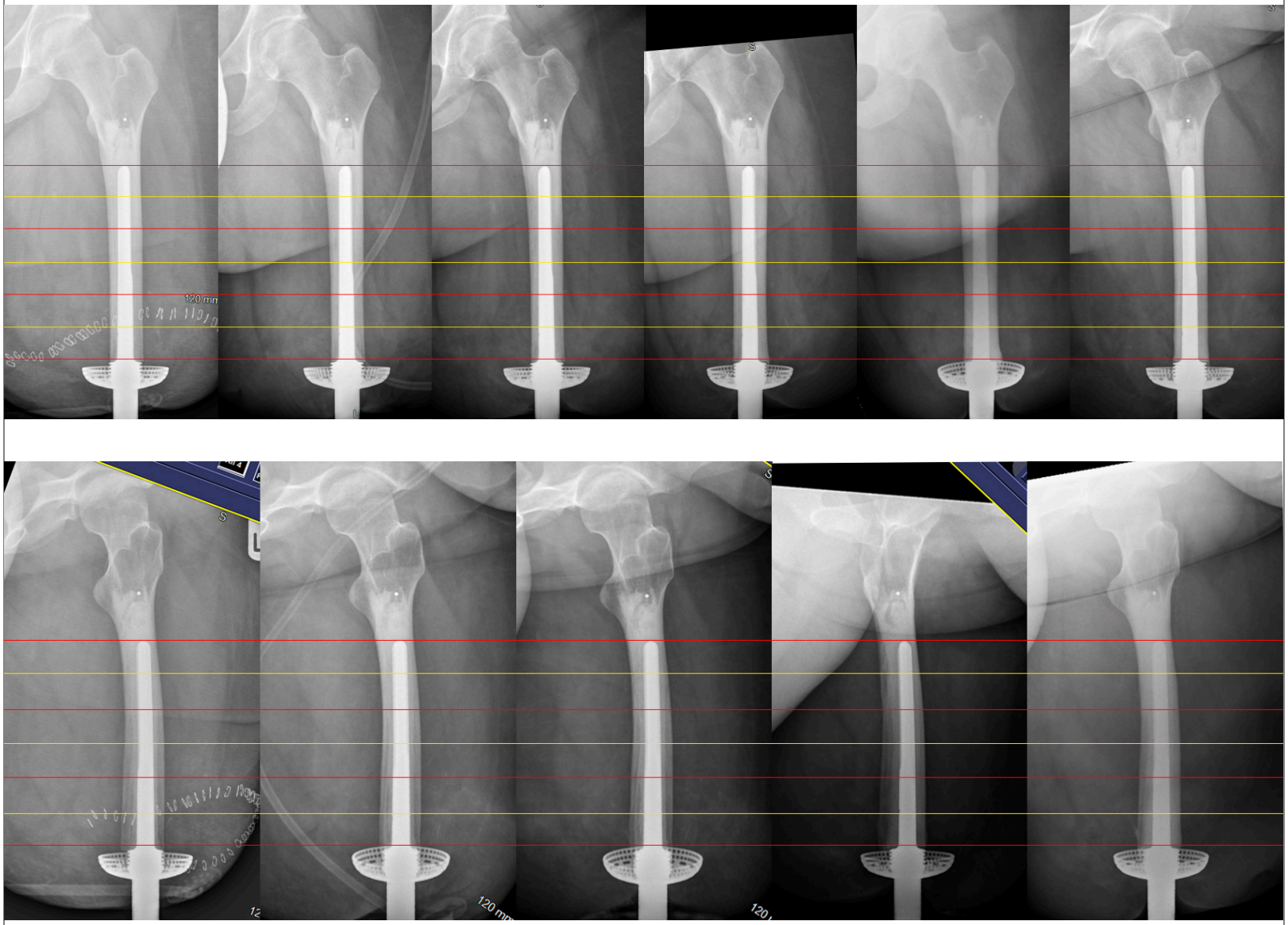

Patient 12

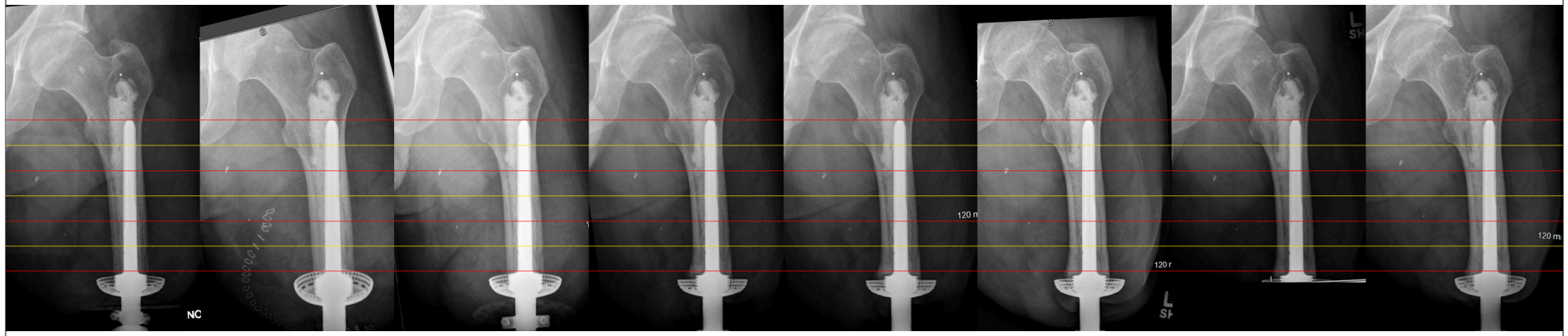

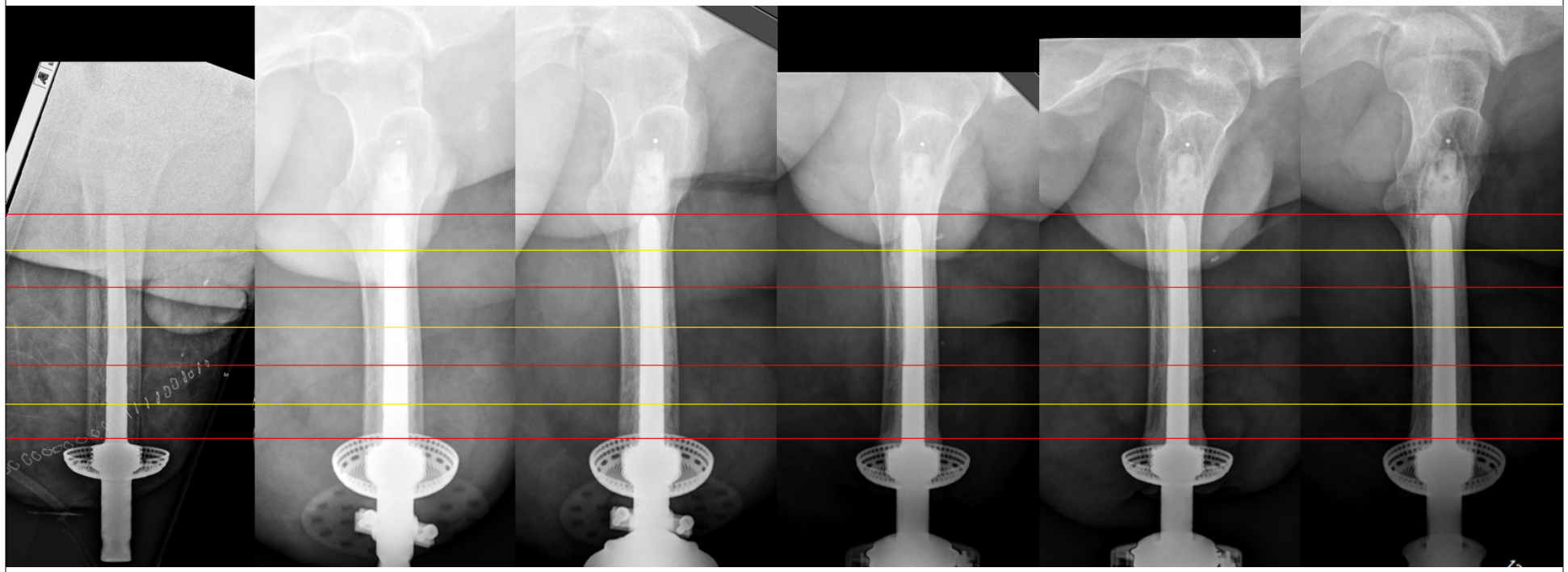

Patient	A.2.2 Patient radiographic detail notes
01	- Lateral cement gap at resection face - Lateral cortical collar thickening predominantly - Posterior cortical collar thickening - General posterior cortical thickening is not evenly distributed along bone length
02	- Lateral surgical gap at resection face - Good cortical collar thickening on medial side - Cortical collar thickening is more prominent and bulbous on the lateral side - Good cortical collar growth on anterior but more prominent posteriorly – however development of abnormal shape bone mass here
03	- REMOVED 2019 (after 9 years) - Pedestal formation laterally from year 2.5 and anteriorly from year 4 - RL gaps due to cutting fins don't change over time - Lateral cortical collar thickening predominantly - Minor anterior posterior cortical collar growth
04	- Cement/surgical gap posteriorly at resection face, this never closed despite bone thickening - Cortical collar thickening in ML both sides predominantly anteriorly - Cortical thickening in AP both sides predominantly laterally - Medial gap developed over time – possibly due/visible to posterior gap
05	- REMOVED due to infection 2017 (after 8 years) - Misalignment; periprosthetic bone at medial tip of ITAP appears removed - Posterior cortical collar thickening - Cortical collar thickening on medial and lateral sides but more prominent laterally - Bone looks moth eaten from the outside to the inside - unlikely infection, may be associated with the biofilm.
06	- Misalignment; ITAP tip very close to anterior - Fracture in the femur at the ITAP tip. Femur was plated secured with screws & wire - RL gap in zone 7 initially, over time it fills - Posterior cement gap at resected femur face - Posterior cortical collar thickening - Lateral cortical collar thickening predominantly - CIG (until the fracture)
07	- REMOVED 2015 (after 5 years) - Cortical Remodelling localised to lateral ITAP tip - RL gaps due to the cutting fins - The cortical collar bone minimal thickening

08	- Bone resection face from 2016 onwards show divergent RL gaps and fluffy bone - possibly reactive bone - Good cortical collar growth on posterior and predominantly anterior - Cortical collar thickening laterally - General cortical bone thickening on medial from base of the longitudinal cement grooves proximally
09	- Misalignment; ITAP tip very close to anterior - Cement/surgical misalignment gap medially and posteriorly at resected femur face - Osteogenesis at collar in gaps between 1.3 and 3.2mm - Good cortical collar growth on lateral and medial sides
10	- Surgical misalignment; ITAP tip very close to anterior - Localised cortical thickening in bone region of anterior ITAP tip - Cement/surgical gap posteriorly at resected face, initially but closed and cortical bone thickened. - RLL remain constant over time. No divergence - Good cortical collar growth on lateral side but more prominent medially
11	- No medial cortical collar thickening - Lateral cortical collar thickening predominantly - Very small cement gap, increases on medial side over time - RL on medial side, anteriorly and posteriorly increases over time
12	- REMOVED 2019 (after 4 years – ITAP fracture) - Cement/surgical misalignment gap at resection face - RL only seen in AP - Medial cortical collar thickening predominantly - Posterior cortical collar thickening predominantly - Misalignment; ITAP tip very close to lateral side - Proximal cortical density increase results in pedestal formation

Appendix 3

A.3.1 Link to cleared observational protocol

https://www.dropbox.com/s/9qpotpcglxvmbwg/authorised%20protocol.pdf?dl=0

A.3.2 Load cell construction

The load cell was built by a member of the research team (Dr Steve Taylor) as follows: The instrumented portion of a previous Ti6Al4V femoral implant force transducer was used as the basis for the device, having five thin film strain gauges located on each of four sides (two of which are shown in Figure A.3.1).

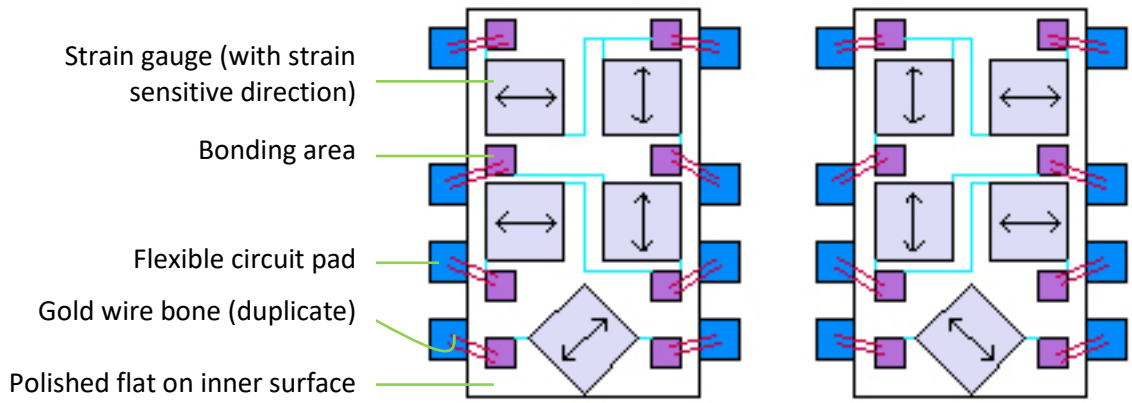

Fig. A.3.1: Principal directions of strain gauges on two adjacent flats. The top pair of each flat are wired for axial compression, the middle pair for bending, and the 45 ° gauge for torque.

The original transducer was cut to a 77.4 mm length and the remainder of the 110 mm space was occupied by the female pyramid fittings. Gauges were 20 kOhms, with principal strain axes as shown and wire bonded to a flexible printed circuit which interconnected the four sides and brought out terminal pads. Electrically, these formed four fully active arm Wheatstone bridges of gauges wired for main sensitivity to axial compression, AP bending, ML bending and torque. A modification was made to this topology such that each of the four gauges at 45 ° were separated into four channels of quarter bridge action only, such that independent measurements of shear force and torque could be made. The axial force and bending bridges were also split into two groups of three half bridges (six channels). Thus, the transducer became instrumented to measure six degrees of freedom (DOF) using ten independent strain measurement channels comprising a mix of half and quarter bridges.

It was accepted that there would be considerable cross-talk between channels wired primarily for one DOF. The matrix method of calibration (Microsoft Excel, v16) was therefore used to identify and

appropriately combine channels sensitive to more than one applied load type. Each channel was wired to a HIPP5 slave PCB (four of these linked to a master PCB with radio transmitter).

A.3.3 Load cell calibration

During calibration, loads were applied to the construct as follows: Axial force was applied using a Hounsfield uniaxial compression rig with balls between load centres and the pyramid fittings. Loads were applied in ~ 100 N steps to 1.25 kN. Bending and shear were applied using a setup whereby the load cell and fittings were mounted horizontally along the axis of the load cell to the shaft of a motor using an extension pole to increase the bending lever arm, Fig. A.3.2, left. A load of 45N was hung on the pole at two distances from the load cell (80 and 250 mm), thus creating two different bending moments but the same shear force at the gauges. This arrangement was used to separate the bending and shear contributions of strain at each gauge channel. The motor was rotated slowly (1 rev in 120sec) to create a sinusoidal distribution of strain around the gauged region with time. The Root Mean Square (RMS) amplitude and relative phase of each channel were recorded with respect to a datum angle marked on the load cell which aligned with one of the anatomical directions during the study. Ideal sinewaves were regressed through these curves so that the amplitude (strain sensitivity) of each channel could be resolved into orthogonal components aligned with AP and ML anatomical axes.

Fig. A.3.2: Left = Bending and shear calibration setup. Right = Torque rig.

Torque was applied using a torque rig comprising a frame support, bending bar with pulleys, string and deadweight for pure torque application, Fig. A.3.2, right. Sensitivities of each strain channel to each applied load were found (10 x 6). Channels were then combined according to their primary contribution to each applied load, and these resulting six combined channels vs the six DOF formed the six-by-six

calibration matrix having units of strain counts per N or per Nm. The channels were combined as follows:

AXF =	(B1(1) + B2(1) + B1(2) + B2(2))/4
B1 =	B1(1) – B1(2)
B2 =	B2(1) – B2(2)
S1 =	S1(1) – S1(2)
S2 =	S2(1) – S2(2)
TOR =	S1(1) – S2(1) + S2(2) – S1(2)

After separating the sensitivities due to shear and bending, in both planes, the six-by-six calibration matrix was found, representing the sensitivities and cross-sensitivities of each combination of strain channels to each pure load type, in counts/N and counts/Nm. Inverting the matrix forms the measurement matrix having units of N/count and Nm/count. Upon multiplying this measurement matrix by each measured strain count vector, and eliminating the strain count offsets, corresponding to zero applied load, produced the six DOF load vector. The calibration matrix calculations were carried out in Excel, and the measurement matrix stored in a LabView GUI.

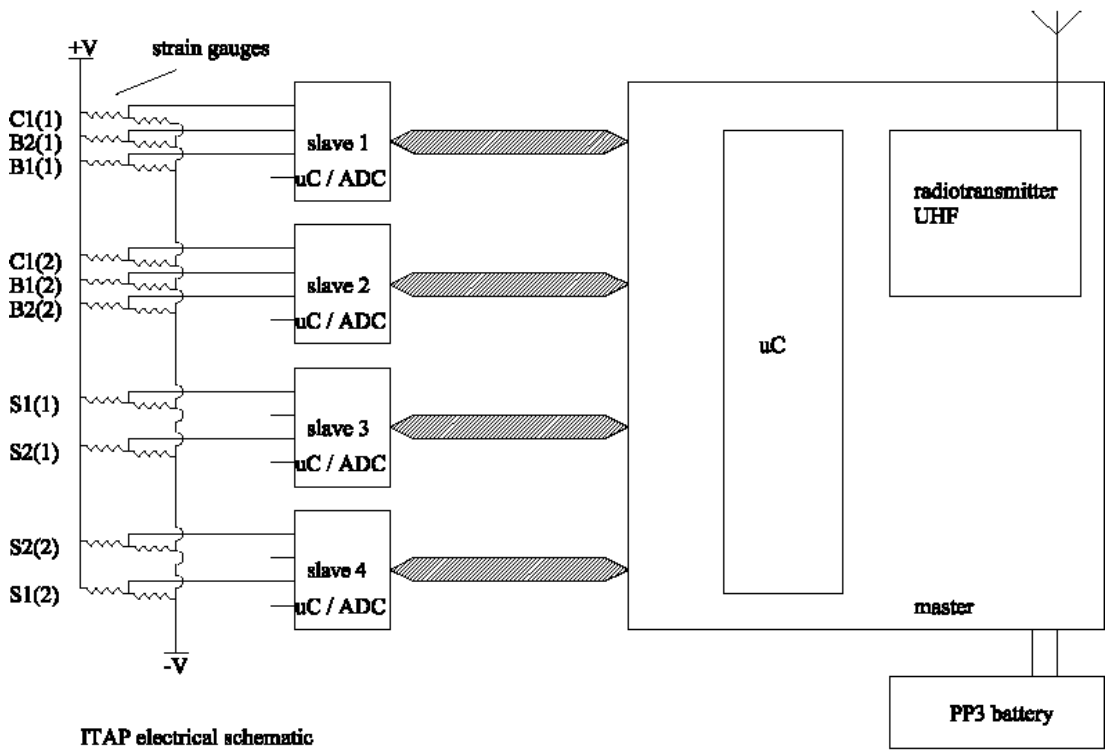

Fig. A.3.3: The load cell full schematic

A.3.4 Transformation of forces
from the load cell coordinate system to the biomechanics software coordinate system:

Firstly, a translation matrix moved the coordinate system proximally 0.153 m along the Y axis (negative) and 0.015 m medially (positive) along the X axis:

$$\begin{Bmatrix} FX \\ FY \\ FZ \\ MX \\ MY \\ MZ \end{Bmatrix} \begin{bmatrix} 1 & 0 & 0 & 0 & 0 & 0 \\ 0 & 1 & 0 & 0 & 0 & 0 \\ 0 & 0 & 1 & 0 & 0 & 0 \\ 0 & -dz & dy & 1 & 0 & 0 \\ dz & 0 & -dx & 0 & 1 & 0 \\ -dy & dx & 0 & 0 & 0 & 1 \end{bmatrix} = \begin{Bmatrix} FX' \\ FY' \\ FZ' \\ MX' \\ MY' \\ MZ' \end{Bmatrix}$$

$$\Downarrow$$

Load cell coordinate system

$$\begin{Bmatrix} FX \\ FY \\ FZ \\ MX \\ MY \\ MZ \end{Bmatrix} \begin{bmatrix} 1 & 0 & 0 & 0 & 0 & 0 \\ 0 & 1 & 0 & 0 & 0 & 0 \\ 0 & 0 & 1 & 0 & 0 & 0 \\ 0 & 0 & -0.153 & 1 & 0 & 0 \\ 0 & 0 & -0.015 & 0 & 1 & 0 \\ 0.153 & 0.015 & 0 & 0 & 0 & 1 \end{bmatrix} = \begin{Bmatrix} FX' \\ FY' \\ FZ' \\ MX' \\ MY' \\ MZ' \end{Bmatrix}$$

Second, the axis rotations were combined into a rotation matrix that first rotates around the X axis and then the Z axis (where ψ = -2 ° = -0.0349 radians and ϕ = 5 ° = 0.0872 radians). As the second rotation was performed around the *local* Z axis, the final orientation of the coordinate system will not be exactly 5 °. In order to remedy this, the solver function in Excel was used and ϕ was calculated as 4.9970 ° thus producing the final rotation matrix (RM):

Rotation around X axis — Rotation around Z axis — RM

$$\begin{bmatrix} 1 & 0 & 0 \\ 0 & \cos\psi & -\sin\psi \\ 0 & \sin\psi & \cos\psi \end{bmatrix} \begin{bmatrix} \cos\phi & -\sin\phi & 0 \\ \sin\phi & \cos\phi & 0 \\ 0 & 0 & 1 \end{bmatrix} = \begin{bmatrix} 0.9962 & -0.0871 & 0 \\ 0.0870 & 0.9956 & 0.0349 \\ -0.0030 & -0.0348 & 0.9994 \end{bmatrix}$$

Finally, the translated forces and moments were rotated using the RM:

$$\begin{Bmatrix} FX' \\ FY' \\ FZ' \\ MX' \\ MY' \\ MZ' \end{Bmatrix} \begin{bmatrix} 0.9962 & -0.0871 & 0 & 0 & 0 & 0 \\ 0.0870 & 0.9956 & 0.0349 & 0 & 0 & 0 \\ -0.0030 & -0.0348 & 0.9994 & 0 & 0 & 0 \\ 0 & 0 & 0 & 0.9962 & -0.0871 & 0 \\ 0 & 0 & 0 & 0.0870 & 0.9956 & 0.0349 \\ 0 & 0 & 0 & -0.0030 & -0.0348 & 0.9994 \end{bmatrix} = \begin{Bmatrix} FX'' \\ FY'' \\ FZ'' \\ MX'' \\ MY'' \\ MZ'' \end{Bmatrix}$$

A.3.5 Load cell sources of error

Load cell construction (pre-test day)

The load cell used was adapted from one designed for an implant that collected much higher forces by the addition of an amplifier and reworking the metal housing to suit the current application. Damaged was suffered to the wire bonds in undertaking the metalwork and these had to be repaired. Furthermore, an error was made in the amplifier size for the HIPP6 PCBs and sadly there was not time to rectify this so HIPP5 PCBs and a power source external to the load cell were used instead.

load cell adaptions (on test day)

The HIPP5 PCBs and power source were strapped externally to the patient; they did not obstruct gait but may have had an (unknown) effect on the limb's inertial properties. Furthermore, it was discovered on test day that the cylindrical plastic liner used to protect the exposed strain gauges obstructed the movement of the load cell. Although this was swiftly adjusted it was an estimation as to how much to remove to allow for free movement whilst preventing damage to the strain gauges.

Load cell calibration

Calibration of the load cell was scheduled before test day however due to the last minute adaptations this was not possible. Furthermore, the fittings were detached from one end of the load cell before calibration. Thus, the retrospective calibration introduced a further source of experimental error.

Appendix 4

A.4.1 FE model build verification steps

A.4.1.1 Flow of force in an idealised 2D axisymmetric bone plug model

In order to verify that the flow of forces through the model behaved as expected (the most stress passing through the stiffest parts) I built another 2D axisymmetric FE model (similar to that of Xu et al. (2000)), using PLANE183 elements. The SAAP stem was dimensioned to match that of ITAP patient 12 (from whom the kinematic and kinetic readings were taken), using measurements from CT scans. Coincident nodes were merged at congruent faces and bone material was considered isotropic (E = 18 GPa, ν = 0.3).

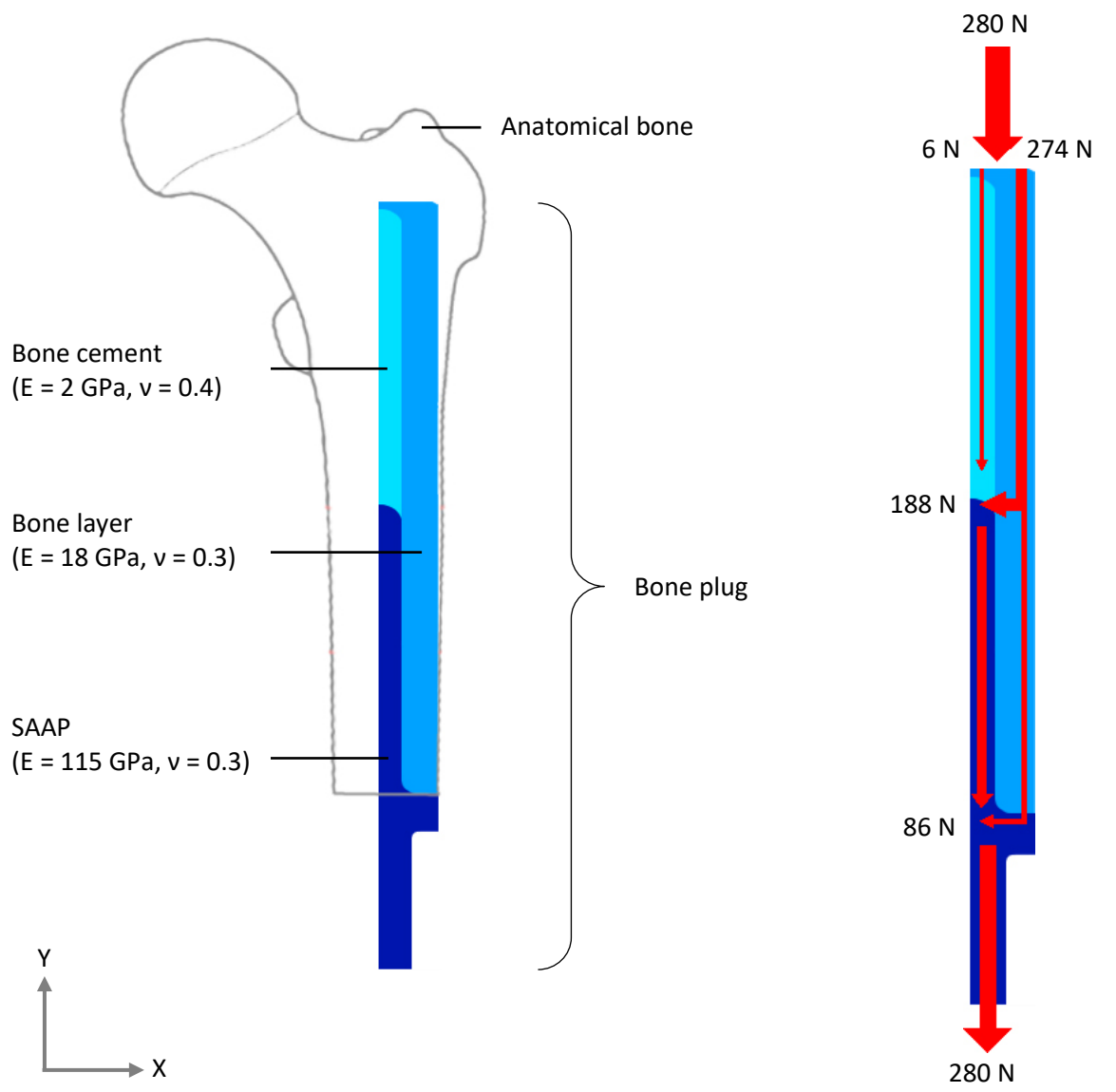

Fig. A.4.1: Left = Idealised 2D axisymmetric model of the bone plug (coloured) inside the anatomical bone (grey). Only the bone plug was used in an axisymmetric study of the force flow. Right = Flow of forces through the axisymmetric model – sum of forces obtained from ANSYS

An axial force of 280 N (in a static linear simulation) representing the axial component of a standing force (Bergmann et al., 2001, Pauwels, 2012) was applied as a pressure across the proximal surface of the bone layer elements and the sum flow of forces observed (Fig. A.4.1).

The model illustrated that an axial force passed through obeying the laws of equilibrium as expected in the statically indeterminant structure. The greatest portion of the shared load travelled from proximal to distal through the stiffer material; proximally this is the cortical bone (E = 18 GPa), distally this is the SAAP (E = 115 GPa). The unloading of the periprosthetic cortical bone under axial loading highlights the risk of bone resorption, however little can be concluded until a bending component is added since this constitutes the largest stress component in the intact femur (Lieberman et al., 2003, Harwood and Stewart, 2016). Since bending, unlike axial force, does not display axisymmetric behaviour it was applied in the 3D models.

A.4.1.2: A 3D quadrant bone plug model

Verification: A simplified axisymmetric model was swept 90° around the longitudinal axis of symmetry to produce the quadrant model and meshed with SOLID186. Once again, the bone was considered isotropic (E = 18 GPa, ν = 0.3), and nodes on congruent surfaces were fully merged. A verification check was run on the development from the 2D to 3D model (Fig. A.4.2); both bone plug models were constrained distally in the Y axis and produced the same stress field (in the Y axis) under a 1000 N axial (-0.171e7 Pa to 247368 Pa).

Introducing bending: The bending moments experienced by the femur are a combination of asymmetrical loading through the femoral head (offset by the femoral neck) and the transverse component of the load. It is influenced by femoral neck length, cross section shape and area, stage of gait and curvature of the bone. To ensure that the quadrant model was behaving correctly and to further understand the effect of introducing a bend into the model, a bending moment was applied as a resultant moment in AP and ML $\left(\sqrt{M_{ap}^2 + M_{ml}^2}\right)$. Since a moment cannot be applied to a node in ANSYS, symmetry and antisymmetry boundary conditions were used to constrain the model in the application of pressure to the top of the bone plug as follows:

M_{ap} = X face symmetry (Uz restrained) , Z face antisymmetry (Uy, Uz restrained)

M_{ml} = Z face antisymmetry (Ux restrained), X face symmetry (Ux, Uy restrained)

Pressure was applied on the quadrant model to produce a resultant bending moment emulating standing in ITAP patient 12 (Fig. A.4.3 b, left and A.4.1.1.4 for calculation of pressure)

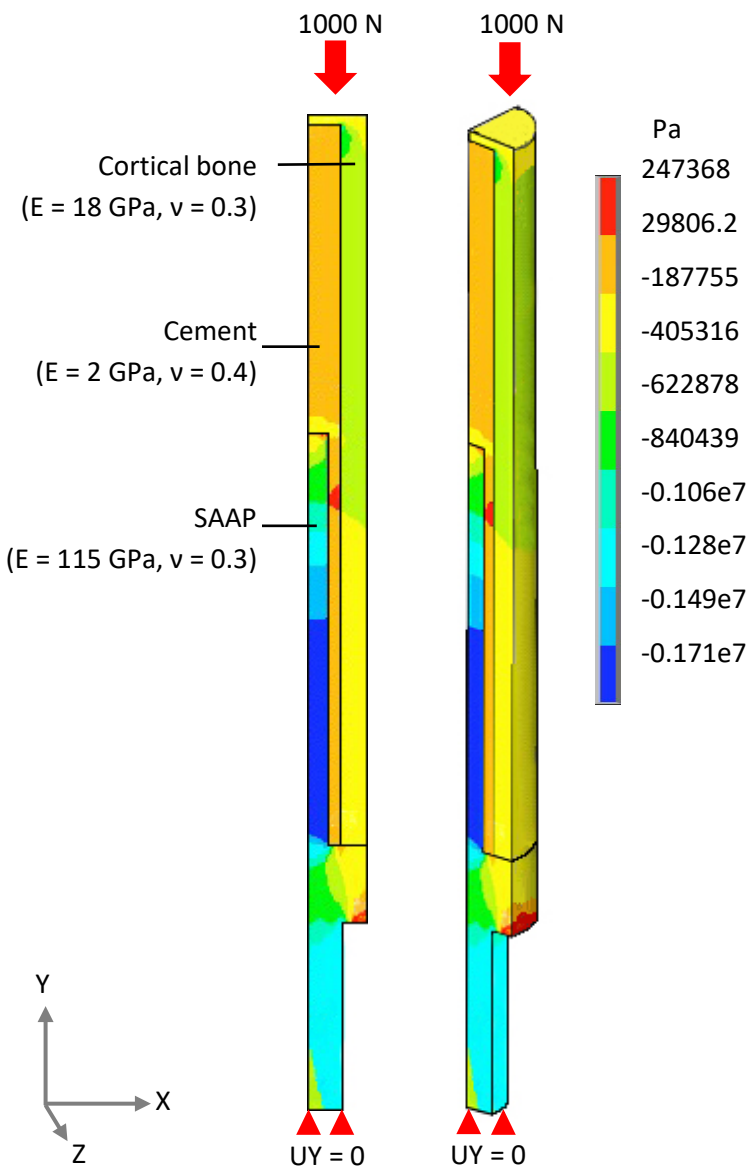

Fig. A.4.2: Verification that the 2D (left) and 3D (right) FE models produce the same stress results under the same loading conditions.

A 1000 N axial distributed load was applied along the most proximal line/area of the models and the stress distribution in Y is plotted for both.

A.4.1.3 Calculating pressure to apply to a quadrant model for resultant bending

To calculate the appropriate pressure to apply on the scaled quadrant bone plug model, the distance between the bone/ITAP midline and the hip contact point on the femoral head (AP moment arm) in CT scans of ITAP patient 12 was measured:

AP moment arm = 0.043 m

Axial load (F) at femoral head = 280 N

M_{ap}= 280 N x 0.043 m = 12.04 Nm

To calculate the pressure to apply to the top of the quadrant model to represent this real life bending moment in the assembly, the following was undertaken:

Since the centroid/moment arm (C) of a quadrant = $\frac{4r}{3\pi}$

And moment (M_{ap}) = 4 × F × C

And F = P × area (A)

Substituting then M_{ap}=4 × P × A × C

$$= \frac{4\,P\,\pi\,r^2}{4} \times \frac{4r}{3\pi}$$

= 2.676 MPa

Therefore if 2.676 MPa of pressure is applied to the proximal quadrant face while uz is restrained on the X face and uy and uz are restrained on the Z face then a bending moment will be produced that reflects the M_{ap} in ITAP patient 12 femur. A similar method was employed to acquire the pressure for M_{ml} in the bone plug model and the effective of the resultant moment (12.39 Nm) was applied as a pressure to the model (Fig. A.4.3 b, left).

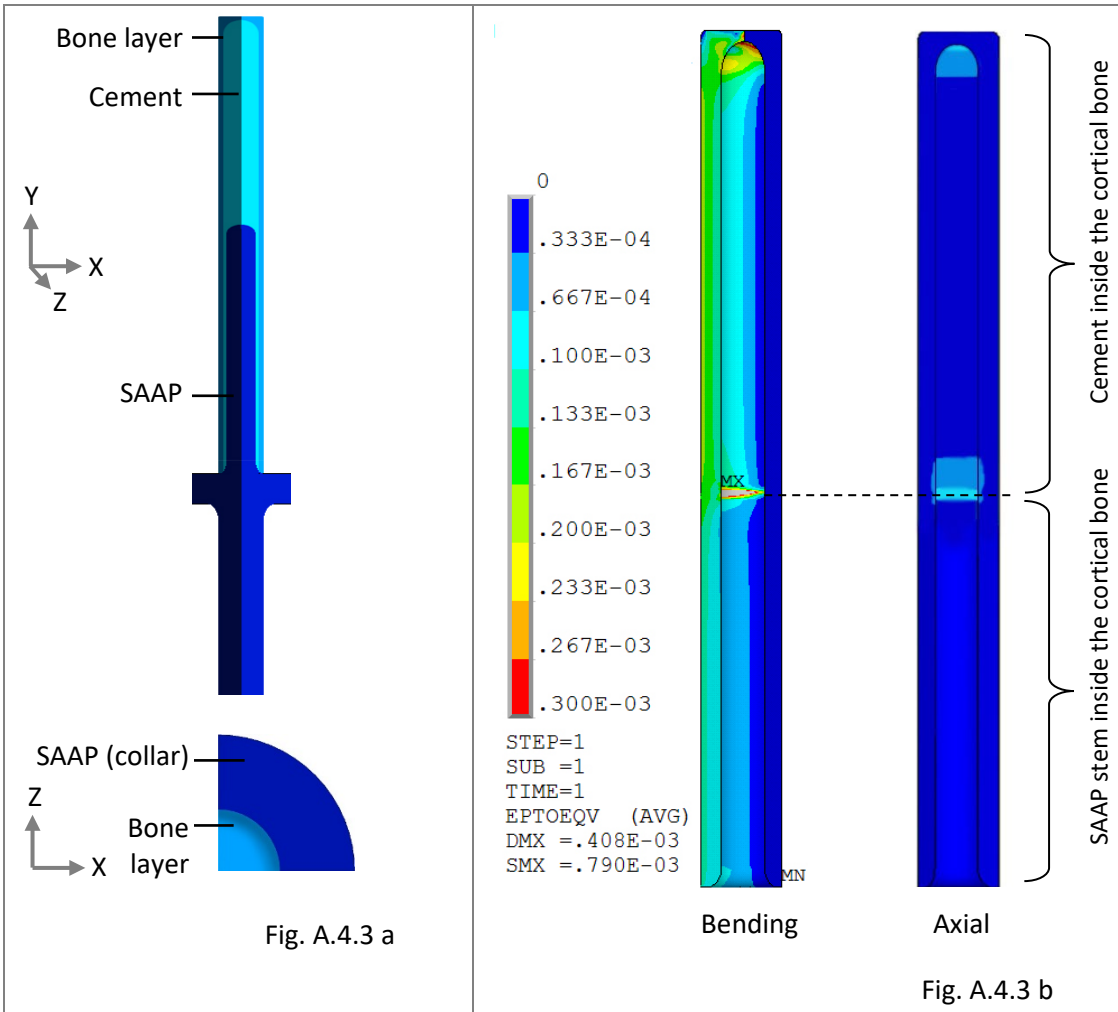

Fig. A.4.3 a: A quadrant bone plug model viewed from the front (top) and top (bottom). Fig. A.4.3 b: Axial (right) and resultant bending (left) Von Mises bone strain in the bone layer of a quadrant model. The axial force was 280 N and the resultant bending moment was 12.39 Nm

The effect of bending in standing on periprosthetic bone compared with axial loading was apparent: 300 µstrain on cortical bone around the proximal cement mantle and 790 µstrain around the proximal tip of

the SAAP. This compared with a maximum of 85 µstrain observed in the application of an axial load. Note also the effect of the bending; where the restrained plane is the neutral line between compression and tension and experienced no strain. Up until this point in model development, interactions had been considered as fully tied (i.e. the nodes of each part had been merged). In real life there is some friction between bone cement and the surface of orthopaedic implants (Gotman, 2014, Gao et al., 2019). This is in part due to the smooth metal surface of the implants but also because bone cement does not behave like a glue, it behaves more like a packing material. As such, it forms a 'tied' bond with the bone since it is applied to the bone cavity in a retrograde high pressure fashion, it interdigitates with the bone surface. Some implants do receive a rough coating (by plasma spraying or manufacturing a rough metallic coating (Heimann, 2018)) prior to implantation to facilitate the adherence to the bone cement, but the cemented SAAP did not. It is important to investigate the effect of this on periprosthetic bone stress and was the next stage of development in the model.

A.4.2 Using Scan IP to hollow a cylindrical core from the anatomical bone in a repeatable way

Method overview: A bone plug was recreated in Scan IP; it's centreline was its axis of symmetry and was oriented along the global Y axis with the global origin at the centre of the distal face of the intramedullary bone plug part. The centreline for the anatomical bone was not straight and so the best cord of fit was used. A cord of fit is the line that joins the centroids of two of the anatomical bone slices; slices were one pixel thick (0.35 mm), slice one was the most distal slice on the bone (number 0) and slice two was 365. Pythagorean theorem gave the length of the cord that connected the slice centroids and therefore the location on the centreline of the bone plug to input into the landmark registration tool. Scan IP moved the anatomical bone into position by superimposing the coordinates of the two parts, the Boolean subtraction was performed, and the anatomical bone was meshed within Scan IP. The anatomical bone *only* was exported, and the result was a meshed anatomical bone with a central core removed of the exact dimensions of the ANSYS bone plug in a repeatable manner.

A.4.3 Material step change in adjacent elements

There is a potential issue with non-homogeneous materials if they are defined on an element-by-element basis, i.e., there is a step change at the element interfaces. The elastic modulus in Fig. A.4.4 of the left-hand region is ten times that of the right-hand region. The model is subject to a uniform load in the X direction which would, for a homogeneous model, lead to constant stress in the X direction. The inhomogeneity leads to disturbance in the stress distribution at the interface between the regions where there is a step change in the elastic modulus. The applied axial stress is 1Pa and this leads to a stress concentration (singularity?) of greater than two for the mesh used. This behaviour is spurious in that it would not occur in the real bone which whilst non-homogeneous, has a continuously varying elastic modulus rather than one that step changes at element boundaries. The real behaviour would be

better modelled by enforcing a continual variation. The way that it is done is to determine unique values at the nodes and then use the element shape-functions to interpolate within the elements. This can be done in ANSYS by defining the elastic modulus to be a function of temperature and then defining nodal temperatures from which the correct value of the elastic modulus can be determined. Re-analysing the problem with a linearly varying temperature field and, therefore, linearly varying elastic modulus and the stresses in the X direction are shown in Fig. A.4.5. The stresses do, of course, vary but this is now a much more realistic representation of what would happen.

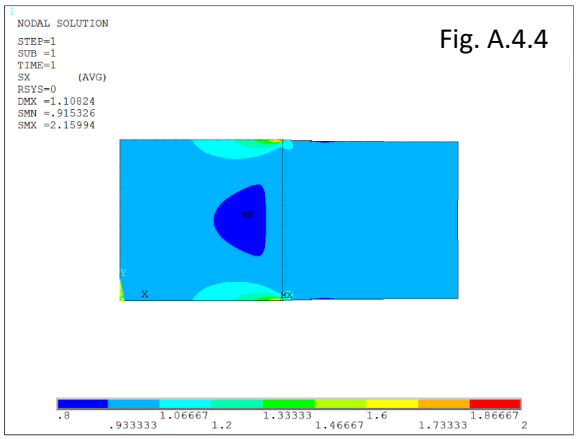

Fig. A.4.4

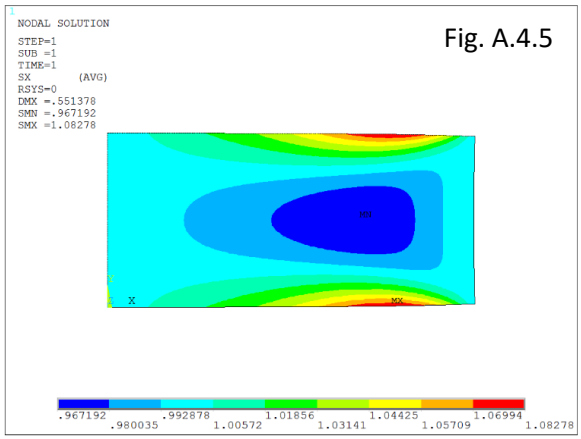

Fig. A.4.5

A.4.4 Coordinate transform with two known angles

Coordinate rotations around X and Z are performed by:

$$R_x = \begin{bmatrix} 1 & 0 & 0 \\ 0 & \cos\alpha_x & -\sin\alpha_x \\ 0 & \sin\alpha_x & \cos\alpha_x \end{bmatrix} \qquad R_z = \begin{bmatrix} \cos\alpha_z & -\sin\alpha_z & 0 \\ \sin\alpha_z & \cos\alpha_z & 0 \\ 0 & 0 & 1 \end{bmatrix}$$

Inputting an adduction and flexion of 6.9 ° and 2 ° respectively gives the rotation matrix, RM ($R_x.R_z$) of:

$$RM = \begin{bmatrix} 0.9928 & 0.1201 & 0.0000 \\ -0.1201 & 0.9922 & 0.0349 \\ 0.0042 & -0.0346 & 0.9994 \end{bmatrix}$$

Such that:

$$\begin{bmatrix} 0.9928 & 0.1201 & 0.0000 \\ -0.1201 & 0.9922 & 0.0349 \\ 0.0042 & -0.0346 & 0.9994 \end{bmatrix} \begin{Bmatrix} 0 \\ -842.8 \\ 0 \end{Bmatrix} = \begin{Bmatrix} -101.2513 \\ -836.1862 \\ 29.2003 \end{Bmatrix} \begin{matrix} F_x \\ F_y \\ F_x \end{matrix}$$

Appendix 5

A.5.1 Bespoke algorithm for calculating inertial properties using V3D segment data and ANSYS inertial tensor

https://www.dropbox.com/s/y4v56ccrh3h2ghi/Segment%20inertia.xlsx?dl=0

A.5.2 Key for the geometry of the 81 FE models

Table A.5.2: 81 models of SAAP designs:
TP = tapered stems (yellow cells).
PR = parallel stems (blue cells).
CPCM = cortical plate, cemented fixation (pink cells).
CPPF = cortical plate, pressfit fixation (pink cells).
S ratio = stem length/residuum length. C = cemented stem. PF = pressfit stem

Model	S:F (S ratio)	Stem length (m)	Taper (°)	Distal radius (m)	Fixation	Cortical plate
TP1	0.4	0.08	0.375	0.005	C	-
TP2	0.4	0.08	0.750	0.005	C	-
TP3	0.4	0.08	1.500	0.005	C	-
TP4	0.4	0.08	0.375	0.006	C	-
TP5	0.4	0.08	0.750	0.006	C	-
TP6	0.4	0.08	1.500	0.006	C	-
TP7	0.4	0.08	0.375	0.007	C	-
TP8	0.4	0.08	0.750	0.007	C	-
TP 9	0.4	0.08	1.500	0.007	C	-
TP10	0.6	0.12	0.375	0.005	C	-
TP11	0.6	0.12	0.750	0.005	C	-
TP12	0.6	0.12	1.500	0.005	C	-
TP13	0.6	0.12	0.375	0.006	C	-
TP14	0.6	0.12	0.750	0.006	C	-
TP15	0.6	0.12	1.500	0.006	C	-
TP16	0.6	0.12	0.375	0.007	C	-
TP17	0.6	0.12	0.750	0.007	C	-
TP18	0.6	0.12	1.500	0.007	C	-
TP19	0.8	0.16	0.375	0.005	C	-
TP20	0.8	0.16	0.750	0.005	C	-
TP21	0.8	0.16	1.500	0.005	C	-
TP22	0.8	0.16	0.375	0.006	C	-
TP23	0.8	0.16	0.750	0.006	C	-
TP24	0.8	0.16	1.500	0.006	C	-
TP25	0.8	0.16	0.375	0.007	C	-
TP26	0.8	0.16	0.750	0.007	C	-
TP27	0.8	0.16	1.500	0.007	C	-
PR28	0.4	0.08	0.000	0.005	C	-
PR29	0.6	0.12	0.000	0.005	C	-
PR30	0.8	0.16	0.000	0.005	C	-
PR31	0.4	0.08	0.000	0.006	C	-
PR32	0.6	0.12	0.000	0.006	C	-
PR33	0.8	0.16	0.000	0.006	C	-
PR34	0.4	0.08	0.000	0.007	C	-
PR35	0.6	0.12	0.000	0.007	C	-

PR36	0.8	0.16	0.000	0.007	C	-
PR37	0.4	0.08	0.000	0.005	PF	-
PR38	0.6	0.12	0.000	0.005	PF	-
PR39	0.8	0.16	0.000	0.005	PF	-
PR40	0.4	0.08	0.000	0.006	PF	-
PR41	0.6	0.12	0.000	0.006	PF	-
PR42	0.8	0.16	0.000	0.006	PF	-
PR43	0.4	0.08	0.000	0.007	PF	-
PR44	0.6	0.12	0.000	0.007	PF	-
PR45	0.8	0.16	0.000	0.007	PF	-
CPCM46	0.4	0.08	0.000	0.005	C	0.04
CPCM47	0.4	0.08	0.000	0.005	C	0.08
CPCM48	0.4	0.08	0.000	0.006	C	0.04
CPCM49	0.4	0.08	0.000	0.006	C	0.08
CPCM50	0.4	0.08	0.000	0.007	C	0.04
CPCM51	0.4	0.08	0.000	0.007	C	0.08
CPCM52	0.6	0.12	0.000	0.005	C	0.06
CPCM53	0.6	0.12	0.000	0.005	C	0.12
CPCM54	0.6	0.12	0.000	0.006	C	0.06
CPCM55	0.6	0.12	0.000	0.006	C	0.12
CPCM56	0.6	0.12	0.000	0.007	C	0.06
CPCM57	0.6	0.12	0.000	0.007	C	0.12
CPCM58	0.8	0.16	0.000	0.005	C	0.08
CPCM59	0.8	0.16	0.000	0.005	C	0.16
CPCM60	0.8	0.16	0.000	0.006	C	0.08
CPCM61	0.8	0.16	0.000	0.006	C	0.16
CPCM62	0.8	0.16	0.000	0.007	C	0.08
CPCM63	0.8	0.16	0.000	0.007	C	0.16
CPPF64	0.4	0.08	0.000	0.005	PF	0.04
CPPF65	0.4	0.08	0.000	0.005	PF	0.08
CPPF66	0.4	0.08	0.000	0.006	PF	0.04
CPPF67	0.4	0.08	0.000	0.006	PF	0.08
CPPF68	0.4	0.08	0.000	0.007	PF	0.04
CPPF69	0.4	0.08	0.000	0.007	PF	0.08
CPPF70	0.6	0.12	0.000	0.005	PF	0.06
CPPF71	0.6	0.12	0.000	0.005	PF	0.12
CPPF72	0.6	0.12	0.000	0.006	PF	0.06
CPPF73	0.6	0.12	0.000	0.006	PF	0.12
CPPF74	0.6	0.12	0.000	0.007	PF	0.06
CPPF75	0.6	0.12	0.000	0.007	PF	0.12
CPPF76	0.8	0.16	0.000	0.005	PF	0.08
CPPF77	0.8	0.16	0.000	0.005	PF	0.16
CPPF78	0.8	0.16	0.000	0.006	PF	0.08
CPPF79	0.8	0.16	0.000	0.006	PF	0.16
CPPF80	0.8	0.16	0.000	0.007	PF	0.08
CPPF81	0.8	0.16	0.000	0.007	PF	0.16

A.5.3 Key for the models and SETS that were used to make the variable comparisons

Table A.5.3: SETS A to V grouped for comparisons in tapered, parallel and cortical plated models showing the model design code for models in each group (see Appendix Table A.5.2). The colours use in the table indicate the governing colour used for each group of models and relates to the charts presented in the results section 5.3

GROUP: TAPERED MODELS		
SET	**Parameter = stem taper AND stem length**	**Models** (refer to Appendix Table A.5.2 for model designs)
A	0.08 m stem length, 5 mm radius 0.12 m stem length, 5 mm radius 0.16 m stem length, 5 mm radius	TP1, TP2, TP3, PR28 TP10, TP11, TP12, PR29 TP19, TP20, TP21, PR30
B	0.08 m stem length, 6 mm radius 0.12 m stem length, 6 mm radius 0.16 m stem length, 6 mm radius	TP4, TP5, TP6, PR31 TP13, TP14, TP15, PR32 TP22, TP23, TP24, PR33
C	0.08 m stem length, 7 mm radius 0.12 m stem length, 7 mm radius 0.16 m stem length, 7 mm radius	TP7, TP8, TP9, PR34 TP16, TP17, TP18, PR35 TP25, TP26, TP27, PR36
Parameter = stem radius		
G	0.08 m stem length, 0.375 ° stem taper 0.08 m stem length, 0.750 ° stem taper 0.08 m stem length, 1.500 ° stem taper	TP1, TP4, TP7 TP2, TP5, TP8 TP3, TP6, TP9
H	0.12 m stem length, 0.375 ° stem taper 0.12 m stem length, 0.750 ° stem taper 0.12 m stem length, 1.500 ° stem taper	TP10, TP13, TP16 TP11, TP14, TP17 TP12, TP15, TP18
I	0.16 m stem length, 0.375 ° stem taper 0.16 m stem length, 0.750 ° stem taper 0.16 m stem length, 1.500 ° stem taper	TP19, TP22, TP25 TP20, TP23, TP26 TP21, TP24, TP27
GROUP: PARALLEL MODELS		
Parameter = fixation type		
J	0.08 m stem length, 5 mm stem radius 0.12 m stem length, 5 mm stem radius 0.16 m stem length, 5 mm stem radius 0.08 m stem length, 6 mm stem radius 0.12 m stem length, 6 mm stem radius 0.16 m stem length, 6 mm stem radius 0.08 m stem length, 7 mm stem radius 0.12 m stem length, 7 mm stem radius 0.16 m stem length, 7 mm stem radius	PR28, PR37 PR29, PR38 PR30, PR39 PR31, PR40 PR32, PR41 PR33, PR42 PR34, PR43 PR35, PR44 PR36, PR45

Parameter = stem radius AND length		
K	0.08 m stem length , cemented 0.12 m stem length, cemented 0.16 m stem length, cemented	PR28, PR31, PR34 PR29, PR32, PR35 PR30, PR33, PR36
L	0.08 m stem length, pressfit 0.12 m stem length, pressfit 0.16 m stem length, pressfit	PR37, PR40, PR43 PR38, PR41, PR44 PR39, PR42, PR45
GROUP: CORTICAL PLATED MODELS		
Compare plate vs non-plated:		
Q	0.05 mm rad, 0.08 m stem length, cemented 0.06 mm rad, 0.08 m stem length, cemented 0.07 mm rad, 0.08 m stem length, cemented	CPCM46, CPCM47, PR28 CPCM48, CPCM49, PR31 CPCM50, CPCM51, PR34
R	0.05 mm rad, 0.12 m stem length, cemented 0.06 mm rad, 0.12 m stem length, cemented 0.07 mm rad, 0.12 m stem length, cemented	CPCM52, CPCM53, PR29 CPCM54, CPCM55, PR32 CPCM56, CPCM57, PR35
S	0.05 mm rad, 0.16 m stem length, cemented 0.06 mm rad, 0.16 m stem length, cemented 0.07 mm rad, 0.16 m stem length, cemented	CPCM58, CPCM59, PR30 CPCM60, CPCM61, PR33 CPCM62, CPCM63, PR36
T	0.05 mm rad, 0.08 m stem length, pressfit 0.06 mm rad, 0.08 m stem length, pressfit 0.07 mm rad, 0.08 m stem length, pressfit	CPPF64, CPPF65, PR37 CPPF66, CPPF67, PR40 CPPF68, CPPF69, PR43
U	0.05 mm rad, 0.12 m stem length, pressfit 0.06 mm rad, 0.12 m stem length, pressfit 0.07 mm rad, 0.12 m stem length, pressfit	CPPF70, CPPF71, PR38 CPPF72, CPPF73, PR41 CPPF74, CPPF75, PR44
V	0.05 mm rad, 0.16 m stem length, pressfit 0.06 mm rad, 0.16 m stem length, pressfit 0.07 mm rad, 0.16 m stem length, pressfit	CPPF76, CPPF77, PR39 CPPF78, CPPF79, PR42 CPPF80, CPPF81, PR45
Parameter = fixation type		
N	0.08 m stem length, 0.04 m cortical plate, 5mm stem radius 0.08 m stem length, 0.08 m cortical plate, 5mm stem radius 0.08 m stem length, 0.04 m cortical plate, 6mm stem radius 0.08 m stem length, 0.08 m cortical plate, 6mm stem radius 0.08 m stem length, 0.04 m cortical plate, 7mm stem radius 0.08 m stem length, 0.08 m cortical plate, 7mm stem radius	CPCM46, CPPF64 CPCM47, CPPF65 CPCM48, CPPF66 CPCM49, CPPF67 CPCM50, CPPF68 CPCM51, CPPF69
O	0.12 m stem length, 0.06 m cortical plate, 5mm stem radius 0.12 m stem length, 0.12 m cortical plate, 5mm stem radius 0.12 m stem length, 0.06 m cortical plate, 6mm stem radius 0.12 m stem length, 0.12 m cortical plate, 6mm stem radius 0.12 m stem length, 0.06 m cortical plate, 7mm stem radius 0.12 m stem length, 0.12 m cortical plate, 7mm stem radius	CPCM52, CPPF70 CPCM53, CPPF71 CPCM54, CPPF72 CPCM55, CPPF73 CPCM56, CPPF74 CPCM57, CPPF75
P	0.16 m stem length, 0.08 m cortical plate, 5mm stem radius 0.16 m stem length, 0.16 m cortical plate, 5mm stem radius 0.16 m stem length, 0.08 m cortical plate, 6mm stem radius 0.16 m stem length, 0.16 m cortical plate, 6mm stem radius 0.16 m stem length, 0.08 m cortical plate, 7mm stem radius 0.16 m stem length, 0.16 m cortical plate, 7mm stem radius	CPCM58, CPPF76 CPCM59, CPPF77 CPCM60, CPPF78 CPCM61, CPPF79 CPCM62, CPPF80 CPCM63, CPPF81

References

AARDEN, E. M., NIJWEIDE, P. J., VAN DER PLAS, A., ALBLAS, M. J., MACKIE, E. J., HORTON, M. A. & HELFRICH, M. H. 1996. Adhesive properties of isolated chick osteocytes in vitro. *Bone,* 18**,** 305-313.

ABDEL-HADY GEPREEL, M. & NIINOMI, M. 2013. Biocompatibility of Ti-alloys for long-term implantation. *J Mech Behav Biomed Mater,* 20**,** 407-15.

ABDUL-KADIR, M. R., HANSEN, U., KLABUNDE, R., LUCAS, D. & AMIS, A. 2008. Finite element modelling of primary hip stem stability: the effect of interference fit. *Journal of biomechanics,* 41**,** 587-594.

AERONAUTICS, A. I. O. & ASTRONAUTICS 1998. *AIAA guide for the verification and validation of computational fluid dynamics simulations*, American Institute of aeronautics and astronautics.

AGATHANGELIDIS, F., BOUTSIADIS, A. & PETSATODIS, G. 2014. Pedestal sign in cementless total hip replacement. *Hippokratia,* 18**,** 378.

AHMAD, N., THOMAS, G. N., GILL, P. & TORELLA, F. 2016. The prevalence of major lower limb amputation in the diabetic and non-diabetic population of England 2003–2013. *Diabetes and Vascular Disease Research,* 13**,** 348-353.

AHMED, K., GREENE, R., ASTON, W., BRIGGS, T., PENDEGRASS, C., MOAZEN, M. & BLUNN, G. 2020. Experimental validation of an ITAP numerical model and the effect of implant stem stiffness on bone strain energy. *Annals of biomedical engineering,* 48**,** 1382-1395.

AL-TAMIMI, A. A., FERNANDES, P. R. A., PEACH, C., COOPER, G., DIVER, C. & BARTOLO, P. J. 2017. Metallic bone fixation implants: a novel design approach for reducing the stress shielding phenomenon. *Virtual and Physical Prototyping,* 12**,** 141-151.

AL MUDERIS, M., KHEMKA, A., LORD, S. J., VAN DE MEENT, H. & FROLKE, J. P. 2016. Safety of Osseointegrated Implants for Transfemoral Amputees: A Two-Center Prospective Cohort Study. *J Bone Joint Surg Am,* 98**,** 900-9.

AL MUDERIS, M., LU, W. & LI, J. J. 2017a. Osseointegrated Prosthetic Limb for the treatment of lower limb amputations : Experience and outcomes. *Unfallchirurg,* 120**,** 306-311.

AL MUDERIS, M., LU, W., TETSWORTH, K., BOSLEY, B. & LI, J. J. 2017b. Single-stage osseointegrated reconstruction and rehabilitation of lower limb amputees: the Osseointegration Group of Australia Accelerated Protocol-2 (OGAAP-2) for a prospective cohort study. *BMJ Open,* 7**,** e013508.

ALEXANDER, N., STRUTZENBERGER, G., KROELL, J., BARNETT, C. T. & SCHWAMEDER, H. 2018. Joint Moments During Downhill and Uphill Walking of a Person with Transfemoral Amputation with a Hydraulic Articulating and a Rigid Prosthetic Ankle—A Case Study. *JPO: Journal of Prosthetics and Orthotics,* 30**,** 46-54.

AMMANN, P. & RIZZOLI, R. 2003. Bone strength and its determinants. *Osteoporosis international,* 14**,** 13-18.

AMPUTEE, S. 2012. *https://advancedamputees.com/amputee-statistics-you-ought-know* [Online]. [Accessed 14/09/20 2020].

ANDERSON, H. C. 2003. Matrix vesicles and calcification. *Curr Rheumatol Rep,* 5**,** 222-6.

ARNO, S., FETTO, J., NGUYEN, N. Q., KINARIWALA, N., TAKEMOTO, R., OH, C. & WALKER, P. S. 2012. Evaluation of femoral strains with cementless proximal-fill femoral implants of varied stem length. *Clinical Biomechanics,* 27**,** 680-685.

ARNOLD, A. S., ANDERSON, F. C., PANDY, M. G. & DELP, S. L. 2005. Muscular contributions to hip and knee extension during the single limb stance phase of normal gait: a framework for investigating the causes of crouch gait. *Journal of biomechanics,* 38**,** 2181-2189.

ASCHOFF, H. H., KENNON, R. E., KEGGI, J. M. & RUBIN, L. E. 2010. Transcutaneous, distal femoral, intramedullary attachment for above-the-knee prostheses: an endo-exo device. *JBJS,* 92**,** 180-186.

ASHBY, M. & GIBSON, L. 1997. Cellular solids: structure and properties. *Press Syndicate of the University of Cambridge, Cambridge, UK***,** 175-231.

ASHMAN, R. B., COWIN, S. C., VAN BUSKIRK, W. C. & RICE, J. C. 1984. A continuous wave technique for the measurement of the elastic properties of cortical bone. *J Biomech,* 17**,** 349-61.

ASTM. 2020. *FEA standards* [Online]. Available: https://www.astm.org/search/fullsite-search.html?query=finite%20element%20analysis&resStart=0&resLength=10&toplevel=products-and-services&sublevel=standards-and-publications&dltype=allstd& [Accessed].

BAE, T. S., CHOI, K., HONG, D. & MUN, M. 2007. Dynamic analysis of above-knee amputee gait. *Clinical Biomechanics,* 22**,** 557-566.

BAGHERI, Z. S., TAVAKKOLI AVVAL, P., BOUGHERARA, H., AZIZ, M. S. R., SCHEMITSCH, E. H. & ZDERO, R. 2014. Biomechanical Analysis of a New Carbon Fiber/Flax/Epoxy Bone Fracture Plate Shows Less Stress Shielding Compared to a Standard Clinical Metal Plate. *Journal of Biomechanical Engineering,* 136.

BARR, J. B., WUTZKE, C. J. & THRELKELD, A. J. 2012. Longitudinal gait analysis of a person with a transfemoral amputation using three different prosthetic knee/foot pairs. *Physiotherapy theory and practice,* 28**,** 407-411.

BARTEL, D., DAVY, D. & KEAVENY, T. 2006. Orthopaedic Biomechanics Mechanics and Design in Musculoskeletal Systems. 2006. Upper Saddle River: Pearson Education, Inc.

BAUM, B. S., SCHNALL, B. L., TIS, J. E. & LIPTON, J. S. 2008. Correlation of residual limb length and gait parameters in amputees. *Injury,* 39**,** 728-733.

BEALS, R. K. & TOWER, S. S. 1996. Periprosthetic fractures of the femur: an analysis of 93 fractures. *Clinical Orthopaedics and Related Research®,* 327**,** 238-246.

BEAUPRÉ, G., ORR, T. & CARTER, D. 1990. An approach for time‐dependent bone modeling and remodeling–theoretical development. *Journal of Orthopaedic Research,* 8**,** 651-661.

BELL, A. L., BRAND, R. A. & PEDERSEN, D. R. 1989. Prediction of hip joint centre location from external landmarks. *Human movement science,* 8**,** 3-16.

BELL, C. G., WEINRAUCH, P., PEARCY, M. & CRAWFORD, R. 2007. In vitro analysis of exeter stem torsional stability. *J Arthroplasty,* 22**,** 1024-30.

BELL, J. C., WOLF, E. J., SCHNALL, B. L., TIS, J. E. & POTTER, B. K. 2014. Transfemoral amputations: is there an effect of residual limb length and orientation on energy expenditure? *Clin Orthop Relat Res,* 472**,** 3055-61.

BENICHOU, C. & WIROTIUS, J. 1982. Articular cartilage atrophy in lower limb amputees. *Arthritis & Rheumatism: Official Journal of the American College of Rheumatology,* 25**,** 80-82.

BERGMANN, G., BENDER, A., DYMKE, J., DUDA, G. & DAMM, P. 2016. Standardized Loads Acting in Hip Implants. *PLoS One,* 11**,** e0155612.

BERGMANN, G., DEURETZBACHER, G., HELLER, M., GRAICHEN, F., ROHLMANN, A., STRAUSS, J. & DUDA, G. N. 2001. Hip contact forces and gait patterns from routine activities. *J Biomech,* 34**,** 859-71.

BERKE, G., BUELL, N., FERGASON, J., GAILEY, R., HAFNER, B., HUBBARD, S. & WILLINGHAM, L. 2008. Transfemoral Amputation: The Basic and Beyond. *Prosthetics Research Study*.

BERTRAM, J. E. & BIEWENER, A. A. 1988. Bone curvature: sacrificing strength for load predictability? *Journal of theoretical biology,* 131**,** 75-92.

BIEGER, R., IGNATIUS, A., DECKING, R., CLAES, L., REICHEL, H. & DÜRSELEN, L. 2012. Primary stability and strain distribution of cementless hip stems as a function of implant design. *Clin Biomech (Bristol, Avon),* 27**,** 158-64.

BIEWENER, A. A. & TAYLOR, C. R. 1986. Bone strain: a determinant of gait and speed? *Journal of Experimental Biology,* 123**,** 383-400.

BILEZIKIAN, J. P. 2002. Intercellular Junctions and Cell-Cell Communication in Bone. *Principles of bone biology /***,** 287-302.

BIOMET, Z. 2018. *Compress device surgical technique* [Online]. Warsaw, Indiana, USA: Zimmer Biomet. Available: http://www.zimmerbiomet.com/ [Accessed].

BOSKEY, A. L. 2001. *Bone mechanics handbook,* Boca Raton, FL. London, Boca Raton, FL. London : CRC Press.

BOUGHERARA, H., ZDERO, R., SHAH, S., MIRIC, M., PAPINI, M., ZALZAL, P. & SCHEMITSCH, E. H. 2010. A biomechanical assessment of modular and monoblock revision hip implants using FE analysis and strain gage measurements. *Journal of orthopaedic surgery and research,* 5**,** 1-12.

BOWER, A. F. 2009. *Applied mechanics of solids*, CRC press.

BRANEMARK, R., BERLIN, O., HAGBERG, K., BERGH, P., GUNTERBERG, B. & RYDEVIK, B. 2014. A novel osseointegrated percutaneous prosthetic system for the treatment of patients with transfemoral amputation: A prospective study of 51 patients. *Bone Joint J,* 96-B**,** 106-13.

BRÅNEMARK, R., BERLIN, Ö., HAGBERG, K., BERGH, P., GUNTERBERG, B. & RYDEVIK, B. 2014. A novel osseointegrated percutaneous prosthetic system for the treatment of patients with transfemoral amputation: A prospective study of 51 patients. *The bone & joint journal,* 96**,** 106-113.

BRASSEY, C. A., MARGETTS, L., KITCHENER, A. C., WITHERS, P. J., MANNING, P. L. & SELLERS, W. I. 2013. Finite element modelling versus classic beam theory: comparing methods for stress estimation in a morphologically diverse sample of vertebrate long bones. *Journal of the Royal Society Interface,* 10**,** 20120823.

BUGBEE, W. D., CULPEPPER, W. J., ENGH, C. A. & ENGH, C. A. 1997. Long-term clinical consequences of stress-shielding after total hip arthroplasty without cement. *JBJS,* 79**,** 1007-12.

BURGER, H. & MARINCEK, C. 2007. Return to work after lower limb amputation. *Disabil Rehabil,* 29**,** 1323-9.

BURSTEIN, A. H., REILLY, D. T. & MARTENS, M. 1976. Aging of bone tissue: mechanical properties. *JBJS,* 58**,** 82-86.

CAITI, G., DOBBE, J. G., BERVOETS, E., BEERENS, M., STRACKEE, S. D., STRIJKERS, G. J. & STREEKSTRA, G. J. 2019. Biomechanical considerations in the design of patient-specific fixation plates for the distal radius. *Medical & biological engineering & computing,* 57**,** 1099-1107.

CALLAGHAN, J. J., FULGHUM, C. S., GLISSON, R. R. & STRANNE, S. K. 1992. The effect of femoral stem geometry on interface motion in uncemented porous-coated total hip prostheses. Comparison of straight-stem and curved-stem designs. *The Journal of bone and joint surgery. American volume,* 74**,** 839-848.

CALVERT, G. T., CUMMINGS, J. E., BOWLES, A. J., JONES, K. B., WURTZ, L. D. & RANDALL, R. L. 2014. A dual-center review of compressive osseointegration for fixation of massive endoprosthetics: 2-to 9-year followup. *Clinical Orthopaedics and Related Research®,* 472**,** 822-829.

CAMAZZOLA, D., HAMMOND, T., GANDHI, R. & DAVEY, J. R. 2009. A Randomized Trial of Hydroxyapatite-Coated Femoral Stems in Total Hip Arthroplasty: A 13-Year Follow-Up. *The Journal of Arthroplasty,* 24**,** 33-37.

CARTER, D. R. 1984. Mechanical loading histories and cortical bone remodeling. *Calcif Tissue Int,* 36 Suppl 1**,** S19-24.

CARTER, D. R. & BEAUPRE, G. S. 2000. Cancellous Bone. *Skeletal Function and Form.*

CHAN, J., KHORIATI, A. A., CHIANG, C. H. & HADITHY, N. A. 2017. Understanding, Interpreting and Reporting a Total Hip Arthroplasty Radiograph. *Orthopedic & Muscular System,* 06.

CHAN, S. C., CHIA, J. W. & TAN, Y. Q. Kinetic and Kinematic Impacts during Level Walking, Uphill walking, Level Running and Uphill Running. 2018 IEEE Student Conference on Research and Development (SCOReD), 2018. IEEE, 1-4.

CHEAL, E. J., HAYES, W. C., WHITE, A. A. & PERREN, S. M. 1983. Stress analysis of a simplified compression plate fixation system for fractured bones. *Computers & Structures,* 17**,** 845-855.

CHEN, Z., LI, B., CHEN, K., FENG, J., WANG, Y., LIU, Z. & HE, C. 2021. Malalignment and distal contact of short tapered stems could be associated with postoperative thigh pain in primary total hip arthroplasty. *Journal of Orthopaedic Surgery and Research,* 16**,** 67.

CHERIAN, J. J., KAPADIA, B. H., BANERJEE, S., JAUREGUI, J. J., ISSA, K. & MONT, M. A. 2014. Mechanical, Anatomical, and Kinematic Axis in TKA: Concepts and Practical Applications. *Curr Rev Musculoskelet Med,* 7**,** 89-95.

CHIMUTENGWENDE-GORDON, M., PENDEGRASS, C., BAYSTON, R. & BLUNN, G. 2014. Preventing infection of osseointegrated transcutaneous implants: Incorporation of silver into preconditioned fibronectin-functionalized hydroxyapatite coatings suppresses Staphylococcus aureus colonization while promoting viable fibroblast growth in vitro. *Biointerphases,* 9**,** 031010.

CHIU, M.-C. & WANG, M.-J. 2007. The effect of gait speed and gender on perceived exertion, muscle activity, joint motion of lower extremity, ground reaction force and heart rate during normal walking. *Gait & posture,* 25**,** 385-392.

CHOCKALINGAM, N., HEALY, A. & NEEDHAM, R. 2016. Interpreting Ground Reaction Forces in Gait. *In:* MÜLLER, B., WOLF, S. I., BRUEGGEMANN, G.-P., DENG, Z., MCINTOSH, A., MILLER, F. & SELBIE, W. S. (eds.) *Handbook of Human Motion.* Cham: Springer International Publishing.

CHOONG, P. F., DOWSEY, M. M. & STONEY, J. D. 2009. Does Accurate Anatomical Alignment Result in Better Function and Quality of Life? Comparing Conventional and Computer-Assisted Total Knee Arthroplasty. *The Journal of Arthroplasty,* 24**,** 560-569.

CHRISTEN, P., ITO, K., ELLOUZ, R., BOUTROY, S., SORNAY-RENDU, E., CHAPURLAT, R. D. & VAN RIETBERGEN, B. 2014. Bone remodelling in humans is load-driven but not lazy. *Nat Commun,* 5**,** 4855.

CHUNG, H. & CHUNG, S. H. 2020. Correlation between anterior thigh pain and morphometric mismatch of femoral stem. *Yeungnam University journal of medicine,* 37**,** 40-46.

CILLA, M., BORGIANI, E., MARTINEZ, J., DUDA, G. N. & CHECA, S. 2017. Machine learning techniques for the optimization of joint replacements: Application to a short-stem hip implant. *PLoS One,* 12**,** e0183755.

CLOHISY, J. C., KAMATH, G. V., BYRD, G. D., STEGER-MAY, K. & WRIGHT, R. W. 2008. Patient compliance with clinical follow-up after total joint arthroplasty. *JBJS,* 90**,** 1848-1854.

COATHUP, M. J., BATTA, V., POLLOCK, R. C., ASTON, W. J., CANNON, S. R., SKINNER, J. A., BRIGGS, T. W., UNWIN, P. S. & BLUNN, G. W. 2013. Long-term survival of cemented distal femoral endoprostheses with a hydroxyapatite-coated collar: a histological study and a radiographic follow-up. *J Bone Joint Surg Am,* 95**,** 1569-75.

COATHUP, M. J., SANGHRAJKA, A., ASTON, W. J., GIKAS, P. D., POLLOCK, R. C., CANNON, S. R., SKINNER, J. A., BRIGGS, T. W. & BLUNN, G. W. 2015. Hydroxyapatite-coated collars reduce radiolucent line progression in cemented distal femoral bone tumor implants. *Clin Orthop Relat Res,* 473**,** 1505-14.

COOK, R. D. 1995. Finite element modeling for stress analysis. *John Wiley & Sons, ISBN: 0-471-10774-3*.

COURANT, R. 1943. Variational methods for the solution of problems of equilibrium and vibrations. *Bulletin of the American Mathematical Society,* 49**,** 1-23.

CRISTOFOLINI, L., CONTI, G., JUSZCZYK, M., CREMONINI, S., JAN, S. V. S. & VICECONTI, M. 2010. Structural behaviour and strain distribution of the long bones of the human lower limbs. *Journal of biomechanics,* 43**,** 826-835.

CRISTOFOLINI, L., TEUTONICO, A. S., MONTI, L., CAPPELLO, A. & TONI, A. 2003. Comparative in vitro study on the long term performance of cemented hip stems: validation of a protocol to discriminate between “good” and “bad” designs. *Journal of Biomechanics,* 36**,** 1603-1615.

CUPPONE, M., SEEDHOM, B. B., BERRY, E. & OSTELL, A. E. 2004. The Longitudinal Young’s Modulus of Cortical Bone in the Midshaft of Human Femur and its Correlation with CT Scanning Data. *Calcified Tissue International,* 74**,** 302-309.

CURREY, J. D. 2003. Role of collagen and other organics in the mechanical properties of bone. *Osteoporosis International,* 14**,** 29-36.

D'ANTONIO, J. A., CAPELLO, W. N. & MANLEY, M. T. 1996. Remodeling of bone around hydroxyapatite-coated femoral stems. *JBJS,* 78**,** 1226-34.

DATTA, H. K., NG, W. F., WALKER, J. A., TUCK, S. P. & VARANASI, S. S. 2008. The cell biology of bone metabolism. *J Clin Pathol,* 61**,** 577-87.

DAVIDSON, J., MISHRA, A., KOVACS, P. & POGGIE, R. 1994. New surface-hardened, low-modulus, corrosion-resistant Ti-13Nb-13Zr alloy for total hip arthroplasty. *Bio-medical materials and engineering,* 4**,** 231-243.

DE MARGERIE, E., SANCHEZ, S., CUBO, J. & CASTANET, J. 2005. Torsional resistance as a principal component of the structural design of long bones: comparative multivariate evidence in birds. *The Anatomical Record Part A: Discoveries in Molecular, Cellular, and Evolutionary Biology: An Official Publication of the American Association of Anatomists,* 282**,** 49-66.

DEBBI, E. M., BERNFELD, B., HERMAN, A., LAUFER, Y., GREENTAL, A., SIGAL, A., ZAULAN, Y., SALAI, M., HAIM, A. & WOLF, A. 2015. Frontal plane biomechanics of the operated and non-operated knees before and after unilateral total knee arthroplasty. *Clinical Biomechanics,* 30**,** 889-894.

DELORME, G., SALTEL, F., BONNELYE, E., JURDIC, P. & MACHUCA‐GAYET, I. 2005. Expression and function of semaphorin 7A in bone cells. *Biology of the Cell,* 97**,** 589-597.

DEN BUIJS, J. O. & DRAGOMIR-DAESCU, D. 2011. Validated finite element models of the proximal femur using two-dimensional projected geometry and bone density. *Computer methods and programs in biomedicine,* 104**,** 168-174.

DEVITA, P., HELSETH, J. & HORTOBAGYI, T. 2007. Muscles do more positive than negative work in human locomotion. *Journal of Experimental Biology,* 210**,** 3361-3373.

DICKINSON, A. S. 2014. Activity and loading influence the predicted bone remodeling around cemented hip replacements. *Journal of biomechanical engineering,* 136.

DICKINSON, A. S., TAYLOR, A. C., OZTURK, H. & BROWNE, M. 2011. Experimental validation of a finite element model of the proximal femur using digital image correlation and a composite bone model. *J Biomech Eng,* 133**,** 014504.

DIFFO KAZE, A., MAAS, S., ARNOUX, P. J., WOLF, C. & PAPE, D. 2017. A finite element model of the lower limb during stance phase of gait cycle including the muscle forces. *Biomed Eng Online,* 16**,** 138.

DILLINGHAM, T. R., PEZZIN, L. E. & MACKENZIE, E. J. 1998. Incidence, acute care length of stay, and discharge to rehabilitation of traumatic amputee patients: an epidemiologic study. *Archives of physical medicine and rehabilitation,* 79**,** 279-287.

DONELAN, J. M., KRAM, R. & KUO, A. D. 2002. Simultaneous positive and negative external mechanical work in human walking. *Journal of biomechanics,* 35**,** 117-124.

DOOLEY, C., TISBO, P., LEE, T. C. & TAYLOR, D. 2012. Rupture of osteocyte processes across microcracks: the effect of crack length and stress. *Biomechanics and modeling in mechanobiology,* 11**,** 759-766.

DUMAS, R., BRANEMARK, R. & FROSSARD, L. 2017. Gait Analysis of Transfemoral Amputees: Errors in Inverse Dynamics Are Substantial and Depend on Prosthetic Design. *IEEE Trans Neural Syst Rehabil Eng,* 25**,** 679-685.

E. HANSSON, K. HAGBERG, M. CAWSON & BRODTKORB, T. H. 2018. Patients with unilateral transfemoral amputation treated with a percutaneous osseointegrated prosthesis A COST EFFECTIVENESS ANALYSIS.pdf.

EAZHIL, R., SWAMINATHAN, S. V., GUNASEELAN, M., KANNAN, G. V. & ALAGESAN, C. 2016. Impact of implant diameter and length on stress distribution in osseointegrated implants: A 3D FEA study. *Journal of International Society of Preventive & Community Dentistry,* 6**,** 590.

EFTEKHAR, V. S. H., ELYASI, L., AMIRIAN, S. R., RAIGAN, P., AKBARI, H., SHEIKHSHOAIEE, M. & BORBOR, A. 2015. Evaluating anthropometric dimensions of the femur using direct and indirect methods.

ENGH, C. A., BOBYN, J. & GLASSMAN, A. H. 1987. Porous-coated hip replacement. The factors governing bone ingrowth, stress shielding, and clinical results. *The Journal of bone and joint surgery. British volume,* 69**,** 45-55.

ENGH, C. A. & BOBYN, J. D. 1988. The influence of stem size and extent of porous coating on femoral bone resorption after primary cementless hip arthroplasty. *Clinical orthopaedics and related research***,** 7-28.

ENGH, C. A., MASSIN, P. & SUTHERS, K. E. 1990. Roentgenographic assessment of the biologic fixation of porous-surfaced femoral components. *Clin Orthop Relat Res***,** 107-28.

ERDEMIR, A., GUESS, T. M., HALLORAN, J., TADEPALLI, S. C. & MORRISON, T. M. 2012. Considerations for reporting finite element analysis studies in biomechanics. *Journal of biomechanics,* 45**,** 625-633.

EVERTS, V., DELAISSE, J. M., KORPER, W., JANSEN, D. C., TIGCHELAAR-GUTTER, W., SAFTIG, P. & BEERTSEN, W. 2002. The bone lining cell: its role in cleaning Howship's lacunae and initiating bone formation. *J Bone Miner Res,* 17**,** 77-90.

FABER, H., VAN SOEST, A. J. & KISTEMAKER, D. A. 2018. Inverse dynamics of mechanical multibody systems: An improved algorithm that ensures consistency between kinematics and external forces. *PloS one,* 13.

FENG, H., ZHOU, Y., JIA, D. & MENG, Q. 2004. Microstructure and mechanical properties of in situ TiB reinforced titanium matrix composites based on Ti–FeMo–B prepared by spark plasma sintering. *Composites Science and Technology,* 64**,** 2495-2500.

FEY, N. P. & NEPTUNE, R. R. 2012. 3D intersegmental knee loading in below-knee amputees across steady-state walking speeds. *Clinical Biomechanics,* 27**,** 409-414.

FEYEN, H. & SHIMMIN, A. J. 2014. Is the length of the femoral component important in primary total hip replacement? *Bone Joint J,* 96-b**,** 442-8.

FITZPATRICK, N. 2008. *Spotlight on: Limb sparing & limb salvage surgery* [Online]. Available: https://www.fitzpatrickreferrals.co.uk/blog/2018/04/spotlight-limb-sparing-limb-salvage-surgery/ [Accessed].

FITZPATRICK, N., SMITH, T. J., PENDEGRASS, C. J., YEADON, R., RING, M., GOODSHIP, A. E. & BLUNN, G. W. 2011. Intraosseous transcutaneous amputation prosthesis (ITAP) for limb salvage in 4 dogs. *Veterinary surgery,* 40**,** 909-925.

FLORENCIO-SILVA, R., SASSO, G. R., SASSO-CERRI, E., SIMOES, M. J. & CERRI, P. S. 2015. Biology of Bone Tissue: Structure, Function, and Factors That Influence Bone Cells. *Biomed Res Int,* 2015**,** 421746.

FRANZ, J. R., LYDDON, N. E. & KRAM, R. 2012. Mechanical work performed by the individual legs during uphill and downhill walking. *Journal of biomechanics,* 45**,** 257-262.

FRATZL, P., GROSCHNER, M., VOGL, G., PLENK, H., JR., ESCHBERGER, J., FRATZL-ZELMAN, N., KOLLER, K. & KLAUSHOFER, K. 1992. Mineral crystals in calcified tissues: a comparative study by SAXS. *J Bone Miner Res,* 7**,** 329-34.

FRATZL, P., GUPTA, H. S., PASCHALIS, E. P. & ROSCHGER, P. 2004. Structure and mechanical quality of the collagen–mineral nano-composite in bone. *Journal of Materials Chemistry,* 14**,** 2115-2123.

FREDDI, A., OLMI, G. & CRISTOFOLINI, L. 2015. Experimental stress analysis for materials and structures. *Stress analysis models for developing design methodologies. Series in solid and structural mechanics,* 1.

FROLKE, J., LEIJENDEKKERS, R. & MEENT, H. 2017. Osseointegrated prosthesis for patients with an amputation: Multidisciplinary team approach in the Netherlands.

FROMME, P., BLUNN, G. W., ASTON, W. J., ABDOOLA, T., KORIS, J. & COATHUP, M. J. 2017. The effect of bone growth onto massive prostheses collars in protecting the implant from fracture. *Med Eng Phys,* 41**,** 19-25.

FROSSARD, L. 2019. Loading characteristics data applied on osseointegrated implant by transfemoral bone-anchored prostheses fitted with basic components during daily activities. *Data Brief,* 26**,** 104492.

FROSSARD, L., BECK, J., DILLON, M. & EVANS, J. 2003. Development and Preliminary Testing of a Device for the Direct Measurement of Forces and Moments in the Prosthetic Limb of Transfemoral Amputees during Activities of Daily Living. *JPO Journal of Prosthetics and Orthotics,* 15**,** 135-142.

FROSSARD, L., GOW, D. L., HAGBERG, K., CAIRNS, N., CONTOYANNIS, B., GRAY, S., BRANEMARK, R. & PEARCY, M. 2010a. Apparatus for monitoring load bearing rehabilitation exercises of a transfemoral amputee fitted with an osseointegrated fixation: a proof-of-concept study. *Gait Posture,* 31**,** 223-8.

FROSSARD, L., HAGBERG, K., HÄGGSTRÖM, E., GOW, D. L., BRÅNEMARK, R. & PEARCY, M. 2010b. Functional outcome of transfemoral amputees fitted with an osseointegrated fixation: temporal gait characteristics. *JPO: Journal of Prosthetics and Orthotics,* 22**,** 11-20.

FROSSARD, L., HAGGSTROM, E., HAGBERG, K. & BRANEMARK, R. 2013. Load applied on bone-anchored transfemoral prosthesis: characterization of a prosthesis-a pilot study. *J Rehabil Res Dev,* 50**,** 619-34.

FROSSARD, L. A., MERLO, G., BURKETT, B., QUINCEY, T. & BERG, D. 2018. Cost-effectiveness of bone-anchored prostheses using osseointegrated fixation: Myth or reality? *Prosthet Orthot Int,* 42**,** 318-327.

FROST, H. M. 1986. *Intermediary organization of the skeleton,* Boca Raton, Fla, Boca Raton, Fla : CRC Press.

FROST, H. M. 1987. Bone "mass" and the "mechanostat": a proposal. *Anat Rec,* 219**,** 1-9.

FURMANSKI, J., CHAKRAVARTULA, A., PRUITT, L. A. & CHAKRAVARTULA, A. M. 2011a. Mechanical behavior of structural tissues. 129-164.

FURMANSKI, J., PRUITT, L. A., PRUITT, L. A. & CHAKRAVARTULA, A. M. 2011b. Viscoelasticity. *Mechanics of Biomaterials.*

GAILEY, R., ALLEN, K., CASTLES, J., KUCHARIK, J. & ROEDER, M. 2008. Review of secondary physical conditions associated with lower-limb amputation and long-term prosthesis use. *J Rehabil Res Dev,* 45**,** 15-29.

GAO, X., FRAULOB, M. & HAÏAT, G. 2019. Biomechanical behaviours of the bone–implant interface: a review. *Journal of the Royal Society Interface,* 16**,** 20190259.

GARD, S. A. 2018. The influence of prosthetic knee joints on gait. *Handbook of Human Motion.* Springer International Publishing.

GENERAL, O. O. T. S. 2004. Bone health and osteoporosis: a report of the Surgeon General.

GENG, K., LU, W., YANG, Z. & ZHANG, D. 2003. In situ preparation of titanium matrix composites reinforced by TiB and Nd2O3. *Materials letters,* 57**,** 4054-4057.

GERALDES, D. M. & PHILLIPS, A. T. 2014. A comparative study of orthotropic and isotropic bone adaptation in the femur. *Int J Numer Method Biomed Eng,* 30**,** 873-89.

GILCHRIST, S., GUY, P. & CRIPTON, P. A. 2013. Development of an inertia-driven model of sideways fall for detailed study of femur fracture mechanics. *Journal of biomechanical engineering,* 135.

GIUSTO, E., PENDEGRASS, C., LIU, C. & BLUNN, G. NANOTUBES IMPROVE HUMAN DERMAL FIBROBLASTS AND KERATINOCYTES ATTACHMENT ON INTRAOSSEOUS TRANSCUTANEOUS AMPUTATION PROSTHESIS. Orthopaedic Proceedings, 2019. The British Editorial Society of Bone & Joint Surgery, 11-11.

GOLACHOWSKI, A., AL GHABRI, M. R., GOLACHOWSKA, B., AL ABRI, H., LUBAK, M. & SUJETA, M. 2019. Implantation of an Intraosseous Transcutaneous Amputation Prosthesis Restoring Ambulation After Amputation of the Distal Aspect of the Left Tibia in an Arabian Tahr (Arabitragus jayakari). *Frontiers in Veterinary Science,* 6.

GOLDBERG, E. J., KAUTZ, S. A. & NEPTUNE, R. R. 2008. Can treadmill walking be used to assess propulsion generation? *Journal of biomechanics,* 41**,** 1805-1808.

GOLDMAN, L. H., MORSE, L. J., O'DONNELL, R. J. & WUSTRACK, R. L. 2016. How often does spindle failure occur in compressive osseointegration endoprostheses for oncologic reconstruction? *Clinical Orthopaedics and Related Research®,* 474**,** 1714-1723.

GOTMAN, I. 2014. Biomechanical and Tribological Aspects of Orthopaedic Implants. *Multiscale Biomechanics and Tribology of Inorganic and Organic Systems.* Springer, Cham.

GOTTSCHALK, F. 1999. Transfemoral amputation. Biomechanics and surgery. *Clin Orthop Relat Res***,** 15-22.

GOTTSCHALK, F. 2016a. The importance of soft tissue stabilization in trans-femoral amputation. *Der Orthopäde,* 45**,** 1-4.

GOTTSCHALK, F. 2016b. The importance of soft tissue stabilization in trans-femoral amputation : English version. *Orthopade,* 45 Suppl 1**,** S1-4.

GOTTSCHALL, J. S. & KRAM, R. 2005. Ground reaction forces during downhill and uphill running. *Journal of biomechanics,* 38**,** 445-452.

GOTTSCHALL, J. S. & KRAM, R. 2006. Mechanical energy fluctuations during hill walking: the effects of slope on inverted pendulum exchange. *Journal of Experimental Biology,* 209**,** 4895-4900.

GRASSI, L., VÄÄNÄNEN, S. P., AMIN YAVARI, S., JURVELIN, J. S., WEINANS, H., RISTINMAA, M., ZADPOOR, A. A. & ISAKSSON, H. 2014. Full-field strain measurement during mechanical testing of the human femur at physiologically relevant strain rates. *Journal of biomechanical engineering,* 136.

GRASSI, L., VAANANEN, S. P., AMIN YAVARI, S., WEINANS, H., JURVELIN, J. S., ZADPOOR, A. A. & ISAKSSON, H. 2013. Experimental validation of finite element model for proximal composite femur using optical measurements. *J Mech Behav Biomed Mater,* 21**,** 86-94.

GRAVES, A. R., CURRAN, P. K., SMITH, C. L. & MINDELL, J. A. 2008. The Cl-/H+ antiporter ClC-7 is the primary chloride permeation pathway in lysosomes. *Nature,* 453**,** 788-92.

GRECU, D., PUCALEV, I., NEGRU, M., TARNITA, D., IONOVICI, N. & DITA, R. 2010. Numerical simulations of the 3D virtual model of the human hip joint, using finite element method. *Rom J Morphol Embryol,* 51**,** 151-155.

GREIWE, R. M. & ARCHDEACON, M. T. 2007. Locking plate technology–current concepts. *The journal of knee surgery,* 20**,** 50-55.

GRIMMER, M. & SEYFARTH, A. 2014. Mimicking human-like leg function in prosthetic limbs. *Neuro-Robotics.* Springer.

GUIRAO, L., SAMITIER, C. B., COSTEA, M., CAMOS, J. M., MAJO, M. & PLEGUEZUELOS, E. 2017. Improvement in walking abilities in transfemoral amputees with a distal weight bearing implant. *Prosthet Orthot Int,* 41**,** 26-32.

GÜNTHER, M., SHOLUKHA, V. A., KESSLER, D., WANK, V. & BLICKHAN, R. 2003. Dealing with skin motion and wobbling masses in inverse dynamics. *Journal of Mechanics in Medicine and Biology,* 3**,** 309-335.

HAASE, K. & ROUHI, G. 2010. A discussion on plating factors that affect stress shielding using finite element analysis. *Journal of Biomechanical Science and Engineering,* 5**,** 129-141.

HADDADI, H. & BELHABIB, S. 2008. Use of rigid-body motion for the investigation and estimation of the measurement errors related to digital image correlation technique. *Optics and Lasers in Engineering,* 46**,** 185-196.

HAGBERG, K., BRANEMARK, R., GUNTERBERG, B. & RYDEVIK, B. 2008. Osseointegrated trans-femoral amputation prostheses: prospective results of general and condition-specific quality of life in 18 patients at 2-year follow-up. *Prosthet Orthot Int,* 32**,** 29-41.

HAGBERG, K., BRÅNEMARK, R. & HÄGG, O. 2004. Questionnaire for Persons with a Transfemoral Amputation (Q-TFA): Initial validity and reliability of a new outcome measure. *Journal of Rehabilitation Research & Development,* 41.

HAGBERG, K., GHASSEMI JAHANI, S.-A., KULBACKA-ORTIZ, K., THOMSEN, P., MALCHAU, H. & REINHOLDT, C. 2020. A 15-year follow-up of transfemoral amputees with bone-anchored transcutaneous prostheses: mechanical complications and patient-reported outcomes. *The bone & joint journal,* 102**,** 55-63.

HAGBERG, K., HAGGSTROM, E., UDEN, M. & BRANEMARK, R. 2005a. Socket versus bone-anchored trans-femoral prostheses: hip range of motion and sitting comfort. *Prosthet Orthot Int,* 29**,** 153-63.

HAGBERG, K., HÄGGSTRÖM, E., UDEN, M. & BRÅNEMARK, R. 2005b. Socket versus bone-anchored trans-femoral prostheses: hip range of motion and sitting comfort. *Prosthetics and orthotics international,* 29**,** 153-163.

HAGBERG, K., HANSSON, E. & BRANEMARK, R. 2014. Outcome of percutaneous osseointegrated prostheses for patients with unilateral transfemoral amputation at two-year follow-up. *Arch Phys Med Rehabil,* 95**,** 2120-7.

HAKET, L. M., FROLKE, J. P. M., VERDONSCHOT, N., TOMASZEWSKI, P. K. & VAN DE MEENT, H. 2016. Periprosthetic cortical bone remodeling in patients with an osseointegrated leg prosthesis. *J Orthop Res,* 35**,** 1237-1241.

HALE, S. A. 1990. Analysis of the swing phase dynamics and muscular effort of the above-knee amputee for varying prosthetic shank loads. *Prosthetics and Orthotics International,* 14**,** 125-135.

HAMBLI, R. 2014. Connecting mechanics and bone cell activities in the bone remodeling process: an integrated finite element modeling. *Front Bioeng Biotechnol,* 2**,** 6.

HARWOOD, P. J. & STEWART, T. D. 2016. Mechanics of musculoskeletal repair devices. *Orthopaedics and Trauma,* 30**,** 192-200.

HAUGE, E. M., QVESEL, D., ERIKSEN, E. F., MOSEKILDE, L. & MELSEN, F. 2001. Cancellous bone remodeling occurs in specialized compartments lined by cells expressing osteoblastic markers. *J Bone Miner Res,* 16**,** 1575-82.

HAYASHI, M., NAKASHIMA, T., TANIGUCHI, M., KODAMA, T., KUMANOGOH, A. & TAKAYANAGI, H. 2012. Osteoprotection by semaphorin 3A. *Nature,* 485**,** 69.

HEBERT, J. S., REHANI, M. & STIEGELMAR, R. 2017. Osseointegration for Lower-Limb Amputation: A Systematic Review of Clinical Outcomes. *JBJS Rev,* 5**,** e10.

HEIMANN, R. B. 2018. Plasma-sprayed hydroxylapatite coatings as biocompatible intermediaries between inorganic implant surfaces and living tissue. *Journal of Thermal Spray Technology,* 27**,** 1212-1237.

HELGASON, B., GILCHRIST, S., ARIZA, O., CHAK, J., ZHENG, G., WIDMER, R., FERGUSON, S., GUY, P. & CRIPTON, P. A. 2014. Development of a balanced experimental–computational approach to understanding the mechanics of proximal femur fractures. *Medical engineering & physics,* 36**,** 793-799.

HERR, H. M. & GRABOWSKI, A. M. 2012. Bionic ankle–foot prosthesis normalizes walking gait for persons with leg amputation. *Proceedings of the Royal Society B: Biological Sciences,* 279**,** 457-464.

HOF, A. L., VAN BOCKEL, R. M., SCHOPPEN, T. & POSTEMA, K. 2007. Control of lateral balance in walking: experimental findings in normal subjects and above-knee amputees. *Gait & posture,* 25**,** 250-258.

HORCH, R. A., GOCHBERG, D. F., NYMAN, J. S. & DOES, M. D. 2011. Non-invasive predictors of human cortical bone mechanical properties: T 2-discriminated 1 H NMR compared with high resolution X-ray. *PloS one,* 6**,** e16359.

HUISKES, H. W. J. J., J.D.; SLOOFF, T.J.J.H. 1983. A detailed comparison of experimental and theoretical stress- analyses of a human femur. *Mechanical properties of bone,* 45**,** 211-234.

HUISKES, R. 1990. The various stress patterns of press-fit, ingrown, and cemented femoral stems. *bone*.

HUISKES, R., RUIMERMAN, R., VAN LENTHE, G. H. & JANSSEN, J. D. 2000. Effects of mechanical forces on maintenance and adaptation of form in trabecular bone. *Nature,* 405**,** 704.

HUISKES, R., WEINANS, H., GROOTENBOER, H. J., DALSTRA, M., FUDALA, B. & SLOOFF, T. J. 1987. Adaptive bone-remodeling theory applied to prosthetic-design analysis. *J Biomech,* 20**,** 1135-50.

HUSSAIN, S. & FINLAYSON, D. STEM SUBSIDENCE AS A FUNCTION OF TAPER ANGLE. Orthopaedic Proceedings, 2008. The British Editorial Society of Bone & Joint Surgery, 539-539.

IKEDA, M., KOMATSU, S.-Y., SOWA, I. & NIINOMI, M. 2002. Aging behavior of the Ti-29Nb-13Ta-4.6 Zr new beta alloy for medical implants. *Metallurgical and Materials Transactions A,* 33**,** 487-493.

INTEGRUM A.B. OPRA Implant System and OPRA RotaSafe.

JAEGERS, S. M., ARENDZEN, J. H. & DE JONGH, H. J. 1995. Prosthetic gait of unilateral transfemoral amputees: a kinematic study. *Archives of physical medicine and rehabilitation,* 76**,** 736-743.

JASTY, M., O'CONNOR, D. O., HENSHAW, R. M., HARRIGAN, T. P. & HARRIS, W. H. 1994. Fit of the uncemented femoral component and the use of cement influence the strain transfer to the femoral cortex. *Journal of orthopaedic research,* 12**,** 648-656.

JEON, S.-W., KIM, K.-I. & SONG, S. J. 2019. Robot-Assisted Total Knee Arthroplasty Does Not Improve Long-Term Clinical and Radiologic Outcomes. *The Journal of Arthroplasty,* 34**,** 1656-1661.

JIANG, P., HE, X., LI, X. A., YU, L. & WANG, H. 2000. Wear resistance of a laser surface alloyed Ti–6Al–4V alloy. *Surface and Coatings Technology,* 130**,** 24-28.

JOHN, C. T., SETH, A., SCHWARTZ, M. H. & DELP, S. L. 2012. Contributions of muscles to mediolateral ground reaction force over a range of walking speeds. *J Biomech,* 45**,** 2438-43.

JUHNKE, D. L., BECK, J. P., JEYAPALINA, S. & ASCHOFF, H. H. 2015. Fifteen years of experience with Integral-Leg-Prosthesis: Cohort study of artificial limb attachment system. *J Rehabil Res Dev,* 52**,** 407-20.

KAHLENBERG, C. A., NWACHUKWU, B. U., SCHAIRER, W. W., STEINHAUS, M. E. & CROSS, M. B. 2017. Patient satisfaction reporting after total hip arthroplasty: a systematic review. *Orthopedics,* 40**,** e400-e404.

KAHN-JETTER, Z. & CHU, T. 1990. Three-dimensional displacement measurements using digital image correlation and photogrammic analysis. *Experimental Mechanics,* 30**,** 10-16.

KANIS, J., JOHNELL, O., ODEN, A., JONSSON, B., DE LAET, C. & DAWSON, A. 2000. Risk of hip fracture according to the World Health Organization criteria for osteopenia and osteoporosis. *Bone,* 27**,** 585-590.

KAUFMAN, K. R., FRITTOLI, S. & FRIGO, C. A. 2012. Gait asymmetry of transfemoral amputees using mechanical and microprocessor-controlled prosthetic knees. *Clinical Biomechanics,* 27**,** 460-465.

KAUFMAN, K. R., LEVINE, J. A., BREY, R., IVERSON, B., MCCRADY, S., PADGETT, D. & JOYNER, M. J. 2007. Gait and balance of transfemoral amputees using passive mechanical and microprocessor-controlled prosthetic knees. *Gait & posture,* 26**,** 489-493.

KAUFMAN, K. R. & SUTHERLAND, D. H. 2006. Human Walking. *In:* (ED), G. J. (ed.) *Human walking.* 3rd ed ed. Philadelphia: Lippincott Williams & Wilkins.

KEAVENY, T. M. & BARTEL, D. L. 1993. Effects of porous coating and collar support on early load transfer for a cementless hip prosthesis. *Journal of biomechanics,* 26**,** 1205-1216.

KEAVENY, T. M. & BARTEL, D. L. 1994. Fundamental load transfer patterns for press-fit, surface-treated intramedullary fixation stems. *Journal of Biomechanics,* 27**,** 1147-1157.

KENNEDY, O. D., HERMAN, B. C., LAUDIER, D. M., MAJESKA, R. J., SUN, H. B. & SCHAFFLER, M. B. 2012. Activation of resorption in fatigue-loaded bone involves both apoptosis and active pro-osteoclastogenic signaling by distinct osteocyte populations. *Bone,* 50**,** 1115-1122.

KIM, Y.-H., KIM, J.-S. & CHO, S.-H. 2001. Strain distribution in the proximal human femur: an in vitro comparison in the intact femur and after insertion of reference and experimental femoral stems. *The Journal of bone and joint surgery. British volume,* 83**,** 295-301.

KIM, Y.-H., KIM, J.-S., OH, S.-H. & KIM, J.-M. 2003. Comparison of porous-coated titanium femoral stems with and without hydroxyapatite coating. *JBJS,* 85**,** 1682-1688.

KITCAT, M., HUNTER, J. E. & MALATA, C. M. 2009. Sciatic neuroma presenting forty years after above-knee amputation. *The open orthopaedics journal,* 3**,** 125-127.

KOBAYASHI, T., ORENDURFF, M. S. & BOONE, D. A. 2013. Effect of alignment changes on socket reaction moments during gait in transfemoral and knee-disarticulation prostheses: case series. *Journal of biomechanics,* 46**,** 2539-2545.

KOLLET, O., DAR, A., SHIVTIEL, S., KALINKOVICH, A., LAPID, K., SZTAINBERG, Y., TESIO, M., SAMSTEIN, R. M., GOICHBERG, P., SPIEGEL, A., ELSON, A. & LAPIDOT, T. 2006. Osteoclasts degrade endosteal components and promote mobilization of hematopoietic progenitor cells. *Nat Med,* 12**,** 657-64.

KOMNIK, I., DAVID, S., FUNKEN, J., HABERER, C., POTTHAST, W. & WEISS, S. 2018. Compromised knee internal rotation in total knee arthroplasty patients during stair climbing. *PloS one,* 13.

KRUGER, J. 1988. Passivity of metals–a materials science perspective. *International materials reviews,* 33**,** 113-130.

KUIKEN, T. A., BUTLER, B. A., SHARKEY, T., IVY, A. D., LI, D. & PEABODY, T. D. 2017. Novel intramedullary device for lengthening transfemoral residual limbs. *Journal of orthopaedic surgery and research,* 12**,** 1-7.

KULKARNI, J., ADAMS, J., THOMAS, E. & SILMAN, A. 1998. Association between amputation, arthritis and osteopenia in British male war veterans with major lower limb amputations. *Clinical Rehabilitation,* 12**,** 348-353.

KURODA, D., NIINOMI, M., MORINAGA, M., KATO, Y. & YASHIRO, T. 1998. Design and mechanical properties of new β type titanium alloys for implant materials. *Materials Science and Engineering: A,* 243**,** 244-249.

KUSTER, M., SAKURAI, S. & WOOD, G. 1995. Kinematic and kinetic comparison of downhill and level walking. *Clinical biomechanics,* 10**,** 79-84.

KUZYK, P. R. & SCHEMITSCH, E. H. 2011. The basic science of peri-implant bone healing. *Indian journal of orthopaedics,* 45**,** 108-115.

LANG, N. P., MOMBELLI, A., TONETTI, M. S., BRÄGGER, U. & HÄMMERLE, C. H. 1997. Clinical trials on therapies for peri‐implant infections. *Annals of periodontology,* 2**,** 343-356.

LANSDOWN, D. A., KUNZE, K., UKWUANI, G., WATERMAN, B. R. & NHO, S. J. 2018. The Importance of Comprehensive Cam Correction: Radiographic Parameters Are Predictive of Patient-Reported Outcome Measures at 2 Years After Hip Arthroscopy. *The American Journal of Sports Medicine,* 46**,** 2072-2078.

LANYON, L. 1987. Functional strain in bone tissue as an objective, and controlling stimulus for adaptive bone remodelling. *Journal of biomechanics,* 20**,** 1083-1093.

LANYON, L. E., GOODSHIP, A. E., PYE, C. & MACFIE, J. 1982. Mechanically adaptive bone remodelling. *Journal of biomechanics,* 15**,** 141-154.

LAY, A. N., HASS, C. J. & GREGOR, R. J. 2006. The effects of sloped surfaces on locomotion: a kinematic and kinetic analysis. *Journal of biomechanics,* 39**,** 1621-1628.

LEE, S. J. & HIDLER, J. 2008. Biomechanics of overground vs. treadmill walking in healthy individuals. *Journal of applied physiology,* 104**,** 747-755.

LEE, W. C., FROSSARD, L. A., HAGBERG, K., HAGGSTROM, E., BRANEMARK, R., EVANS, J. H. & PEARCY, M. J. 2007. Kinetics of transfemoral amputees with osseointegrated fixation performing common activities of daily living. *Clin Biomech (Bristol, Avon),* 22**,** 665-73.

LEE, W. C., FROSSARD, L. A., HAGBERG, K., HAGGSTROM, E., GOW, D. L., GRAY, S. & BRANEMARK, R. 2008. Magnitude and variability of loading on the osseointegrated implant of transfemoral amputees during walking. *Med Eng Phys,* 30**,** 825-33.

LI, X., FENG, Y.-F., WANG, C.-T., LI, G.-C., LEI, W., ZHANG, Z.-Y. & WANG, L. 2012. Evaluation of biological properties of electron beam melted Ti6Al4V implant with biomimetic coating in vitro and in vivo. *Plos one,* 7**,** e52049.

LI, Y. & BRANEMARK, R. 2017. Osseointegrated prostheses for rehabilitation following amputation : The pioneering Swedish model. *Unfallchirurg,* 120**,** 285-292.

LI, Y. & BRÅNEMARK, R. 2017. Osseointegrated prostheses for rehabilitation following amputation. *Der Unfallchirurg,* 120**,** 285-292.

LIEBERMAN, D. E., PEARSON, O. M., POLK, J. D., DEMES, B. & CROMPTON, A. W. 2003. Optimization of bone growth and remodeling in response to loading in tapered mammalian limbs. *Journal of Experimental Biology,* 206**,** 3125.

LIEBERMAN, D. E., POLK, J. D. & DEMES, B. 2004. Predicting long bone loading from cross‐sectional geometry. *American Journal of Physical Anthropology: The Official Publication of the American Association of Physical Anthropologists,* 123**,** 156-171.

LIN, L. & TORBECK, L. D. 1998. Coefficient of accuracy and concordance correlation coefficient: new statistics for methods comparison. *PDA Journal of Pharmaceutical Science and Technology,* 52**,** 55-59.

LING, S., LEE, A., GIE, G., TIMPERLEY, A. J., HUBBLE, M., HOWELL, J. & WHITEHOUSE, S. 2010. The Exeter Hip: 40 years of innovation in total hip arthroplasty.

LINKHART, T. A., MOHAN, S. & BAYLINK, D. J. 1996. Growth factors for bone growth and repair: IGF, TGFβ and BMP. 19**,** S1-S12.

LIU, M. Q., ANDERSON, F. C., SCHWARTZ, M. H. & DELP, S. L. 2008. Muscle contributions to support and progression over a range of walking speeds. *Journal of biomechanics,* 41**,** 3243-3252.

LIU, W. & NIGG, B. M. 2000. A mechanical model to determine the influence of masses and mass distribution on the impact force during running. *Journal of biomechanics,* 33**,** 219-224.

LOUDON, J. K., SWIFT, M. & BELL, S. 2008. *The clinical orthopedic assessment guide*, Human Kinetics.

MAGGS, J. & WILSON, M. 2017. The relative merits of cemented and uncemented prostheses in total hip arthroplasty. *Indian journal of orthopaedics,* 51**,** 377-385.

MAHON, C. E., PRUZINER, A. L., HENDERSHOT, B. D., WOLF, E. J., DARTER, B. J., FOREMAN, K. B. & WEBSTER, J. B. 2017. Gait and Functional Outcomes for Young, Active Males With Traumatic Unilateral Transfemoral Limb Loss. *Mil Med,* 182**,** e1913-e1923.

MALLOY, P., MORGAN, A., MEINERZ, C., GEISER, C. F. & KIPP, K. 2016. Hip external rotator strength is associated with better dynamic control of the lower extremity during landing tasks. *Journal of strength and conditioning research,* 30**,** 282.

MALONE, A. M., ANDERSON, C. T., TUMMALA, P., KWON, R. Y., JOHNSTON, T. R., STEARNS, T. & JACOBS, C. R. 2007. Primary cilia mediate mechanosensing in bone cells by a calcium-independent mechanism. *Proceedings of the National Academy of Sciences,* 104**,** 13325-13330.

MARASOVIĆ, T., CECIĆ, M. & ZANCHI, V. 2009. Analysis and interpretation of ground reaction forces in normal gait. *WSEAS transactions on systems,* 8**,** 1105-14.

MARCUS, R., FELDMAN, D. & KELSEY, J. 2001. *Osteoporosis, Two-Volume Set*, Academic Press.

MARKS, L. J. & MICHAEL, J. W. 2001. Artificial limbs. *Bmj,* 323**,** 732-735.

MATTHEWS, D. J., ARASTU, M., UDEN, M., SULLIVAN, J. P., BOLSAKOVA, K., ROBINSON, K., SOORIAKUMARAN, S. & WARD, D. 2018. UK trial of the Osseointegrated Prosthesis for the Rehabilitation for Amputees: 1995-2018. *Prosthet Orthot Int*, 309364618791616.

MAUNDER, E., DE ALMEIDA, J. M. & RAMSAY, A. 1996. A general formulation of equilibrium macro‐elements with control of spurious kinematic modes: the exorcism of an old curse. *International journal for numerical methods in engineering,* 39, 3175-3194.

MAVROGENIS, A., DIMITRIOU, R., PARVIZI, J. & BABIS, G. C. 2009. Biology of implant osseointegration. *J Musculoskelet Neuronal Interact,* 9, 61-71.

MCGOUGH, R. L., GOODMAN, M. A., RANDALL, R. L., FORSBERG, J. A., POTTER, B. K. & LINDSEY, B. 2017. The Compress(R) transcutaneous implant for rehabilitation following limb amputation. *Unfallchirurg,* 120, 300-305.

MCINTOSH, A. S., BEATTY, K. T., DWAN, L. N. & VICKERS, D. R. 2006. Gait dynamics on an inclined walkway. *Journal of biomechanics,* 39, 2491-2502.

MELLAL, A., WISKOTT, H. W., BOTSIS, J., SCHERRER, S. S. & BELSER, U. C. 2004. Stimulating effect of implant loading on surrounding bone. Comparison of three numerical models and validation by in vivo data. *Clin Oral Implants Res,* 15, 239-48.

MENGELKOCH, L. J., KAHLE, J. T. & HIGHSMITH, M. J. 2017. Energy costs and performance of transfemoral amputees and non-amputees during walking and running: A pilot study. *Prosthetics and orthotics international,* 41, 484-491.

MEULENBELT, H. E., GEERTZEN, J. H., DIJKSTRA, P. U. & JONKMAN, M. F. 2007. Skin problems in lower limb amputees: an overview by case reports. *Journal of the European Academy of Dermatology and Venereology,* 21, 147-155.

MEYER, J. S., FREITAG, T., REICHEL, H. & BIEGER, R. 2019. Periprosthetic Bone Mineral Density Changes After Implantation of a Curved Bone Preserving Hip Stem Compared to a Standard Length Straight Stem: 5-Yr Results of a Prospective, Randomized DXA-Analysis. *Journal of Clinical Densitometry,* 22, 96-103.

MIRZA, S. B., DUNLOP, D. G., PANESAR, S. S., NAQVI, S. G., GANGOO, S. & SALIH, S. 2010a. Basic science considerations in primary total hip replacement arthroplasty. *The open orthopaedics journal,* 4, 169-180.

MIRZA, S. B., DUNLOP, D. G., PANESAR, S. S., NAQVI, S. G., GANGOO, S. & SALIH, S. 2010b. Basic science considerations in primary total hip replacement arthroplasty. *The open orthopaedics journal,* 4, 169.

MOAZEN, M., MAK, J. H., ETCHELS, L. W., JIN, Z., WILCOX, R. K., JONES, A. C. & TSIRIDIS, E. 2013. The effect of fracture stability on the performance of locking plate fixation in periprosthetic femoral fractures. *The Journal of arthroplasty,* 28, 1589-1595.

MOLINA, C. S. & FAULK, J. 2019. Lower extremity amputation. *StatPearls [Internet].* StatPearls Publishing.

MOORE, M. S., MCAULEY, J. P., YOUNG, A. M. & ENGH SR, C. A. 2006. Radiographic signs of osseointegration in porous-coated acetabular components. *Clinical Orthopaedics and Related Research®,* 444, 176-183.

MORGAN, E. F., BAYRAKTAR, H. H. & KEAVENY, T. M. 2003. Trabecular bone modulus–density relationships depend on anatomic site. *Journal of Biomechanics,* 36, 897-904.

MORGAN, E. F., YEH, O. C., CHANG, W. C. & KEAVENY, T. M. 2000. Nonlinear behavior of trabecular bone at small strains. *J. Biomech. Eng.,* 123**,** 1-9.

MORGENROTH, D. C., ROLAND, M., PRUZINER, A. L. & CZERNIECKI, J. M. 2018. Transfemoral amputee intact limb loading and compensatory gait mechanics during down slope ambulation and the effect of prosthetic knee mechanisms. *Clinical Biomechanics,* 55**,** 65-72.

MORGENROTH, D. C., SEGAL, A. D., ZELIK, K. E., CZERNIECKI, J. M., KLUTE, G. K., ADAMCZYK, P. G., ORENDURFF, M. S., HAHN, M. E., COLLINS, S. H. & KUO, A. D. 2011. The effect of prosthetic foot push-off on mechanical loading associated with knee osteoarthritis in lower extremity amputees. *Gait & posture,* 34**,** 502-507.

MORITA, S., YAMAMOTO, H. & FURUYA, K. 1995. Gait analysis of hemiplegic patients by measurement of ground reaction force. *Scandinavian journal of rehabilitation medicine,* 27**,** 37-42.

MUIR, S. W., AL-AHAIDEB, A., HUCKELL, J., JOHNSON, M. A., JOHNSTON, D. B. C. & BEAUPRE, L. A. 2011. Radiographic assessment of uncemented total hip arthroplasty: reliability of the Engh Grading Scale. *Canadian Journal of Surgery,* 54**,** 185.

MULLENDER, M. & HUISKES, R. 1995. Proposal for the regulatory mechanism of Wolff's law. *Journal of orthopaedic research,* 13**,** 503-512.

MULLENDER, M., HUISKES, R. & WEINANS, H. 1994. A physiological approach to the simulation of bone remodeling as a self-organizational control process. *Journal of biomechanics,* 27**,** 1389-1394.

MYERS, C. A., LAZ, P. J., SHELBURNE, K. B., JUDD, D. L., HUFF, D. N., WINTERS, J. D., STEVENS-LAPSLEY, J. E. & RULLKOETTER, P. J. 2018. The impact of hip implant alignment on muscle and joint loading during dynamic activities. *Clinical Biomechanics,* 53**,** 93-100.

NAMIKI, Y., HASHIZUME, S., MURAI, A., KOBAYASHI, Y., TAKEMURA, H. & HOBARA, H. 2019. Joint moments during sprinting in unilateral transfemoral amputees wearing running-specific prostheses. *Biology open,* 8**,** bio039206.

NEBERGALL, A., BRAGDON, C., ANTONELLIS, A., KARRHOLM, J., BRANEMARK, R. & MALCHAU, H. 2012. Stable fixation of an osseointegated implant system for above-the-knee amputees: titel RSA and radiographic evaluation of migration and bone remodeling in 55 cases. *Acta Orthop,* 83**,** 121-8.

NEGISHI-KOGA, T., SHINOHARA, M., KOMATSU, N., BITO, H., KODAMA, T., FRIEDEL, R. H. & TAKAYANAGI, H. 2011. Suppression of bone formation by osteoclastic expression of semaphorin 4D. *Nature medicine,* 17**,** 1473.

NEIL, M. 2015. Pain after amputation. *BJA Education,* 16**,** 107-112.

NEWCOMBE, L., DEWAR, M., BLUNN, G. W. & FROMME, P. 2013. Effect of amputation level on the stress transferred to the femur by an artificial limb directly attached to the bone. *Med Eng Phys,* 35**,** 1744-53.

NOLAN, L., WIT, A., DUDZIÑSKI, K., LEES, A., LAKE, M. & WYCHOWAÑSKI, M. 2003. Adjustments in gait symmetry with walking speed in trans-femoral and trans-tibial amputees. *Gait & posture,* 17**,** 142-151.

O'CONNOR, J., LANYON, L. & MACFIE, H. 1982. The influence of strain rate on adaptive bone remodelling. *Journal of biomechanics,* 15**,** 767-781.

ORESKES, N., SHRADER-FRECHETTE, K. & BELITZ, K. 1994. Verification, validation, and confirmation of numerical models in the earth sciences. *Science,* 263**,** 641-646.

ÖRGEL, M., LIODAKIS, E., JARATJITWILAI, P., HARB, A., WIRRIES, N., OMAR, M., KRETTEK, C. & ASCHOFF, H.-H. 2020. Three-year follow-up of changes of cortical bone thickness after implantation of Endo-Exo-Prosthesis (EEP) for transfemoral amputees. *Journal of orthopaedic surgery and research,* 15**,** 1-10.

ORTIZ-CATALAN, M., MASTINU, E., SASSU, P., ASZMANN, O. & BRANEMARK, R. 2020. Self-Contained Neuromusculoskeletal Arm Prostheses. *N Engl J Med,* 382**,** 1732-1738.

ORWOLL, E. S. 2003. Toward an expanded understanding of the role of the periosteum in skeletal health. *Journal of Bone and Mineral Research,* 18**,** 949-954.

ORWOLL, E. S. & BLIZIOTES, M. 2002. *Osteoporosis: pathophysiology and clinical management*, Springer Science & Business Media.

ØSTBYHAUG, P. O., KLAKSVIK, J., ROMUNDSTAD, P. & AAMODT, A. 2013. Shortening of an anatomical stem, how short is short enough? An in vitro study of load transfer and primary stability. *Proceedings of the Institution of Mechanical Engineers, Part H: Journal of Engineering in Medicine,* 227**,** 481-489.

OSTERHOFF, G., MORGAN, E. F., SHEFELBINE, S. J., KARIM, L., MCNAMARA, L. M. & AUGAT, P. 2016. Bone mechanical properties and changes with osteoporosis. *Injury,* 47**,** S11-S20.

PARFITT, A. 2002. Targeted and nontargeted bone remodeling: relationship to basic multicellular unit origination and progression. *Bone,* 1**,** 5-7.

PARFITT, A. M. 1994. Osteonal and hemi-osteonal remodeling: The spatial and temporal framework for signal traffic in adult human bone. *Journal of Cellular Biochemistry,* 55**,** 273-286.

PARK, J. & LAKES, R. S. 2007. *Biomaterials: an introduction*, Springer Science & Business Media.

PARVATANENI, K., PLOEG, L., OLNEY, S. J. & BROUWER, B. 2009. Kinematic, kinetic and metabolic parameters of treadmill versus overground walking in healthy older adults. *Clinical biomechanics,* 24**,** 95-100.

PASCALE, B. A. & POTTER, B. K. 2014. Residual Limb Complications and Management Strategies. *Current Physical Medicine and Rehabilitation Reports,* 2**,** 241-249.

PATERNÒ, L., IBRAHIMI, M., GRUPPIONI, E., MENCIASSI, A. & RICOTTI, L. 2018. Sockets for limb prostheses: a review of existing technologies and open challenges. *IEEE Transactions on Biomedical Engineering,* 65**,** 1996-2010.

PAUWELS, F. 2012. *Biomechanics of the locomotor apparatus: contributions on the functional anatomy of the locomotor apparatus*, Springer Science & Business Media.

PEDERSON, L., RUAN, M., WESTENDORF, J. J., KHOSLA, S. & OURSLER, M. J. 2008. Regulation of bone formation by osteoclasts involves Wnt/BMP signaling and the chemokine sphingosine-1-phosphate. *Proceedings of the National Academy of Sciences,* 105**,** 20764-20769.

PENG, L., BAI, J., ZENG, X. & ZHOU, Y. 2006. Comparison of isotropic and orthotropic material property assignments on femoral finite element models under two loading conditions. *Med Eng Phys,* 28**,** 227-33.

PERRY, J. 2010. *Gait analysis : normal and pathological function / Jacquelin Perry, Judith M. Burnfield illustrated by Lydia M. Cabico,* Thorofare, N.J., Thorofare, N.J. : SLACK.

PETERS, W. & RANSON, W. 1982. Digital imaging techniques in experimental stress analysis. *Optical engineering,* 21**,** 213427.

PETRIE, C. S. & WILLIAMS, J. L. 2005. Comparative evaluation of implant designs: influence of diameter, length, and taper on strains in the alveolar crest: A three‐dimensional finite‐element analysis. *Clinical oral implants research,* 16**,** 486-494.

PHAN, T. C., XU, J. & ZHENG, M. H. 2004. Interaction between osteoblast and osteoclast: impact in bone disease. *Histol Histopathol,* 19**,** 1325-44.

PHEDY, P., ISMAIL, H. D., HOO, C. & DJAJA, Y. P. 2017. Total hip replacement: A meta-analysis to evaluate survival of cemented, cementless and hybrid implants. *World journal of orthopedics,* 8**,** 192.

PIDAPARTI, R. & TURNER, C. 1997. Cancellous bone architecture: advantages of nonorthogonal trabecular alignment under multidirectional joint loading. *Journal of biomechanics,* 30**,** 979-983.

PIERSON, J. L., SMALL, S. R., RODRIGUEZ, J. A., KANG, M. N. & GLASSMAN, A. H. 2015. The effect of taper angle and spline geometry on the initial stability of tapered, splined modular titanium stems. *The Journal of arthroplasty,* 30**,** 1254-1259.

PILZ, M., STAATS, K., TOBUDIC, S., ASSADIAN, O., PRESTERL, E., WINDHAGER, R. & HOLINKA, J. 2019. Zirconium Nitride Coating Reduced Staphylococcus epidermidis Biofilm Formation on Orthopaedic Implant Surfaces: An In Vitro Study. *Clinical Orthopaedics and Related Research®,* 477**,** 461-466.

PLUOT, E., DAVIS, E., REVELL, M., DAVIES, A. & JAMES, S. 2009a. Hip arthroplasty. Part 2: normal and abnormal radiographic findings. *Clinical radiology,* 64**,** 961-971.

PLUOT, E., DAVIS, E. T., REVELL, M., DAVIES, A. M. & JAMES, S. L. 2009b. Hip arthroplasty. Part 2: normal and abnormal radiographic findings. *Clin Radiol,* 64**,** 961-71.

POTTER, M. B. K., FORSBERG, L. J. A., DAVIS, T. A., EVANS, C. K. N., HAWKSWORTH, M. J. S., TADAKI, D., BROWN, T. S., CRANE, N. J., BURNS, M. T. C. & O'BRIEN, C. F. P. 2010. Heterotopic ossification following combat-related trauma. *JBJS,* 92**,** 74-89.

RABUFFETTI, M., RECALCATI, M. & FERRARIN, M. 2005. Trans-femoral amputee gait: Socket–pelvis constraints and compensation strategies. *Prosthetics and orthotics international,* 29**,** 183-192.

RAMAKRISHNA, K., SRIDHAR, I., SIVASHANKER, S., KHONG, K. S. & GHISTA, D. N. 2004. Design of Fracture Fixation Plate for Necessary and Sufficient Bone Stress Shielding. *JSME International Journal Series C Mechanical Systems, Machine Elements and Manufacturing,* 47**,** 1086-1094.

RAMSAY, A. 2018. *Distributed point load (DPL) software* [Online]. Angus Ramsay. Available: https://www.ramsay-maunder.co.uk/software/distributed-point-load-dpl/ [Accessed].

RANZ, E. C., WILKEN, J. M., GAJEWSKI, D. A. & NEPTUNE, R. R. 2017. The influence of limb alignment and transfemoral amputation technique on muscle capacity during gait. *Computer methods in BiomeChaniCs and BiomediCal engineering,* 20**,** 1167-1174.

RASTOGI, P. K. & HACK, E. 2013. *Optical methods for solid mechanics: a full-field approach*, John Wiley & Sons.

RAZFAR, N., REEVES, J. M., LANGOHR, D. G., WILLING, R., ATHWAL, G. S. & JOHNSON, J. A. 2016. Comparison of proximal humeral bone stresses between stemless, short stem, and standard stem length: a finite element analysis. *Journal of Shoulder and Elbow Surgery,* 25**,** 1076-1083.

REDFERN, M. S. & DIPASQUALE, J. 1997. Biomechanics of descending ramps. *Gait & posture,* 6**,** 119-125.

REILLY, G. C., HAUT, T. R., YELLOWLEY, C. E., J DONAHUE, H. & JACOBS, C. R. 2003. Fluid flow induced PGE 2 release by bone cells is reduced by glycocalyx degradation whereas calcium signals are not. *Biorheology,* 40**,** 591-603.

RICHARDSON, L. F. & GAUNT, J. A. 1927. VIII. The deferred approach to the limit. *Philosophical Transactions of the Royal Society of London. Series A, containing papers of a mathematical or physical character,* 226**,** 299-361.

RILEY, P. O., PAOLINI, G., DELLA CROCE, U., PAYLO, K. W. & KERRIGAN, D. C. 2007. A kinematic and kinetic comparison of overground and treadmill walking in healthy subjects. *Gait & posture,* 26**,** 17-24.

RITTER, M. A., DAVIS, K. E., MEDING, J. B., PIERSON, J. L., BEREND, M. E. & MALINZAK, R. A. 2011. The effect of alignment and BMI on failure of total knee replacement. *JBJS,* 93**,** 1588-1596.

ROACHE, P. J. 1998. Verification of codes and calculations. *AIAA journal,* 36**,** 696-702.

ROBERTSON, D. G. E., CALDWELL, G. E., HAMILL, J., KAMEN, G. & WHITTLESEY, S. 2013. *Research methods in biomechanics*, Human kinetics.

ROBLING, A. G., CASTILLO, A. B. & TURNER, C. H. 2006. Biomechanical and molecular regulation of bone remodeling. *Annu Rev Biomed Eng,* 8**,** 455-98.

ROCHEFORT, G. Y., PALLU, S. & BENHAMOU, C. L. 2010. Osteocyte: the unrecognized side of bone tissue. *Osteoporos Int,* 21**,** 1457-69.

ROUX, W. 1881. Der zuchtende Kampf der Teile, oder die “Teilauslese” im Organismus (Theorie der “funktionellen Anpassung”). *Leipzig: Wilhelm Engelmann*.

ROYER, T. D. & WASILEWSKI, C. A. 2006. Hip and knee frontal plane moments in persons with unilateral, trans-tibial amputation. *Gait & posture,* 23**,** 303-306.

RUBIN, C., GROSS, T., QIN, Y. X., FRITTON, S., GUILAK, F. & MCLEOD, K. 1996. Differentiation of the bone-tissue remodeling response to axial and torsional loading in the turkey ulna. *J Bone Joint Surg Am,* 78**,** 1523-33.

RUFF, C., HOLT, B. & TRINKAUS, E. 2006. Who's afraid of the big bad Wolff?:“Wolff's law” and bone functional adaptation. *American Journal of Physical Anthropology: The Official Publication of the American Association of Physical Anthropologists,* 129**,** 484-498.

RUIMERMAN, R., HUISKES, R., VAN LENTHE, G. & JANSSEN, J. 2001. A computer-simulation model relating bone-cell metabolism to mechanical adaptation of trabecular architecture. *Computer Methods in Biomechanics and Biomedical Engineering,* 4**,** 433-448.

RUSH, P. J., WONG, J. S.-W., KIRSH, J. & DEVLIN, M. 1994. Osteopenia in patients with above knee amputation. *Archives of physical medicine and rehabilitation,* 75**,** 112-115.

RUTKOWSKA-KUCHARSKA, A., KOWAL, M. & WINIARSKI, S. 2018. Relationship between asymmetry of gait and muscle torque in patients after unilateral transfemoral amputation. *Applied bionics and biomechanics,* 2018.

S.N.BERGER, J. E. E., S.FISHMAN 1990. *Lower-limb prosthetics,* [New York], New York University, Postgraduate Medical School, Prosthetics and Orthotics, New York University, Post-Graduate Medical School.

SAGAWA JR, Y., TURCOT, K., ARMAND, S., THEVENON, A., VUILLERME, N. & WATELAIN, E. 2011. Biomechanics and physiological parameters during gait in lower-limb amputees: a systematic review. *Gait & posture,* 33**,** 511-526.

SAIDPOUR, S. H. 2006. Assessment of Carbon Fibre Composite Fracture Fixation Plate Using Finite Element Analysis. *Annals of Biomedical Engineering,* 34**,** 1157-1163.

SALAWU, A., MIDDLETON, C., GILBERTSON, A., KODAVALI, K. & NEUMANN, V. 2006. Stump ulcers and continued prosthetic limb use. *Prosthetics and orthotics international,* 30**,** 279-285.

SAN ANTONIO, T., CIACCIA, M., MULLER-KARGER, C. & CASANOVA, E. 2012. Orientation of orthotropic material properties in a femur FE model: a method based on the principal stresses directions. *Med Eng Phys,* 34**,** 914-9.

SARGENT, R. G. 1984. A tutorial on verification and validation of simulation models. Institute of Electrical and Electronics Engineers (IEEE).

SCHAARSCHMIDT, M., LIPFERT, S. W., MEIER-GRATZ, C., SCHOLLE, H.-C. & SEYFARTH, A. 2012. Functional gait asymmetry of unilateral transfemoral amputees. *Human movement science,* 31**,** 907-917.

SCHMALZ, T., BELLMANN, M., PROEBSTING, E. & BLUMENTRITT, S. 2014. Effects of adaptation to a functionally new prosthetic lower-limb component: Results of biomechanical tests immediately after fitting and after 3 months of use. *JPO: Journal of Prosthetics and Orthotics,* 26**,** 134-143.

SCHMITZ, M., CLIFT, S., TAYLOR, W., HERTIG, D., WARNER, M., PLOEG, H. & BEREITER, H. 2004. Investigating the effect of remodelling signal type on the finite element based predictions of bone remodelling around the thrust plate prosthesis: a patient-specific comparison. *Proceedings of the Institution of Mechanical Engineers, Part H: Journal of Engineering in Medicine,* 218**,** 417-424.

SCHMITZ, R. J., HARRISON, D., WANG, H.-M. & SHULTZ, S. J. 2017. Sagittal-plane knee moment during gait and knee cartilage thickness. *Journal of athletic training,* 52**,** 560-566.

SCHROER, W. C., BEREND, K. R., LOMBARDI, A. V., BARNES, C. L., BOLOGNESI, M. P., BEREND, M. E., RITTER, M. A. & NUNLEY, R. M. 2013. Why are total knees failing today? Etiology of total knee revision in 2010 and 2011. *The Journal of arthroplasty,* 28**,** 116-119.

SCHULTE, F. A., RUFFONI, D., LAMBERS, F. M., CHRISTEN, D., WEBSTER, D. J., KUHN, G. & MÜLLER, R. 2013. Local mechanical stimuli regulate bone formation and resorption in mice at the tissue level. *PloS one,* 8**,** e62172.

SCHWARZE, M., HURSCHLER, C., SEEHAUS, F., OEHLER, S. & WELKE, B. 2013. Loads on the prosthesis–socket interface of above-knee amputees during normal gait: validation of a multi-body simulation. *Journal of biomechanics,* 46**,** 1201-1206.

SCHWER, L. E. 2007. An overview of the PTC 60/V&V 10: guide for verification and validation in computational solid mechanics. *Engineering with Computers,* 23**,** 245-252.

SCUDERI, G. R., BOURNE, R. B., NOBLE, P. C., BENJAMIN, J. B., LONNER, J. H. & SCOTT, W. 2012. The new knee society knee scoring system. *Clinical Orthopaedics and Related Research®,* 470**,** 3-19.

SEGAL, A. D., ORENDURFF, M. S., CZERNIECKI, J. M., SCHOEN, J. & KLUTE, G. K. 2011. Comparison of transtibial amputee and non-amputee biomechanics during a common turning task. *Gait & posture,* 33**,** 41-47.

SEGAL, A. D., ORENDURFF, M. S., KLUTE, G. K., MCDOWELL, M. L., PECORARO, J. A., SHOFER, J. & CZERNIECKI, J. M. 2006. Kinematic and kinetic comparisons of transfemoral amputee gait using C-Leg and Mauch SNS prosthetic knees. *Journal of Rehabilitation Research & Development,* 43.

SELLES, R. W., BUSSMANN, J. B., VAN SOEST, A. K. & STAM, H. J. 2004. The effect of prosthetic mass properties on the gait of transtibial amputees—a mathematical model. *Disability and rehabilitation,* 26**,** 694-704.

SHEN, G. 1998. Femoral stem fixation. An engineering interpretation of the long-term outcome of Charnley and Exeter stems. *J Bone Joint Surg Br,* 80**,** 754-6.

SHERK, V. D., BEMBEN, M. G. & BEMBEN, D. A. 2008. BMD and bone geometry in transtibial and transfemoral amputees. *J Bone Miner Res,* 23**,** 1449-57.

SHEVTSOV, M. A., YUDINTCEVA, N., BLINOVA, M., PINAEV, G., GALIBIN, O., POTOKIN, I., POPAT, K. C. & PITKIN, M. 2015. Application of the skin and bone integrated pylon with titanium oxide nanotubes and seeded with dermal fibroblasts. *Prosthetics and orthotics international,* 39**,** 477-486.

SILVERMAN, A. K., FEY, N. P., PORTILLO, A., WALDEN, J. G., BOSKER, G. & NEPTUNE, R. R. 2008. Compensatory mechanisms in below-knee amputee gait in response to increasing steady-state walking speeds. *Gait & posture,* 28**,** 602-609.

SIW 2017. ITAP Clinical investigation Final Report.

SKINNER, H. B. & EFFENEY, D. J. 1985. Gait analysis in amputees. *American journal of physical medicine,* 64**,** 82-89.

SOUTAS-LITTLE, R. W. 1998. Motion Analysis and Biomechanics. *J Rehabil Res Dev***,** 49-68.

STAGNI, R., LEARDINI, A., CAPPOZZO, A., BENEDETTI, M. G. & CAPPELLO, A. 2000. Effects of hip joint centre mislocation on gait analysis results. *Journal of biomechanics,* 33**,** 1479-1487.

STRUYF, P. A., VAN HEUGTEN, C. M., HITTERS, M. W. & SMEETS, R. J. 2009. The prevalence of osteoarthritis of the intact hip and knee among traumatic leg amputees. *Archives of physical medicine and rehabilitation,* 90**,** 440-446.

STUDY, P. R. 2008. *Transfemoral Amputation: The Basics and Beyond*, Prosthetics Research Study.

SUGIYAMA, T., MEAKIN, L. B., BROWNE, W. J., GALEA, G. L., PRICE, J. S. & LANYON, L. E. 2012. Bones' adaptive response to mechanical loading is essentially linear between the low strains associated with disuse and the high strains associated with the lamellar/woven bone transition. *Journal of bone and mineral research,* 27**,** 1784-1793.

SULLAVIN, J. & ZAHEDI, S. Transfemoral osseointegrated failsafe device requirements. International Society of Prosthetics and Orthotics, ISPO workshop, 18th Janurary 2018 Southampton, UK.

SULLIVAN, J., UDEN, M., ROBINSON, K. & SOORIAKUMARAN, S. 2003. Rehabilitation of the trans‐femoral amputee with an osseointegrated prosthesis: The United Kingdom experience. *Prosthetics and orthotics international,* 27**,** 114-120.

TAYLOR 2002. Determination of orthotropic bone elastic constants using FEA and modal analysis.

TAYTON, E., EVANS, S. & O'DOHERTY, D. 2010. Mapping the strain distribution on the proximal femur with titanium and flexible-stemmed implants using digital image correlation. *The Journal of bone and joint surgery. British volume,* 92**,** 1176-1181.

TEENY, S. M., YORK, S. C., MESKO, J. W. & REA, R. E. 2003. Long-term follow-up care recommendations after total hip and knee arthroplasty: results of the American Association of Hip and Knee Surgeons' member survey. *The Journal of arthroplasty,* 18**,** 954-962.

TESIO, L. & ROTA, V. 2019. The motion of body center of mass during walking: a review oriented to clinical applications. *Frontiers in neurology,* 10**,** 999.

THESLEFF, A., BRANEMARK, R., HAKANSSON, B. & ORTIZ-CATALAN, M. 2018a. Biomechanical Characterisation of Bone-anchored Implant Systems for Amputation Limb Prostheses: A Systematic Review. *Ann Biomed Eng,* 46**,** 377-391.

THESLEFF, A., BRÅNEMARK, R., HÅKANSSON, B. & ORTIZ-CATALAN, M. 2018b. Biomechanical characterisation of bone-anchored implant systems for amputation limb prostheses: a systematic review. *Annals of biomedical engineering,* 46**,** 377-391.

THOMPSON D'ARCY, W. 1917. On growth and form. *Cambridge: Cambridge University Press,* 16**,** 794.

THOMPSON, M., SCHELL, H., LIENAU, J. & DUDA, G. 2007. Digital image correlation: a technique for determining local mechanical conditions within early bone callus. *Medical engineering & physics,* 29**,** 820-823.

THOMSON, S., THOMSON, A., TETSWORTH, K., LU, W., ZREIQAT, H. & AL MUDERIS, M. 2019. Radiographic Evaluation of Bone Remodeling Around Osseointegration Implants Among Transfemoral Amputees. *J Orthop Trauma,* 33**,** e303-e308.

TILLANDER, J., HAGBERG, K., BERLIN, O., HAGBERG, L. & BRANEMARK, R. 2017. Osteomyelitis Risk in Patients With Transfemoral Amputations Treated With Osseointegration Prostheses. *Clin Orthop Relat Res,* 475**,** 3100-3108.

TOMASZEWSKI, P., VERDONSCHOT, N., BULSTRA, S., RIETMAN, J. S. & VERKERKE, G. J. 2012a. Simulated bone remodeling around two types of osseointegrated implants for direct fixation of upper-leg prostheses. *Journal of the mechanical behavior of biomedical materials,* 15**,** 167-175.

TOMASZEWSKI, P. K., VAN DIEST, M., BULSTRA, S. K., VERDONSCHOT, N. & VERKERKE, G. J. 2012b. Numerical analysis of an osseointegrated prosthesis fixation with reduced bone failure risk and periprosthetic bone loss. *J Biomech,* 45**,** 1875-80.

TONG, X., BURTON, I. S., ISAKSSON, H., JURVELIN, J. S. & KRÖGER, H. 2015. Cortical bone histomorphometry in male femoral neck: the investigation of age-association and regional differences. *Calcified tissue international,* 96**,** 295-306.

TRENT, A. & VAN DYKE, M. E. 2019. Development and characterization of a biomimetic coating for percutaneous devices. *Colloids and Surfaces B: Biointerfaces,* 182**,** 110351.

TURNER, C. H. 1998. Three rules for bone adaptation to mechanical stimuli. *Bone,* 23**,** 399-407.

TURNER, C. H. & BURR, D. B. 1993. Basic biomechanical measurements of bone: a tutorial. *Bone,* 14**,** 595-608.

TURNER, C. H., RHO, J., TAKANO, Y., TSUI, T. Y. & PHARR, G. M. 1999. The elastic properties of trabecular and cortical bone tissues are similar: results from two microscopic measurement techniques. *Journal of Biomechanics,* 32**,** 437-441.

TURNER, M. J., CLOUGH, R. W., MARTIN, H. C. & TOPP, L. 1956. Stiffness and deflection analysis of complex structures. *journal of the Aeronautical Sciences,* 23**,** 805-823.

TYROVOLA, J. B., SPYROPOULOS, M. N., MAKOU, M. & PERREA, D. 2008. Root resorption and the OPG/RANKL/RANK system: a mini review. *Journal of Oral Science,* 50**,** 367-376.

VAN DE MEENT, H., HOPMAN, M. T. & FRÖLKE, J. P. 2013. Walking ability and quality of life in subjects with transfemoral amputation: a comparison of osseointegration with socket prostheses. *Archives of physical medicine and rehabilitation,* 94**,** 2174-2178.

VAN INGEN SCHENAU, G. 1980. Some fundamental aspects of the biomechanics of overground versus treadmill locomotion. *Medicine and science in sports and exercise,* 12**,** 257-261.

VERDINI, F., MARCUCCI, M., BENEDETTI, M. & LEO, T. 2006. Identification and characterisation of heel strike transient. *Gait & posture,* 24**,** 77-84.

VERTRIEST, S., COOREVITS, P., HAGBERG, K., BRANEMARK, R., HAGGSTROM, E. E., VANDERSTRAETEN, G. & FROSSARD, L. A. 2017. Static load bearing exercises of individuals with transfemoral amputation fitted with an osseointegrated implant: Loading compliance. *Prosthet Orthot Int,* 41**,** 393-401.

VICECONTI, M., MUCCINI, R., BERNAKIEWICZ, M., BALEANI, M. & CRISTOFOLINI, L. 2000. Large-sliding contact elements accurately predict levels of bone–implant micromotion relevant to osseointegration. *Journal of biomechanics,* 33**,** 1611-1618.

VICECONTI, M., OLSEN, S., NOLTE, L. P. & BURTON, K. 2005. Extracting clinically relevant data from finite element simulations. *Clin Biomech (Bristol, Avon),* 20**,** 451-4.

WAGERMAIER, W., GUPTA, H. S., GOURRIER, A., BURGHAMMER, M., ROSCHGER, P. & FRATZL, P. 2006. Spiral twisting of fiber orientation inside bone lamellae. *Biointerphases,* 1**,** 1.

WATERS, R. L. & MULROY, S. 1999. The energy expenditure of normal and pathologic gait. *Gait & posture,* 9**,** 207-231.

WEAVER, M. J. 2017. Periprosthetic Femoral Fractures in the Emergency Department: What the Orthopedic Surgeon Wants to Know 1.

WEINANS, H., HUISKES, R. & GROOTENBOER, H. J. 1992. The behavior of adaptive bone-remodeling simulation models. *J Biomech,* 25**,** 1425-41.

WELLER, C. 2009. 4 - Interactive dressings and their role in moist wound management. *In:* RAJENDRAN, S. (ed.) *Advanced Textiles for Wound Care.* Woodhead Publishing.

WENTINK, E. C., PRINSEN, E. C., RIETMAN, J. S. & VELTINK, P. H. 2013. Comparison of muscle activity patterns of transfemoral amputees and control subjects during walking. *J Neuroeng Rehabil,* 10**,** 87.

WILLIAMS, D. F. 2008. On the mechanisms of biocompatibility. *Biomaterials,* 29**,** 2941-2953.

WINIARSKI, S. & RUTKOWSKA-KUCHARSKA, A. 2009. Estimated ground reaction force in normal and pathological gait. *Acta Bioeng Biomech,* 11**,** 53-60.

WINTER, D. A. 2009. *Biomechanics and motor control of human movement*, John Wiley & Sons.

WOLFF, J. 1892. Das gesetz der transformation der knochen. *A Hirshwald,* 1**,** 1-152.

WÜHR, J., VELTMANN, U., LINKEMEYER, L., DRERUP, B. & WETZ, H. 2007. Influence of modern above-knee prostheses on the biomechanics of gait. *Advances in Medical Engineering.* Springer.

XILLOC MEDICAL B.V. 2019. *Xilloc Click Safety Adapter* [Online]. Available: https://clicksafetyadapter.com/products_services/click-safety-adapters/click-safety-adapter/ [Accessed 18/12/19].

XU, W., CROCOMBE, A. D. & HUGHES, S. C. 2000. Finite element analysis of bone stress and strain around a distal osseointegrated implant for prosthetic limb attachment. *Proc Inst Mech Eng H,* 214**,** 595-602.

XU, W. & ROBINSON, K. 2008. X-ray image review of the bone remodeling around an osseointegrated trans-femoral implant and a finite element simulation case study. *Ann Biomed Eng,* 36**,** 435-43.

YANG, P., BRÜGGEMANN, G.-P. & RITTWEGER, J. 2011. What do we currently know from in vivo bone strain measurements in humans? *Journal of Musculoskeletal and Neuronal Interactions,* 11**,** 8-20.

YEOM, J. & PARK, S. 2011. A gravitational impulse model predicts collision impulse and mechanical work during a step-to-step transition. *Journal of Biomechanics,* 44**,** 59-67.

ZAID, M. B., O'DONNELL, R. J., POTTER, B. K. & FORSBERG, J. A. 2019a. Orthopaedic Osseointegration: State of the Art. *JAAOS - Journal of the American Academy of Orthopaedic Surgeons,* 27**,** e977-e985.

ZAID, M. B., O'DONNELL, R. J., POTTER, B. K. & FORSBERG, J. A. 2019b. Orthopaedic Osseointegration: State of the Art. *J Am Acad Orthop Surg,* 27**,** e977-e985.

ZAID, M. B., WUSTRACK, R. L., GARIBALDI, M., GEIGER, E., ANDAYA, V. & O'DONNELL, R. J. Prospective study of percutaneous bone-anchored implants in transfemoral amputees: Brain-machine platform technology for external prosthetic control and feedback. 2019 9th International IEEE/EMBS Conference on Neural Engineering (NER), 2019c. IEEE, 13-16.

ZHAO, C., IRIE, N., TAKADA, Y., SHIMODA, K., MIYAMOTO, T., NISHIWAKI, T., SUDA, T. & MATSUO, K. 2006. Bidirectional ephrinB2-EphB4 signaling controls bone homeostasis. *Cell metabolism,* 4**,** 111-121.